

Terrestrial Environmental Sciences

Olaf Kolditz · Hua Shao  
Wenqing Wang  
Sebastian Bauer *Editors*

# Thermo-Hydro- Mechanical-Chemical Processes in Fractured Porous Media: Modelling and Benchmarking

Closed-Form Solutions

 Springer

# **Terrestrial Environmental Sciences**

## **Series editors**

Olaf Kolditz  
Hua Shao  
Wenqing Wang  
Uwe-Jens Görke  
Sebastian Bauer

## **Guest editors**

Peter Vogel  
Jobst Maßmann

## **Managing editors**

Leslie Jakobs  
Barbara Kolditz

More information about this series at <http://www.springer.com/series/13468>

Olaf Kolditz · Hua Shao · Wenqing Wang  
Sebastian Bauer  
Editors

# Thermo-Hydro-Mechanical- Chemical Processes in Fractured Porous Media: Modelling and Benchmarking

Closed-Form Solutions

 Springer

*Editors*

Olaf Kolditz  
Wenqing Wang  
Environmental Informatics  
Helmholtz Centre for Environmental  
Research (UFZ)  
Leipzig  
Germany

Sebastian Bauer  
Institute of Geosciences  
Christian-Albrechts-Universität zu Kiel  
Kiel  
Germany

Hua Shao  
Federal Institute for Geosciences  
and Natural Resources (BGR)  
Hannover  
Germany

ISSN 2363-6181

ISBN 978-3-319-11893-2

DOI 10.1007/978-3-319-11894-9

ISSN 2363-619X (electronic)

ISBN 978-3-319-11894-9 (eBook)

Library of Congress Control Number: 2014955064

Springer Cham Heidelberg New York Dordrecht London

© Springer International Publishing Switzerland 2015

This work is subject to copyright. All rights are reserved by the Publisher, whether the whole or part of the material is concerned, specifically the rights of translation, reprinting, reuse of illustrations, recitation, broadcasting, reproduction on microfilms or in any other physical way, and transmission or information storage and retrieval, electronic adaptation, computer software, or by similar or dissimilar methodology now known or hereafter developed. Exempted from this legal reservation are brief excerpts in connection with reviews or scholarly analysis or material supplied specifically for the purpose of being entered and executed on a computer system, for exclusive use by the purchaser of the work. Duplication of this publication or parts thereof is permitted only under the provisions of the Copyright Law of the Publisher's location, in its current version, and permission for use must always be obtained from Springer. Permissions for use may be obtained through RightsLink at the Copyright Clearance Center. Violations are liable to prosecution under the respective Copyright Law.

The use of general descriptive names, registered names, trademarks, service marks, etc. in this publication does not imply, even in the absence of a specific statement, that such names are exempt from the relevant protective laws and regulations and therefore free for general use.

While the advice and information in this book are believed to be true and accurate at the date of publication, neither the authors nor the editors nor the publisher can accept any legal responsibility for any errors or omissions that may be made. The publisher makes no warranty, express or implied, with respect to the material contained herein.

Printed on acid-free paper

Springer is part of Springer Science+Business Media ([www.springer.com](http://www.springer.com))

# Contents

<b>1</b>	<b>Introduction</b> . . . . .	<b>1</b>
	Olaf Kolditz, Uwe-Jens Görke, Hua Shao, Wenqing Wang and Sebastian Bauer	
1.1	Motivation . . . . .	1
1.2	Application Areas . . . . .	3
1.3	Scope of This Book . . . . .	5
	References. . . . .	8

## Part I Closed Form Solutions

<b>2</b>	<b>Verification Tests</b> . . . . .	<b>13</b>
	Peter Vogel and Jobst Maßmann	
2.1	Heat Conduction. . . . .	14
2.1.1	A 1D Steady-State Temperature Distribution, Boundary Conditions of 1st Kind . . . . .	14
2.1.2	A 1D Steady-State Temperature Distribution, Boundary Conditions of 1st and 2nd Kind . . . . .	15
2.1.3	A 2D Steady-State Temperature Distribution, Boundary Conditions of 1st Kind . . . . .	16
2.1.4	A 2D Steady-State Temperature Distribution, Boundary Conditions of 1st and 2nd Kind . . . . .	17
2.1.5	A 3D Steady-State Temperature Distribution . . . . .	18
2.1.6	A Transient 1D Temperature Distribution, Time-Dependent Boundary Conditions of 1st Kind . . .	19
2.1.7	Transient 1D Temperature Distributions, Time-Dependent Boundary Conditions of 2nd Kind. . .	20
2.1.8	Transient 1D Temperature Distributions, Non-Zero Initial Temperature, Boundary Conditions of 1st and 2nd Kind . . . . .	21

2.1.9	A Transient 2D Temperature Distribution, Non-Zero Initial Temperature, Boundary Conditions of 1st and 2nd Kind . . . . .	23
2.2	Liquid Flow . . . . .	27
2.2.1	A 1D Steady-State Pressure Distribution, Boundary Conditions of 1st Kind . . . . .	27
2.2.2	A 1D Steady-State Pressure Distribution, Boundary Conditions of 1st and 2nd Kind . . . . .	27
2.2.3	A 2D Steady-State Pressure Distribution, Boundary Conditions of 1st Kind . . . . .	29
2.2.4	A 2D Steady-State Pressure Distribution, Boundary Conditions of 1st and 2nd Kind . . . . .	30
2.2.5	A 3D Steady-State Pressure Distribution . . . . .	31
2.2.6	A Hydrostatic Pressure Distribution . . . . .	32
2.2.7	A Transient 1D Pressure Distribution, Time-Dependent Boundary Conditions of 1st Kind . . . . .	32
2.2.8	Transient 1D Pressure Distributions, Time-Dependent Boundary Conditions of 2nd Kind . . . . .	33
2.2.9	Transient 1D Pressure Distributions, Non-Zero Initial Pressure, Boundary Conditions of 1st and 2nd Kind . . . . .	35
2.2.10	A Transient 2D Pressure Distribution, Non-Zero Initial Pressure, Boundary Conditions of 1st and 2nd Kind . . . . .	37
2.3	Gas Flow . . . . .	40
2.3.1	A 1D Steady-State Gas Pressure Distribution, Boundary Conditions of 1st Kind . . . . .	40
2.3.2	A 1D Steady-State Gas Pressure Distribution, Boundary Conditions of 1st and 2nd Kind . . . . .	41
2.3.3	A 2D Steady-State Gas Pressure Distribution . . . . .	42
2.3.4	A 3D Steady-State Gas Pressure Distribution . . . . .	43
2.4	Deformation Processes . . . . .	45
2.4.1	An Elastic Beam Undergoes Axial Load . . . . .	45
2.4.2	An Elastic Plate Undergoes Simple Shear . . . . .	46
2.4.3	An Elastic Cuboid Undergoes Load Due to Gravity . . . . .	47
2.4.4	Stresses Relax in a Deformed Cube of Norton Material . . . . .	48
2.4.5	A Cube of Norton Material Creeps Under Constant Stress . . . . .	51
2.4.6	A Cube of Norton Material Undergoes Tensile Strain Increasing Linearly with Time . . . . .	53
2.4.7	A Cube of Norton Material Undergoes Compressive Stress Increasing Linearly with Time . . . . .	55

2.5	Mass Transport . . . . .	57
2.5.1	Solute Transport Along Permeable Beams, Hydraulic and Solute Boundary Conditions of 1st and 2nd Kind . . . . .	57
2.5.2	Solute Transport Along Permeable Beams with an Inert, a Decaying, and an Adsorbing Solute, Time-Dependent Boundary Conditions of 1st Kind. . . . .	61
2.5.3	A Transient 2D Solute Distribution . . . . .	65
2.6	Hydrothermal Processes . . . . .	69
2.6.1	A Transient 1D Temperature Distribution in a Moving Liquid . . . . .	69
2.6.2	A Transient 2D Temperature Distribution in a Moving Liquid . . . . .	72
2.7	Hydromechanical Coupling . . . . .	76
2.7.1	A Permeable Elastic Beam Deforms Under Steady-State Internal Liquid Pressure . . . . .	76
2.7.2	A Permeable Elastic Square Deforms Under Constant Internal Liquid Pressure . . . . .	78
2.7.3	A Permeable Elastic Cube Deforms Under Constant Internal Liquid Pressure . . . . .	79
2.7.4	A Permeable Elastic Cuboid Undergoes Static Load Due to Gravity and Hydrostatic Liquid Pressure. . . . .	80
2.7.5	A Permeable Elastic Beam Deforms Under Transient Internal Liquid Pressure. Specified Boundary Conditions are Time-Dependent and of 1st Kind. . . . .	81
2.7.6	A Permeable Elastic Beam Deforms Under Transient Internal Liquid Pressure. Specified Boundary Conditions are Time-Dependent and of 1st and 2nd Kind . . . . .	84
2.7.7	Biot's 1D Consolidation Problem: Squeezing of a Pressurized Column Causes the Liquid to Discharge from the Domain . . . . .	87
2.8	Thermomechanics . . . . .	90
2.8.1	An Elastic Beam Deforms Due to an Instant Temperature Change . . . . .	90
2.8.2	An Elastic Square Deforms Due to an Instant Temperature Change . . . . .	92
2.8.3	An Elastic Cube Deforms Due to an Instant Temperature Change . . . . .	93
2.8.4	An Elastic Cuboid Undergoes Load Due to Gravity and Instant Temperature Change . . . . .	94

2.8.5	An Elastic Beam Deforms Due to a Transient Temperature Change. Temperature Boundary Conditions are Time-Dependent and of 1st Kind . . . . .	96
2.8.6	Elastic Beams Deform Due to a Transient Temperature Change. Temperature Boundary Conditions are Time-Dependent and of 2nd Kind . . . . .	98
2.8.7	Stresses Relax in a Cube of Norton Material Undergoing an Instant Temperature Change . . . . .	101
2.9	Thermo-Hydro-Mechanical Coupling . . . . .	104
2.9.1	A Permeable Elastic Cuboid Deforms Due to Gravity, Internal Liquid Pressure, and Instant Temperature Change . . . . .	104
2.9.2	A Permeable Elastic Beam Deforms Due to Cooling Liquid Injection . . . . .	106
	References. . . . .	110

## Part II Single Processes

<b>3</b>	<b>Groundwater Flow—Theis' Revisited.</b> . . . . .	115
	Wenkui He	
3.1	Problem Definition . . . . .	115
3.2	Theis' 1.5D and 2.5D . . . . .	115
3.3	Theis' 2D . . . . .	117
3.4	Theis' 3D . . . . .	118
3.5	Results . . . . .	118
	Reference . . . . .	120
<b>4</b>	<b>Richards Flow</b> . . . . .	121
	Thomas Kalbacher, Xi Chen, Ying Dai, Jürgen Hesser, Xuerui Wang and Wenqing Wang	
4.1	Comparison with Differential Transform Method (DTM) . . . . .	121
4.2	Undrained Heating . . . . .	124
4.2.1	Definition (1D) . . . . .	126
4.2.2	Heating a Saturated Sample . . . . .	127
4.2.3	Heating an Unsaturated Sample. . . . .	129
4.2.4	Results. . . . .	130
	References. . . . .	130
<b>5</b>	<b>Multi-Componential Fluid Flow.</b> . . . . .	131
	Ashok Singh	
5.1	Basic Equations . . . . .	131
5.1.1	Mass Balance Equation . . . . .	132
5.1.2	Fractional Mass Transport Equation. . . . .	132

5.1.3	Heat Transport Equation . . . . .	133
5.1.4	Equation of State . . . . .	135
5.2	Examples . . . . .	139
5.2.1	Tracer Test. . . . .	139
5.2.2	Bottom Hole Pressure . . . . .	141
5.2.3	Plume Migration . . . . .	144
5.2.4	CO <sub>2</sub> Leakage Through Abandoned Well . . . . .	146
5.2.5	Thermo-Chemical Energy Storage . . . . .	148
	References. . . . .	152
<b>6</b>	<b>Random Walk Particle Tracking . . . . .</b>	<b>153</b>
	Yuanyuan Sun, Chan-Hee Park, Geraldine Pichot and Joshua Taron	
6.1	Particle Tracking in Porous Medium . . . . .	156
6.1.1	Particle Tracking in Porous Medium: 1D Case Study . . . . .	156
6.1.2	Particle Tracking in Porous Medium: 2D Case Study . . . . .	160
6.1.3	Particle Tracking in Porous Medium: 3D Case Study . . . . .	162
6.2	Particle Tracking in Pore Scale . . . . .	165
6.2.1	Particle Tracking in Pore Scale: 2D Case Study . . . . .	166
6.2.2	Particle Tracking in Pore Scale: 3D Case Study . . . . .	170
6.3	Particle Tracking with Different Flow Processes . . . . .	174
6.3.1	Forchheimer Term. . . . .	174
6.3.2	Forchheimer Flow in 1D Porous Medium. . . . .	176
6.3.3	Groundwater Flow Regimes . . . . .	180
6.4	Particle Tracking in Fractured Porous Media . . . . .	181
6.4.1	Uncertainty in Flow, Preferential Flow. . . . .	183
	References. . . . .	183
<b>7</b>	<b>Mechanical Processes . . . . .</b>	<b>185</b>
	Thomas Nagel and Norbert Böttcher	
7.1	Theory and Implementation . . . . .	185
7.2	Deformation of a Steel Tubing . . . . .	186
7.2.1	Analytical Solution—Linear Elasticity . . . . .	186
7.2.2	Numerical Solution . . . . .	188
7.3	Deformation of a Thick-Walled, Hollow Sphere . . . . .	189
7.3.1	Analytical Solution—Linear Elasticity . . . . .	189
7.3.2	Numerical Solution—Linear Elasticity . . . . .	191
7.3.3	Analytical Solution—Elastoplasticity . . . . .	193
7.3.4	Numerical Solution—Elastoplastic Deformation of a Sphere . . . . .	195

7.4	Deformation of an Artificial Salt Cavern . . . . .	196
7.4.1	Linear Elastic Material. . . . .	196
7.4.2	Elastoplastic Material. . . . .	199
	References. . . . .	201

### Part III Coupled Processes

<b>8</b>	<b>Density-Dependent Flow . . . . .</b>	<b>205</b>
	Marc Walther, Leonard Stoeckl, Jens-Olaf Delfs and Thomas Graf	
8.1	Haline Setups . . . . .	206
8.1.1	Development and Degregation of a Freshwater Lens . . . . .	206
8.2	Thermohaline Setups . . . . .	208
8.2.1	Stability in Rayleigh Convection. . . . .	208
	References. . . . .	212
<b>9</b>	<b>Multiphase Flow and Transport with OGS-ECLIPSE. . . . .</b>	<b>213</b>
	Wolf Tilmann Pfeiffer, Christof Beyer, Bastian Graupner and Sebastian Bauer	
9.1	Introduction . . . . .	213
9.2	Test Cases . . . . .	215
9.2.1	Two-Phase Flow with Two-Phase Transport. . . . .	215
9.2.2	Gas Phase Partitioning. . . . .	217
	References. . . . .	219
<b>10</b>	<b>Coupled THM Processes . . . . .</b>	<b>221</b>
	Fabien Magri, Jobst Maßmann, Wenqing Wang and Katharina Benisch	
10.1	HM/THM Processes in a Faulted Aquifer. . . . .	221
10.1.1	Definition. . . . .	221
10.1.2	Initial and Boundary Conditions . . . . .	223
10.1.3	Material Properties . . . . .	223
10.1.4	Results. . . . .	224
10.1.5	Initial Conditions Effects . . . . .	226
10.1.6	Temperature Effects THM Simulation . . . . .	226
10.2	Injection Induced Hydromechanical (HM) Processes . . . . .	232
10.2.1	Definition. . . . .	232
10.2.2	Solution. . . . .	232
10.2.3	Model Description. . . . .	232
10.2.4	Results. . . . .	235

10.3	AnSichT THM Test Case. . . . .	238
10.3.1	Definition. . . . .	238
10.3.2	Results. . . . .	241
10.4	Consolidation Under Two-Phase Flow Condition: Five Spot Example . . . . .	241
	References. . . . .	245
<b>11</b>	<b>Thermo-Mechanics: Stress-Induced Heating of Elastic Solids . . . .</b>	<b>247</b>
	Norihiro Watanabe, Guido Blöcher, Harald Milsch and Andreas Reinicke	
11.1	Theory. . . . .	247
11.2	Problem Definition . . . . .	249
11.3	Analytical Solution . . . . .	251
11.4	Numerical Solution . . . . .	252
11.5	Results . . . . .	252
	References. . . . .	254
<b>12</b>	<b>Reactive Transport . . . . .</b>	<b>255</b>
	Christof Beyer, Thomas Nagel and Haibing Shao	
12.1	Kinetic Dissolution of Non-aqueous Phase Liquids . . . . .	255
12.1.1	Hansen and Kueper Benchmark . . . . .	257
12.2	Kinetic Mineral Dissolution/Precipitation . . . . .	261
12.2.1	Simulation of a Kinetic Calcite/Dolomite Dissolution Front . . . . .	262
12.3	Local Thermal Nonequilibrium and Gas–Solid Reactions . . . . .	264
12.3.1	Introduction . . . . .	264
12.3.2	Interphase Heat Transfer . . . . .	264
12.3.3	Interphase Mass Transfer and Heat of Reaction. . . . .	266
12.3.4	Interphase Friction. . . . .	269
12.3.5	Steady State Heat Conduction with Heat Generation and Convection Boundary Conditions . . . . .	270
	References. . . . .	274
	<b>Appendix A: Introduction to OpenGeoSys (OGS): OGS—Overview. . .</b>	<b>277</b>
	<b>Appendix B: OGS—Software Engineering . . . . .</b>	<b>287</b>
	<b>Appendix C: Data Preprocessing and Model Setup with OGS . . . . .</b>	<b>291</b>
	<b>Appendix D: GINA-OGS . . . . .</b>	<b>297</b>
	<b>Appendix E: Scientific Visualization and Virtual Reality . . . . .</b>	<b>301</b>
	<b>Appendix F: OGS High-Performance-Computing . . . . .</b>	<b>307</b>

# Contributing Authors

Sebastian Bauer, Christian-Albrechts University of Kiel (CAU)  
Katharina Benisch, Christian-Albrechts University of Kiel (CAU)  
Christof Beyer, Christian-Albrechts University of Kiel (CAU)  
Lars Bilke, Helmholtz Centre for Environmental Research (UFZ)  
Guido Blöcher, GFZ German Research Centre for Geosciences  
Norbert Boettcher, Helmholtz Centre for Environmental Research (UFZ)  
Xi Chen, Tongji University, Shanghai, China  
Ying Dai, Tongji University, Shanghai, China  
Jens-Olaf Delfs, Helmholtz Centre for Environmental Research (UFZ)  
Peter Dietrich, Helmholtz Centre for Environmental Research (UFZ)  
Thomas Fischer, Helmholtz Centre for Environmental Research (UFZ)  
Thomas Graf, Leibniz Universität Hannover  
Uwe-Jens Görke, Helmholtz Centre for Environmental Research (UFZ)  
Bastian Graupner, ENSI, Switzerland  
Wenkui He, Helmholtz Centre for Environmental Research (UFZ)  
Carolin Helbig, Helmholtz Centre for Environmental Research (UFZ)  
Jürgen Hesser, Federal Institute for Geosciences and Natural Resources (BGR)  
Michael Jobmann, DBE-Technology GmbH, Peine, Germany  
Thomas Kalbacher, Helmholtz Centre for Environmental Research (UFZ)  
Thomas Kempka, GFZ German Research Centre for Geosciences  
Olaf Kolditz, Helmholtz Centre for Environmental Research (UFZ); Technische  
Universität Dresden (TUD)  
Georg Kosakowski, Paul-Scherrer-Institute (PSI), Switzerland  
Sha Li, DBE-Technology GmbH, Peine, Germany  
Fabien Magri, GFZ German Research Centre for Geosciences  
Jobst Maßmann, Federal Institute for Geosciences and Natural Resources (BGR)  
Christopher McDermott, University of Edinburgh (UE), UK  
Harald Milsch, GFZ German Research Centre for Geosciences  
Thomas Nagel, Helmholtz Centre for Environmental Research (UFZ)  
Thomas Nowak, Federal Institute for Geosciences and Natural Resources (BGR)

Chan-Hee Park, Korea Institute of Geoscience and Mineral Resources (KIGAM),  
Korea

Wolf Tilmann Pfeiffer, Christian-Albrechts University of Kiel (CAU)

Andreas Reinicke, GFZ German Research Centre for Geosciences

Karsten Rink, Helmholtz Centre for Environmental Research (UFZ)

Agnes Sachse, Helmholtz Centre for Environmental Research (UFZ)

Sophie Schelenz, Helmholtz Centre for Environmental Research (UFZ)

Haibing Shao, Helmholtz Centre for Environmental Research (UFZ); TU  
Bergakademie Freiberg; Chinese Academy of Sciences, Institute of Energy  
Conversion, Guangzhou, China

Hua Shao, Federal Institute for Geosciences and Natural Resources (BGR)

Ashok K. Singh, Helmholtz Centre for Environmental Research (UFZ); University  
of Southern Denmark, Odense, Denmark

Leonard Stoeckl, Federal Institute for Geosciences and Natural Resources (BGR)

Yuanyuan Sun, Helmholtz Centre for Environmental Research (UFZ)

Joshua Taron, United States Geological Survey (USGS)

Elena Tillner, GFZ German Research Centre for Geosciences

Thomas Vienken, Helmholtz Centre for Environmental Research (UFZ)

Peter Vogel, Federal Institute for Geosciences and Natural Resources (BGR)

Marc Walther, Helmholtz Centre for Environmental Research (UFZ); Technische  
Universität Dresden (TUD)

Wenqing Wang, Helmholtz Centre for Environmental Research (UFZ)

Xuerui Wang, Federal Institute for Geosciences and Natural Resources (BGR)

Norihiro Watanabe, Helmholtz Centre for Environmental Research (UFZ)

Björn Zehner, TU Bergakademie Freiberg

Günter Zimmermann, GFZ German Research Centre for Geosciences



# Chapter 1

## Introduction

Olaf Kolditz, Uwe-Jens Görke, Hua Shao, Wenqing Wang  
and Sebastian Bauer

### 1.1 Motivation

In nature, processes are coupled strongly with each other. Much progress has been achieved towards understanding the complicated processes in deep geological disposal of radioactive waste, CO<sub>2</sub> subsurface sequences, geothermal applications and energy storage.

Numerical tools dealing with the coupled thermal, hydraulic, mechanical, chemical and biological processes have been developed to analyze experimental outputs, field observations, laboratory tests. One important issue in the development of numerical codes is of course the code validation and model comparison. Therefore, different international benchmarking projects have been announced for this purpose, such as DECOVALEX project (1992–2015), CO<sub>2</sub>Bench, SSBench, and Sim-SEQ.

For long-term performance and safety assessment of nuclear waste isolation in deep geological formations, an important issue is the need to guarantee the isolation of an underground repository. To answer this question, radioactive nuclide transport processes under the coupled conditions involving mechanical stability, thermal loading from the high-level waste, and chemistry in the groundwater should be predicted numerically to get quantitative assessment of a repository. For these purposes, underground laboratories in the different geological formations have been constructed for extensive research covering geomechanical, geohydraulic, geochemical investigations of geological circumstances, geotechnical materials and their interaction.

---

O. Kolditz (✉) · U-J. Görke · W. Wang  
Helmholtz Centre for Environmental Research UFZ, Permoserstr. 15, 04318 Leipzig, Germany  
e-mail: Olaf.Kolditz@ufz.de

H. Shao  
Federal Institute for Geosciences and Natural Resources (BGR), Hannover, Germany

S. Bauer  
Christian-Albrechts University of Kiel (CAU), Kiel, Germany

© Springer International Publishing Switzerland 2015

O. Kolditz et al. (eds.), *Thermo-Hydro-Mechanical-Chemical Processes in Fractured Porous Media: Modelling and Benchmarking*, Terrestrial Environmental Sciences,  
DOI 10.1007/978-3-319-11894-9\_1

In Europe, underground laboratories have been constructed in recent decades, e.g. Grimsel Test Site (Switzerland) and Hard Rock Laboratories Äspö (Sweden) in the granitic rock; Rock laboratories Mont Terri (Switzerland) and Bure (France) in clay rock. Different field experiments have been conducted for the understanding of processes under the in situ conditions. To implement experimental data gained from the in situ test, a multiple-process coupled code is required (Fig. 1.1).

In the course of the quick development of computer technology, numerical codes with capability to analyze problems in the coupled manner have become possible. However, the understanding of the complicated coupled processes based on the experimental data available and implementation of the developed algorithm into the numerical codes are a major challenge for scientists, which require interdisciplinary cooperation and interactive procedures.

Quality management and controlling is nowadays a standard tool for production and development to ensure a high quality of a produced result. A numerical code dealing with the coupled THMC process is highly complicated software product,

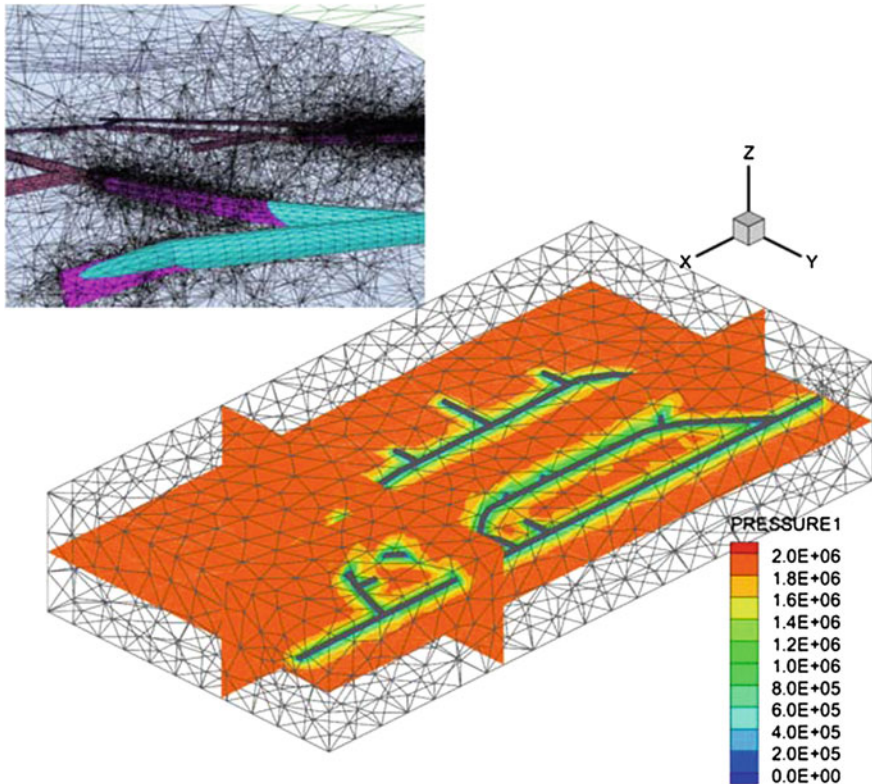


**Fig. 1.1** Pore water pressure distribution of Rock Laboratory Mont Terri (Switzerland) after 10 years, calculated using code OGS in a 3D total mesh taking geological bedding, fault zone and geotechnical tunnel into consideration

since the different processes have different characteristic features, e.g. time and spatial scales, nonlinearities, and interaction degree, etc. To keep the high quality of the developed code, benchmark testing is therefore necessary, especially in case scientists from different disciplinary and different organizations are working on the same code. Therefore, code verification and validation of selected test cases are documented, and finally a benchmarking book for code developers (DBB) is produced and quality-ensured.

## 1.2 Application Areas

The coupling phenomena of thermal (T), hydraulic (H), and mechanical (M) processes are important for the analysis of deep geosystems under high temperature, pressure and stress conditions. Application areas of THM coupled models are e.g. geothermal energy utilization, nuclear waste disposal, and carbon dioxide storage in the deep geological formation (Fig. 1.2).

The following slides illustrate that the understanding of THM processes, including chemical reactions (C process) is important to a large variety of geotechnical and geothermal applications. The physical basics are exactly the same for these applications. Different is simply

- the geological environment and different rock types, i.e. crystalline rocks, volcanic rocks, sandstones, clay, bentonite, ...
- the geofluids, i.e. water, brines, vapour, methane, carbon dioxide, ...
- the thermodynamic conditions, i.e. temperature, stress, pressure, salinity, ...

There are several concepts concerning host rock for the disposal of hazardous waste in deep geological media, i.e. crystalline, salt, sediment, and volcanic formations. Different concepts use different buffer systems as geotechnical barriers for the

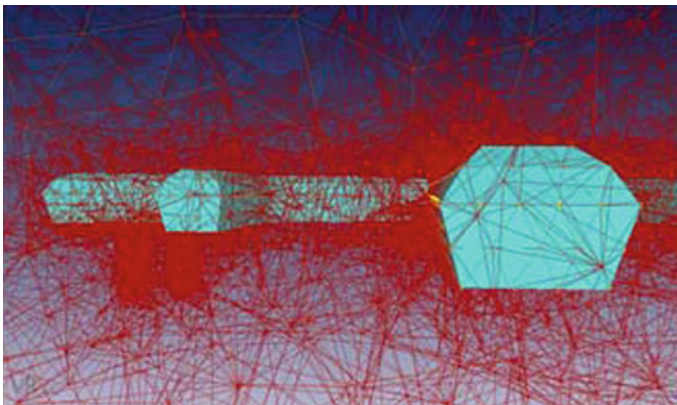


**Fig. 1.2** Tunnel system (Visualization by B. Zehner)

waste isolation, i.e. crushed salt, bentonite, and bentonite/sand mixture. THM/C coupled modelling is required for the long-term analysis of possible processes which might result in a release of contaminants from the repository [1]. In that case it is important to know, how long it will take until the contaminants return into the biosphere.

Figure 1.3 illustrates the application area: **Carbon Capture Storage (CCS)**. The idea is to capture the  $\text{CO}_2$  from the power plants, liquefy it and inject it into the subsurface for long-term storage. Two basic concepts for appropriate geological systems are under proof now: depleted gas reservoirs and deep saline aquifers. After many years of operation many former gas reservoirs are depleted. These reservoirs are in an under pressurized status and can take up large volumes of fluids. Keeping the reservoir under pressurized and the impervious cap rocks are important considerations for storage. THM/C modelling is required in order to calculate the possible fluid storage capacity and to better understand the highly coupled processes in the  $\text{CO}_2$  injection area as well as their consequences for the storage concept [2].

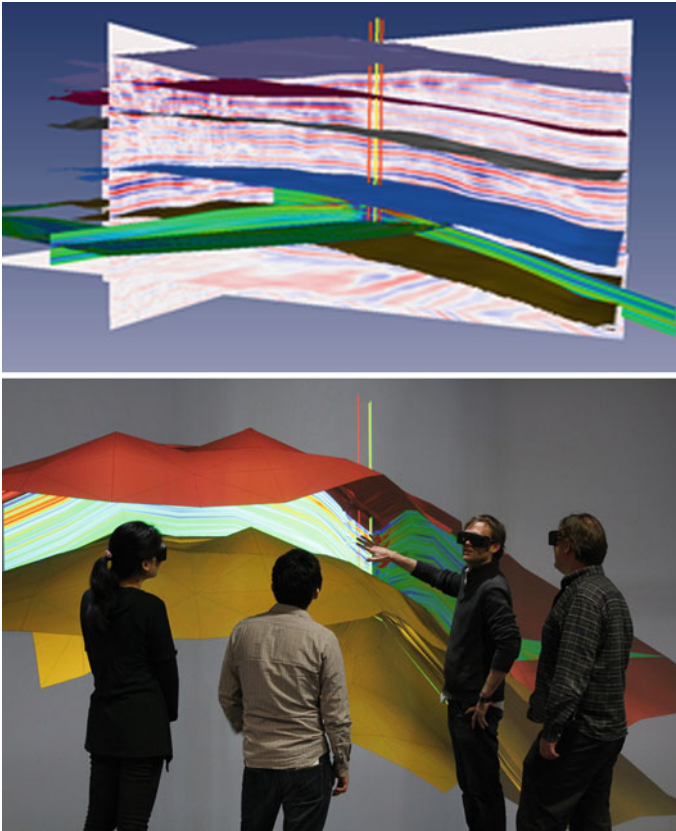


**Fig. 1.3** Subsurface reservoir for  $\text{CO}_2$  storage

### 1.3 Scope of This Book

This is the second volume of “Thermo-Hydro-Mechanical/Chemical Processes in Porous-Fractured Media” [3] presenting new benchmarks and examples for THMC processes. The theoretical background as well as numerical methods are not repeated as can be found in the first volume. Access to OGS source code, executables for different platforms as well as benchmark configuration files are available through the OGS community webpage [www.opengeosys.org](http://www.opengeosys.org).

Figure 1.4 depicts the application area: **Geothermal energy**, which is one of the alternative future energy resources under consideration. So-called shallow and deep geothermal systems are distinguished. Shallow systems are already commercially used e.g. for heating purposes. Deep geothermal reservoirs can be used for electric power production as high temperatures up to 200C can be produced. THM/C modeling is required to design these geothermal power plants, e.g. in order to optimize

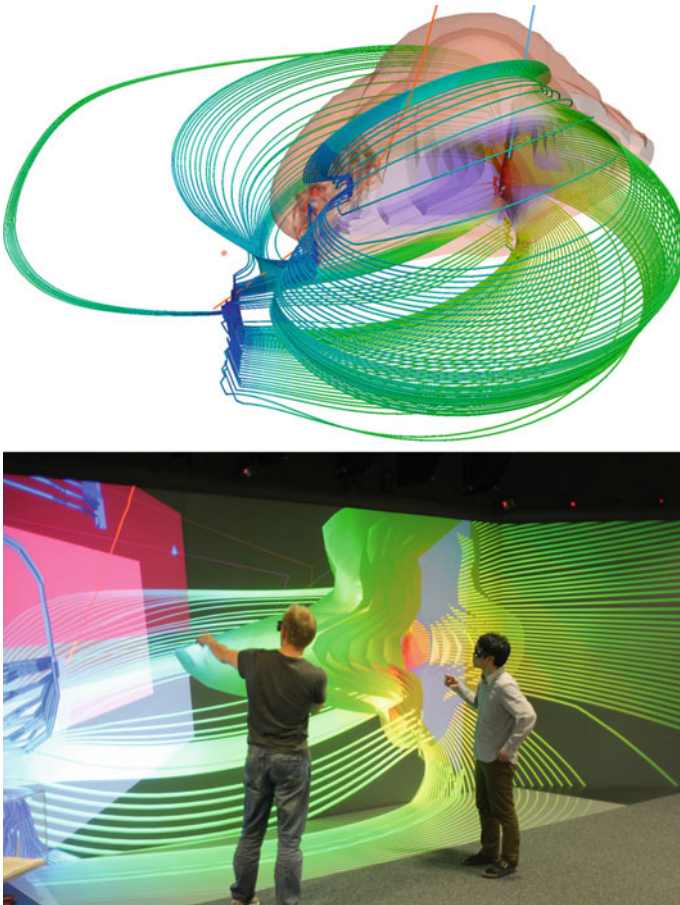
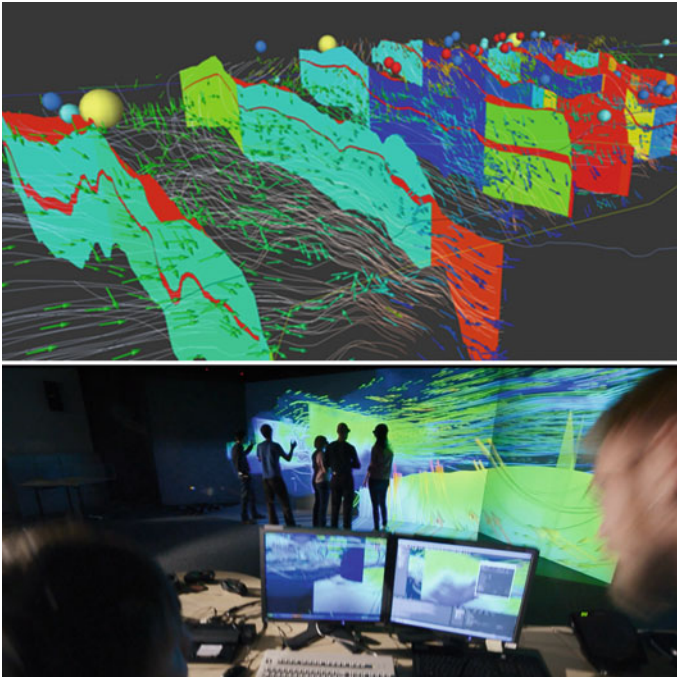


Fig. 1.4 Geothermal reservoir simulation

production efficiency and reservoir lifetime. The significant cooling of the reservoir due to fluid reinjection gives rise to thermo-mechanical effects which need to be controlled in order to avoid reservoir damage [4].

The second application area for coupled process simulation is **hydrology**. River basins or catchments are also subject to THMC coupled processes, but include however a completely different range of thermodynamic conditions than deep geological systems. Hydrological processes are very complex to describe as they vary highly in time and space. The evaluation of groundwater recharge is vital to a sustainable water resources management (so called safe yield). To this purpose, i.e. the understanding of small scale phenomena such as root/soil water interaction is of tremendous significance [5]. Typically groundwater models are used for management purposes particularly in semi-arid areas such as the Jordan Valley in the Middle East [6] (Fig. 1.5).

Because water availability is an important issue in semi-arid and arid regions, groundwater quality deterioration is a critical concern in many urban areas of the world. Figure 1.6 shows as an example part of a groundwater quality model prepared for the Nankou basin in the greater Beijing area. The idea of this modelling project is to identify possible sources of nitrate contamination originating from intense agriculture and fertilizer production [8]. Land use and climate changes will impact the



**Fig. 1.5** Groundwater model of Western Jordan Valley

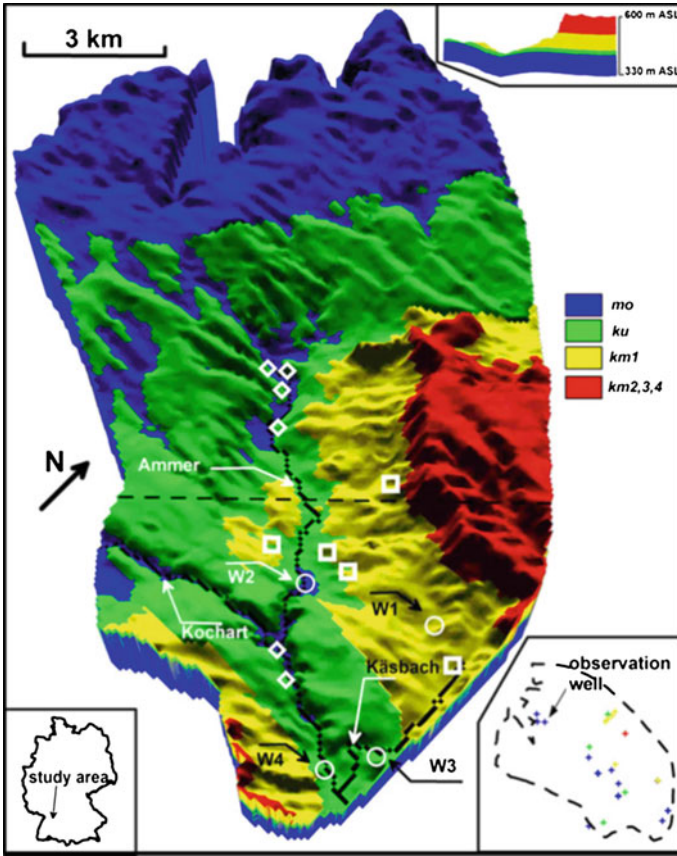


Fig. 1.6 Ammer groundwater model [7]

availability and quality of water resources to a large degree in the future. The modelling should help to develop scenarios for improving the groundwater quality in the long term. Areas subject to large groundwater extraction are also subject to severe land subsidence.

A very recent research area for THMC modelling has become **energy storage**. The economy and feasibility of renewable energy sources will depend a large degree on efficient energy storage systems. Figure 1.7 shows the numerical simulation of flow and heat distribution in a solid thermal energy storage block, which will be used to store solar energy collected during the daytime for use at night (so called solar-thermics). The long term stability and efficiency of those energy storage devices can be optimized using THMC modelling (i.e. solving the inverse geothermal problem). In addition to thermal storage, thermo-chemical concepts are under development, i.e. storing thermal energy by triggering endothermic reactions and gaining thermal energy back on demand with the reverse reaction (exothermic).

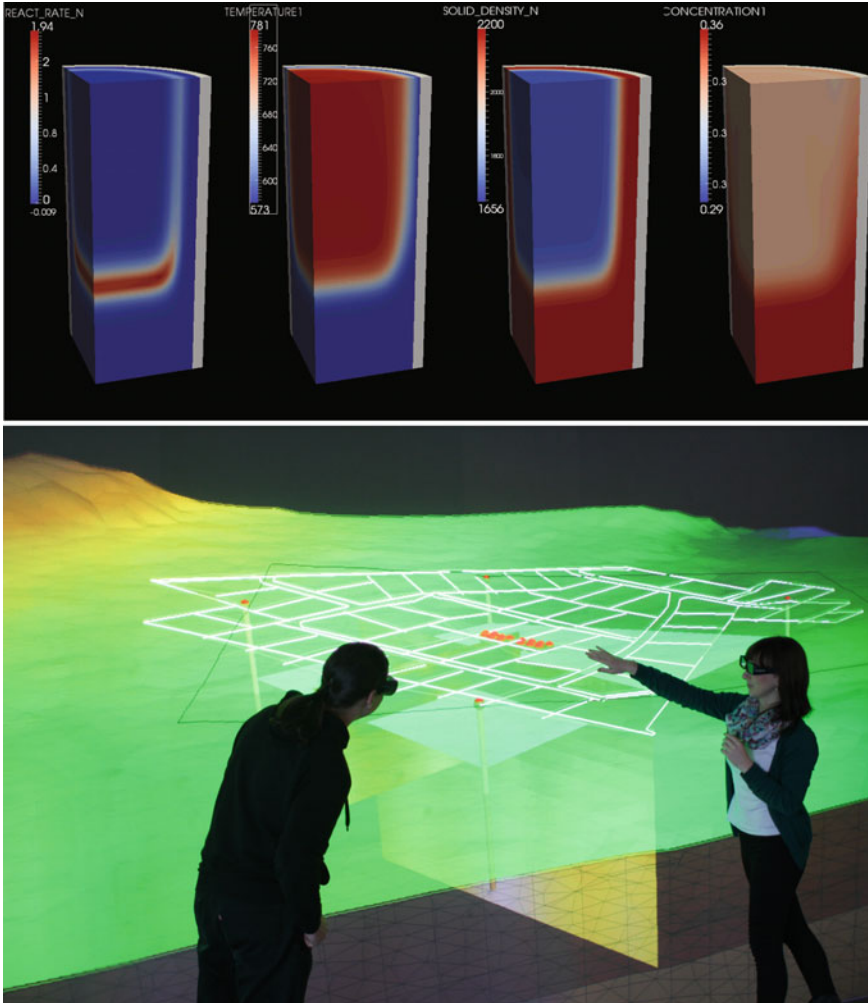


Fig. 1.7 Optimizing energy storage concepts [9] and geothermal energy in urban areas

## References

1. T. Nowak, H. Kunz, D. Dixon, W. Wang, U.-J. Goerke, and O. Kolditz. Coupled 3-d thermo-hydro-mechanical analysis of geotechnological in situ tests. *International Journal of Rock Mechanics and Mining Sciences*, 48(1):1–15, 2011.
2. U.-J. Goerke, C.-H. Park, W. Wang, A.K. Singh, and O. Kolditz. Numerical simulation of multiphase hydromechanical processes induced by co<sub>2</sub> injection into deep saline aquifers. *Oil and Gas Science and Technology*, 66(1):105–118, 2011.
3. O. Kolditz, H. Shao, U.-J. Goerke, and W. (eds) Wang. *Thermo-hydro-mechanical-chemical processes in fractured porous media*. Springer, Heidelberg, 2012.

4. N. Watanabe, B. Zehner, W. Wang, C.I. McDermott, T. Taniguchi, and O. Kolditz. Numerical analysis and visualization of uncertainty effects in thermo-hydro-mechanical coupled processes in a hot-dry-rock geothermal reservoir. volume 341, pages 57–62, 2011.
5. T. Kalbacher, C.L. Schneider, W. Wang, A. Hildebrandt, S. Attinger, and O. Kolditz. Modeling soil-coupled water uptake of multiple root systems with automatic time stepping. *Vadose Zone Journal*, 10(2):727–735, 2011.
6. A. Graebe, T. Roediger, K. Rink, T. Fischer, F. Sun, W. Wang, C. Siebert, and O. Kolditz. Numerical analysis of the groundwater regime in the western dead sea escarpment, israel / west bank. *Environmental Earth Sciences*, 69(2):571–585, 2013.
7. B. Selle, K. Rink, and O. Kolditz. Recharge and discharge controls on groundwater travel times and flow paths to production wells for the ammer catchment in southwestern germany. *Environmental Earth Sciences*, 69(2):443–452, 2013.
8. F. Sun, H. Shao, W. Wang, N. Watanabe, L. Bilke, Z. Yang, Z. Huang, and O. Kolditz. Groundwater deterioration in nankou-a suburban area of beijing: data assessment and remediation scenarios. *Environmental Earth Sciences*, 67(6):1573–1586, 2012.
9. T. Nagel, H. Shao, A.K. Singh, N. Watanabe, C. Roszkopf, M. Linder, A. Woerner, and O. Kolditz. Non-equilibrium thermochemical heat storage in porous media: Part 1 - conceptual model. *Energy*, 60:254–270, 2013.

**Part I**  
**Closed Form Solutions**

# Chapter 2

## Verification Tests

Peter Vogel and Jobst Maßmann

This chapter presents a set of closed form solutions that may serve as THMC test examples. The material has been arranged in sections of simulation exercises. All examples have been checked by OGS, FE-meshes and time steps are designed to reproduce the closed form solutions. The observed deviations are always less than one percent and are smaller by several orders of magnitude in many cases.

Throughout this chapter we will be concerned with the formal aspects of each exercise and present the closed form solution of the underlying initial or boundary value problem. The first four sections focus on single processes. Within each section we start from 1D problems and move to more advanced levels covering steady-state and transient problems up to 2D or 3D. Most of the material has been adopted from standard references. The series representations involved proved to converge rapidly and to serve well for numerical evaluation.

From section five onwards we will be concerned with coupled processes. Various transient problems will be solved with the aid of operational calculus; the Laplace transform solution method turns out to be an appropriate tool. Once that the Laplace transform is known numerical inversion will be employed to obtain the required values of the inverse transform.

The numerical method returns values of the function  $f(t)$  for that the Laplace transform

$$\bar{f}(s) = \int_0^{\infty} e^{-st} f(t) dt \tag{2.1}$$

is known. The method selected subsequently is based on a theorem by Crump [1]: Let  $a = \max\{Re(P); P \text{ is a singularity of } \bar{f}\}$  and  $T > 0$ . Except from the relative error  $E$  for every  $t$  in  $(0, T)$  the value of the inverse Laplace transform is given by the

---

P. Vogel (✉) · J. Maßmann  
Federal Institute for Geosciences and Natural Resources BGR, Stilleweg 2,  
30655 Hannover, Germany  
e-mail: Peter.Vogel@bgr.de

trigonometric series

$$f(t) = \frac{2}{T} e^{At} \left[ \frac{1}{2} \bar{f}(A) + \sum_{k=1}^{\infty} c(k) \right], \quad (2.2)$$

where  $A = a - \ln(E)/T$  and for  $k = 1, 2, \dots$

$$c(k) = \operatorname{Re}[\bar{f}(A + \frac{2k\pi i}{T})] \cos \frac{2k\pi t}{T} - \operatorname{Im}[\bar{f}(A + \frac{2k\pi i}{T})] \sin \frac{2k\pi t}{T}. \quad (2.3)$$

The algorithm outlined above may easily be applied to the various transforms cited below. The convergence of the trigonometric series has been accelerated as described in [2].

## 2.1 Heat Conduction

The examples presented here have either been adopted from Carslaw and Jaeger [3] or they are based on ideas outlined there. Throughout this section we are concerned with the evaluation of temperature distributions.

### 2.1.1 A 1D Steady-State Temperature Distribution, Boundary Conditions of 1st Kind

The domain is a rectangular beam extending along the positive x-axis. It is composed of  $10 \times 1 \times 1$  cubic elements of 10 m edge size each, the material has been assigned a thermal conductivity of  $1 \text{ W}/(\text{m} \cdot \text{K})$ . Specified temperatures prevail at the beam ends with prescribed values of  $T_0 = 1^\circ\text{C}$  at  $x = L = 100 \text{ m}$  and zero temperature at  $x = 0 \text{ m}$ . The simulation comprises one time step to establish the steady-state temperature distribution  $T(x)$ .

The Laplace equation is the governing equation describing the steady-state temperature distribution. It reads

$$\frac{d^2 T}{dx^2} = 0 \quad (2.4)$$

for 1D heat flow along the x-axis, hence, the temperature is given by

$$T(x) = ax + b. \quad (2.5)$$

The free constants,  $a$  and  $b$ , have to be determined from the specified boundary conditions at  $x = L$  and  $x = 0 \text{ m}$ , therefore,

$$T(x) = T_0 \frac{x}{L}. \quad (2.6)$$

### 2.1.2 A 1D Steady-State Temperature Distribution, Boundary Conditions of 1st and 2nd Kind

The domain is a rectangular beam of length  $L = 100\text{m}$  extending along the positive  $x$ -axis and composed of  $10 \times 1 \times 1$  cubic elements. The domain is composed of two groups of materials, thermal conductivities  $\lambda_1 = 100\text{W}/(\text{m} \cdot \text{K})$  and  $\lambda_2 = 300\text{W}/(\text{m} \cdot \text{K})$  have been assigned for  $x < 2L/5$  and  $x > 2L/5$ , respectively. A specified temperature  $T_0 = 1^\circ\text{C}$  prevails at  $x = 0\text{m}$ , the specific heat flow  $q_{th} = -1.5\text{W}/\text{m}^2$  is prescribed at  $x = L$ , which acts as heat source to the domain. The simulation comprises one time step to establish the steady-state temperature distribution  $T(x)$  (Fig. 2.1).

The Laplace equation is the governing equation describing the steady-state temperature distribution. It reads

$$\frac{d^2T}{dx^2} = 0 \quad (2.7)$$

for 1D heat flow along the  $x$ -axis, hence, the temperature is given by

$$T(x) = \begin{cases} a_1x + b_1 & \text{for } x \leq 2L/5, \\ a_2x + b_2 & \text{for } x > 2L/5. \end{cases} \quad (2.8)$$

The constants  $a_1$ ,  $b_1$ ,  $a_2$ , and  $b_2$ , have to be determined from the specified boundary conditions and continuity of temperature and energy flow at the material boundary. Temperature  $T_0$  prevails at  $x = 0$ , hence,

$$b_1 = T_0. \quad (2.9)$$

Specific heat flow  $q_{th}$  has been assigned at  $x = L$ . Then, by Fourier's law,

$$q_{th} = -\lambda_2 \frac{dT}{dx} \Big|_{x=L} = -\lambda_2 a_2. \quad (2.10)$$

Continuity of the heat flow at the material boundary (i.e.  $x = 2L/5$ ) yields

$$a_1 \lambda_1 = \lambda_2 a_2, \quad (2.11)$$

and via continuity of temperature at the material boundary

$$b_2 + a_2 2L/5 = a_1 2L/5 + b_1. \quad (2.12)$$

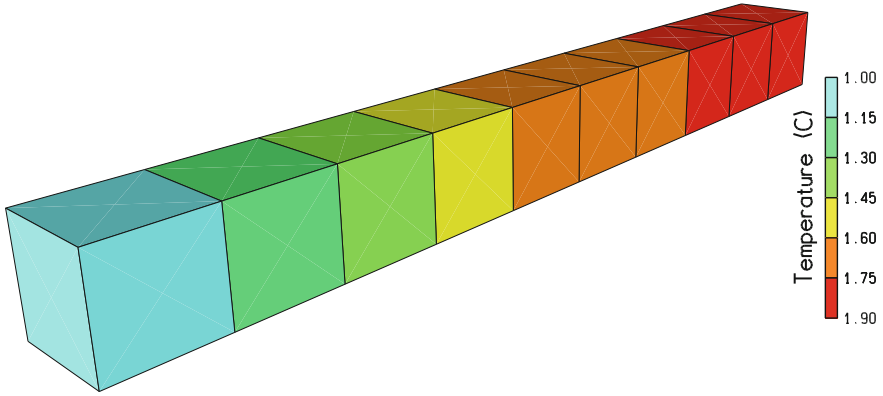


**Fig. 2.1** Temperature distribution

The temperature distribution  $T(x)$  thus becomes

$$T(x) = \begin{cases} -\frac{q_{th}}{\lambda_1}x + T_0 & \text{for } x \leq 2L/5, \\ -\frac{q_{th}}{\lambda_2}x + T_0 + q_{th} \frac{2L}{5} \left( \frac{1}{\lambda_2} - \frac{1}{\lambda_1} \right) & \text{for } x > 2L/5. \end{cases} \quad (2.13)$$

### 2.1.3 A 2D Steady-State Temperature Distribution, Boundary Conditions of 1st Kind

Given length  $L = 1$  m the domain represents the square  $[0, L] \times [0, L]$  in the x-y-plane. It is discretized by  $50 \times 50 \times 1$  equally sized hexahedral elements, the material has been assigned a thermal conductivity of  $1 \text{ W}/(\text{m} \cdot \text{K})$ . Prescribed temperatures prevail at the lateral boundaries of the domain as specified below. The simulation comprises one time step to establish the steady-state temperature distribution  $T(x, y)$ . The Laplace equation is the governing equation describing the steady-state temperature distribution. It reads

$$\frac{\partial^2 T}{\partial x^2} + \frac{\partial^2 T}{\partial y^2} = 0 \quad (2.14)$$

for 2D heat flow in the x-y-plane. With the aid of temperature  $T_0 = 1^\circ \text{C}$  the applied boundary conditions read

$$\begin{aligned}
T(x, 0) &= 0 && \text{for } 0 \leq x \leq L, \\
T(0, y) &= 0 && \text{for } 0 \leq y \leq L, \\
T(x, L) &= T_0 \frac{x}{L} && \text{for } 0 \leq x \leq L, \\
T(L, y) &= T_0 \frac{y}{L} && \text{for } 0 \leq y \leq L.
\end{aligned} \tag{2.15}$$

The temperature distribution

$$T(x, y) = T_0 \frac{x}{L} \frac{y}{L} \tag{2.16}$$

satisfies the Laplace equation and the boundary conditions, hence, this is the closed form solution of the above boundary value problem.

#### ***2.1.4 A 2D Steady-State Temperature Distribution, Boundary Conditions of 1st and 2nd Kind***

Given length  $L = 1$  m the domain represents the rectangle  $[0, 2L] \times [0, L]$  in the x-y-plane. It is discretized by an irregular mesh of hexahedral elements, the material has been assigned the thermal conductivity  $\lambda = 1$  W/(m · K). Prescribed conditions prevail at the lateral boundaries of the domain as specified below. The simulation comprises one time step to establish the steady-state temperature distribution  $T(x, y)$ .

The Laplace equation is the governing equation describing the steady-state temperature distribution. It reads

$$\frac{\partial^2 T}{\partial x^2} + \frac{\partial^2 T}{\partial y^2} = 0 \tag{2.17}$$

for 2D heat flow in the x-y-plane. With the aid of temperature  $T_0 = 1$  °C the applied boundary conditions read

$$\begin{aligned}
T(x, 0) &= \frac{T_0}{L} x && \text{for } 0 \leq x \leq 2L, \\
T(x, L) &= \frac{T_0}{L} (x + 2L) && \text{for } 0 \leq x \leq 2L, \\
T(2L, y) &= \frac{T_0}{L} (2L + 2y) && \text{for } 0 \leq y \leq L, \\
\frac{\partial T}{\partial x}(0, y) &= \frac{T_0}{L} && \text{for } 0 \leq y \leq L.
\end{aligned} \tag{2.18}$$

The temperature distribution

$$T(x, y) = \frac{T_0}{L} (x + 2y) \tag{2.19}$$

satisfies the Laplace equation and the boundary conditions, hence, this is the closed form solution of the above boundary value problem.

Data input represents the second kind boundary condition with the aid of a specific heat flow  $q_{th}$  assigned at the face  $x = 0$  m. By Fourier's law,

$$q_{th} = -\lambda \frac{\partial T}{\partial x} \Big|_{x=0}. \quad (2.20)$$

Hence, for the present example

$$q_{th} = -\lambda \frac{T_0}{L} = -1 \text{ W/m}^2, \quad (2.21)$$

specified at the face  $x = 0$  m.

### 2.1.5 A 3D Steady-State Temperature Distribution

Given length  $L = 1$  m the domain represents the cube  $[0, L] \times [0, L] \times [0, L]$  discretized by  $5 \times 5 \times 6$  equally sized hexahedral elements, the material has been assigned a thermal conductivity of  $1 \text{ W/(m} \cdot \text{K)}$ . Prescribed temperatures prevail at the surface of the domain as specified below. The simulation comprises one time step to establish the steady-state temperature distribution  $T(x, y, z)$ .

The Laplace equation is the governing equation describing the steady-state temperature distribution. It reads

$$\frac{\partial^2 T}{\partial x^2} + \frac{\partial^2 T}{\partial y^2} + \frac{\partial^2 T}{\partial z^2} = 0. \quad (2.22)$$

With the aid of temperature  $T_0 = 1^\circ\text{C}$  the applied boundary conditions read

$$\begin{aligned} T(0, y, z) &= T_0 \left( 0 + \frac{y}{L} + \frac{z}{L} \right) \text{ on the face } x = 0, \\ T(x, 0, z) &= T_0 \left( \frac{x}{L} + 0 + \frac{z}{L} \right) \text{ on the face } y = 0, \\ T(x, y, 0) &= T_0 \left( \frac{x}{L} + \frac{y}{L} + 0 \right) \text{ on the face } z = 0, \\ T(L, y, z) &= T_0 \left( 1 + \frac{y}{L} + \frac{z}{L} \right) \text{ on the face } x = L, \\ T(x, L, z) &= T_0 \left( \frac{x}{L} + 1 + \frac{z}{L} \right) \text{ on the face } y = L, \\ T(x, y, L) &= T_0 \left( \frac{x}{L} + \frac{y}{L} + 1 \right) \text{ on the face } z = L. \end{aligned} \quad (2.23)$$

The temperature distribution

$$T(x, y, z) = T_0 \left( \frac{x}{L} + \frac{y}{L} + \frac{z}{L} \right) \quad (2.24)$$

satisfies the Laplace equation and the boundary conditions, hence, this is the closed form solution of the above boundary value problem.

### ***2.1.6 A Transient 1D Temperature Distribution, Time-Dependent Boundary Conditions of 1st Kind***

Given length  $L = 50$  m the domain is a beam extending from  $-L$  to  $L$  along the  $x$ -axis, it is subdivided into  $200 \times 1 \times 1$  equally sized hexahedral elements. Explicitly assigned properties of the material are thermal conductivity  $\lambda = 0.5787037$  W/(m · K), heat capacity  $c = 0.01$  J/(kg · K), and density  $\rho = 2,500$  kg/m<sup>3</sup>. The temperature  $T_1 \cdot t$  ( $T_1 = 2^\circ\text{C/d}$ ) increases linearly with time  $t$ , it is applied at the beam ends for times  $t > 0$ . Starting from zero initial temperature the simulation evaluates the transient temperature distribution  $T(x, t)$  with output after 0.25 days and 0.5 days.

The heat conduction equation is the governing equation describing the transient temperature distribution. It reads

$$\rho c \frac{\partial T}{\partial t} = \lambda \nabla \cdot \nabla T. \quad (2.25)$$

Introducing the notation

$$\chi = \frac{\lambda}{\rho c} \quad (2.26)$$

the present 1D problem is governed by the parabolic equation

$$\frac{1}{\chi} \frac{\partial T}{\partial t} = \frac{\partial^2 T}{\partial x^2}, \quad (2.27)$$

the initial condition

$$T(x, 0) = 0 \quad \text{for } -L \leq x \leq L, \quad (2.28)$$

and linearly increasing temperatures imposed at the beam ends

$$\begin{aligned} T(-L, t) &= T_1 \cdot t \quad \text{for } t > 0, \\ T(L, t) &= T_1 \cdot t \quad \text{for } t > 0. \end{aligned} \quad (2.29)$$

The closed form solution of the above problem is given by Carslaw and Jaeger [3], who arrive at the series representation

$$\begin{aligned}
T(x, t) = & T_1 \cdot t + \frac{T_1 \cdot (x^2 - L^2)}{2\chi} + \frac{16 \cdot T_1 \cdot L^2}{\chi \pi^3} \\
& \times \sum_{n=0}^{\infty} \frac{(-1)^n}{(2n+1)^3} \cos\left(\frac{(2n+1)\pi x}{2L}\right) \exp\left(-\chi(2n+1)^2 \pi^2 \frac{t}{4L^2}\right).
\end{aligned} \tag{2.30}$$

### 2.1.7 Transient 1D Temperature Distributions, Time-Dependent Boundary Conditions of 2nd Kind

The domain is composed of two beams in parallel (Beam1 and Beam2) extending along the positive x-axis, each  $L = 25$  m long and subdivided into  $25 \times 1 \times 1$  cubic elements. Explicitly assigned properties of the material are density  $\rho = 2000 \text{ kg/m}^3$ , thermal conductivity  $\lambda = 1.1574074 \text{ W/(m} \cdot \text{K)}$ , and heat capacities  $c_1 = 0.01 \text{ J/(kg} \cdot \text{K)}$  and  $c_2 = 0.02 \text{ J/(kg} \cdot \text{K)}$  assigned to Beam1 and Beam2, respectively. No-flow boundary conditions prevail at the  $x = 0$  m faces. A specific heat flow is prescribed at  $x = L$  for times  $t > 0$ . It acts as heat source to the domain and increases linearly with time via  $q_{th1} \cdot t$ , where  $q_{th1} = 0.385802 \text{ W/(d} \cdot \text{m}^2)$  has been assumed. Starting from zero initial temperature the simulation evaluates the transient temperature distributions with output after 0.045 and 0.09 days (Fig. 2.2).

Let  $\lambda$  denote any of  $\lambda_1$  or  $\lambda_2$ . The heat conduction equation is the governing equation describing the transient temperature distribution. It reads

$$\rho c \frac{\partial T}{\partial t} = \lambda \nabla \cdot \nabla T. \tag{2.31}$$

Introducing the notation

$$\chi = \frac{\lambda}{\rho c} \tag{2.32}$$

the present 1D problems are governed by the parabolic equation

$$\frac{1}{\chi} \frac{\partial T}{\partial t} = \frac{\partial^2 T}{\partial x^2}, \tag{2.33}$$

the initial condition

$$T(x, 0) = 0 \quad \text{for } 0 \leq x \leq L, \tag{2.34}$$

and the boundary conditions

$$\begin{aligned}
\frac{\partial T}{\partial x}(0, t) &= 0 & \text{for } t > 0, \\
\lambda \frac{\partial T}{\partial x}(L, t) &= q_{th1} \cdot t & \text{for } t > 0.
\end{aligned} \tag{2.35}$$

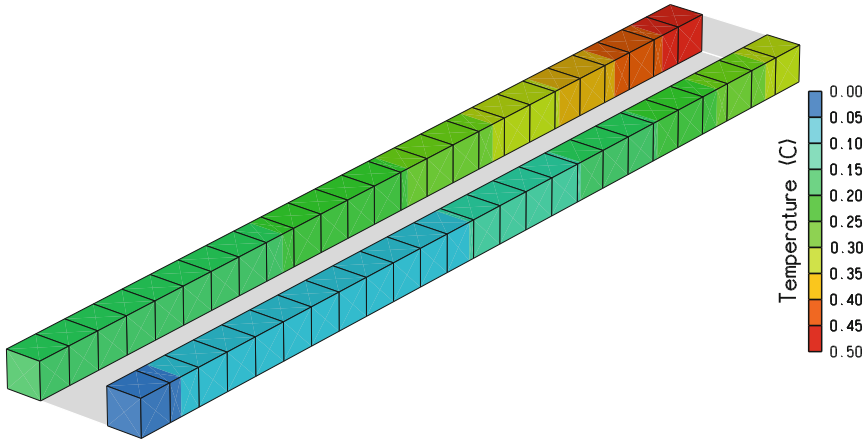


**Fig. 2.2** Temperature distributions after 0.09 days

The closed form solution of the above problem is given by Carslaw and Jaeger [3], who arrive at the series representation

$$T(x, t) = \frac{8q_{th1}\sqrt{\chi t^3}}{\lambda} \sum_{n=0}^{\infty} \left[ i^3 \operatorname{erfc} \frac{(2n+1)L-x}{2\sqrt{\chi t}} + i^3 \operatorname{erfc} \frac{(2n+1)L+x}{2\sqrt{\chi t}} \right], \quad (2.36)$$

where  $i^3 \operatorname{erfc}$  denotes the third repeated integral of the complementary error function. See [4] for its numerical evaluation.

### 2.1.8 Transient 1D Temperature Distributions, Non-Zero Initial Temperature, Boundary Conditions of 1st and 2nd Kind

The domain is composed of two beams in parallel (T1-beam and T2-beam) extending along the positive x-axis, each  $L = 100$  m long and subdivided into  $100 \times 1 \times 1$  cubic elements. Explicitly assigned properties of the material are thermal conductivity  $\lambda = 0.5787037$  W/(m·K), heat capacity  $c = 0.01$  J/(kg·K), and density  $\rho = 2,000$  kg/m<sup>3</sup>. Prescribed conditions prevail at the beams ends as specified below. Given temperature  $T_0 = 1$  °C and

$$f(x) = \begin{cases} 0 & \text{for } 0 \leq x \leq \frac{L}{10}, \\ \frac{10}{3L}x - \frac{1}{3} & \text{for } \frac{L}{10} \leq x \leq \frac{4L}{10}, \\ 1 & \text{for } \frac{4L}{10} \leq x \leq \frac{6L}{10}, \\ 3 - \frac{10}{3L}x & \text{for } \frac{6L}{10} \leq x \leq \frac{9L}{10}, \\ 0 & \text{for } \frac{9L}{10} \leq x \leq L, \end{cases} \quad (2.37)$$

the simulation starts from the initial temperature distribution  $T(x, 0) = T_0 \cdot f(x)$  and evaluates the transient temperature distribution  $T(x, t)$  with output after 0.05 days and 0.1 days.

The heat conduction equation is the governing equation describing the transient temperature distribution. It reads

$$\rho c \frac{\partial T}{\partial t} = \lambda \nabla \cdot \nabla T. \quad (2.38)$$

Introducing the notation

$$\chi = \frac{\lambda}{\rho c} \quad (2.39)$$

the present 1D problems are governed by the parabolic equation

$$\frac{1}{\chi} \frac{\partial T}{\partial t} = \frac{\partial^2 T}{\partial x^2}, \quad (2.40)$$

the initial condition

$$T(x, 0) = T_0 \cdot f(x) \quad \text{for } 0 \leq x \leq L, \quad (2.41)$$

and the boundary conditions imposed at the beams ends. These boundary conditions are specified zero temperatures for the T1-beam,

$$\begin{aligned} T(0, t) &= 0 \quad \text{for } t > 0, \\ T(L, t) &= 0 \quad \text{for } t > 0, \end{aligned} \quad (2.42)$$

and no-flow boundary conditions for the T2-beam,

$$\begin{aligned} \frac{\partial T}{\partial x}(0, t) &= 0 \quad \text{for } t > 0, \\ \frac{\partial T}{\partial x}(L, t) &= 0 \quad \text{for } t > 0. \end{aligned} \quad (2.43)$$

Closed form solutions of the above problems are given by Carslaw and Jaeger [3], who arrive at series representations that read for the T1-beam

$$\begin{aligned} T(x, t)/T_0 &= T1(x, t) \\ &= \frac{2}{L} \sum_{n=1}^{\infty} \sin \frac{n\pi x}{L} \exp\left(-\chi n^2 \pi^2 \frac{t}{L^2}\right) \int_0^L f(x') \sin \frac{n\pi x'}{L} dx' \end{aligned} \quad (2.44)$$

and for the T2-beam

$$\begin{aligned} T(x, t)/T_0 &= T2(x, t) \\ &= \frac{1}{L} \int_0^L f(x') dx' + \frac{2}{L} \sum_{n=1}^{\infty} \cos \frac{n\pi x}{L} \exp\left(-\chi n^2 \pi^2 \frac{t}{L^2}\right) \int_0^L f(x') \cos \frac{n\pi x'}{L} dx'. \end{aligned} \quad (2.45)$$

Now, with  $f(x)$  as defined above, the integrals involved may be evaluated by elementary analytical methods. The series representations take the form

$$\begin{aligned} T1(x, t) &= \sum_{n=1}^{\infty} \sin \frac{n\pi x}{L} \exp\left(-\chi n^2 \pi^2 \frac{t}{L^2}\right) \\ &\quad \times \frac{80}{3(n\pi)^2} \sin \frac{n\pi}{2} \sin \frac{n\pi}{4} \sin \frac{3n\pi}{20}, \end{aligned} \quad (2.46)$$

$$\begin{aligned} T2(x, t) &= \frac{1}{2} + \sum_{n=1}^{\infty} \cos \frac{n\pi x}{L} \exp\left(-\chi n^2 \pi^2 \frac{t}{L^2}\right) \\ &\quad \times \frac{80}{3(n\pi)^2} \cos \frac{n\pi}{2} \sin \frac{n\pi}{4} \sin \frac{3n\pi}{20}. \end{aligned} \quad (2.47)$$

### ***2.1.9 A Transient 2D Temperature Distribution, Non-Zero Initial Temperature, Boundary Conditions of 1st and 2nd Kind***

The domain represents the square  $[0, L] \times [0, L]$  with an edge size of  $L = 100$  m, located in the x-y-plane and subdivided into  $100 \times 100 \times 1$  cubic elements. Explicitly assigned properties of the material are thermal conductivity  $\lambda = 0.5787037$  W/(m · K), heat capacity  $c = 0.01$  J/(kg · K), and density  $\rho = 2000$  kg/m<sup>3</sup>. Prescribed conditions prevail at the lateral boundaries of the domain as specified below. Given temperature  $T_0 = 1$  °C and

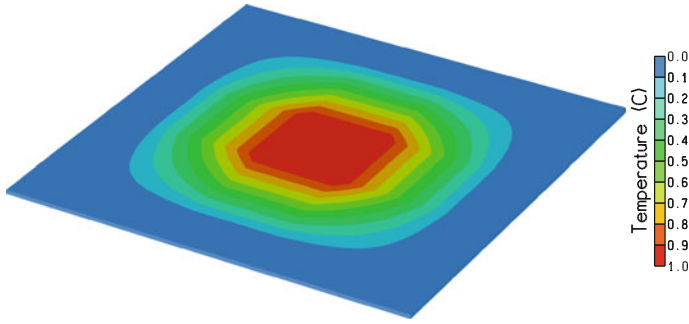


Fig. 2.3 Initial temperature distribution

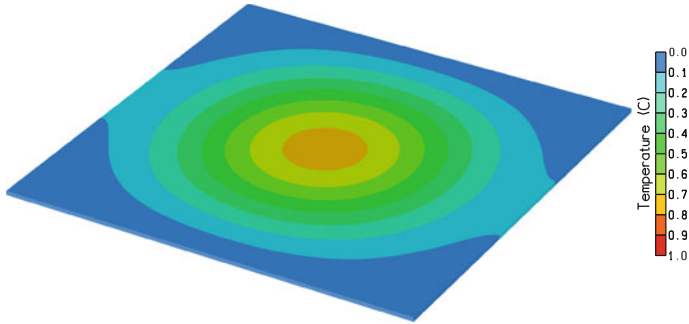


Fig. 2.4 Temperature distribution after 0.04 days

$$f(x) = \begin{cases} 0 & \text{for } 0 \leq x \leq \frac{L}{10}, \\ \frac{10}{3L}x - \frac{1}{3} & \text{for } \frac{L}{10} \leq x \leq \frac{4L}{10}, \\ 1 & \text{for } \frac{4L}{10} \leq x \leq \frac{6L}{10}, \\ 3 - \frac{10}{3L}x & \text{for } \frac{6L}{10} \leq x \leq \frac{9L}{10}, \\ 0 & \text{for } \frac{9L}{10} \leq x \leq L, \end{cases} \quad (2.48)$$

the simulation starts from the initial temperature distribution  $T(x, y, 0) = T_0 \cdot f(x) \cdot f(y)$  (Fig. 2.3) and evaluates the transient temperature distribution  $T(x, y, t)$  with output after 0.02 and 0.04 days (Fig. 2.4).

The heat conduction equation is governing equation describing the transient temperature distribution. It reads

$$\rho c \frac{\partial T}{\partial t} = \lambda \nabla \cdot \nabla T. \quad (2.49)$$

Introducing the notation

$$\chi = \frac{\lambda}{\rho c} \quad (2.50)$$

the present 2D problem is governed by the parabolic equation

$$\frac{1}{\chi} \frac{\partial T}{\partial t} = \frac{\partial^2 T}{\partial x^2} + \frac{\partial^2 T}{\partial y^2}, \quad (2.51)$$

the initial condition

$$T(x, y, 0) = T_0 \cdot f(x) \cdot f(y) \quad \text{for } 0 \leq x, y \leq L, \quad (2.52)$$

and the applied boundary conditions. These are specified zero temperatures at  $x = 0$  and  $x = L$

$$T(0, y, t) = 0 \quad \text{for } 0 \leq y \leq L, \quad (2.53)$$

$$T(L, y, t) = 0 \quad \text{for } 0 \leq y \leq L, \quad (2.54)$$

and no-flow boundary conditions at  $y = 0$  and  $y = L$

$$\frac{\partial T}{\partial y}(x, 0, t) = 0 \quad \text{for } 0 \leq x \leq L, \quad (2.55)$$

$$\frac{\partial T}{\partial y}(x, L, t) = 0 \quad \text{for } 0 \leq x \leq L. \quad (2.56)$$

The closed form solution of the above problem is obtained in terms of the 1D T1-beam and T2-beam solutions given in the context of the previous example

$$\begin{aligned} T1(x, t) &= \sum_{n=1}^{\infty} \sin \frac{n\pi x}{L} \exp\left(-\chi n^2 \pi^2 \frac{t}{L^2}\right) \\ &\quad \times \frac{80}{3(n\pi)^2} \sin \frac{n\pi}{2} \sin \frac{n\pi}{4} \sin \frac{3n\pi}{20}, \end{aligned} \quad (2.57)$$

$$\begin{aligned} T2(x, t) &= \frac{1}{2} + \sum_{n=1}^{\infty} \cos \frac{n\pi x}{L} \exp\left(-\chi n^2 \pi^2 \frac{t}{L^2}\right) \\ &\quad \times \frac{80}{3(n\pi)^2} \cos \frac{n\pi}{2} \sin \frac{n\pi}{4} \sin \frac{3n\pi}{20}. \end{aligned} \quad (2.58)$$

We will next verify that the closed form solution of the above problem is given by

$$T(x, y, t) = T_0 \cdot T1(x, t) \cdot T2(y, t). \quad (2.59)$$

Both,  $T1(x, t)$  and  $T2(x, t)$ , satisfy the initial condition

$$T1(x, 0) = T2(x, 0) = f(x). \quad (2.60)$$

Then

$$T(x, y, 0) = T_0 \cdot T1(x, 0) \cdot T2(y, 0) = T_0 \cdot f(x) \cdot f(y), \quad (2.61)$$

hence,  $T(x, y, t)$  satisfies the initial condition.

Both,  $T1(x, t)$  and  $T2(y, t)$ , satisfy the 1D heat conduction equation. Then

$$\begin{aligned} \frac{1}{\chi} \frac{\partial T}{\partial t} &= T_0 \left[ \frac{1}{\chi} T2 \frac{\partial T1}{\partial t} + \frac{1}{\chi} T1 \frac{\partial T2}{\partial t} \right] \\ &= T_0 \left[ T2 \frac{\partial^2 T1}{\partial x^2} + T1 \frac{\partial^2 T2}{\partial y^2} \right] \\ &= \frac{\partial^2 T}{\partial x^2} + \frac{\partial^2 T}{\partial y^2}, \end{aligned} \quad (2.62)$$

hence,  $T(x, y, t)$  satisfies the differential equation.

Zero boundary temperatures are satisfied by  $T1(x, t)$

$$T1(0, t) = 0 \quad \text{for } t > 0, \quad (2.63)$$

$$T1(L, t) = 0 \quad \text{for } t > 0, \quad (2.64)$$

no-flow boundary conditions are satisfied by  $T2(y, t)$

$$\frac{\partial T2}{\partial y}(0, t) = 0 \quad \text{for } t > 0, \quad (2.65)$$

$$\frac{\partial T2}{\partial y}(L, t) = 0 \quad \text{for } t > 0 \quad (2.66)$$

Then

$$\begin{aligned} T(0, y, t) &= T_0 \cdot T1(0, t) \cdot T2(y, t) = 0 \cdot T2(y, t) = 0, \\ T(L, y, t) &= T_0 \cdot T1(L, t) \cdot T2(y, t) = 0 \cdot T2(y, t) = 0, \\ \frac{\partial T}{\partial y}(x, 0, t) &= T_0 \cdot T1(x, t) \cdot \frac{\partial T2}{\partial y}(0, t) = T_0 \cdot T1(x, t) \cdot 0 = 0, \\ \frac{\partial T}{\partial y}(x, L, t) &= T_0 \cdot T1(x, t) \cdot \frac{\partial T2}{\partial y}(L, t) = T_0 \cdot T1(x, t) \cdot 0 = 0, \end{aligned} \quad (2.67)$$

hence,  $T(x, y, t)$  satisfies the boundary conditions.

## 2.2 Liquid Flow

The same tools that work for the solution of heat conduction problems may also be applied to liquid flow problems. Here we are concerned with the evaluation of pressure distributions, for the underlying theory see Freeze and Cherry [5].

### 2.2.1 A 1D Steady-State Pressure Distribution, Boundary Conditions of 1st Kind

The domain is a rectangular beam extending along the positive x-axis and composed of  $10 \times 1 \times 1$  cubic elements of 10m edge size each. An isotropic permeability of  $10^{-15} \text{ m}^2$  is assumed for the material. Liquid viscosity is  $1 \text{ mPa} \cdot \text{s}$  and gravity is neglected via zero liquid density. Specified pressures prevail at the beam ends with prescribed values of  $p_0 = 1 \text{ MPa}$  at  $x = L = 100 \text{ m}$  and zero pressure at  $x = 0 \text{ m}$ . The simulation comprises one time step to establish the steady-state pressure distribution  $p(x)$ .

For incompressible liquids Darcy's law and continuity equation yield the Laplace equation as the governing equation describing the steady-state pressure distribution. It reads

$$\frac{d^2 p}{dx^2} = 0 \quad (2.68)$$

for 1D flow along the x-axis, hence, the pressure is given by

$$p(x) = ax + b. \quad (2.69)$$

The free constants,  $a$  and  $b$ , have to be determined from the specified boundary conditions at  $x = L$  and  $x = 0 \text{ m}$ , therefore,

$$p(x) = p_0 \frac{x}{L}. \quad (2.70)$$

### 2.2.2 A 1D Steady-State Pressure Distribution, Boundary Conditions of 1st and 2nd Kind

The domain is a rectangular beam of length  $L = 100 \text{ m}$  extending along the positive x-axis and composed of  $10 \times 1 \times 1$  cubic elements. The domain is composed of two groups of permeable materials with isotropic permeabilities  $k_1 = 10^{-12} \text{ m}^2$  and  $k_2 = 3 \times 10^{-12} \text{ m}^2$  for  $x < 2L/5$  and  $x > 2L/5$ , respectively. Liquid viscosity is  $\mu = 1 \text{ mPa} \cdot \text{s}$  and gravity is neglected via zero liquid density. The specified pressure  $p_0 = 1 \text{ MPa}$  prevails at  $x = 0 \text{ m}$ , the specific discharge  $q = -1.5 \times 10^{-5} \text{ m/s}$  is

prescribed at  $x = L$ , which acts as a source to the domain. The simulation comprises one time step to establish the steady-state pressure distribution  $p(x)$ .

For incompressible liquids Darcy's law and continuity equation yield the Laplace equation as the governing equation describing the steady-state pressure distribution. It reads

$$\frac{d^2 p}{dx^2} = 0 \quad (2.71)$$

for 1D flow along the  $x$ -axis, hence, the pressure is given by

$$p(x) = \begin{cases} a_1 x + b_1 & \text{for } x \leq 2L/5, \\ a_2 x + b_2 & \text{for } x > 2L/5. \end{cases} \quad (2.72)$$

The constants  $a_1$ ,  $b_1$ ,  $a_2$ , and  $b_2$ , have to be determined from the specified boundary conditions and continuity of pressure and specific discharge at the material boundary.

Pressure  $p_0$  prevails at  $x = 0$ , hence,

$$b_1 = p_0. \quad (2.73)$$

Specific discharge  $q$  has been assigned at  $x = L$ . Then, by Darcy's law,

$$q = -\frac{k_2}{\mu} \frac{dp}{dx} \Big|_{x=L} = -\frac{k_2}{\mu} a_2. \quad (2.74)$$

Continuity of the specific discharge at the material boundary (i.e.  $x = 2L/5$ ) yields

$$a_1 \frac{k_1}{\mu} = \frac{k_2}{\mu} a_2, \quad (2.75)$$

and via continuity of pressure at the material boundary

$$b_2 + a_2 2L/5 = a_1 2L/5 + b_1. \quad (2.76)$$

The pressure distribution  $p(x)$  thus becomes

$$p(x) = \begin{cases} -\frac{q\mu}{k_1} x + p_0 & \text{for } x \leq 2L/5, \\ -\frac{q\mu}{k_2} x + p_0 + q\mu \frac{2L}{5} \left( \frac{1}{k_2} - \frac{1}{k_1} \right) & \text{for } x > 2L/5. \end{cases} \quad (2.77)$$

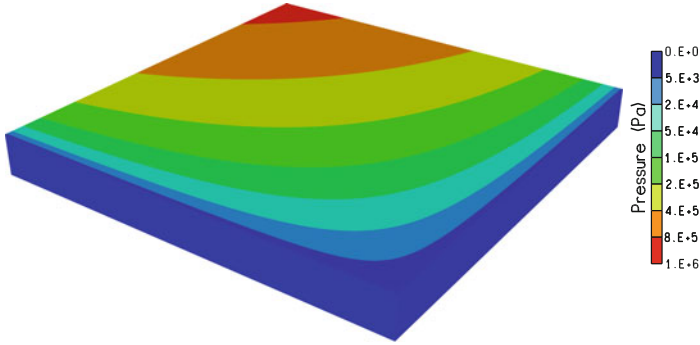


**Fig. 2.5** Pressure distribution

### 2.2.3 A 2D Steady-State Pressure Distribution, Boundary Conditions of 1st Kind

Given length  $L = 1$  m the domain represents the square  $[0, L] \times [0, L]$  in the x-y-plane, discretized by  $50 \times 50 \times 1$  equally sized hexahedral elements. An isotropic permeability of  $10^{-15} \text{ m}^2$  is assumed for the material. Liquid viscosity is  $1 \text{ mPa} \cdot \text{s}$  and gravity is neglected via zero liquid density. Prescribed pressures prevail at the lateral boundaries of the domain as specified below. The simulation comprises one time step to establish the steady-state pressure distribution  $p(x, y)$  (Fig. 2.5).

For incompressible liquids Darcy's law and continuity equation yield the Laplace equation as the governing equation describing the steady-state pressure distribution. It reads

$$\frac{\partial^2 p}{\partial x^2} + \frac{\partial^2 p}{\partial y^2} = 0 \quad (2.78)$$

for 2D flow in the x-y-plane. With the aid of pressure  $p_0 = 1 \text{ MPa}$  the applied boundary conditions read

$$\begin{aligned} p(x, 0) &= 0 && \text{for } 0 \leq x \leq L, \\ p(0, y) &= 0 && \text{for } 0 \leq y \leq L, \\ p(x, L) &= p_0 \frac{x}{L} && \text{for } 0 \leq x \leq L, \\ p(L, y) &= p_0 \frac{y}{L} && \text{for } 0 \leq y \leq L. \end{aligned} \quad (2.79)$$

The pressure distribution

$$p(x, y) = p_0 \frac{x}{L} \frac{y}{L} \quad (2.80)$$

satisfies the Laplace equation and the boundary conditions, hence, this is the closed form solution of the above boundary value problem.

### 2.2.4 A 2D Steady-State Pressure Distribution, Boundary Conditions of 1st and 2nd Kind

Given length  $L = 1$  m the domain represents the rectangle  $[0, 2L] \times [0, L]$  in the x-y-plane, discretized by an irregular mesh of hexahedral elements. An isotropic permeability  $k = 10^{-14} \text{ m}^2$  is assumed for the material. Liquid viscosity is  $\mu = 1 \text{ mPa} \cdot \text{s}$  and gravity is neglected via zero liquid density. Prescribed conditions prevail at the lateral boundaries of the domain as specified below. The simulation comprises one time step to establish the steady-state pressure distribution  $p(x, y)$ .

For incompressible liquids Darcy's law and continuity equation yield the Laplace equation as the governing equation describing the steady-state pressure distribution. It reads

$$\frac{\partial^2 p}{\partial x^2} + \frac{\partial^2 p}{\partial y^2} = 0 \quad (2.81)$$

for 2D flow in the x-y-plane. With the aid of pressure  $p_0 = 1 \text{ MPa}$  the applied boundary conditions read

$$\begin{aligned} p(x, 0) &= \frac{p_0}{L}x && \text{for } 0 \leq x \leq 2L, \\ p(x, L) &= \frac{p_0}{L}(x + 2L) && \text{for } 0 \leq x \leq 2L, \\ p(2L, y) &= \frac{p_0}{L}(2L + 2y) && \text{for } 0 \leq y \leq L, \\ \frac{\partial p}{\partial x}(0, y) &= \frac{p_0}{L} && \text{for } 0 \leq y \leq L. \end{aligned} \quad (2.82)$$

The pressure distribution

$$p(x, y) = \frac{p_0}{L}(x + 2y) \quad (2.83)$$

satisfies the Laplace equation and the boundary conditions, hence, this is the closed form solution of the above boundary value problem.

Data input represents the second kind boundary condition with the aid of a specific discharge  $q$  assigned at the face  $x = 0$  m. By Darcy's law,

$$q = -\frac{k}{\mu} \frac{\partial p}{\partial x} \Big|_{x=0}. \quad (2.84)$$

Hence, for the present example

$$q = -\frac{k}{\mu} \frac{p_0}{L} = -10^{-5} \text{ m/s}, \quad (2.85)$$

specified at the face  $x = 0$  m.

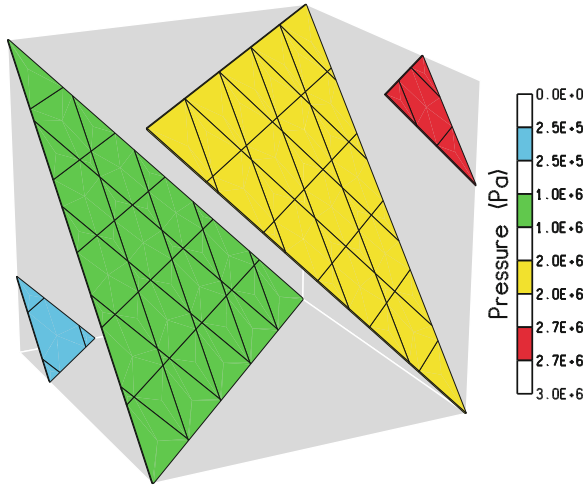


**Fig. 2.6** Pressure contours

### 2.2.5 A 3D Steady-State Pressure Distribution

Given length  $L = 1$  m the domain represents the cube  $[0, L] \times [0, L] \times [0, L]$  discretized by  $5 \times 5 \times 6$  equally sized hexahedral elements. An isotropic permeability of  $10^{-10} \text{ m}^2$  is assumed for the material. Liquid viscosity is  $1 \text{ mPa} \cdot \text{s}$  and gravity is neglected via zero liquid density. Prescribed pressures prevail at the surface of the domain as specified below. The simulation comprises one time step to establish the steady-state pressure distribution  $p(x, y, z)$  (Fig. 2.6).

For incompressible liquids Darcy's law and continuity equation yield the Laplace equation as the governing equation describing the steady-state pressure distribution. It reads

$$\frac{\partial^2 p}{\partial x^2} + \frac{\partial^2 p}{\partial y^2} + \frac{\partial^2 p}{\partial z^2} = 0. \quad (2.86)$$

With the aid of pressure  $p_0 = 1 \text{ MPa}$  the applied boundary conditions read

$$\begin{aligned} p(0, y, z) &= p_0 \left( 0 + \frac{y}{L} + \frac{z}{L} \right) \text{ on the face } x = 0, \\ p(x, 0, z) &= p_0 \left( \frac{x}{L} + 0 + \frac{z}{L} \right) \text{ on the face } y = 0, \\ p(x, y, 0) &= p_0 \left( \frac{x}{L} + \frac{y}{L} + 0 \right) \text{ on the face } z = 0, \\ p(L, y, z) &= p_0 \left( 1 + \frac{y}{L} + \frac{z}{L} \right) \text{ on the face } x = L, \\ p(x, L, z) &= p_0 \left( \frac{x}{L} + 1 + \frac{z}{L} \right) \text{ on the face } y = L, \end{aligned} \quad (2.87)$$

$$p(x, y, L) = p_0 \left( \frac{x}{L} + \frac{y}{L} + 1 \right) \text{ on the face } z = L.$$

The pressure distribution

$$p(x, y, z) = p_0 \left( \frac{x}{L} + \frac{y}{L} + \frac{z}{L} \right) \quad (2.88)$$

satisfies the Laplace equation and the boundary conditions, hence, this is the closed form solution of the above boundary value problem.

### ***2.2.6 A Hydrostatic Pressure Distribution***

The domain is a cuboid of height  $H = 30$  m and edges parallel to the x-y-z coordinate axes. It is discretized by an irregular mesh of hexahedral elements. The domain is composed of four groups of isotropic permeable materials,  $\rho = 1019.368 \text{ kg/m}^3$  is the liquid density. The simulation setup employs a prescribed zero pressure at the top and explicitly specified no-flow conditions along the lateral boundaries and bottom (unless otherwise specified, no-flow boundary conditions will be assigned by default). The simulation comprises one time step to establish the hydrostatic pressure distribution  $p(x, y, z)$ .

The hydrostatic pressure distribution neither depends on the material properties nor on the coordinates x and y and is given by

$$p(x, y, z) = \rho g(H - z), \quad (2.89)$$

where  $g = 9.81 \text{ m}^2/\text{s}$  is the magnitude of gravity, and  $z$  is the vertical coordinate extending from 0 to  $H$ .

### ***2.2.7 A Transient 1D Pressure Distribution, Time-Dependent Boundary Conditions of 1st Kind***

Given length  $L = 50$  m the domain is a beam extending from  $-L$  to  $L$  along the x-axis, it is subdivided into  $200 \times 1 \times 1$  equally sized hexahedral elements. A permeable material represents the porous medium, which contains a liquid of small and constant compressibility. Gravity is neglected via zero liquid density. Explicitly assigned properties of matrix and liquid are an isotropic permeability  $k = 10^{-14} \text{ m}^2$  and liquid viscosity  $\mu = 1.728 \text{ mPa} \cdot \text{s}$ . Porosity  $\phi$  and liquid compressibility  $\kappa$  have been incorporated in the storage  $\phi\kappa = 2.5 \times 10^{-10} \text{ 1/Pa}$ . The pressure  $p_1 \cdot t$  ( $p_1 = 2 \times 10^6 \text{ Pa/d}$ ) increases linearly with time  $t$ , it is applied at the beam ends for times  $t > 0$ . Starting from zero initial pressure the simulation evaluates the transient pressure distribution  $p(x, t)$  with output after 0.25 and 0.5 days.

For liquids of small and constant compressibility Darcy's law and continuity equation yield the pressure conduction equation as the governing equation describing the transient pressure distribution. It reads

$$\phi\kappa \frac{\partial p}{\partial t} = \frac{k}{\mu} \nabla \cdot \nabla p. \quad (2.90)$$

Introducing the notation

$$\chi = \frac{k}{\phi\mu\kappa} \quad (2.91)$$

the present 1D problem is governed by the parabolic equation

$$\frac{1}{\chi} \frac{\partial p}{\partial t} = \frac{\partial^2 p}{\partial x^2}, \quad (2.92)$$

the initial condition

$$p(x, 0) = 0 \quad \text{for } -L \leq x \leq L, \quad (2.93)$$

and linearly increasing pressures imposed at the beam ends

$$\begin{aligned} p(-L, t) &= p_1 \cdot t \quad \text{for } t > 0, \\ p(L, t) &= p_1 \cdot t \quad \text{for } t > 0. \end{aligned} \quad (2.94)$$

The closed form solution of the above problem is given by Carslaw and Jaeger [3], who arrive at the series representation

$$\begin{aligned} p(x, t) &= p_1 \cdot t + \frac{p_1 \cdot (x^2 - L^2)}{2\chi} + \frac{16 \cdot p_1 \cdot L^2}{\chi\pi^3} \\ &\times \sum_{n=0}^{\infty} \frac{(-1)^n}{(2n+1)^3} \cos\left(\frac{(2n+1)\pi x}{2L}\right) \exp\left(-\chi(2n+1)^2\pi^2 \frac{t}{4L^2}\right). \end{aligned} \quad (2.95)$$

### ***2.2.8 Transient 1D Pressure Distributions, Time-Dependent Boundary Conditions of 2nd Kind***

The domain is composed of two beams in parallel (Beam1 and Beam2) extending along the positive x-axis, each  $L = 25$  m long and subdivided into  $25 \times 1 \times 1$  cubic elements. A permeable material represents the porous medium, which contains a liquid of small and constant compressibility. Gravity is neglected via zero liquid density. Explicitly assigned properties of matrix and liquid are an isotropic permeability  $k = 10^{-14}$  m<sup>2</sup> and liquid viscosity  $\mu = 0.864$  mPa·s. Porosity  $\phi$  and liquid compressibility  $\kappa$  have been incorporated in the storage  $\phi\kappa$  with values of

$2 \times 10^{-10}$  1/Pa and  $4 \times 10^{-10}$  1/Pa assigned to Beam1 and Beam2, respectively. No-flow boundary conditions prevail at the  $x = 0$  m faces. A specific discharge is prescribed at  $x = L$  for times  $t > 0$ . It acts as a source to the domain and increases linearly with time via  $q_1 \cdot t$ , where  $q_1 = 3.85802 \times 10^{-6}$  m/(s · d) has been assumed. Starting from zero initial pressure the simulation evaluates the transient pressure distributions with output after 0.045 and 0.09 days.

For liquids of small and constant compressibility Darcy's law and continuity equation yield the pressure conduction equation as the governing equation describing the transient pressure distribution. It reads

$$\phi\kappa \frac{\partial p}{\partial t} = \frac{k}{\mu} \nabla \cdot \nabla p. \quad (2.96)$$

Introducing the notation

$$\chi = \frac{k}{\phi\mu\kappa} \quad (2.97)$$

the present 1D problems are governed by the parabolic equation

$$\frac{1}{\chi} \frac{\partial p}{\partial t} = \frac{\partial^2 p}{\partial x^2}, \quad (2.98)$$

the initial condition

$$p(x, 0) = 0 \quad \text{for } 0 \leq x \leq L, \quad (2.99)$$

and the boundary conditions

$$\begin{aligned} \frac{\partial p}{\partial x}(0, t) &= 0 \quad \text{for } t > 0, \\ \frac{k}{\mu} \frac{\partial p}{\partial x}(L, t) &= q_1 \cdot t \quad \text{for } t > 0. \end{aligned} \quad (2.100)$$

The closed form solution of the above problem is given by Carslaw and Jaeger [3], who arrive at the series representation

$$p(x, t) = \frac{8q_1\sqrt{\chi t^3}}{k/\mu} \sum_{n=0}^{\infty} \left[ i^3 \operatorname{erfc} \frac{(2n+1)L-x}{2\sqrt{\chi t}} + i^3 \operatorname{erfc} \frac{(2n+1)L+x}{2\sqrt{\chi t}} \right], \quad (2.101)$$

where  $i^3 \operatorname{erfc}$  denotes the third repeated integral of the complementary error function. See [4] for its numerical evaluation.

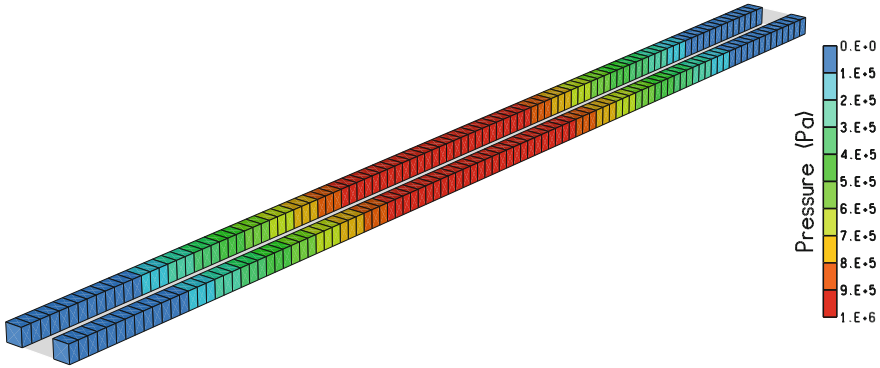


Fig. 2.7 Initial pressure distributions

### 2.2.9 Transient 1D Pressure Distributions, Non-Zero Initial Pressure, Boundary Conditions of 1st and 2nd Kind

The domain is composed of two beams in parallel (p1-beam and p2-beam) extending along the positive  $x$ -axis, each  $L = 100\text{m}$  long and subdivided into  $100 \times 1 \times 1$  cubic elements. A permeable material represents the porous medium, which contains a liquid of small and constant compressibility. Gravity is neglected via zero liquid density. Explicitly assigned properties of matrix and liquid are an isotropic permeability  $k = 10^{-14}\text{m}^2$  and liquid viscosity  $\mu = 1.728\text{mPa}\cdot\text{s}$ . Porosity  $\phi$  and liquid compressibility  $\kappa$  have been incorporated in the storage  $\phi\kappa = 2 \times 10^{-10}\text{1/Pa}$ . Prescribed conditions prevail at the beams ends as specified below. Given pressure  $p_0 = 1\text{MPa}$  and

$$f(x) = \begin{cases} 0 & \text{for } 0 \leq x \leq \frac{L}{10}, \\ \frac{10}{3L}x - \frac{1}{3} & \text{for } \frac{L}{10} \leq x \leq \frac{4L}{10}, \\ 1 & \text{for } \frac{4L}{10} \leq x \leq \frac{6L}{10}, \\ 3 - \frac{10}{3L}x & \text{for } \frac{6L}{10} \leq x \leq \frac{9L}{10}, \\ 0 & \text{for } \frac{9L}{10} \leq x \leq L, \end{cases} \quad (2.102)$$

the simulation starts from the initial pressure distribution  $p(x, 0) = p_0 \cdot f(x)$  (Fig. 2.7) and evaluates the transient pressure distribution  $p(x, t)$  with output after 0.05 and 0.1 days (Fig. 2.8).

For liquids of small and constant compressibility Darcy's law and continuity equation yield the pressure conduction equation as the governing equation describing

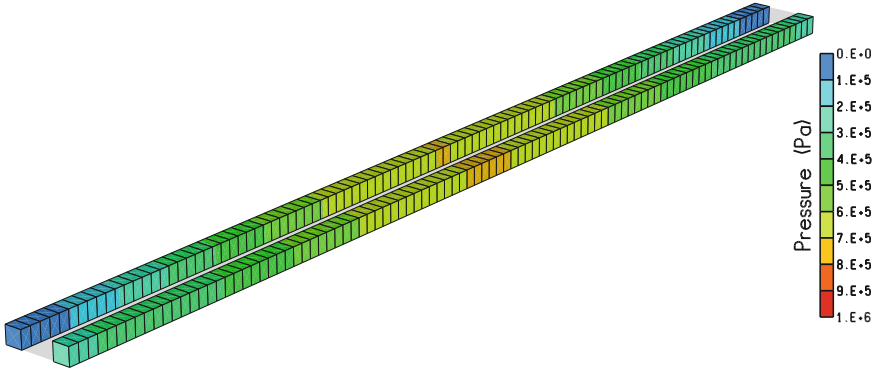


**Fig. 2.8** Pressure distributions after 0.1 days

the transient pressure distribution. It reads

$$\phi\kappa \frac{\partial p}{\partial t} = \frac{k}{\mu} \nabla \cdot \nabla p. \quad (2.103)$$

Introducing the notation

$$\chi = \frac{k}{\phi\mu\kappa} \quad (2.104)$$

the present 1D problems are governed by the parabolic equation

$$\frac{1}{\chi} \frac{\partial p}{\partial t} = \frac{\partial^2 p}{\partial x^2}, \quad (2.105)$$

the initial condition

$$p(x, 0) = p_0 \cdot f(x) \quad \text{for } 0 \leq x \leq L, \quad (2.106)$$

and the boundary conditions imposed at the beams ends. These boundary conditions are specified zero pressures for the p1-beam,

$$\begin{aligned} p(0, t) &= 0 \quad \text{for } t > 0, \\ p(L, t) &= 0 \quad \text{for } t > 0, \end{aligned} \quad (2.107)$$

and no-flow boundary conditions for the p2-beam,

$$\begin{aligned}\frac{\partial p}{\partial x}(0, t) &= 0 \quad \text{for } t > 0, \\ \frac{\partial p}{\partial x}(L, t) &= 0 \quad \text{for } t > 0.\end{aligned}\tag{2.108}$$

Closed form solutions of the above problems are given by Carslaw and Jaeger [3], who arrive at series representations that read for the p1-beam

$$\begin{aligned}p(x, t)/p_0 &= p1(x, t) \\ &= \frac{2}{L} \sum_{n=1}^{\infty} \sin \frac{n\pi x}{L} \exp\left(-\chi n^2 \pi^2 \frac{t}{L^2}\right) \int_0^L f(x') \sin \frac{n\pi x'}{L} dx'\end{aligned}\tag{2.109}$$

and for the p2-beam

$$\begin{aligned}p(x, t)/p_0 &= p2(x, t) \\ &= \frac{1}{L} \int_0^L f(x') dx' + \frac{2}{L} \sum_{n=1}^{\infty} \cos \frac{n\pi x}{L} \exp\left(-\chi n^2 \pi^2 \frac{t}{L^2}\right) \int_0^L f(x') \cos \frac{n\pi x'}{L} dx'.\end{aligned}\tag{2.110}$$

Now, with  $f(x)$  as defined above, the integrals involved may be evaluated by elementary analytical methods. The series representations take the form

$$\begin{aligned}p1(x, t) &= \sum_{n=1}^{\infty} \sin \frac{n\pi x}{L} \exp\left(-\chi n^2 \pi^2 \frac{t}{L^2}\right) \\ &\quad \times \frac{80}{3(n\pi)^2} \sin \frac{n\pi}{2} \sin \frac{n\pi}{4} \sin \frac{3n\pi}{20},\end{aligned}\tag{2.111}$$

$$\begin{aligned}p2(x, t) &= \frac{1}{2} + \sum_{n=1}^{\infty} \cos \frac{n\pi x}{L} \exp\left(-\chi n^2 \pi^2 \frac{t}{L^2}\right) \\ &\quad \times \frac{80}{3(n\pi)^2} \cos \frac{n\pi}{2} \sin \frac{n\pi}{4} \sin \frac{3n\pi}{20}.\end{aligned}\tag{2.112}$$

### ***2.2.10 A Transient 2D Pressure Distribution, Non-Zero Initial Pressure, Boundary Conditions of 1st and 2nd Kind***

The domain represents the square  $[0, L] \times [0, L]$  with an edge size of  $L = 100$  m, located in the x-y-plane and subdivided into  $100 \times 100 \times 1$  cubic elements. A permeable material represents the porous medium, which contains a liquid of small

and constant compressibility. Gravity is neglected via zero liquid density. Explicitly assigned properties of matrix and liquid are an isotropic permeability  $k = 10^{-14} \text{ m}^2$  and liquid viscosity  $\mu = 1.728 \text{ mPa} \cdot \text{s}$ . Porosity  $\phi$  and liquid compressibility  $\kappa$  have been incorporated in the storage  $\phi\kappa = 2 \times 10^{-10} \text{ 1/Pa}$ . Prescribed conditions prevail at the lateral boundaries of the domain as specified below. Given pressure  $p_0 = 1 \text{ MPa}$  and

$$f(x) = \begin{cases} 0 & \text{for } 0 \leq x \leq \frac{L}{10}, \\ \frac{10}{3L}x - \frac{1}{3} & \text{for } \frac{L}{10} \leq x \leq \frac{4L}{10}, \\ 1 & \text{for } \frac{4L}{10} \leq x \leq \frac{6L}{10}, \\ 3 - \frac{10}{3L}x & \text{for } \frac{6L}{10} \leq x \leq \frac{9L}{10}, \\ 0 & \text{for } \frac{9L}{10} \leq x \leq L, \end{cases} \quad (2.113)$$

the simulation starts from the initial pressure distribution  $p(x, y, 0) = p_0 \cdot f(x) \cdot f(y)$  and evaluates the transient pressure distribution  $p(x, y, t)$  with output after 0.02 and 0.04 days.

For liquids of small and constant compressibility Darcy's law and continuity equation yield the pressure conduction equation as the governing equation describing the transient pressure distribution. It reads

$$\phi\kappa \frac{\partial p}{\partial t} = \frac{k}{\mu} \nabla \cdot \nabla p. \quad (2.114)$$

Introducing the notation

$$\chi = \frac{k}{\phi\mu\kappa} \quad (2.115)$$

the present 2D problem is governed by the parabolic equation

$$\frac{1}{\chi} \frac{\partial p}{\partial t} = \frac{\partial^2 p}{\partial x^2} + \frac{\partial^2 p}{\partial y^2}, \quad (2.116)$$

the initial condition

$$p(x, y, 0) = p_0 \cdot f(x) \cdot f(y) \quad \text{for } 0 \leq x, y \leq L, \quad (2.117)$$

and the applied boundary conditions. These are specified zero pressures at  $x = 0$  and  $x = L$

$$p(0, y, t) = 0 \quad \text{for } 0 \leq y \leq L, \quad (2.118)$$

$$p(L, y, t) = 0 \quad \text{for } 0 \leq y \leq L, \quad (2.119)$$

and no-flow boundary conditions at  $y = 0$  and  $y = L$

$$\frac{\partial p}{\partial y}(x, 0, t) = 0 \quad \text{for } 0 \leq x \leq L, \quad (2.120)$$

$$\frac{\partial p}{\partial y}(x, L, t) = 0 \quad \text{for } 0 \leq x \leq L. \quad (2.121)$$

The closed form solution of the above problem is obtained in terms of the 1D p1-beam and p2-beam solutions given in the context of the previous example

$$\begin{aligned} p1(x, t) &= \sum_{n=1}^{\infty} \sin \frac{n\pi x}{L} \exp\left(-\chi n^2 \pi^2 \frac{t}{L^2}\right) \\ &\quad \times \frac{80}{3(n\pi)^2} \sin \frac{n\pi}{2} \sin \frac{n\pi}{4} \sin \frac{3n\pi}{20}, \end{aligned} \quad (2.122)$$

$$\begin{aligned} p2(x, t) &= \frac{1}{2} + \sum_{n=1}^{\infty} \cos \frac{n\pi x}{L} \exp\left(-\chi n^2 \pi^2 \frac{t}{L^2}\right) \\ &\quad \times \frac{80}{3(n\pi)^2} \cos \frac{n\pi}{2} \sin \frac{n\pi}{4} \sin \frac{3n\pi}{20}. \end{aligned} \quad (2.123)$$

We will next verify that the closed form solution of the above problem is given by

$$p(x, y, t) = p_0 \cdot p1(x, t) \cdot p2(y, t). \quad (2.124)$$

Both,  $p1(x, t)$  and  $p2(x, t)$ , satisfy the initial condition

$$p1(x, 0) = p2(x, 0) = f(x). \quad (2.125)$$

Then

$$p(x, y, 0) = p_0 \cdot p1(x, 0) \cdot p2(y, 0) = p_0 \cdot f(x) \cdot f(y), \quad (2.126)$$

hence,  $p(x, y, t)$  satisfies the initial condition.

Both,  $p1(x, t)$  and  $p2(y, t)$ , satisfy the 1D pressure conduction equation. Then

$$\begin{aligned} \frac{1}{\chi} \frac{\partial p}{\partial t} &= p_0 \left[ \frac{1}{\chi} p2 \frac{\partial p1}{\partial t} + \frac{1}{\chi} p1 \frac{\partial p2}{\partial t} \right] \\ &= p_0 \left[ p2 \frac{\partial^2 p1}{\partial x^2} + p1 \frac{\partial^2 p2}{\partial y^2} \right] \\ &= \frac{\partial^2 p}{\partial x^2} + \frac{\partial^2 p}{\partial y^2}, \end{aligned} \quad (2.127)$$

hence,  $p(x, y, t)$  satisfies the differential equation.

Zero boundary pressures are satisfied by  $p_1(x, t)$

$$p_1(0, t) = 0 \quad \text{for } t > 0, \quad (2.128)$$

$$p_1(L, t) = 0 \quad \text{for } t > 0, \quad (2.129)$$

no-flow boundary conditions are satisfied by  $p_2(y, t)$

$$\frac{\partial p_2}{\partial y}(0, t) = 0 \quad \text{for } t > 0, \quad (2.130)$$

$$\frac{\partial p_2}{\partial y}(L, t) = 0 \quad \text{for } t > 0. \quad (2.131)$$

Then

$$\begin{aligned} p(0, y, t) &= p_0 \cdot p_1(0, t) \cdot p_2(y, t) = 0 \cdot p_2(y, t) = 0, \\ p(L, y, t) &= p_0 \cdot p_1(L, t) \cdot p_2(y, t) = 0 \cdot p_2(y, t) = 0, \\ \frac{\partial p}{\partial y}(x, 0, t) &= p_0 \cdot p_1(x, t) \cdot \frac{\partial p_2}{\partial y}(0, t) = p_0 \cdot p_1(x, t) \cdot 0 = 0, \\ \frac{\partial p}{\partial y}(x, L, t) &= p_0 \cdot p_1(x, t) \cdot \frac{\partial p_2}{\partial y}(L, t) = p_0 \cdot p_1(x, t) \cdot 0 = 0, \end{aligned} \quad (2.132)$$

hence,  $p(x, y, t)$  satisfies the boundary conditions.

## 2.3 Gas Flow

Because the gas density strongly depends on pressure, the governing equations become non-linear. We present a few steady-state solutions of isothermal flow problems, for the underlying theory see Freeze and Cherry [5].

### 2.3.1 A 1D Steady-State Gas Pressure Distribution, Boundary Conditions of 1st Kind

The domain is a rectangular beam extending along the positive x-axis and composed of  $40 \times 1 \times 1$  equally sized hexahedral elements. An isotropic permeability of  $10^{-15} \text{ m}^2$  is assumed for the material, gas viscosity has been assigned  $10^{-5} \text{ Pa} \cdot \text{s}$ , gravity is neglected by default. Specified pressures prevail at the beam ends with prescribed values of  $p_1 = 10^5 \text{ Pa}$  at  $x = L = 100 \text{ m}$  and  $p_0 = 2 \times 10^5 \text{ Pa}$  at  $x = 0 \text{ m}$ . The simulation comprises one time step to establish the steady-state pressure distribution  $p(x)$ .

Darcy's law and continuity equation yield the Laplace equation governing the square of the steady-state gas pressure distribution. It reads

$$\frac{d^2 p^2}{dx^2} = 0 \quad (2.133)$$

for 1D gas flow along the x-axis, hence, the pressure is given by

$$p(x) = \sqrt{ax + b}. \quad (2.134)$$

The free constants,  $a$  and  $b$ , have to be determined from the specified boundary conditions at  $x = L$  and  $x = 0$  m, therefore,

$$p(x) = \sqrt{(p_1^2 - p_0^2) \frac{x}{L} + p_0^2}. \quad (2.135)$$

### 2.3.2 A 1D Steady-State Gas Pressure Distribution, Boundary Conditions of 1st and 2nd Kind

The domain is a rectangular beam of length  $L = 100$  m extending along the positive x-axis and composed of  $40 \times 1 \times 1$  equally sized hexahedral elements. An isotropic permeability  $k = 10^{-15} \text{ m}^2$  is assumed for the material, gas viscosity  $\mu = 10^{-5} \text{ Pa} \cdot \text{s}$  has been assigned, gravity is neglected by default. Prescribed boundary conditions prevail at the beam ends as specified below. The simulation comprises one time step to establish the steady-state pressure distribution  $p(x)$ .

Darcy's law and continuity equation yield the Laplace equation governing the square of the steady-state gas pressure distribution. It reads

$$\frac{d^2 p^2}{dx^2} = 0 \quad (2.136)$$

for 1D gas flow along the x-axis, hence, the pressure is given by

$$p(x) = \sqrt{ax + b}. \quad (2.137)$$

The free constants,  $a$  and  $b$ , have to be determined from the specified boundary conditions at  $x = L$  and  $x = 0$  m. Pressure  $p_1 = 10^5 \text{ Pa}$  prevails at  $x = L$ , hence,

$$b = p_1^2 - aL. \quad (2.138)$$

Specific gas flow  $Q = 0.17 \text{ Pa} \cdot \text{m/s}$  has been assigned at  $x = 0$  m. Then, by Darcy's law,

$$Q = -\frac{k}{\mu} p \frac{dp}{dx} \Big|_{x=0} = -\frac{k}{2\mu} \frac{dp^2}{dx} \Big|_{x=0} = -\frac{k}{2\mu} a. \quad (2.139)$$

The pressure distribution  $p(x)$  thus becomes

$$p(x) = \sqrt{\frac{2Q\mu}{k}(L - x) + p_1^2}. \quad (2.140)$$

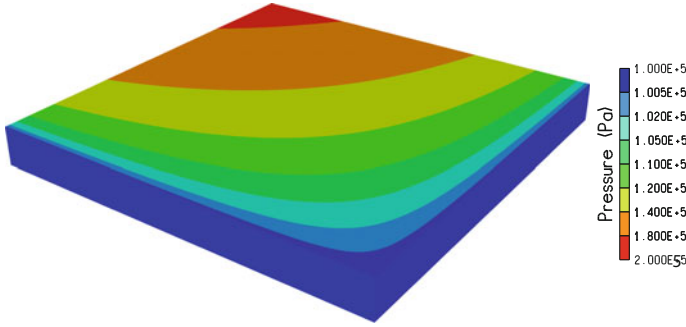


**Fig. 2.9** Pressure distribution

### 2.3.3 A 2D Steady-State Gas Pressure Distribution

Given length  $L = 1$  m the domain represents the square  $[0, L] \times [0, L]$  in the  $x$ - $y$ -plane, discretized by an irregular mesh of hexahedral elements. An isotropic permeability  $k = 10^{-15} \text{ m}^2$  is assumed for the material, gas viscosity  $\mu = 10^{-5} \text{ Pa} \cdot \text{s}$  has been assigned, gravity is neglected by default. Prescribed conditions prevail at the lateral boundaries of the domain as specified below. The simulation comprises one time step to establish the steady-state pressure distribution  $p(x, y)$  (Fig. 2.9).

Darcy's law and continuity equation yield the Laplace equation governing the square of the steady-state gas pressure distribution. It reads

$$\frac{\partial^2 p^2}{\partial x^2} + \frac{\partial^2 p^2}{\partial y^2} = 0 \quad (2.141)$$

for 2D gas flow in the  $x$ - $y$ -plane. With the aid of pressure  $p_0 = 10^5 \text{ Pa}$  the applied boundary conditions read

$$\begin{aligned} p^2(0, y) &= p_0^2 && \text{for } 0 \leq y \leq L, \\ p^2(x, 0) &= p_0^2 && \text{for } 0 \leq x \leq L, \\ \frac{\partial p^2}{\partial x}(L, y) &= 3 \frac{p_0^2}{L} \frac{y}{L} && \text{for } 0 \leq y \leq L, \\ \frac{\partial p^2}{\partial y}(x, L) &= 3 \frac{p_0^2}{L} \frac{x}{L} && \text{for } 0 \leq x \leq L. \end{aligned} \quad (2.142)$$

The pressure distribution

$$p(x, y) = p_0 \sqrt{1 + 3 \frac{xy}{L^2}} \quad (2.143)$$

satisfies the differential equation and the boundary conditions, hence, this is the closed form solution of the above boundary value problem.

Data input represents the second kind boundary conditions with the aid of a specific gas flow  $Q$ , which acts as a gas source to the domain at the faces  $x = L$  and  $y = L$ . By Darcy's law,

$$Q = \frac{k}{\mu} p \frac{dp}{dx} \Big|_{x=L} = \frac{k}{2\mu} \frac{dp^2}{dx} \Big|_{x=L} = \frac{3k}{2\mu} \frac{p_0^2}{L} \frac{y}{L} \quad (2.144)$$

at the face  $x = L$ , and

$$Q = \frac{k}{\mu} p \frac{dp}{dy} \Big|_{y=L} = \frac{k}{2\mu} \frac{dp^2}{dy} \Big|_{y=L} = \frac{3k}{2\mu} \frac{p_0^2}{L} \frac{x}{L} \quad (2.145)$$

at the face  $y = L$ .

### 2.3.4 A 3D Steady-State Gas Pressure Distribution

Given length  $L = 1$  m the domain represents the cube  $[0, L] \times [0, L] \times [0, L]$  discretized by  $21 \times 22 \times 23$  equally sized hexahedral elements. An isotropic permeability  $k = 10^{-15}$  m<sup>2</sup> is assumed for the material, gas viscosity  $\mu = 10^{-5}$  Pa · s has been assigned, gravity is neglected by default. Prescribed 2nd kind boundary conditions prevail at the entire surface of the domain as specified below. The simulation comprises one time step to establish the steady-state pressure distribution  $p(x, y, z)$  (Fig. 2.10).

Darcy's law and continuity equation yield the Laplace equation governing the square of the steady-state gas pressure distribution. It reads

$$\frac{\partial^2 p^2}{\partial x^2} + \frac{\partial^2 p^2}{\partial y^2} + \frac{\partial^2 p^2}{\partial z^2} = 0. \quad (2.146)$$

With the aid of pressure  $p_0 = 10^5$  Pa the applied boundary conditions read

$$\begin{aligned} p^2(0, 0, 0) &= p_0^2, \\ \frac{\partial p^2}{\partial x}(0, y, z) &= \frac{3}{2} \frac{p_0^2}{L} \frac{y}{L} \quad \text{on the face } x = 0, \\ \frac{\partial p^2}{\partial x}(L, y, z) &= \frac{3}{2} \frac{p_0^2}{L} \frac{y}{L} \quad \text{on the face } x = L, \\ \frac{\partial p^2}{\partial y}(x, 0, z) &= \frac{3}{2} \frac{p_0^2}{L} \frac{x}{L} \quad \text{on the face } y = 0, \\ \frac{\partial p^2}{\partial y}(x, L, z) &= \frac{3}{2} \frac{p_0^2}{L} \frac{x}{L} \quad \text{on the face } y = L, \end{aligned} \quad (2.147)$$

$$\begin{aligned} \frac{\partial p^2}{\partial z}(x, y, 0) &= \frac{3}{2} \frac{p_0^2}{L} && \text{on the face } z = 0, \\ \frac{\partial p^2}{\partial z}(x, y, L) &= \frac{3}{2} \frac{p_0^2}{L} && \text{on the face } z = L. \end{aligned}$$

The pressure distribution

$$p(x, y, z) = p_0 \sqrt{1 + \frac{3}{2} \left( \frac{x}{L} \cdot \frac{y}{L} + \frac{z}{L} \right)} \tag{2.148}$$

satisfies the differential equation and the boundary conditions, hence, this is the closed form solution of the above boundary value problem.

Data input represents the second kind boundary conditions with the aid of a specific gas flow  $Q$ . It acts as a gas source to the domain on the faces  $x = L$ ,  $y = L$ , and  $z = L$  and acts as a sink on the remainder. On the face  $x = L$  we have by Darcy's law

$$Q = \frac{k}{\mu} p \frac{\partial p}{\partial x} \Big|_{x=L} = \frac{k}{2\mu} \frac{\partial p^2}{\partial x} \Big|_{x=L} = \frac{3k}{4\mu} \frac{p_0^2}{L} \frac{y}{L}, \tag{2.149}$$

and similarly for the five other faces.

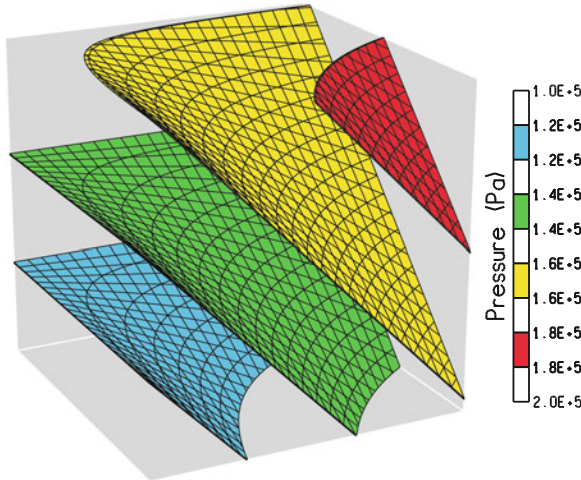


**Fig. 2.10** Pressure contours

## 2.4 Deformation Processes

The linear elastic material is subject of the steady-state problems. Our transient problems focus on the Norton material. For the underlying theory see Jaeger and Cook [6].

### 2.4.1 An Elastic Beam Undergoes Axial Load

The domain is a rectangular beam extending along the positive x-axis. It has three faces located on the coordinate planes and is discretized by  $20 \times 2 \times 2$  cubic elements of 0.05 m edge size each. The beam is represented by an elastic material. Poisson's ratio  $\nu = 0.25$  and Young's modulus  $E = 10,000$  MPa have been assigned, gravity is neglected via zero material density. Faces on the coordinate planes are sliding planes, the top and the rear face of the beam are free, a tensile stress  $\sigma_0 = 2$  MPa is applied at the  $x = 1$  m face. The simulation comprises one time step to establish the stresses, strains, and displacements.

Let  $\sigma$  denote the stress tensor. The equation of mechanical equilibrium

$$\nabla \cdot \sigma = 0 \quad (2.150)$$

is satisfied by zero shear and constant stresses

$$\begin{aligned} \sigma_{11} &= \sigma_0, \\ \sigma_{22} &= \sigma_{33} = 0. \end{aligned} \quad (2.151)$$

Then, with principal axes equal to coordinate axes, Hooke's law gives for the strains

$$\begin{aligned} \epsilon_{11} &= \frac{1}{E}[\sigma_{11} - \nu(\sigma_{22} + \sigma_{33})] = \frac{\sigma_0}{E}, \\ \epsilon_{22} &= \frac{1}{E}[\sigma_{22} - \nu(\sigma_{11} + \sigma_{33})] = -\nu \frac{\sigma_0}{E}, \\ \epsilon_{33} &= \frac{1}{E}[\sigma_{33} - \nu(\sigma_{11} + \sigma_{22})] = -\nu \frac{\sigma_0}{E}. \end{aligned} \quad (2.152)$$

Integrating the strains with respect to the fixities at the coordinate planes yields the displacement vector  $(u_x, u_y, u_z)$

$$\begin{aligned} u_x(x) &= \frac{\sigma_0}{E}x, \\ u_y(y) &= -\nu \frac{\sigma_0}{E}y, \\ u_z(z) &= -\nu \frac{\sigma_0}{E}z. \end{aligned} \quad (2.153)$$

### 2.4.2 An Elastic Plate Undergoes Simple Shear

The domain is a rectangular plate located in the first octant. It has an extent of 10 m in  $x$ - and  $y$ -direction and is discretized by  $8 \times 8 \times 2$  equally sized hexahedral elements. The plate is represented by an elastic material. Young's modulus  $E = 10,000$  MPa and Poisson's ratio  $\nu = 0.25$  have been assigned, gravity is neglected via zero material density. Load is applied with the aid of prescribed displacements which cover the entire surface. The simulation comprises two time steps with increasing deformation as specified below.

The equation of mechanical equilibrium and Hooke's law yield the Navier equations describing mechanical equilibrium in terms of the displacement vector  $(u_x, u_y, u_z)$ . Employing the notation

$$\frac{\partial u_x}{\partial x} + \frac{\partial u_y}{\partial y} + \frac{\partial u_z}{\partial z} = e \quad (2.154)$$

the Navier equations read

$$\begin{aligned} \frac{\partial^2 u_x}{\partial x^2} + \frac{\partial^2 u_x}{\partial y^2} + \frac{\partial^2 u_x}{\partial z^2} + \frac{1}{1-2\nu} \frac{\partial e}{\partial x} &= 0, \\ \frac{\partial^2 u_y}{\partial x^2} + \frac{\partial^2 u_y}{\partial y^2} + \frac{\partial^2 u_y}{\partial z^2} + \frac{1}{1-2\nu} \frac{\partial e}{\partial y} &= 0, \\ \frac{\partial^2 u_z}{\partial x^2} + \frac{\partial^2 u_z}{\partial y^2} + \frac{\partial^2 u_z}{\partial z^2} + \frac{1}{1-2\nu} \frac{\partial e}{\partial z} &= 0. \end{aligned} \quad (2.155)$$

With the aid of slope  $m$  the specified boundary conditions are given by

$$\begin{aligned} u_x(x, y, z) &= 0 \quad \text{on the entire surface,} \\ u_y(x, y, z) &= m x \quad \text{on the entire surface,} \\ u_z(x, y, z) &= 0 \quad \text{on the entire surface.} \end{aligned} \quad (2.156)$$

The displacement vector

$$\begin{aligned} u_x(x, y, z) &= 0, \\ u_y(x, y, z) &= m x, \\ u_z(x, y, z) &= 0 \end{aligned} \quad (2.157)$$

satisfies the Navier equations and the specified boundary conditions, hence, this is the required solution of the above boundary value problem. The only non-zero strain is

$$\epsilon_{12} = \frac{\partial u_y}{\partial x} = m, \quad (2.158)$$

and Hooke's law yields for the associated stress

$$\sigma_{12} = \frac{E}{2(1 + \nu)} m. \tag{2.159}$$

The two time steps have  $m$  assigned the values  $-0.1$  and  $-0.2$ , respectively.

### 2.4.3 An Elastic Cuboid Undergoes Load Due to Gravity

The domain is a cuboid of height  $H = 30$  m and edges parallel to the  $x$ - $y$ - $z$  coordinate axes. It is discretized by an irregular mesh of hexahedral elements. The cuboid is represented by four groups of elastic materials, where each has been assigned density  $\rho = 3058.104$  kg/m<sup>3</sup>, Poisson’s ratio  $\nu = 0.25$  and Young’s modulus  $E = 10,000$  MPa. The bottom and the lateral faces are sliding planes, the top face is free. Gravity is the only load applied,  $g = 9.81$  m/s<sup>2</sup> is the magnitude of gravity. The simulation comprises one time step to establish the stresses, strains, and displacements (Fig. 2.11).

Let  $\sigma$  denote the stress tensor. The equation of mechanical equilibrium

$$0 = \nabla \cdot \sigma - (0, 0, \rho g) \tag{2.160}$$

is satisfied by zero shear, if the horizontal stresses  $\sigma_{11}$  and  $\sigma_{22}$  are functions of the vertical coordinate  $z$  only and the vertical stress  $\sigma_{33}$  satisfies

$$\frac{\partial \sigma_{33}}{\partial z} = \rho g. \tag{2.161}$$

The face  $z = H$  is free, hence, integration gives

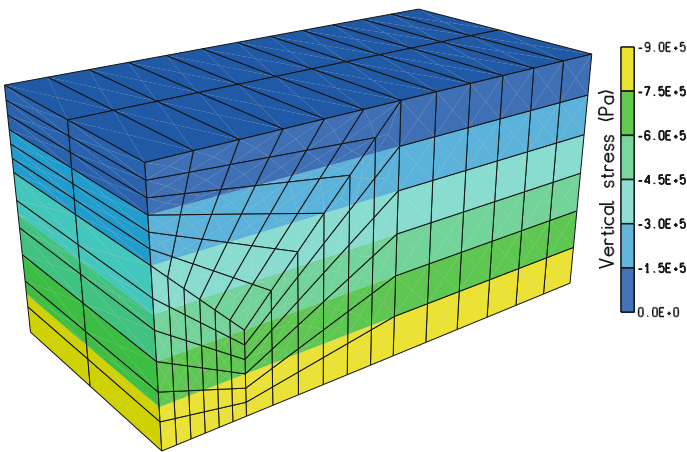


Fig. 2.11 Vertical stress

$$\sigma_{33} = \rho(-g)(H - z). \quad (2.162)$$

Assuming that there is no horizontal displacement anywhere we have for the horizontal strains

$$\epsilon_{11} = \epsilon_{22} = 0. \quad (2.163)$$

Then, with principal axes equal to coordinate axes, Hooke's law gives

$$\begin{aligned} 0 &= \sigma_{11} - \nu(\sigma_{22} + \sigma_{33}), \\ 0 &= \sigma_{22} - \nu(\sigma_{11} + \sigma_{33}), \\ E\epsilon_{33} &= \sigma_{33} - \nu(\sigma_{11} + \sigma_{22}). \end{aligned} \quad (2.164)$$

Solving for  $\sigma_{11}$ ,  $\sigma_{22}$ , and the vertical strain  $\epsilon_{33}$  yields

$$\begin{aligned} \sigma_{11} = \sigma_{22} &= \frac{\nu}{1-\nu} \sigma_{33} = \frac{\nu}{1-\nu} \rho(-g)(H - z), \\ \epsilon_{33} &= \frac{1}{E} \left( 1 - \frac{2\nu^2}{1-\nu} \right) \rho(-g)(H - z) \end{aligned} \quad (2.165)$$

in terms of the vertical coordinate. Integrating the strains with respect to the prescribed fixities yields the displacement vector  $(u_x, u_y, u_z)$

$$\begin{aligned} u_x &= u_y = 0, \\ u_z(z) &= \frac{1}{E} \left( 1 - \frac{2\nu^2}{1-\nu} \right) \rho(-g) \left( Hz - \frac{1}{2}z^2 \right). \end{aligned} \quad (2.166)$$

#### 2.4.4 Stresses Relax in a Deformed Cube of Norton Material

The domain is a single cube with edge size  $L = 1$  m located in the first octant. It has three faces located on the coordinate planes and is discretized by  $2 \times 2 \times 2$  cubic elements. The cube is represented by a Norton material. Poisson's ratio  $\nu = 0.27$  and Young's modulus  $E = 25,000$  MPa have been assigned, gravity is neglected via zero material density. Various additional parameters are involved in the rheological model, details are given below. Faces on the coordinate planes are sliding planes. The constant vertical displacement  $w = 0.0012$  m is applied at the top face for times  $t > 0$ . Starting from an initial setup free of load the simulation evaluates stresses, strains, and displacements through time with output after 0.1 and 1.1 days.

Let  $\sigma$  denote the stress tensor,  $\mathbf{I}$  the unit tensor,

$$\sigma^D = \sigma - \frac{\text{tr}\sigma}{3} \mathbf{I} \quad (2.167)$$

the stress deviator, and

$$\sigma_{\text{eff}} = \sqrt{\frac{3}{2} \sum_{i=1}^3 \sum_{j=1}^3 \sigma_{ij}^D \sigma_{ji}^D} \quad (2.168)$$

the v. Mises or effective stress. The rheological model involved yields the fundamental stress/strain relationships as a system of differential equations for the creep strains

$$\frac{\partial \epsilon^{cr}}{\partial t} = \frac{3}{2} \frac{\sigma^D}{\sigma_{\text{eff}}} (N \sigma_{\text{eff}}^n) \quad (2.169)$$

and the total strains

$$\epsilon^{tot} = \epsilon^{el} + \epsilon^{cr}, \quad (2.170)$$

where  $\epsilon^{el}$  denotes the elastic strains via Hooke's law. Both equations have to be solved with respect to the imposed initial and boundary conditions.

For the present example the behaviour of the Norton material is specified with the aid of the parameters

$$\begin{aligned} n &= 5, \\ N &= A \exp\left(-\frac{Q}{RT}\right), \end{aligned} \quad (2.171)$$

where  $R = 8.31441 \text{ J}/(\text{mol} \cdot \text{K})$  is the gas constant,  $T$  is the absolute temperature (we have  $T = 273.15 \text{ K}$  by default), and experimental data obtained from rock salt yield

$$\begin{aligned} A &= 0.18 \text{ 1}/(\text{d} \cdot \text{MPa}^5), \\ Q &= 54,000 \text{ J/mol}. \end{aligned} \quad (2.172)$$

Note that day is required as unit of time and stresses have to be in MPa.

Due to the example setup the principal axes are identical to the coordinate axes and the vertical stress is the only non-zero element of the stress tensor. Therefore,

$$\sigma = \begin{pmatrix} 0 & 0 & 0 \\ 0 & 0 & 0 \\ 0 & 0 & \sigma_{33} \end{pmatrix}, \quad (2.173)$$

the trace of  $\sigma$

$$\text{tr} \sigma = \sigma_{33}, \quad (2.174)$$

the stress deviator

$$\sigma^D = \frac{\sigma_{33}}{3} \begin{pmatrix} -1 & 0 & 0 \\ 0 & -1 & 0 \\ 0 & 0 & 2 \end{pmatrix}, \quad (2.175)$$

the v. Mises or effective stress

$$\sigma_{\text{eff}} = |\sigma_{33}| \frac{\sqrt{3/2}}{3} \sqrt{1^2 + 1^2 + 2^2} = |\sigma_{33}|, \quad (2.176)$$

and the time derivative of the creep strains

$$\frac{\partial \epsilon^{cr}}{\partial t} = \frac{N}{2} \sigma_{33}^5 \begin{pmatrix} -1 & 0 & 0 \\ 0 & -1 & 0 \\ 0 & 0 & 2 \end{pmatrix}. \quad (2.177)$$

The entire domain is initially free of creep strains. Hence, integrating with respect to time  $t$  the creep strains become

$$\epsilon^{cr} = \frac{N}{2} \begin{pmatrix} -1 & 0 & 0 \\ 0 & -1 & 0 \\ 0 & 0 & 2 \end{pmatrix} \int_0^t \sigma_{33}^5 dt. \quad (2.178)$$

The elastic strains are obtained from the stress  $\sigma$  via Hooke's law

$$\epsilon^{el} = \frac{\sigma_{33}}{E} \begin{pmatrix} -\nu & 0 & 0 \\ 0 & -\nu & 0 \\ 0 & 0 & 1 \end{pmatrix}. \quad (2.179)$$

The total strains in terms of  $\sigma_{33}$  and the displacements  $(u_x, u_y, u_z)$  read

$$\begin{aligned} \epsilon^{tot} &= \epsilon^{el} + \epsilon^{cr} = \begin{pmatrix} \partial u_x / \partial x & 0 & 0 \\ 0 & \partial u_y / \partial y & 0 \\ 0 & 0 & \partial u_z / \partial z \end{pmatrix} \\ &= \frac{\sigma_{33}}{E} \begin{pmatrix} -\nu & 0 & 0 \\ 0 & -\nu & 0 \\ 0 & 0 & 1 \end{pmatrix} + \frac{N}{2} \begin{pmatrix} -1 & 0 & 0 \\ 0 & -1 & 0 \\ 0 & 0 & 2 \end{pmatrix} \int_0^t \sigma_{33}^5 dt. \end{aligned} \quad (2.180)$$

Due to the simulation setup

$$\epsilon_{33}^{tot} = \frac{\partial u_z}{\partial z} = \frac{w}{L} \quad (2.181)$$

is the specified constant strain along the z-axis. Then

$$\frac{w}{L} = \frac{1}{E} \sigma_{33} + N \int_0^t \sigma_{33}^5 dt. \quad (2.182)$$

This integral equation is transformed into the ordinary differential equation

$$0 = \frac{1}{E} \frac{d\sigma_{33}}{dt} + N \sigma_{33}^5. \quad (2.183)$$

Separation of variables and integration yields

$$\sigma_{33}(t) = \frac{w}{L} \frac{E}{\sqrt[4]{4E^5(w/L)^4 Nt + 1}}, \quad (2.184)$$

and the strains  $\partial u_x/\partial x$  and  $\partial u_y/\partial y$  are obtained in terms of  $\sigma_{33}(t)$

$$\begin{aligned} \epsilon_{11}^{tot}(t) &= \frac{\partial u_x}{\partial x} = -\frac{w}{2L} + \frac{1-2\nu}{2E} \sigma_{33}(t), \\ \epsilon_{22}^{tot}(t) &= \frac{\partial u_y}{\partial y} = -\frac{w}{2L} + \frac{1-2\nu}{2E} \sigma_{33}(t). \end{aligned} \quad (2.185)$$

Integrating the strains with respect to the fixities at the coordinate planes yields the displacement vector  $(u_x, u_y, u_z)$

$$\begin{aligned} u_x(x, t) &= x \left( -\frac{w}{2L} + \frac{1-2\nu}{2E} \sigma_{33}(t) \right), \\ u_y(y, t) &= y \left( -\frac{w}{2L} + \frac{1-2\nu}{2E} \sigma_{33}(t) \right), \\ u_z(z, t) &= z \frac{w}{L} \end{aligned} \quad (2.186)$$

again in terms of  $\sigma_{33}(t)$  derived above.

### 2.4.5 A Cube of Norton Material Creeps Under Constant Stress

The domain is a single cube with an edge size of 1 m located in the first octant. It has three faces located on the coordinate planes and is discretized by  $2 \times 2 \times 2$  cubic elements. The cube is represented by a Norton material. Poisson's ratio  $\nu = 0.27$  and Young's modulus  $E = 25,000$  MPa have been assigned, gravity is neglected via zero material density. The additional parameters involved in the rheological model are identical to those of the previous example. Faces on the coordinate planes are sliding planes. The constant vertical stress  $\sigma_0 = -20$  MPa is applied at the top face for times  $t > 0$ . Starting from an initial setup free of load the simulation evaluates stresses, strains, and displacements through time with output after 10 and 20 days.

The rheological model of the Norton material and its underlying theory have been sketched just before; we focus on the special features of the present example. Due to the setup the principal axes are identical to the coordinate axes and the specified vertical stress is the only non-zero element of the stress tensor. Therefore,

$$\boldsymbol{\sigma} = \begin{pmatrix} 0 & 0 & 0 \\ 0 & 0 & 0 \\ 0 & 0 & \sigma_0 \end{pmatrix}, \quad (2.187)$$

the trace of  $\sigma$

$$\text{tr}\sigma = \sigma_0, \quad (2.188)$$

the stress deviator

$$\sigma^D = \frac{\sigma_0}{3} \begin{pmatrix} -1 & 0 & 0 \\ 0 & -1 & 0 \\ 0 & 0 & 2 \end{pmatrix}, \quad (2.189)$$

the v. Mises or effective stress

$$\sigma_{\text{eff}} = |\sigma_0| \frac{\sqrt{3/2}}{3} \sqrt{1^2 + 1^2 + 2^2} = |\sigma_0|, \quad (2.190)$$

and the time derivative of the creep strains

$$\frac{\partial \epsilon^{cr}}{\partial t} = \frac{N}{2} \sigma_0^5 \begin{pmatrix} -1 & 0 & 0 \\ 0 & -1 & 0 \\ 0 & 0 & 2 \end{pmatrix}. \quad (2.191)$$

The entire domain is initially free of creep strains. Hence, integrating with respect to time  $t$  the creep strains become

$$\epsilon^{cr} = \frac{N}{2} \sigma_0^5 \begin{pmatrix} -t & 0 & 0 \\ 0 & -t & 0 \\ 0 & 0 & 2t \end{pmatrix}. \quad (2.192)$$

The elastic strains are obtained from the stress  $\sigma$  via Hooke's law

$$\epsilon^{el} = \frac{\sigma_0}{E} \begin{pmatrix} -\nu & 0 & 0 \\ 0 & -\nu & 0 \\ 0 & 0 & 1 \end{pmatrix}. \quad (2.193)$$

The total strains in terms of the displacements  $(u_x, u_y, u_z)$  read

$$\epsilon^{tot} = \epsilon^{el} + \epsilon^{cr} = \begin{pmatrix} \partial u_x / \partial x & 0 & 0 \\ 0 & \partial u_y / \partial y & 0 \\ 0 & 0 & \partial u_z / \partial z \end{pmatrix}. \quad (2.194)$$

The strains  $\partial u_x / \partial x$ ,  $\partial u_y / \partial y$ , and  $\partial u_z / \partial z$  are thus given by

$$\begin{aligned}
\epsilon_{11}^{tot}(t) &= \frac{\partial u_x}{\partial x} = -\frac{\nu\sigma_0}{E} - \frac{N}{2}\sigma_0^5 t, \\
\epsilon_{22}^{tot}(t) &= \frac{\partial u_y}{\partial y} = -\frac{\nu\sigma_0}{E} - \frac{N}{2}\sigma_0^5 t, \\
\epsilon_{33}^{tot}(t) &= \frac{\partial u_z}{\partial z} = \frac{\sigma_0}{E} + N\sigma_0^5 t.
\end{aligned}
\tag{2.195}$$

Integrating the strains with respect to the fixities at the coordinate planes yields the displacement vector  $(u_x, u_y, u_z)$

$$\begin{aligned}
u_x(x, t) &= x \left( -\frac{\nu\sigma_0}{E} - \frac{N}{2}\sigma_0^5 t \right), \\
u_y(y, t) &= y \left( -\frac{\nu\sigma_0}{E} - \frac{N}{2}\sigma_0^5 t \right), \\
u_z(z, t) &= z \left( \frac{\sigma_0}{E} + N\sigma_0^5 t \right).
\end{aligned}
\tag{2.196}$$

#### 2.4.6 A Cube of Norton Material Undergoes Tensile Strain Increasing Linearly with Time

The domain is a single cube with edge size  $L = 1$  m located in the first octant. It has three faces located on the coordinate planes and is discretized by  $2 \times 2 \times 2$  cubic elements. The cube is represented by a Norton material. Poisson's ratio  $\nu = 0.27$  and Young's modulus  $E = 2.5 \times 10^7$  MPa have been assigned, gravity is neglected via zero material density. Except from the stress exponent  $n$ , which now has  $n = 2$ , the values of the additional parameters involved in the rheological model are identical to those of the two previous examples. Faces on the coordinate planes are sliding planes. The vertical displacement  $w_1 \cdot t$  ( $w_1 = 0.0001$  m/d) increases linearly with time  $t$ , it is applied at the top face for times  $t > 0$ . Starting from an initial setup free of load the simulation evaluates stresses, strains, and displacements through time with output after 1.5 and 3.0 days.

The rheological model of the Norton material and its underlying theory have already been outlined before; we focus on the special features of the present example. Due to the setup the principal axes are identical to the coordinate axes and the vertical stress is the only non-zero element of the stress tensor. Therefore,

$$\boldsymbol{\sigma} = \begin{pmatrix} 0 & 0 & 0 \\ 0 & 0 & 0 \\ 0 & 0 & \sigma_{33} \end{pmatrix},
\tag{2.197}$$

the trace of  $\boldsymbol{\sigma}$

$$\text{tr}\boldsymbol{\sigma} = \sigma_{33},
\tag{2.198}$$

the stress deviator

$$\boldsymbol{\sigma}^D = \frac{\sigma_{33}}{3} \begin{pmatrix} -1 & 0 & 0 \\ 0 & -1 & 0 \\ 0 & 0 & 2 \end{pmatrix}, \quad (2.199)$$

the v. Mises or effective stress

$$\sigma_{\text{eff}} = |\sigma_{33}| \frac{\sqrt{3/2}}{3} \sqrt{1^2 + 1^2 + 2^2} = |\sigma_{33}|, \quad (2.200)$$

and the time derivative of the (positive) creep strains

$$\frac{\partial \boldsymbol{\epsilon}^{cr}}{\partial t} = \frac{N}{2} \sigma_{33}^2 \begin{pmatrix} -1 & 0 & 0 \\ 0 & -1 & 0 \\ 0 & 0 & 2 \end{pmatrix}. \quad (2.201)$$

The entire domain is initially free of creep strains. Hence, integrating with respect to time  $t$  the creep strains become

$$\boldsymbol{\epsilon}^{cr} = \frac{N}{2} \begin{pmatrix} -1 & 0 & 0 \\ 0 & -1 & 0 \\ 0 & 0 & 2 \end{pmatrix} \int_0^t \sigma_{33}^2 dt. \quad (2.202)$$

The elastic strains are obtained from the stress  $\boldsymbol{\sigma}$  via Hooke's law

$$\boldsymbol{\epsilon}^{el} = \frac{\sigma_{33}}{E} \begin{pmatrix} -\nu & 0 & 0 \\ 0 & -\nu & 0 \\ 0 & 0 & 1 \end{pmatrix}. \quad (2.203)$$

The total strains in terms of  $\sigma_{33}$  and the displacements  $(u_x, u_y, u_z)$  read

$$\begin{aligned} \boldsymbol{\epsilon}^{tot} &= \boldsymbol{\epsilon}^{el} + \boldsymbol{\epsilon}^{cr} = \begin{pmatrix} \partial u_x / \partial x & 0 & 0 \\ 0 & \partial u_y / \partial y & 0 \\ 0 & 0 & \partial u_z / \partial z \end{pmatrix} \\ &= \frac{\sigma_{33}}{E} \begin{pmatrix} -\nu & 0 & 0 \\ 0 & -\nu & 0 \\ 0 & 0 & 1 \end{pmatrix} + \frac{N}{2} \begin{pmatrix} -1 & 0 & 0 \\ 0 & -1 & 0 \\ 0 & 0 & 2 \end{pmatrix} \int_0^t \sigma_{33}^2 dt. \end{aligned} \quad (2.204)$$

Due to the simulation setup

$$\epsilon_{33}^{tot} = \frac{\partial u_z}{\partial z} = \frac{w_1}{L} t \quad (2.205)$$

is the specified strain along the z-axis. Then

$$\frac{w_1}{L} t = \frac{1}{E} \sigma_{33} + N \int_0^t \sigma_{33}^2 dt. \quad (2.206)$$

This integral equation is transformed into the ordinary differential equation

$$\frac{w_1}{L} = \frac{1}{E} \frac{d\sigma_{33}}{dt} + N\sigma_{33}^2. \quad (2.207)$$

Separation of variables and integration yields

$$ENt = \sqrt{\frac{LN}{4w_1}} \ln \left| \frac{\sqrt{w_1/(LN)} + \sigma_{33}}{\sqrt{w_1/(LN)} - \sigma_{33}} \right|, \quad (2.208)$$

the vertical stress  $\sigma_{33}$  becomes

$$\sigma_{33}(t) = \sqrt{\frac{w_1}{LN}} \tanh(\sqrt{w_1 N/L} E t), \quad (2.209)$$

and the strains  $\partial u_x/\partial x$  and  $\partial u_y/\partial y$  are obtained in terms of  $\sigma_{33}(t)$

$$\begin{aligned} \epsilon_{11}^{tot}(t) &= \frac{\partial u_x}{\partial x} = -\frac{w_1}{2L} t + \frac{1-2\nu}{2E} \sigma_{33}(t), \\ \epsilon_{22}^{tot}(t) &= \frac{\partial u_y}{\partial y} = -\frac{w_1}{2L} t + \frac{1-2\nu}{2E} \sigma_{33}(t). \end{aligned} \quad (2.210)$$

Integrating the strains with respect to the fixities at the coordinate planes yields the displacement vector  $(u_x, u_y, u_z)$

$$\begin{aligned} u_x(x, t) &= x \left( -\frac{w_1}{2L} t + \frac{1-2\nu}{2E} \sigma_{33}(t) \right), \\ u_y(y, t) &= y \left( -\frac{w_1}{2L} t + \frac{1-2\nu}{2E} \sigma_{33}(t) \right), \\ u_z(z, t) &= z \frac{w_1}{L} t \end{aligned} \quad (2.211)$$

again in terms of  $\sigma_{33}(t)$  derived above.

### 2.4.7 A Cube of Norton Material Undergoes Compressive Stress Increasing Linearly with Time

The domain is a single cube with an edge size of 1 m located in the first octant. It has three faces located on the coordinate planes and is discretized by  $2 \times 2 \times 2$  cubic elements. The cube is represented by a Norton material. Poisson's ratio  $\nu = 0.27$  and Young's modulus  $E = 25,000$  MPa have been assigned, gravity is neglected via zero material density. Except from the stress exponent  $n$ , which now has  $n = 5$  again, the values of the additional parameters involved in the rheological model are identical

to those of the three previous examples. Faces on the coordinate planes are sliding planes. The vertical stress  $\sigma_1 \cdot t$  ( $\sigma_1 = -1$  MPa/d) depends linearly on time  $t$ , it is applied at the top face for times  $t > 0$ . Starting from an initial setup free of load the simulation evaluates stresses, strains, and displacements through time with output after 15 and 30 days.

The rheological model of the Norton material and its underlying theory have already been outlined before; we focus on the special features of the present example. Due to the setup the principal axes are identical to the coordinate axes and the specified vertical stress is the only non-zero element of the stress tensor. Therefore,

$$\boldsymbol{\sigma} = \begin{pmatrix} 0 & 0 & 0 \\ 0 & 0 & 0 \\ 0 & 0 & \sigma_1 \cdot t \end{pmatrix}, \quad (2.212)$$

the trace of  $\boldsymbol{\sigma}$

$$\text{tr}\boldsymbol{\sigma} = \sigma_1 \cdot t, \quad (2.213)$$

the stress deviator

$$\boldsymbol{\sigma}^D = \frac{\sigma_1 \cdot t}{3} \begin{pmatrix} -1 & 0 & 0 \\ 0 & -1 & 0 \\ 0 & 0 & 2 \end{pmatrix}, \quad (2.214)$$

the v. Mises or effective stress

$$\sigma_{\text{eff}} = |\sigma_1 \cdot t| \frac{\sqrt{3/2}}{3} \sqrt{1^2 + 1^2 + 2^2} = |\sigma_1 \cdot t|, \quad (2.215)$$

and the time derivative of the creep strains

$$\frac{\partial \boldsymbol{\epsilon}^{cr}}{\partial t} = \frac{N}{2} (\sigma_1 \cdot t)^5 \begin{pmatrix} -1 & 0 & 0 \\ 0 & -1 & 0 \\ 0 & 0 & 2 \end{pmatrix}. \quad (2.216)$$

The entire domain is initially free of creep strains. Hence, integrating with respect to time  $t$  the creep strains become

$$\boldsymbol{\epsilon}^{cr} = \frac{N}{12} \sigma_1^5 t^6 \begin{pmatrix} -1 & 0 & 0 \\ 0 & -1 & 0 \\ 0 & 0 & 2 \end{pmatrix}. \quad (2.217)$$

The elastic strains are obtained from the stress  $\boldsymbol{\sigma}$  via Hooke's law

$$\boldsymbol{\epsilon}^{el} = \frac{\sigma_1 \cdot t}{E} \begin{pmatrix} -\nu & 0 & 0 \\ 0 & -\nu & 0 \\ 0 & 0 & 1 \end{pmatrix}. \quad (2.218)$$

The total strains in terms of the displacements ( $u_x, u_y, u_z$ ) read

$$\epsilon^{tot} = \epsilon^{el} + \epsilon^{cr} = \begin{pmatrix} \partial u_x / \partial x & 0 & 0 \\ 0 & \partial u_y / \partial y & 0 \\ 0 & 0 & \partial u_z / \partial z \end{pmatrix}, \quad (2.219)$$

the strains  $\partial u_x / \partial x$ ,  $\partial u_y / \partial y$ , and  $\partial u_z / \partial z$  are thus given by

$$\begin{aligned} \epsilon_{11}^{tot}(t) &= \frac{\partial u_x}{\partial x} = -\frac{\nu \sigma_1 t}{E} - \frac{N}{12} \sigma_1^5 t^6, \\ \epsilon_{22}^{tot}(t) &= \frac{\partial u_y}{\partial y} = -\frac{\nu \sigma_1 t}{E} - \frac{N}{12} \sigma_1^5 t^6, \\ \epsilon_{33}^{tot}(t) &= \frac{\partial u_z}{\partial z} = \frac{\sigma_1 t}{E} + \frac{N}{6} \sigma_1^5 t^6, \end{aligned} \quad (2.220)$$

and integration with respect to the fixities at the coordinate planes yields the displacement vector ( $u_x, u_y, u_z$ )

$$\begin{aligned} u_x(x, t) &= x \left( -\frac{\nu \sigma_1 t}{E} - \frac{N}{12} \sigma_1^5 t^6 \right), \\ u_y(y, t) &= y \left( -\frac{\nu \sigma_1 t}{E} - \frac{N}{12} \sigma_1^5 t^6 \right), \\ u_z(z, t) &= z \left( \frac{\sigma_1 t}{E} + \frac{N}{6} \sigma_1^5 t^6 \right). \end{aligned} \quad (2.221)$$

## 2.5 Mass Transport

The Laplace transform solution method proves to be a powerful tool in solving mass transport problems. From the variety of closed form solutions available in the literature we adopted some basic examples from standard references. We made no attempt to trace back the entire material to its original sources.

### 2.5.1 Solute Transport Along Permeable Beams, Hydraulic and Solute Boundary Conditions of 1st and 2nd Kind

The domain comprises four parallel beams of length  $L = 10$  m extending along the positive  $x$ -axis, each composed of  $200 \times 1 \times 1$  equally sized hexahedral elements (Fig. 2.12). An isotropic permeability  $k = 10^{-11} \text{ m}^2$  holds for all beams, porosities are listed below, the liquid is incompressible with viscosity  $\mu = 1 \text{ mPa} \cdot \text{s}$ . The diffusion coefficient assumes the constant value  $D = 10^{-4} \text{ m}^2/\text{s}$  comprising molecular diffusion and mechanical dispersion. Gravity is neglected via zero liquid density.

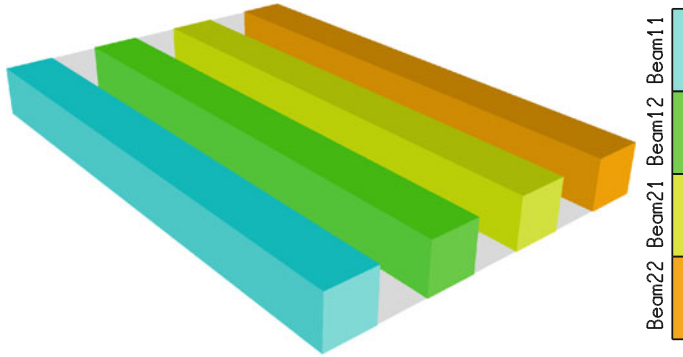


Fig. 2.12 Example setup

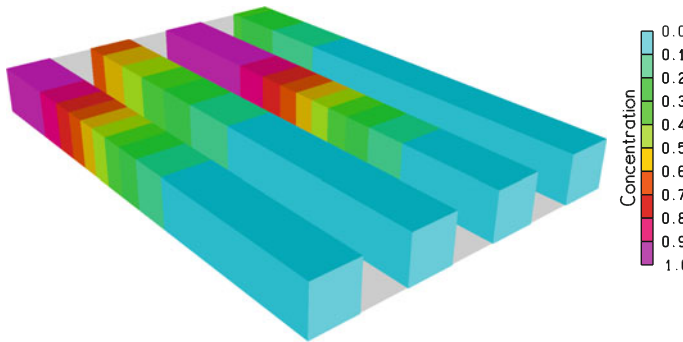


Fig. 2.13 Solute distributions after 20,000 s

Zero pressure prevails at the beams outlets ( $x = L$ ). Hydraulic and solute boundary conditions of 1st and 2nd kind are imposed at the inlets ( $x = 0$  m) and are listed below. Starting from zero initial solute concentration the simulation evaluates the transient solute distributions with output after 10,000 and 20,000 s (Fig. 2.13).

The formal solution proceeds in two steps, first to solve for the pressure and second to determine the solute distributions.

For incompressible liquids Darcy’s law and continuity equation yield the Laplace equation as the governing equation describing the steady-state pressure distribution. It reads

$$\frac{d^2 p}{dx^2} = 0 \tag{2.222}$$

for 1D flow along the x-axis, hence, the pressure is given by

$$p(x) = ax + b. \tag{2.223}$$

**Table 2.1** Example overview

	Beam11	Beam12	Beam21	Beam22
Porosity $\phi$	0.6	0.4	0.4	0.6
Inlet pressure $p_0$	$10^5$ Pa	$10^5$ Pa		
Specific discharge $q$			$10^{-4}$ m/s	$10^{-4}$ m/s
Inlet concentration	1		1	
Solute input $j = -\phi D \nabla c$		$5 \times 10^{-6}$ m/s		$5 \times 10^{-6}$ m/s

The free constants,  $a$  and  $b$ , have to be determined from the specified boundary conditions at  $x = L$  and  $x = 0$  m. Hence, in case of specified inlet pressure (Beam11 and Beam12)

$$p(x) = p_0 \left(1 - \frac{x}{L}\right) \quad (2.224)$$

and by Darcy's law

$$p(x) = \frac{\mu}{k} q L \left(1 - \frac{x}{L}\right) \quad (2.225)$$

in case of specified specific discharge (Beam21 and Beam22). Employing the data given above both result in identical pressure distributions and a unique specific discharge  $q$  applied to all beams (Table 2.1).

We will next focus on the closed form solution of the transport problems, i.e. we will solve the solute transport equation subject to the imposed initial and boundary conditions. The solute distributions along Beam11 and Beam21 ( $c1$ -distributions) are based on a 1st kind solute boundary condition. Due to free outflow at  $x = L$  these distributions represent those of a solute in steady linear flow downstream ( $x > 0$ ) the source

$$c1(0, t) = 1 \quad \text{for } t > 0. \quad (2.226)$$

The formal problem is to determine the solution  $c1(x, t)$  of the 1D transport equation

$$\frac{\partial c1}{\partial t} + \frac{q}{\phi} \frac{\partial c1}{\partial x} = D \frac{\partial^2 c1}{\partial x^2} \quad (2.227)$$

subject to the initial condition

$$c1(x, 0) = 0 \quad \text{for } x > 0, \quad (2.228)$$

and the boundary conditions

$$\begin{aligned} c1(0, t) &= 1 \quad \text{for } t > 0, \\ \lim_{x \rightarrow \infty} c1(x, t) &= 0 \quad \text{for } t > 0. \end{aligned} \quad (2.229)$$

Applying the Laplace transform with respect to  $t$  yields the ordinary differential equation

$$D \bar{c}1'' - \frac{q}{\phi} \bar{c}1' - s \bar{c}1 = 0, \quad (2.230)$$

where  $\bar{c}1$  is the transform of  $c1$ ,  $s$  is the transformation parameter, and the prime denotes the derivative with respect to  $x$ . This equation has to be solved with respect to transformed boundary conditions. This yields

$$\bar{c}1(x, s) = \frac{1}{s} \exp \left[ x \left( \frac{q}{2\phi D} - \sqrt{\left( \frac{q}{2\phi D} \right)^2 + \frac{s}{D}} \right) \right]. \quad (2.231)$$

Churchill [7] outlines how to obtain the solution  $c1(x, t)$  from their transform with the aid of operational calculus.

looseness-1 The solute distributions along Beam12 and Beam22 ( $c2$ -distributions) are based on a 2nd kind solute boundary condition. Due to free outflow at  $x = L$  these distributions represent those of a solute in steady linear flow downstream ( $x > 0$ ) the source

$$\frac{\partial c2}{\partial x}(0, t) = -\frac{j}{\phi D} \quad \text{for } t > 0. \quad (2.232)$$

The formal problem is to determine the solution  $c2(x, t)$  of the 1D transport equation

$$\frac{\partial c2}{\partial t} + \frac{q}{\phi} \frac{\partial c2}{\partial x} = D \frac{\partial^2 c2}{\partial x^2} \quad (2.233)$$

subject to the initial condition

$$c2(x, 0) = 0 \quad \text{for } x > 0, \quad (2.234)$$

and the boundary conditions

$$\begin{aligned} \frac{\partial c2}{\partial x}(0, t) &= -\frac{j}{\phi D} \quad \text{for } t > 0, \\ \lim_{x \rightarrow \infty} c2(x, t) &= 0 \quad \text{for } t > 0. \end{aligned} \quad (2.235)$$

Applying the Laplace transform with respect to  $t$  yields the ordinary differential equation

$$D \bar{c}2'' - \frac{q}{\phi} \bar{c}2' - s \bar{c}2 = 0, \quad (2.236)$$

where  $\bar{c}2$  is the transform of  $c2$ ,  $s$  is the transformation parameter, and the prime denotes the derivative with respect to  $x$ . This equation has to be solved with respect to the transformed boundary conditions. This yields

$$\bar{c}2(x, s) = -\frac{j}{\phi D s} \frac{\exp\left[x\left(\frac{q}{2\phi D} - \sqrt{\left(\frac{q}{2\phi D}\right)^2 + \frac{s}{D}}\right)\right]}{\frac{q}{2\phi D} - \sqrt{\left(\frac{q}{2\phi D}\right)^2 + \frac{s}{D}}}. \quad (2.237)$$

The entire solution may now be obtained from the transforms of the solute distributions. The numerical inversion scheme outlined in the introductory section may easily be applied to give the required values of  $c1(x, t)$  and  $c2(x, t)$  (Fig. 2.13).

### 2.5.2 Solute Transport Along Permeable Beams with an Inert, a Decaying, and an Adsorbing Solute, Time-Dependent Boundary Conditions of 1st Kind

The domain comprises three parallel beams of length  $L = 10\text{m}$  extending along the positive  $x$ -axis, each composed of  $200 \times 1 \times 1$  equally sized hexahedral elements (Fig. 2.14). An isotropic permeability  $k = 10^{-11}\text{m}^2$  holds for all beams, porosities have been assigned  $\phi = 0.4$ . The liquid is incompressible with viscosity  $\mu = 1\text{mPa} \cdot \text{s}$ . The diffusion coefficient assumes the constant value  $D = 10^{-4}\text{m}^2/\text{s}$  comprising molecular diffusion and mechanical dispersion. Gravity is neglected via zero liquid density. The decaying solute (half life  $T$ ) undergoes first order decay with decay constant  $(\ln 2)/T = 0.5 \times 10^{-4}\text{1/s}$ . For the adsorbing solute the adsorbed mass fraction is related to the solute mass fraction by a linear equilibrium sorption model. Input data require the distribution coefficient  $K_d = 6.8 \times 10^{-4}\text{m}^3/\text{kg}$  and the density of the solid grain ( $\rho_s = 2,000\text{kg/m}^3$ ), for more details see below. Pressure  $p_0 = 10^5\text{Pa}$  prevails at the beams inlets ( $x = 0\text{m}$ ), zero pressure prevails at the beams outlets ( $x = L$ ). Along the inlets concentration 1 is specified for times less than  $t_0 = 15,000\text{s}$  and zero afterward. Starting from zero initial solute concentration the simulation evaluates the transient solute distributions with output after 10,000 and 20,000 s (Fig. 2.15).

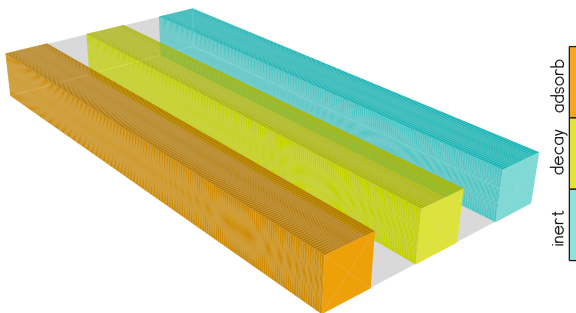
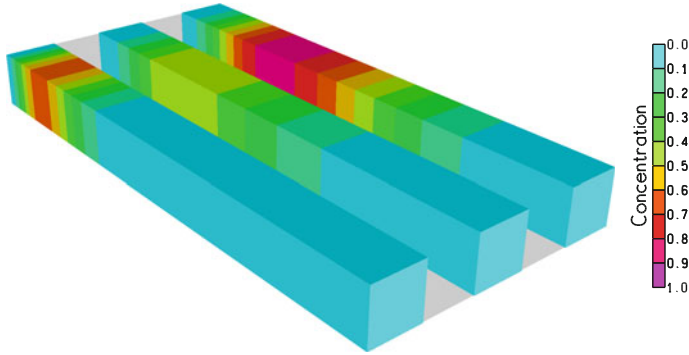


Fig. 2.14 Example setup



**Fig. 2.15** Solute distributions after 20,000 s

The formal solution proceeds in two steps, first to solve for pressure  $p(x)$  and specific discharge  $q$  and second to determine the solute distributions.

For incompressible liquids Darcy's law and continuity equation yield the Laplace equation as the governing equation describing the steady-state pressure distribution. It reads

$$\frac{d^2 p}{dx^2} = 0 \quad (2.238)$$

for 1D flow along the  $x$ -axis, hence, the pressure is given by

$$p(x) = p_0 \left(1 - \frac{x}{L}\right), \quad (2.239)$$

and the specific discharge  $q$  is obtained by Darcy's law

$$q = \frac{k}{\mu} \frac{p_0}{L}. \quad (2.240)$$

We will next focus on the closed form solution of the transport problems, i.e. we will solve 1D solute transport equations

$$\frac{\partial c}{\partial t} + \frac{q}{\phi} \frac{\partial c}{\partial x} = D \frac{\partial^2 c}{\partial x^2} - r(x, t), \quad (2.241)$$

where  $r(x, t)$  depends on the various reactions involved.

Due to free outflow at  $x = L$  the distribution of the inert solute ( $c_3$ -distribution) represents that of a solute in steady linear flow downstream ( $x > 0$ ) the source

$$c_3(0, t) = \begin{cases} 1 & \text{for } t_0 > t > 0, \\ 0 & \text{for } t > t_0, \end{cases} \quad (2.242)$$

and the formal problem is to determine the solution  $c3(x, t)$  of the 1D transport equation

$$\frac{\partial c3}{\partial t} + \frac{q}{\phi} \frac{\partial c3}{\partial x} = D \frac{\partial^2 c3}{\partial x^2} \quad (2.243)$$

subject to the initial condition

$$c3(x, 0) = 0 \quad \text{for } x > 0, \quad (2.244)$$

and the boundary conditions

$$c3(0, t) = \begin{cases} 1 & \text{for } t_0 > t > 0, \\ 0 & \text{for } t > t_0, \end{cases} \quad (2.245)$$

$$\lim_{x \rightarrow \infty} c3(x, t) = 0 \quad \text{for } t > 0. \quad (2.246)$$

Applying the Laplace transform with respect to  $t$  yields the ordinary differential equation

$$D \bar{c}3'' - \frac{q}{\phi} \bar{c}3' - s \bar{c}3 = 0, \quad (2.247)$$

where  $\bar{c}3$  is the transform of  $c3$ ,  $s$  is the transformation parameter, and the prime denotes the derivative with respect to  $x$ . This equation has to be solved with respect to the transformed boundary conditions. This yields

$$\bar{c}3(x, s) = \frac{1 - \exp(-t_0 s)}{s} \exp \left[ x \left( \frac{q}{2\phi D} - \sqrt{\left( \frac{q}{2\phi D} \right)^2 + \frac{s}{D}} \right) \right]. \quad (2.248)$$

Churchill [7] outlines how to obtain the solution  $c3(x, t)$  from their transform with the aid of operational calculus.

Due to free outflow at  $x = L$  the distribution of the decaying solute (c2-distribution) represents that of a solute in steady linear flow downstream ( $x > 0$ ) the source

$$c2(0, t) = \begin{cases} 1 & \text{for } t_0 > t > 0, \\ 0 & \text{for } t > t_0, \end{cases} \quad (2.249)$$

and formal problem is to determine the solution  $c2(x, t)$  of the 1D transport equation

$$\frac{\partial c2}{\partial t} + \frac{q}{\phi} \frac{\partial c2}{\partial x} = D \frac{\partial^2 c2}{\partial x^2} - \frac{\ln 2}{T} c2 \quad (2.250)$$

subject to the initial condition

$$c2(x, 0) = 0 \quad \text{for } x > 0, \quad (2.251)$$

and the boundary conditions

$$c_2(0, t) = \begin{cases} 1 & \text{for } t_0 > t > 0, \\ 0 & \text{for } t > t_0, \end{cases} \quad (2.252)$$

$$\lim_{x \rightarrow \infty} c_2(x, t) = 0 \quad \text{for } t > 0. \quad (2.253)$$

Applying the Laplace transform with respect to  $t$  yields the ordinary differential equation

$$D \bar{c}_2'' - \frac{q}{\phi} \bar{c}_2' - \left(s + \frac{\ln 2}{T}\right) \bar{c}_2 = 0, \quad (2.254)$$

where  $\bar{c}_2$  is the transform of  $c_2$ ,  $s$  is the transformation parameter, and the prime denotes the derivative with respect to  $x$ . This equation has to be solved with respect to the transformed boundary conditions. This yields

$$\bar{c}_2(x, s) = \frac{1 - \exp(-t_0 s)}{s} \exp \left[ x \left( \frac{q}{2\phi D} - \sqrt{\left(\frac{q}{2\phi D}\right)^2 + \frac{\ln 2}{DT} + \frac{s}{D}} \right) \right]. \quad (2.255)$$

Following Churchill [7] again the solution  $c_2(x, t)$  may be obtained from their transform with the aid of operational calculus.

The transport equation associated to the distribution  $c_1(x, t)$  of an adsorbing solute is obtained from a mass balance of solute in the liquid and on the porous matrix. Let  $\rho_l$  denote the density of the liquid, and let  $\rho_s$  denote the density of the solid grain. Continuity of solute mass in the liquid yields

$$\frac{\partial(\phi \rho_l c_1)}{\partial t} + \frac{q}{\phi} \frac{\partial(\phi \rho_l c_1)}{\partial x} = D \frac{\partial^2(\phi \rho_l c_1)}{\partial x^2} - a_1(x, t), \quad (2.256)$$

where  $a_1(x, t)$  denotes the change of solute mass in the liquid due to interaction with the porous matrix. On the matrix the solute mass changes due to liquid/matrix-interaction again

$$\frac{\partial[(1 - \phi)\rho_s s_1]}{\partial t} = a_1(x, t), \quad (2.257)$$

and the adsorbed mass fraction  $s_1$  is related to the solute mass fraction  $c_1$  by the linear equilibrium sorption model

$$\rho_s s_1 = (K_d \rho_s) \rho_l c_1. \quad (2.258)$$

Introducing the notation

$$R = 1 + \frac{1 - \phi}{\phi} K_d \rho_s, \quad (2.259)$$

yields the formal problem to determine the solution  $c1(x, t)$  of the 1D transport equation

$$\frac{\partial c1}{\partial t} + \frac{q}{\phi R} \frac{\partial c1}{\partial x} = \frac{D}{R} \frac{\partial^2 c1}{\partial x^2} \quad (2.260)$$

subject to the initial condition

$$c1(x, 0) = 0 \quad \text{for } x > 0, \quad (2.261)$$

and the boundary conditions

$$c1(0, t) = \begin{cases} 1 & \text{for } t_0 > t > 0, \\ 0 & \text{for } t > t_0, \end{cases} \quad (2.262)$$

$$\lim_{x \rightarrow \infty} c1(x, t) = 0 \quad \text{for } t > 0. \quad (2.263)$$

Applying the Laplace transform with respect to  $t$  yields the ordinary differential equation

$$\frac{D}{R} \bar{c}1'' - \frac{q}{\phi R} \bar{c}1' - s \bar{c}1 = 0, \quad (2.264)$$

where  $\bar{c}1$  is the transform of  $c1$ ,  $s$  is the transformation parameter, and the prime denotes the derivative with respect to  $x$ . This equation has to be solved with respect to the transformed boundary conditions. This yields

$$\bar{c}1(x, s) = \frac{1 - \exp(-t_0 s)}{s} \exp \left[ x \left( \frac{q}{2\phi D} - \sqrt{\left( \frac{q}{2\phi D} \right)^2 + \frac{sR}{D}} \right) \right]. \quad (2.265)$$

The entire solution may now be obtained from the transforms of the solute distributions. The numerical inversion scheme outlined in the introductory section may easily be applied to give the required values of  $c1(x, t)$ ,  $c2(x, t)$ , and  $c3(x, t)$ .

### 2.5.3 A Transient 2D Solute Distribution

Given length  $L = 1$  m the domain represents the rectangle  $[0, 2L] \times [-0.75L, 0.75L]$  located in the  $x$ - $y$ -plane and subdivided into  $80 \times 60 \times 1$  cubic elements. A permeable material represents the porous medium, with isotropic permeability  $k = 10^{-11}$  m<sup>2</sup> and porosity  $\phi = 0.5$ . The liquid is incompressible with viscosity  $\mu = 1$  mPa·s, the diffusion coefficient assumes the constant value  $D = 3 \times 10^{-6}$  m<sup>2</sup>/s comprising molecular diffusion and mechanical dispersion. Gravity is neglected via zero liquid density. Pressure  $p_0 = 2 \times 10^4$  Pa at the liquid inlet ( $x = 0$  m) and zero pressure the

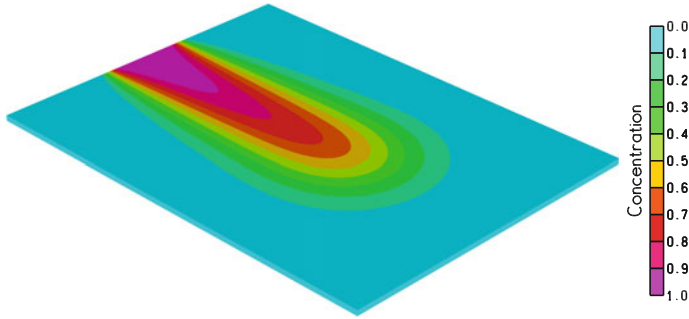


**Fig. 2.16** Solute distribution after 7,000 s

liquid outlet ( $x = 2L$ ) generate steady-state 1D flow along the x-axis. At the liquid inlet a non-zero solute concentration is specified along a line segment of the y-axis. Given  $a = 0.15$  m and  $b = 0.25$  m the specified inlet concentration reads

$$g(y) = \begin{cases} 0 & \text{for } y \leq -b, \\ \frac{b+y}{b-a} & \text{for } -b \leq y \leq -a, \\ 1 & \text{for } -a \leq y \leq a, \\ \frac{b-y}{b-a} & \text{for } a \leq y \leq b, \\ 0 & \text{for } b \leq y. \end{cases} \quad (2.266)$$

Starting from zero initial solute concentration the simulation evaluates the transient solute distribution  $c(x, y, t)$  with output after 3,500 and 7,000 s (Fig. 2.16).

The formal solution proceeds in two steps, first to solve for pressure  $p(x)$  and specific discharge  $q$  and second to determine the solute distributions.

For incompressible liquids Darcy's law and continuity equation yield the Laplace equation as the governing equation describing the steady-state pressure distribution. It reads

$$\frac{d^2 p}{dx^2} = 0 \quad (2.267)$$

for 1D flow along the x-axis, hence, the pressure is given by

$$p(x) = p_0 \left(1 - \frac{x}{2L}\right), \quad (2.268)$$

and the specific discharge  $q$  is obtained by Darcy's law

$$q = \frac{k}{\mu} \frac{p_0}{2L}. \quad (2.269)$$

We will next focus on the closed form solution of the transport problem and solve the 2D solute transport equation with the aid of successive integral transforms as

described by Leij and Dane [8]. The formal problem is to determine the solution  $c(x, y, t)$  of the 2D transport equation

$$\frac{\partial c}{\partial t} + \frac{q}{\phi} \frac{\partial c}{\partial x} = D \left( \frac{\partial^2 c}{\partial x^2} + \frac{\partial^2 c}{\partial y^2} \right) \quad (2.270)$$

subject to the initial condition

$$c(x, y, 0) = 0 \quad \text{for } x, y > 0, \quad (2.271)$$

and the boundary conditions

$$\begin{aligned} c(0, y, t) &= g(y) && \text{for } t > 0, \\ \lim_{x \rightarrow \infty} c(x, y, t) &= 0 && \text{for } t > 0, \\ \lim_{y \rightarrow \infty} c(x, y, t) &= 0 && \text{for } t > 0, \\ \lim_{y \rightarrow -\infty} c(x, y, t) &= 0 && \text{for } t > 0. \end{aligned} \quad (2.272)$$

Applying the Laplace transform with respect to  $t$  yields the differential equation

$$s \bar{c} + \frac{q}{\phi} \frac{\partial \bar{c}}{\partial x} = D \left( \frac{\partial^2 \bar{c}}{\partial x^2} + \frac{\partial^2 \bar{c}}{\partial y^2} \right), \quad (2.273)$$

where  $\bar{c}$  is the Laplace transform of  $c$ , and  $s$  is the transformation parameter. The boundary conditions become

$$\begin{aligned} \bar{c}(0, y, s) &= \frac{g(y)}{s}, \\ \lim_{x \rightarrow \infty} \bar{c}(x, y, s) &= 0, \\ \lim_{y \rightarrow \infty} \bar{c}(x, y, s) &= 0, \\ \lim_{y \rightarrow -\infty} \bar{c}(x, y, s) &= 0. \end{aligned} \quad (2.274)$$

Applying next the Fourier transform with respect to  $y$  yields the ordinary differential equation

$$D \bar{C}'' - \frac{q}{\phi} \bar{C}' - (s + Dr^2) \bar{C} = 0, \quad (2.275)$$

where  $\bar{C}$  is the Fourier transform of  $\bar{c}$ ,  $r$  is the Fourier transformation parameter, and the prime denotes the derivative with respect to  $x$ . The boundary conditions read

$$\begin{aligned} \bar{C}(0, r, s) &= \frac{G(r)}{s}, \\ \lim_{x \rightarrow \infty} \bar{C}(x, r, s) &= 0, \end{aligned} \quad (2.276)$$

where  $G(r)$  is the Fourier transform of  $g(y)$ . The ordinary differential equation above has to be solved with respect to the twofold transformed boundary conditions.

This yields

$$\bar{C}(x, r, s) = \frac{G(r)}{s} \exp \left[ x \left( \frac{q}{2\phi D} - \sqrt{\left( \frac{q}{2\phi D} \right)^2 + \frac{s}{D} + r^2} \right) \right]. \quad (2.277)$$

The solution in the  $x, y, t$  domain will be obtained from their transforms, the invers Laplace transformation is carried out first. Knowing (e.g. Abramowitz and Stegun [9]) the inverse Laplace transform

$$L^{-1}\{\exp(-x\sqrt{s/D})\} = \frac{x \exp(-x^2/(4Dt))}{2(\pi Dt^3)^{1/2}}, \quad (2.278)$$

it follows with the aid of the property on substitution

$$\begin{aligned} L^{-1} \left\{ \exp \left( -x \sqrt{\frac{1}{D} \left[ \left( \frac{q}{4D} \right)^2 + Dr^2 + s \right]} \right) \right\} \\ = \frac{x \exp(-x^2/(4Dt))}{2(\pi Dt^3)^{1/2}} \exp \left( - \left[ \frac{1}{4D} \left( \frac{q}{\phi} \right)^2 + Dr^2 \right] t \right). \end{aligned} \quad (2.279)$$

The Fourier transform  $C(x, r, t)$  of the solute concentration is thus obtained by the convolution theorem

$$C(x, r, t) = \frac{x}{(4\pi D)^{1/2}} \int_0^t \frac{G(r) \exp(-Dr^2t')}{(t')^{3/2}} \exp \left( - \frac{(x - t'q/\phi)^2}{4Dt'} \right) dt'. \quad (2.280)$$

The last step of the solution procedure is the application of the invers Fourier transform.  $G(r)$  has the invers  $g(y)$ , and knowing the invers Fourier transform

$$F^{-1}\{\exp(-Dr^2t')\} = \frac{\exp(-y^2/(4Dt'))}{(2Dt')^{1/2}} \quad (2.281)$$

the convolution theorem of the Fourier transformation yields

$$\begin{aligned} F^{-1}\{G(r) \exp(-Dr^2t')\} &= (2\pi)^{-1/2} \int_{-\infty}^{\infty} \frac{g(v)}{(2Dt')^{1/2}} \exp\left(-\frac{(y-v)^2}{4Dt'}\right) dv \\ &= \int_{-b}^{-a} \frac{(2\pi)^{-1/2}}{(2Dt')^{1/2}} \frac{b+v}{b-a} \exp\left(-\frac{(y-v)^2}{4Dt'}\right) dv \\ &\quad + \int_{-a}^a \frac{(2\pi)^{-1/2}}{(2Dt')^{1/2}} \exp\left(-\frac{(y-v)^2}{4Dt'}\right) dv \\ &\quad + \int_a^b \frac{(2\pi)^{-1/2}}{(2Dt')^{1/2}} \frac{b-v}{b-a} \exp\left(-\frac{(y-v)^2}{4Dt'}\right) dv. \end{aligned} \quad (2.282)$$

The integrals involved may be evaluated by elementary analytical methods. The solution  $c(x, y, t)$  of the 2D transport problem takes the form

$$\begin{aligned}
c(x, y, t) = & \frac{x}{4(\pi D)^{1/2}} \cdot \int_0^t \exp\left(-\frac{(x - t'q/\phi)^2}{4Dt'}\right) \\
& \times \left\{ \left[ \operatorname{erf}\left(\frac{b+y}{(4Dt')^{1/2}}\right) - \operatorname{erf}\left(\frac{a+y}{(4Dt')^{1/2}}\right) \right] \frac{b+y}{b-a} \right. \\
& + \left[ \exp\left(\frac{-(b+y)^2}{4Dt'}\right) - \exp\left(\frac{-(a+y)^2}{4Dt'}\right) \right] \frac{(4Dt')^{1/2}\pi^{-1/2}}{b-a} \\
& + \left[ \operatorname{erf}\left(\frac{a+y}{(4Dt')^{1/2}}\right) + \operatorname{erf}\left(\frac{a-y}{(4Dt')^{1/2}}\right) \right] \\
& + \left[ \operatorname{erf}\left(\frac{b-y}{(4Dt')^{1/2}}\right) - \operatorname{erf}\left(\frac{a-y}{(4Dt')^{1/2}}\right) \right] \frac{b-y}{b-a} \\
& \left. + \left[ \exp\left(\frac{-(b-y)^2}{4Dt'}\right) - \exp\left(\frac{-(a-y)^2}{4Dt'}\right) \right] \frac{(4Dt')^{1/2}\pi^{-1/2}}{b-a} \right\} t'^{-3/2} dt'. \tag{2.283}
\end{aligned}$$

The remaining integral was evaluated numerically, the Romberg integration scheme may conveniently be employed. For the numerical evaluation of the error function see [4].

## 2.6 Hydrothermal Processes

Heat transport in a moving liquid is the subject of this section. Closed form solutions may be obtained from corresponding mass transport problems. We present two examples, for the underlying theory see Bear [10].

### 2.6.1 A Transient 1D Temperature Distribution in a Moving Liquid

The domain is a rectangular beam of length  $L = 10$  m extending along the positive  $x$ -axis. It is discretized by  $100 \times 1 \times 1$  equally sized hexahedral elements. A permeable material represents the porous medium, with isotropic permeability  $k = 10^{-11} \text{ m}^2$  and porosity  $\phi = 0.1$ . The liquid is incompressible and has viscosity  $\mu = 1 \text{ mPa} \cdot \text{s}$ . Densities, heat capacities, and thermal conductivities of liquid and solid grain are given below, gravity has explicitly been neglected (Table 2.2).

Pressure  $p_0 = 10^5 \text{ Pa}$  at the liquid inlet ( $x = 0$  m) and zero pressure the liquid outlet ( $x = L$ ) generate steady-state 1D flow along the  $x$ -axis. At the liquid inlet a constant temperature  $T_0 = 10^\circ \text{C}$  is specified for times  $t > 0$ . Starting from zero initial temperature the simulation evaluates the transient temperature distribution  $T(x, t)$  with output after 10,000 and 20,000 s (Fig. 2.17).

**Table 2.2** Example overview

	Liquid	Solid grain
Density	$\rho_l = 1000 \text{ kg/m}^3$	$\rho_s = 2000 \text{ kg/m}^3$
Specific heat capacity	$c_l = 1100 \text{ J/(kg} \cdot \text{K)}$	$c_s = 250 \text{ J/(kg} \cdot \text{K)}$
Thermal conductivity	$\lambda_l = 10 \text{ W/(m} \cdot \text{K)}$	$\lambda_s = 50 \text{ W/(m} \cdot \text{K)}$

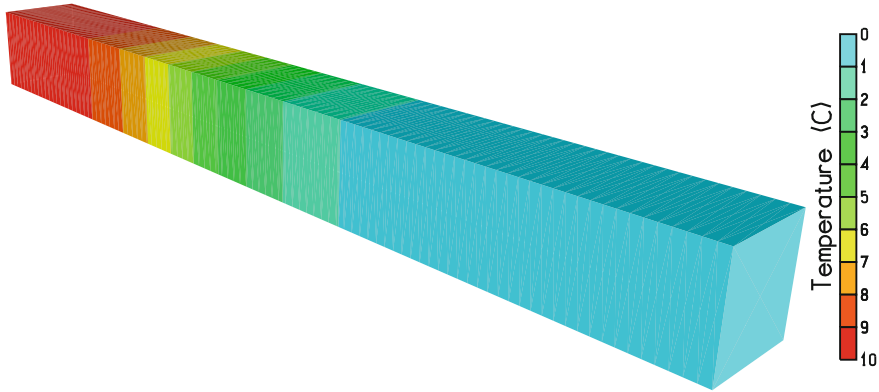


**Fig. 2.17** Temperature distribution after 20,000 s

The formal solution proceeds in two steps, first to solve for pressure  $p(x)$  and specific discharge  $q$  and second to determine the temperature distribution.

For incompressible liquids Darcy’s law and continuity equation yield the Laplace equation as the governing equation describing the steady-state pressure distribution. It reads

$$\frac{\partial^2 p}{\partial x^2} = 0 \tag{2.284}$$

for 1D flow along the  $x$ -axis, hence, the pressure is given by

$$p(x) = p_0 \left(1 - \frac{x}{L}\right), \tag{2.285}$$

and the specific discharge  $q$  is obtained by Darcy’s law

$$q = \frac{k}{\mu} \frac{p_0}{L}. \tag{2.286}$$

We will next focus on the closed form solution of the heat transport problem. Based on the setup of the present example the heat transport equation reads

$$(\phi \rho_l c_l + (1 - \phi) \rho_s c_s) \frac{\partial T}{\partial t} + (\phi \rho_l c_l) \frac{q}{\phi} \frac{\partial T}{\partial x} = (\phi \lambda_l + (1 - \phi) \lambda_s) \frac{\partial^2 T}{\partial x^2}. \tag{2.287}$$

Introducing the notation

$$\begin{aligned} w &= \frac{\phi \rho_l c_l}{\phi \rho_l c_l + (1 - \phi) \rho_s c_s} \frac{q}{\phi}, \\ \chi &= \frac{\phi \lambda_l + (1 - \phi) \lambda_s}{\phi \rho_l c_l + (1 - \phi) \rho_s c_s}, \end{aligned} \quad (2.288)$$

the heat transport equation becomes

$$\frac{\partial T}{\partial t} + w \frac{\partial T}{\partial x} = \chi \frac{\partial^2 T}{\partial x^2}. \quad (2.289)$$

Due to free outflow at  $x = L$  the formal problem is to determine the solution  $T(x, t)$  of the above heat transport equation subject to the initial condition

$$T(x, 0) = 0 \quad \text{for } x > 0, \quad (2.290)$$

and the boundary conditions

$$\begin{aligned} T(0, t) &= T_0 \quad \text{for } t > 0, \\ \lim_{x \rightarrow \infty} T(x, t) &= 0 \quad \text{for } t > 0. \end{aligned} \quad (2.291)$$

Applying the Laplace transform with respect to  $t$  yields the ordinary differential equation

$$\chi \bar{T}'' - w \bar{T}' - s \bar{T} = 0, \quad (2.292)$$

where  $\bar{T}$  is the transform of  $T$ ,  $s$  is the transformation parameter, and the prime denotes the derivative with respect to  $x$ . This equation has to be solved with respect to transformed boundary conditions. This yields

$$\bar{T}(x, s) = \frac{T_0}{s} \exp \left[ x \left( \frac{w}{2\chi} - \sqrt{\left( \frac{w}{2\chi} \right)^2 + \frac{s}{\chi}} \right) \right]. \quad (2.293)$$

The solution may now be obtained from the transform of the temperature distribution, Churchill [7] outlines how to proceed with the aid of operational calculus. We note, that the present example is well suited for numerical inversion. The numerical inversion scheme outlined in the introductory section may easily be applied to give the required values of the temperature distribution  $T(x, t)$  (Fig. 2.17).

**Table 2.3** Example overview

	Liquid	Solid grain
Density	$\rho_l = 1000 \text{ kg/m}^3$	$\rho_s = 2000 \text{ kg/m}^3$
Specific heat capacity	$c_l = 1100 \text{ J/(kg} \cdot \text{K)}$	$c_s = 250 \text{ J/(kg} \cdot \text{K)}$
Thermal conductivity	$\lambda_l = 0.5 \text{ W/(m} \cdot \text{K)}$	$\lambda_s = 2.0 \text{ W/(m} \cdot \text{K)}$

### 2.6.2 A Transient 2D Temperature Distribution in a Moving Liquid

Given length  $L = 1 \text{ m}$  the domain represents the rectangle  $[0, 2L] \times [-0.75L, 0.75L]$  located in the  $x$ - $y$ -plane and subdivided into  $80 \times 60 \times 1$  cubic elements. A permeable material represents the porous medium, with isotropic permeability  $k = 10^{-11} \text{ m}^2$  and porosity  $\phi = 0.1$ . The liquid is incompressible and has viscosity  $\mu = 1 \text{ mPa} \cdot \text{s}$ . Densities, heat capacities, and thermal conductivities of liquid and solid grain are given below, gravity has explicitly been neglected (Table 2.3).

Pressure  $p_0 = 2 \times 10^4 \text{ Pa}$  at the liquid inlet ( $x = 0$ ) and zero pressure the liquid outlet ( $x = 2L$ ) generate steady-state 1D flow along the  $x$ -axis. At the liquid inlet a non-zero temperature is specified along a line segment of the  $y$ -axis. Given temperature  $T_0 = 10^\circ\text{C}$  as well as  $a = 0.15 \text{ m}$  and  $b = 0.25 \text{ m}$  the specified inlet temperature reads

$$g(y) = \begin{cases} 0 & \text{for } y \leq -b, \\ T_0 \frac{b+y}{b-a} & \text{for } -b \leq y \leq -a, \\ T_0 & \text{for } -a \leq y \leq a, \\ T_0 \frac{b-y}{b-a} & \text{for } a \leq y \leq b, \\ 0 & \text{for } b \leq y. \end{cases} \quad (2.294)$$

Starting from zero initial temperature the simulation evaluates the transient temperature distribution  $T(x, y, t)$  with output after 3,500 and 7,000 s (Fig. 2.18).

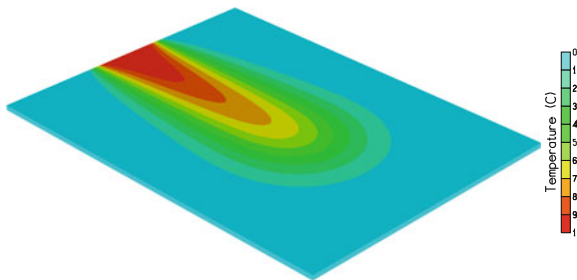


**Fig. 2.18** Temperature distribution after 7,000 s

The formal solution proceeds in two steps, first to solve for pressure  $p(x)$  and specific discharge  $q$  and second to determine the solute distributions.

For incompressible liquids Darcy's law and continuity equation yield the Laplace equation as the governing equation describing the steady-state pressure distribution. It reads

$$\frac{d^2 p}{dx^2} = 0 \quad (2.295)$$

for 1D flow along the  $x$ -axis, hence, the pressure is given by

$$p(x) = p_0 \left(1 - \frac{x}{2L}\right), \quad (2.296)$$

and the specific discharge  $q$  is obtained by Darcy's law

$$q = \frac{k}{\mu} \frac{p_0}{2L}. \quad (2.297)$$

We will next focus on the closed form solution of the heat transport problem. Based on the setup of the present example the heat transport equation reads

$$\begin{aligned} & (\phi \rho_l c_l + (1 - \phi) \rho_s c_s) \frac{\partial T}{\partial t} + (\phi \rho_l c_l) \frac{q}{\phi} \frac{\partial T}{\partial x} \\ & = (\phi \lambda_l + (1 - \phi) \lambda_s) \left( \frac{\partial^2 T}{\partial x^2} + \frac{\partial^2 T}{\partial y^2} \right). \end{aligned} \quad (2.298)$$

Introducing the notation

$$\begin{aligned} w &= \frac{\phi \rho_l c_l}{\phi \rho_l c_l + (1 - \phi) \rho_s c_s} \frac{q}{\phi}, \\ \chi &= \frac{\phi \lambda_l + (1 - \phi) \lambda_s}{\phi \rho_l c_l + (1 - \phi) \rho_s c_s}, \end{aligned} \quad (2.299)$$

the heat transport equation becomes

$$\frac{\partial T}{\partial t} + w \frac{\partial T}{\partial x} = \chi \left( \frac{\partial^2 T}{\partial x^2} + \frac{\partial^2 T}{\partial y^2} \right). \quad (2.300)$$

The formal problem is to determine the solution  $T(x, y, t)$  of the above heat transport equation subject to the initial condition

$$T(x, y, 0) = 0 \quad \text{for } x, y > 0, \quad (2.301)$$

and the boundary conditions

$$\begin{aligned}
T(0, y, t) &= g(y) && \text{for } t > 0, \\
\lim_{x \rightarrow \infty} T(x, y, t) &= 0 && \text{for } t > 0, \\
\lim_{y \rightarrow \infty} T(x, y, t) &= 0 && \text{for } t > 0, \\
\lim_{y \rightarrow -\infty} T(x, y, t) &= 0 && \text{for } t > 0.
\end{aligned} \tag{2.302}$$

The closed form solution of this problem will be obtained with the aid of successive Laplace and Fourier transforms as described by Leij and Dane [8]. Applying the Laplace transform with respect to  $t$  yields the differential equation

$$s \bar{T} + w \frac{\partial \bar{T}}{\partial x} = \chi \left( \frac{\partial^2 \bar{T}}{\partial x^2} + \frac{\partial^2 \bar{T}}{\partial y^2} \right), \tag{2.303}$$

where  $\bar{T}$  is the Laplace transform of  $T$ , and  $s$  is the transformation parameter. The boundary conditions become

$$\begin{aligned}
\bar{T}(0, y, s) &= \frac{g(y)}{s}, \\
\lim_{x \rightarrow \infty} \bar{T}(x, y, s) &= 0, \\
\lim_{y \rightarrow \infty} \bar{T}(x, y, s) &= 0, \\
\lim_{y \rightarrow -\infty} \bar{T}(x, y, s) &= 0.
\end{aligned} \tag{2.304}$$

Applying next the Fourier transform with respect to  $y$  yields the ordinary differential equation

$$\chi \bar{U}'' - w \bar{U}' - (s + \chi r^2) \bar{U} = 0, \tag{2.305}$$

where  $\bar{U}$  is the Fourier transform of  $\bar{T}$ ,  $r$  is the Fourier transformation parameter, and the prime denotes the derivative with respect to  $x$ . The boundary conditions read

$$\begin{aligned}
\bar{U}(0, r, s) &= \frac{G(r)}{s}, \\
\lim_{x \rightarrow \infty} \bar{U}(x, r, s) &= 0,
\end{aligned} \tag{2.306}$$

where  $G(r)$  is the Fourier transform of  $g(y)$ . The ordinary differential equation above has to be solved with respect to the twofold transformed boundary conditions. This yields

$$\bar{U}(x, r, s) = \frac{G(r)}{s} \exp \left[ x \left( \frac{w}{2\chi} - \sqrt{\left( \frac{w}{2\chi} \right)^2 + \frac{s}{\chi} + r^2} \right) \right]. \tag{2.307}$$

The solution in the  $x, y, t$  domain will be obtained from their transforms, the invers Laplace transformation is carried out first. Knowing (e.g. Abramowitz and Stegun [9]) the inverse Laplace transform

$$L^{-1}\{\exp(-x\sqrt{s/\chi})\} = \frac{x \exp(-x^2/(4\chi t))}{2(\pi\chi t^3)^{1/2}}, \quad (2.308)$$

it follows with the aid of the property on substitution

$$\begin{aligned} L^{-1} \left\{ \exp \left( -x \sqrt{\frac{1}{\chi} \left[ \frac{1}{4\chi} (w)^2 + \chi r^2 \right] + s} \right) \right\} \\ = \frac{x \exp(-x^2/(4\chi t))}{2(\pi\chi t^3)^{1/2}} \exp \left( -\left[ \frac{1}{4\chi} (w)^2 + \chi r^2 \right] t \right). \end{aligned} \quad (2.309)$$

The Fourier transform  $U(x, r, t)$  of the temperature is thus obtained by the convolution theorem

$$U(x, r, t) = \frac{x}{(4\pi\chi)^{1/2}} \int_0^t \frac{G(r) \exp(-\chi r^2 t')}{(t')^{3/2}} \exp \left( -\frac{(x - t'w)^2}{4\chi t'} \right) dt'. \quad (2.310)$$

The last step of the solution procedure is the application of the invers Fourier transform.  $G(r)$  has the invers  $g(y)$ , and knowing the invers Fourier transform

$$F^{-1}\{\exp(-\chi r^2 t')\} = \frac{\exp(-y^2/(4\chi t'))}{(2\chi t')^{1/2}} \quad (2.311)$$

the convolution theorem of the Fourier transformation yields

$$\begin{aligned} F^{-1}\{G(r) \exp(-\chi r^2 t')\} &= (2\pi)^{-1/2} \int_{-\infty}^{\infty} \frac{g(v)}{(2\chi t')^{1/2}} \exp\left(-\frac{(y-v)^2}{4\chi t'}\right) dv \\ &= T_0 \int_{-b}^{-a} \frac{(2\pi)^{-1/2} b+v}{(2\chi t')^{1/2} b-a} \exp\left(-\frac{(y-v)^2}{4\chi t'}\right) dv \\ &\quad + T_0 \int_{-a}^a \frac{(2\pi)^{-1/2}}{(2\chi t')^{1/2}} \exp\left(-\frac{(y-v)^2}{4\chi t'}\right) dv \\ &\quad + T_0 \int_a^b \frac{(2\pi)^{-1/2} b-v}{(2\chi t')^{1/2} b-a} \exp\left(-\frac{(y-v)^2}{4\chi t'}\right) dv. \end{aligned} \quad (2.312)$$

The integrals involved may be evaluated by elementary analytical methods. Employing  $w$  and  $\chi$  as defined above the solution  $T(x, y, t)$  of the 2D heat transport problem takes the form

$$\begin{aligned}
T(x, y, t) = & \frac{T_0 x}{4(\pi \chi)^{1/2}} \cdot \int_0^t \exp\left(-\frac{(x-t'w)^2}{4\chi t'}\right) \\
& \times \left\{ \left[ \operatorname{erf}\left(\frac{b+y}{(4\chi t')^{1/2}}\right) - \operatorname{erf}\left(\frac{a+y}{(4\chi t')^{1/2}}\right) \right] \frac{b+y}{b-a} \right. \\
& + \left[ \exp\left(\frac{-(b+y)^2}{4\chi t'}\right) - \exp\left(\frac{-(a+y)^2}{4\chi t'}\right) \right] \frac{(4\chi t')^{1/2} \pi^{-1/2}}{b-a} \\
& + \left[ \operatorname{erf}\left(\frac{a+y}{(4\chi t')^{1/2}}\right) + \operatorname{erf}\left(\frac{a-y}{(4\chi t')^{1/2}}\right) \right] \\
& + \left[ \operatorname{erf}\left(\frac{b-y}{(4\chi t')^{1/2}}\right) - \operatorname{erf}\left(\frac{a-y}{(4\chi t')^{1/2}}\right) \right] \frac{b-y}{b-a} \\
& \left. + \left[ \exp\left(\frac{-(b-y)^2}{4\chi t'}\right) - \exp\left(\frac{-(a-y)^2}{4\chi t'}\right) \right] \frac{(4\chi t')^{1/2} \pi^{-1/2}}{b-a} \right\} t'^{-3/2} dt'. \tag{2.313}
\end{aligned}$$

The remaining integral was evaluated numerically, the Romberg integration scheme may conveniently be employed. For the numerical evaluation of the error function see [4].

## 2.7 Hydromechanical Coupling

The presence of a fluid pressure affects the mechanical load on the porous matrix. This interaction constitutes the subject of Biot's theory, see Biot [11] or see Jaeger and Cook [6]. We note, that the setup of our time-dependent problems has been adopted from Kolditz et al. [12].

### 2.7.1 A Permeable Elastic Beam Deforms Under Steady-State Internal Liquid Pressure

The domain is a rectangular beam of length  $L = 1$  m extending along the positive  $x$ -axis. It has three faces located on the coordinate planes and is discretized by  $20 \times 2 \times 2$  cubic elements. The solid material has been selected elastic with Poisson's ratio  $\nu = 0.25$ , Young's modulus  $E = 25,000$  MPa, and Biot number equal one. An isotropic permeability of  $10^{-12}$  m<sup>2</sup> and zero porosity is assumed for the material, liquid viscosity is 1 mPa · s and gravity is neglected via zero material and liquid densities. The face  $x = 0$  is free, all other faces of the beam are sliding planes. The simulation comprises one time step with pressure  $p_1 = 1$  MPa at  $x = L$  and zero pressure applied at  $x = 0$ .

The formal solution proceeds in two steps, first to solve for the pressure distribution  $p(x)$  and second to determine stresses, strains and displacements (Fig. 2.19).

The Laplace equation is the governing equation describing the steady-state pressure distribution. It reads

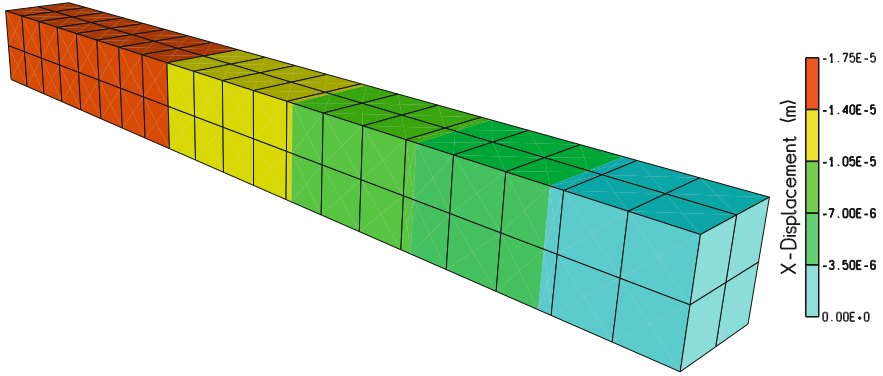


**Fig. 2.19** X-Displacements

$$\frac{d^2 p}{dx^2} = 0 \quad (2.314)$$

for 1D flow along the  $x$ -axis. The pressure distribution  $p(x)$  is given by

$$p(x) = p_1 \cdot \frac{x}{L}, \quad (2.315)$$

which satisfies the specified pressure boundary conditions at  $x = 0$  and  $x = L$ .

Let  $\boldsymbol{\sigma}$  denote the stress tensor and  $\mathbf{I}$  the unit tensor. Employing Biot's simplified theory (i.e. Biot number equal one) the equation of mechanical equilibrium reads

$$0 = \nabla \cdot (\boldsymbol{\sigma} - p\mathbf{I}). \quad (2.316)$$

It is satisfied by zero shear, if the stresses  $\sigma_{22}$  and  $\sigma_{33}$  are functions of  $x$  only and the horizontal stress  $\sigma_{11}$  satisfies

$$\frac{d}{dx}(\sigma_{11} - p) = 0. \quad (2.317)$$

The face  $x = 0$  is free of load, hence, integration gives

$$\sigma_{11} = p = p_1 \frac{x}{L}. \quad (2.318)$$

Due to the  $y$ - and  $z$ -fixities along the front, rear, top, and bottom, and with principal axes equal to coordinate axes, Hooke's law gives for the strains

$$\begin{aligned} E \cdot \epsilon_{11} &= \sigma_{11} - \nu(\sigma_{22} + \sigma_{33}), \\ 0 &= E \cdot \epsilon_{22} = \sigma_{22} - \nu(\sigma_{11} + \sigma_{33}), \\ 0 &= E \cdot \epsilon_{33} = \sigma_{33} - \nu(\sigma_{11} + \sigma_{22}), \end{aligned} \quad (2.319)$$

and therefore

$$\begin{aligned}\sigma_{22} = \sigma_{33} &= \frac{\nu}{1-\nu} \sigma_{11} = \frac{\nu}{1-\nu} p = \frac{p_1}{L} \frac{\nu}{1-\nu} x, \\ \epsilon_{11} &= \frac{1}{E} \left( 1 - \frac{2\nu^2}{1-\nu} \right) \sigma_{11} = \frac{p_1}{E L} \left( 1 - \frac{2\nu^2}{1-\nu} \right) x.\end{aligned}\quad (2.320)$$

Integrating the strains with respect to the fixities at the sliding planes yields the displacement vector  $(u_x, u_y, u_z)$

$$\begin{aligned}u_x(x) &= \frac{p_1}{2 E L} \left( 1 - \frac{2\nu^2}{1-\nu} \right) (x^2 - L^2), \\ u_y &= 0, \\ u_z &= 0.\end{aligned}\quad (2.321)$$

### 2.7.2 A Permeable Elastic Square Deforms Under Constant Internal Liquid Pressure

The domain represents the unit square  $[0, 1] \times [0, 1]$  in the x-y-plane. It has three faces located on the coordinate planes and is discretized by  $5 \times 5 \times 2$  equally sized hexahedral elements. The solid material has been selected elastic with Poisson's ratio  $\nu = 0.25$ , Young's modulus  $E = 10,000$  MPa, and Biot number equal one. An isotropic permeability of  $10^{-11} \text{ m}^2$  and zero porosity is assumed for the material, liquid viscosity is  $1 \text{ mPa} \cdot \text{s}$  and gravity is neglected via zero material and liquid densities. Top and bottom as well as the lateral faces on the coordinate planes are sliding planes. The simulation comprises one time step applying a constant liquid pressure  $p_0 = 0.8$  MPa at the bottom of the domain.

The formal solution proceeds in two steps, first to solve for the pressure distribution and then to evaluate stresses, strains and displacements. However, due to the setup the pressure  $p$  has constant value  $p_0$  throughout the entire domain, and we will focus on the mechanical aspects of the problem.

Let  $\sigma$  denote the stress tensor and  $\mathbf{I}$  the unit tensor. Employing Biot's simplified theory (i.e. Biot number equal one) the equation of mechanical equilibrium reads

$$0 = \nabla \cdot (\sigma - p \mathbf{I}). \quad (2.322)$$

It is satisfied by zero shear and constant stresses. Due to the setup

$$\sigma_{11} = \sigma_{22} = p_0 \quad (2.323)$$

and with principal axes equal to coordinate axes, Hooke's law gives for the strains

$$\begin{aligned}
0 &= \epsilon_{33} = \frac{1}{E}[\sigma_{33} - \nu(\sigma_{11} + \sigma_{22})] = \frac{1}{E}(\sigma_{33} - 2\nu \cdot p_0), \\
\epsilon_{22} &= \frac{1}{E}[\sigma_{22} - \nu(\sigma_{11} + \sigma_{33})] = (1 - \nu - 2\nu^2) \frac{p_0}{E}, \\
\epsilon_{11} &= \frac{1}{E}[\sigma_{11} - \nu(\sigma_{22} + \sigma_{33})] = (1 - \nu - 2\nu^2) \frac{p_0}{E}.
\end{aligned} \tag{2.324}$$

Integrating the strains with respect to the fixities at the sliding planes yields the displacement vector  $(u_x, u_y, u_z)$

$$\begin{aligned}
u_x(x) &= (1 - \nu - 2\nu^2) \frac{p_0}{E} x, \\
u_y(y) &= (1 - \nu - 2\nu^2) \frac{p_0}{E} y, \\
u_z &= 0.
\end{aligned} \tag{2.325}$$

### 2.7.3 A Permeable Elastic Cube Deforms Under Constant Internal Liquid Pressure

The domain is a cube with an edge size of 1 m. It has three faces located on the coordinate planes and is discretized by  $4 \times 4 \times 4$  cubic elements. The solid material has been selected elastic with Poisson's ratio  $\nu = 0.25$ , Young's modulus  $E = 10,000$  MPa, and Biot number equal one. An isotropic permeability of  $10^{-10}$  m<sup>2</sup> and zero porosity is assumed for the material, liquid viscosity is 1 mPa · s and gravity is neglected via zero material and liquid densities. The faces on the coordinate planes are sliding planes. The simulation comprises one time step applying a constant liquid pressure  $p_0 = 20$  MPa at the top of the domain.

The formal solution proceeds in two steps, first to solve for the pressure distribution and then to evaluate stresses, strains and displacements. However, due to the setup the pressure  $p$  has constant value  $p_0$  throughout the entire domain, and we will focus on the mechanical aspects of the problem.

Let  $\sigma$  denote the stress tensor and  $\mathbf{I}$  the unit tensor. Employing Biot's simplified theory (i.e. Biot number equal one) the equation of mechanical equilibrium reads

$$0 = \nabla \cdot (\sigma - p \mathbf{I}). \tag{2.326}$$

It is satisfied by zero shear and constant stresses. Due to the setup

$$\sigma_{11} = \sigma_{22} = \sigma_{33} = p_0 \tag{2.327}$$

and with principal axes equal to coordinate axes, Hooke's law gives for the strains

$$\begin{aligned}
\epsilon_{11} &= \frac{1}{E} [\sigma_{11} - \nu(\sigma_{22} + \sigma_{33})] = (1 - 2\nu) \frac{p_0}{E}, \\
\epsilon_{22} &= \frac{1}{E} [\sigma_{22} - \nu(\sigma_{11} + \sigma_{33})] = (1 - 2\nu) \frac{p_0}{E}, \\
\epsilon_{33} &= \frac{1}{E} [\sigma_{33} - \nu(\sigma_{11} + \sigma_{22})] = (1 - 2\nu) \frac{p_0}{E}.
\end{aligned} \tag{2.328}$$

Integrating the strains with respect to the fixities at the coordinate planes yields the displacement vector  $(u_x, u_y, u_z)$

$$\begin{aligned}
u_x(x) &= (1 - 2\nu) \frac{p_0}{E} x, \\
u_y(y) &= (1 - 2\nu) \frac{p_0}{E} y, \\
u_z(z) &= (1 - 2\nu) \frac{p_0}{E} z.
\end{aligned} \tag{2.329}$$

#### 2.7.4 A Permeable Elastic Cuboid Undergoes Static Load Due to Gravity and Hydrostatic Liquid Pressure

The domain is a cuboid of height  $H = 30$  m and edges parallel to the x-y-z coordinate axes. It is discretized by an irregular mesh of hexahedral elements. The domain is composed of four groups of isotropic permeable materials with zero porosity. Liquid viscosity is  $1 \text{ mPa} \cdot \text{s}$  and  $\rho_l = 1019.368 \text{ kg/m}^3$  is the liquid density. Each of the material groups has been assigned solid density  $\rho_s = 3058.104 \text{ kg/m}^3$ , Poisson's ratio  $\nu = 0.25$ , Young's modulus  $E = 10,000 \text{ MPa}$ , and Biot number equal one. Zero pressure is applied at the top face  $z = H$ . This face is free, all other faces are sliding planes. The simulation comprises one time step to establish the hydrostatic pressure distribution as well as the mechanical load.

The formal solution proceeds in two steps, first to solve for the pressure distribution and second to determine stresses, strains, and displacements.

The simulation setup employs a prescribed zero pressure at the top ( $z = H$ ), therefore the pressure distribution is hydrostatic, does not depend on the coordinates  $x$  and  $y$  and is given by

$$p(z) = \rho_l g (H - z), \tag{2.330}$$

where  $g = 9.81 \text{ m/s}^2$  is the magnitude of gravity, and  $z$  is the vertical coordinate extending from 0 to  $H$ .

Let  $\boldsymbol{\sigma}$  denote the stress tensor and  $\mathbf{I}$  the unit tensor. Employing Biot's simplified theory (i.e. Biot number equal one) the equation of mechanical equilibrium reads

$$0 = \nabla \cdot (\boldsymbol{\sigma} - p \mathbf{I}) - (0, 0, \rho_s g). \tag{2.331}$$

It is satisfied by zero shear, if pressure  $p$  and the horizontal stresses  $\sigma_{11}$  and  $\sigma_{22}$  are functions of the vertical coordinate  $z$  only and the vertical stress  $\sigma_{33}$  satisfies

$$\frac{d\sigma_{33}}{dz} = \rho_s g + \frac{dp}{dz} = (\rho_s - \rho_l) g. \quad (2.332)$$

The face  $z = H$  is free, hence, integration gives

$$\sigma_{33} = (\rho_s - \rho_l) (-g) (H - z). \quad (2.333)$$

Assuming that there is no horizontal displacement anywhere we have for the horizontal strains

$$\epsilon_{11} = \epsilon_{22} = 0. \quad (2.334)$$

Then, with principal axes equal to coordinate axes, Hooke's law gives

$$\begin{aligned} 0 &= \sigma_{11} - \nu(\sigma_{22} + \sigma_{33}), \\ 0 &= \sigma_{22} - \nu(\sigma_{11} + \sigma_{33}), \\ E \epsilon_{33} &= \sigma_{33} - \nu(\sigma_{11} + \sigma_{22}). \end{aligned} \quad (2.335)$$

Solving for  $\sigma_{11}$ ,  $\sigma_{22}$ , and the vertical strain  $\epsilon_{33}$  yields

$$\begin{aligned} \sigma_{11} = \sigma_{22} &= \frac{\nu}{1 - \nu} \sigma_{33} = \frac{\nu}{1 - \nu} (\rho_s - \rho_l) (-g) (H - z), \\ \epsilon_{33} &= \frac{1}{E} \left( 1 - \frac{2\nu^2}{1 - \nu} \right) (\rho_s - \rho_l) (-g) (H - z) \end{aligned} \quad (2.336)$$

in terms of the vertical coordinate. Integrating the strains with respect to the fixities at the sliding planes yields the displacement vector  $(u_x, u_y, u_z)$

$$\begin{aligned} u_x = u_y &= 0, \\ u_z(z) &= \frac{1}{E} \left( 1 - \frac{2\nu^2}{1 - \nu} \right) (\rho_s - \rho_l) (-g) \left( Hz - \frac{z^2}{2} \right). \end{aligned} \quad (2.337)$$

### ***2.7.5 A Permeable Elastic Beam Deforms Under Transient Internal Liquid Pressure. Specified Boundary Conditions are Time-Dependent and of 1st Kind***

The domain is a rectangular beam of length  $L = 1$  m extending along the positive  $x$ -axis. It has three faces located on the coordinate planes and is discretized by hexahedral elements with section  $0 \leq x \leq 0.6L$  composed of  $10 \times 1 \times 1$  and section  $0.6L \leq x \leq L$  composed of  $60 \times 1 \times 1$  elements. The solid material has

been selected elastic with Poisson's ratio  $\nu = 0.2$ , Young's modulus  $E = 27,000 \text{ Pa}$ , and Biot number equal one. An isotropic permeability  $k = 10^{-10} \text{ m}^2$  and zero porosity is assumed for the material, liquid viscosity is  $\mu = 1 \text{ mPa} \cdot \text{s}$ , and gravity is neglected via zero material and liquid densities. The face  $x = 0$  is free, all other faces of the beam are sliding planes. Zero pressure has been specified at the face  $x = 0$ , the pressure  $p_1 \cdot t$  ( $p_1 = 100 \text{ Pa/s}$ ) increases linearly with time  $t$ , it is applied at the face  $x = L$  for times  $t > 0$ . Starting from zero initial pressure the simulation evaluates the transient pressure distribution  $p(x, t)$  as well as stresses, strains, and displacements with output after 5 and 10 s (Fig. 2.20).

Let  $\boldsymbol{\sigma}$  denote the stress tensor and  $\mathbf{I}$  the unit tensor. Employing Biot's simplified theory (i.e. Biot number equal one) the equation of mechanical equilibrium reads

$$\mathbf{0} = \nabla \cdot (\boldsymbol{\sigma} - p \mathbf{I}). \quad (2.338)$$

It is satisfied by zero shear, if the stresses  $\sigma_{22}$  and  $\sigma_{33}$  are functions of  $x$  only and the horizontal stress  $\sigma_{11}$  satisfies

$$\frac{\partial}{\partial x} (\sigma_{11} - p) = 0. \quad (2.339)$$

With respect to prescribed boundary conditions at  $x = 0 \text{ m}$  the last equation yields

$$\sigma_{11} = p. \quad (2.340)$$

Due to the  $y$ - and  $z$ -fixities along the front, rear, top, and bottom and with principal axes equal to coordinate axes, Hooke's law gives for the strains

$$\begin{aligned} E \cdot \epsilon_{11} &= \sigma_{11} - \nu (\sigma_{22} + \sigma_{33}), \\ 0 &= E \cdot \epsilon_{22} = \sigma_{22} - \nu (\sigma_{11} + \sigma_{33}), \\ 0 &= E \cdot \epsilon_{33} = \sigma_{33} - \nu (\sigma_{11} + \sigma_{22}). \end{aligned} \quad (2.341)$$

In terms of pressure  $p(x, t)$  the non-zero stresses and strains take the form

$$\begin{aligned} \sigma_{22} = \sigma_{33} &= \frac{\nu}{1 - \nu} \sigma_{11} = \frac{\nu}{1 - \nu} p, \\ \epsilon_{11} &= \frac{1}{E} \left( 1 - \frac{2\nu^2}{1 - \nu} \right) \sigma_{11} = \frac{1}{E} \left( 1 - \frac{2\nu^2}{1 - \nu} \right) p. \end{aligned} \quad (2.342)$$

Let  $(u_x, u_y, u_z)$  denote the displacement vector and  $q$  the specific discharge via Darcy's law

$$q = -\frac{k}{\mu} \nabla p. \quad (2.343)$$

Conservation of momentum yields

$$\nabla \cdot (q + \frac{\partial}{\partial t} (u_x, u_y, u_z)) = 0. \quad (2.344)$$

For the present 1D example this reduces to

$$\begin{aligned}
 0 &= -\frac{k}{\mu} \frac{\partial^2 p}{\partial x^2} + \frac{\partial}{\partial t} \frac{\partial u_x}{\partial x} \\
 &= -\frac{k}{\mu} \frac{\partial^2 p}{\partial x^2} + \frac{1}{E} \left(1 - \frac{2\nu^2}{1-\nu}\right) \frac{\partial p}{\partial t}
 \end{aligned}
 \tag{2.345}$$

the 1D pressure conduction equation, which has to be solved subject to the initial condition

$$p(x, 0) = 0 \quad \text{for } 0 \leq x \leq L,
 \tag{2.346}$$

and the boundary conditions

$$\begin{aligned}
 p(0, t) &= 0 & \text{for } t > 0, \\
 p(L, t) &= p_1 t & \text{for } t > 0,
 \end{aligned}
 \tag{2.347}$$

arising from the problem setup. Once that the pressure distribution  $p(x, t)$  has been found, the remaining non-zero stresses and strains may be obtained.

It is therefore sufficient to solve the pressure conduction equation with respect to the imposed initial and boundary conditions. Introducing the notation

$$\chi = \frac{kE}{\mu} / \left(1 - \frac{2\nu^2}{1-\nu}\right)
 \tag{2.348}$$

the formal problem is to determine the solution  $p(x, t)$  of the parabolic equation

$$\frac{\partial p}{\partial t} = \chi \frac{\partial^2 p}{\partial x^2}
 \tag{2.349}$$

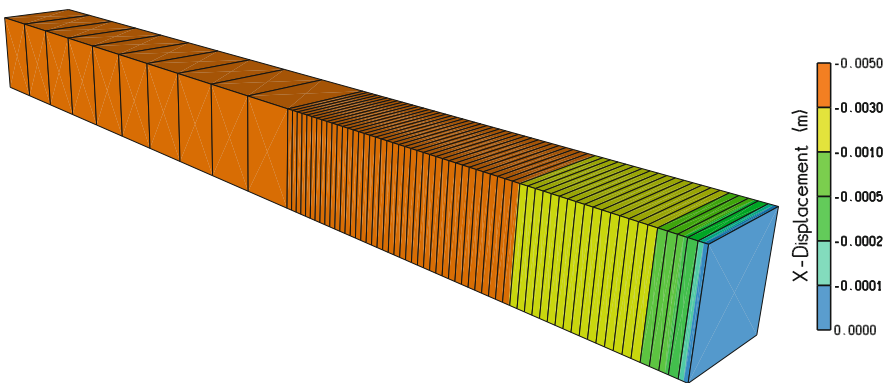


**Fig. 2.20** X-Displacements after 10s

subject to the initial and boundary conditions cited above. Applying the Laplace transform with respect to  $t$  yields the ordinary differential equation

$$\chi \bar{p}'' - s \bar{p} = 0, \quad (2.350)$$

where  $\bar{p}$  is the transform of  $p$ , the prime denotes the derivative with respect to  $x$ , and  $s$  is the transformation parameter. This equation has to be solved with respect to the transformed boundary conditions. This yields

$$\bar{p}(x, s) = p_1 \frac{\sinh(\sqrt{s/\chi} x)}{s^2 \sinh(\sqrt{s/\chi} L)}. \quad (2.351)$$

Integrating the strains with respect to the fixities at the sliding planes yields the displacement vector  $(u_x, u_y, u_z)$ , and this also holds for the Laplace transforms. Because  $\sigma_{11} = p$  the transform of the only non-zero displacement  $u_x(x, t)$  becomes

$$\bar{u}_x(x, s) = \frac{p_1}{E} \left( 1 - \frac{2\nu^2}{1-\nu} \right) \frac{\cosh(\sqrt{s/\chi} x) - \cosh(\sqrt{s/\chi} L)}{s^2 \sqrt{s/\chi} \sinh(\sqrt{s/\chi} L)}. \quad (2.352)$$

The entire solution may now be obtained from the transforms of pressure and  $x$ -displacement. The numerical inversion scheme outlined in the introductory section may easily be applied to give the required values of  $p(x, t)$  and  $u_x(x, t)$  (Fig. 2.20).

### ***2.7.6 A Permeable Elastic Beam Deforms Under Transient Internal Liquid Pressure. Specified Boundary Conditions are Time-Dependent and of 1st and 2nd Kind***

The domain is a rectangular beam of length  $L = 1$  m extending along the positive  $x$ -axis. It has three faces located on the coordinate planes and is discretized by hexahedral elements with section  $0 \leq x \leq 0.6L$  composed of  $10 \times 1 \times 1$  and section  $0.6L \leq x \leq L$  composed of  $60 \times 1 \times 1$  elements. The solid material has been selected elastic with Poisson's ratio  $\nu = 0.2$ , Young's modulus  $E = 27,000$  Pa, and Biot number equal one. An isotropic permeability  $k = 10^{-10}$  m<sup>2</sup> and zero porosity is assumed for the material, liquid viscosity is  $\mu = 1$  mPa·s, and gravity is neglected via zero material and liquid densities. The face  $x = 0$  is free, all other faces of the beam are sliding planes. Zero pressure has been specified at the face  $x = 0$ , the specific discharge  $q_1 \cdot t$  ( $q_1 = 7.6 \times 10^{-5}$  m/s<sup>2</sup>) increases linearly with time  $t$ , it is applied at the face  $x = L$  for times  $t > 0$  and acts as a source to the domain. Starting from zero initial pressure the simulation evaluates the transient pressure distribution  $p(x, t)$  as well as stresses, strains, and displacements with output after 5 and 10 s (Fig. 2.21).

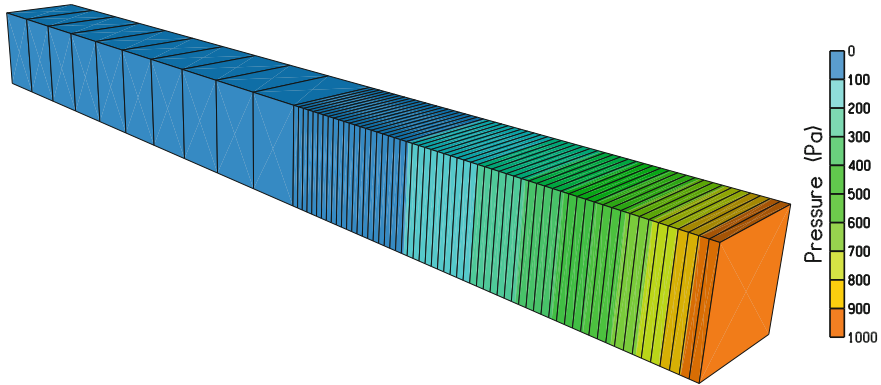


**Fig. 2.21** Pressure distribution after 10 s

Let  $\boldsymbol{\sigma}$  denote the stress tensor and  $\mathbf{I}$  the unit tensor. Employing Biot's simplified theory (i.e. Biot number equal one) the equation of mechanical equilibrium reads

$$0 = \nabla \cdot (\boldsymbol{\sigma} - p \mathbf{I}). \quad (2.353)$$

It is satisfied by zero shear, if the stresses  $\sigma_{22}$  and  $\sigma_{33}$  are functions of  $x$  only and the horizontal stress  $\sigma_{11}$  satisfies

$$\frac{\partial}{\partial x} (\sigma_{11} - p) = 0. \quad (2.354)$$

With respect to prescribed boundary conditions at  $x = 0$  m the last equation yields

$$\sigma_{11} = p. \quad (2.355)$$

Due to the  $y$ - and  $z$ -fixities along the front, rear, top, and bottom and with principal axes equal to coordinate axes, Hooke's law gives for the strains

$$\begin{aligned} E \cdot \epsilon_{11} &= \sigma_{11} - \nu (\sigma_{22} + \sigma_{33}), \\ 0 &= E \cdot \epsilon_{22} = \sigma_{22} - \nu (\sigma_{11} + \sigma_{33}), \\ 0 &= E \cdot \epsilon_{33} = \sigma_{33} - \nu (\sigma_{11} + \sigma_{22}). \end{aligned} \quad (2.356)$$

In terms of pressure  $p(x, t)$  the non-zero stresses and strains take the form

$$\begin{aligned} \sigma_{22} = \sigma_{33} &= \frac{\nu}{1 - \nu} \sigma_{11} = \frac{\nu}{1 - \nu} p, \\ \epsilon_{11} &= \frac{1}{E} \left( 1 - \frac{2\nu^2}{1 - \nu} \right) \sigma_{11} = \frac{1}{E} \left( 1 - \frac{2\nu^2}{1 - \nu} \right) p. \end{aligned} \quad (2.357)$$

Let  $(u_x, u_y, u_z)$  denote the displacement vector and  $q$  the specific discharge via Darcy's law

$$q = -\frac{k}{\mu} \nabla p. \quad (2.358)$$

Conservation of momentum yields

$$\nabla \cdot (q + \frac{\partial}{\partial t}(u_x, u_y, u_z)) = 0. \quad (2.359)$$

For the present 1D example this reduces to

$$\begin{aligned} 0 &= -\frac{k}{\mu} \frac{\partial^2 p}{\partial x^2} + \frac{\partial}{\partial t} \frac{\partial u_x}{\partial x} \\ &= -\frac{k}{\mu} \frac{\partial^2 p}{\partial x^2} + \frac{1}{E} \left(1 - \frac{2\nu^2}{1-\nu}\right) \frac{\partial p}{\partial t} \end{aligned} \quad (2.360)$$

the 1D pressure conduction equation, which has to be solved subject to the initial condition

$$p(x, 0) = 0 \quad \text{for } 0 \leq x \leq L, \quad (2.361)$$

and the boundary conditions

$$\begin{aligned} p(0, t) &= 0 & \text{for } t > 0, \\ \frac{\partial p}{\partial x}(L, t) &= q_1 \frac{\mu}{k} t & \text{for } t > 0, \end{aligned} \quad (2.362)$$

arising from the problem setup. Once that the pressure distribution  $p(x, t)$  has been found, the remaining non-zero stresses and strains may be obtained.

It is therefore sufficient to solve the pressure conduction equation with respect to the imposed initial and boundary conditions. Introducing the notation

$$\chi = \frac{kE}{\mu} / \left(1 - \frac{2\nu^2}{1-\nu}\right) \quad (2.363)$$

the formal problem is to determine the solution  $p(x, t)$  of the parabolic equation

$$\frac{\partial p}{\partial t} = \chi \frac{\partial^2 p}{\partial x^2} \quad (2.364)$$

subject to the initial and boundary conditions cited above. Applying the Laplace transform with respect to  $t$  yields the ordinary differential equation

$$\chi \bar{p}'' - s \bar{p} = 0, \quad (2.365)$$

where  $\bar{p}$  is the transform of  $p$ , the prime denotes the derivative with respect to  $x$ , and  $s$  is the transformation parameter. This equation has to be solved with respect to the transformed boundary conditions. This yields

$$\bar{p}(x, s) = q_1 \frac{\mu}{k} \frac{\sinh(\sqrt{s/\chi} x)}{s^2 \sqrt{s/\chi} \cosh(\sqrt{s/\chi} L)}. \quad (2.366)$$

Integrating the strains with respect to the fixities at the sliding planes yields the displacement vector  $(u_x, u_y, u_z)$ , and this also holds for the Laplace transforms. Because  $\sigma_{11} = p$  the transform of the only non-zero displacement  $u_x(x, t)$  becomes

$$\bar{u}_x(x, s) = q_1 \frac{\cosh(\sqrt{s/\chi} x) - \cosh(\sqrt{s/\chi} L)}{s^3 \cosh(\sqrt{s/\chi} L)}. \quad (2.367)$$

The entire solution may now be obtained from the transforms of pressure and x-displacement. The numerical inversion scheme outlined in the introductory section may easily be applied to give the required values of  $p(x, t)$  and  $u_x(x, t)$ .

### 2.7.7 Biot's 1D Consolidation Problem: Squeezing of a Pressurized Column Causes the Liquid to Discharge from the Domain

The domain is a rectangular beam of length  $L = 1$  m extending along the positive x-axis. It has three faces located on the coordinate planes and is discretized by hexahedral elements with section  $0 \leq x \leq 0.6L$  composed of  $10 \times 1 \times 1$  and section  $0.6L \leq x \leq L$  composed of  $60 \times 1 \times 1$  elements. The solid material has been selected elastic with Poisson's ratio  $\nu = 0.2$ , Young's modulus  $E = 30,000$  Pa, and Biot number equal one. An isotropic permeability  $k = 10^{-10}$  m<sup>2</sup> and zero porosity is assumed for the material, liquid viscosity is  $\mu = 1$  mPa·s and gravity is neglected via zero material and liquid densities. Except from the face  $x = L$  all faces of the beam are sliding planes. At the face  $x = L$  pressure and mechanical boundary conditions have explicitly been assigned: a compressive stress of 1,000 Pa acts in negative x-direction and pressure is assigned zero for times  $t > 0$ . Starting from initial equilibrium, i.e. pressure  $p_i = 1,000$  Pa and zero mechanical stress, the simulation evaluates the transient pressure distribution  $p(x, t)$  as well as stresses, strains, and displacements with output after 5 and 10 s (Fig. 2.22).

Let  $\sigma$  denote the stress tensor and  $\mathbf{I}$  the unit tensor. Employing Biot's simplified theory (i.e. Biot number equal one) the equation of mechanical equilibrium reads

$$0 = \nabla \cdot (\sigma - p \mathbf{I}). \quad (2.368)$$

It is satisfied by zero shear, if the stresses  $\sigma_{22}$  and  $\sigma_{33}$  are functions of  $x$  only and the horizontal stress  $\sigma_{11}$  satisfies

$$\frac{\partial}{\partial x} (\sigma_{11} - p) = 0. \quad (2.369)$$

With respect to the initial and prescribed boundary conditions at  $x = L$  the last equation yields

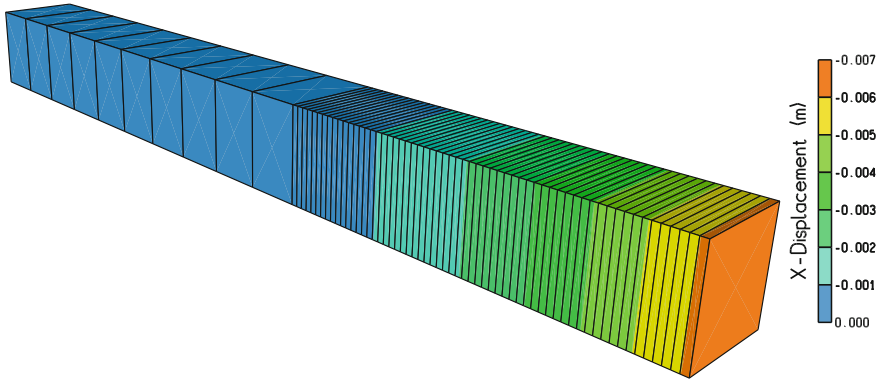


**Fig. 2.22** X-Displacements after 10s

$$p = \sigma_{11} + p_i. \tag{2.370}$$

Due to the y- and z-fixities along the front, rear, top, and bottom and with principal axes equal to coordinate axes, Hooke’s law gives for the strains

$$\begin{aligned} E \cdot \epsilon_{11} &= \sigma_{11} - \nu (\sigma_{22} + \sigma_{33}), \\ 0 &= E \cdot \epsilon_{22} = \sigma_{22} - \nu (\sigma_{11} + \sigma_{33}), \\ 0 &= E \cdot \epsilon_{33} = \sigma_{33} - \nu (\sigma_{11} + \sigma_{22}). \end{aligned} \tag{2.371}$$

In terms of the stress  $\sigma_{11}(x, t)$  the remaining non-zero stresses and strains take the form

$$\begin{aligned} \sigma_{22} = \sigma_{33} &= \frac{\nu}{1 - \nu} \sigma_{11}, \\ \epsilon_{11} &= \frac{1}{E} \left( 1 - \frac{2\nu^2}{1 - \nu} \right) \sigma_{11}. \end{aligned} \tag{2.372}$$

Let  $(u_x, u_y, u_z)$  denote the displacement vector and  $q$  the specific discharge via Darcy’s law

$$q = -\frac{k}{\mu} \nabla p. \tag{2.373}$$

Conservation of momentum yields

$$\nabla \cdot \left( q + \frac{\partial}{\partial t} (u_x, u_y, u_z) \right) = 0. \tag{2.374}$$

For the present 1D example this reduces to

$$\begin{aligned}
0 &= -\frac{k}{\mu} \frac{\partial^2 p}{\partial x^2} + \frac{\partial}{\partial t} \frac{\partial u_x}{\partial x} \\
&= -\frac{k}{\mu} \frac{\partial^2 \sigma_{11}}{\partial x^2} + \frac{1}{E} \left(1 - \frac{2\nu^2}{1-\nu}\right) \frac{\partial \sigma_{11}}{\partial t}
\end{aligned} \tag{2.375}$$

the 1D pressure conduction equation, which has to be solved subject to the initial condition

$$\sigma_{11}(x, 0) = 0 \quad \text{for } 0 \leq x \leq L, \tag{2.376}$$

and the boundary conditions

$$\begin{aligned}
\frac{\partial \sigma_{11}}{\partial x}(0, t) &= 0 \quad \text{for } t > 0, \\
\sigma_{11}(L, t) &= -p_i \quad \text{for } t > 0,
\end{aligned} \tag{2.377}$$

arising from the problem setup. Once that the stress  $\sigma_{11}(x, t)$  has been found, the pressure and the remaining non-zero stresses and strains may be obtained.

It is therefore sufficient to solve the pressure conduction equation with respect to the imposed initial and boundary conditions. Introducing the notation

$$\chi = \frac{kE}{\mu} \bigg/ \left(1 - \frac{2\nu^2}{1-\nu}\right) \tag{2.378}$$

the formal problem is to determine the solution  $\sigma_{11}(x, t)$  of the parabolic equation

$$\frac{\partial \sigma_{11}}{\partial t} = \chi \frac{\partial^2 \sigma_{11}}{\partial x^2} \tag{2.379}$$

subject to the initial and boundary conditions cited above. Applying the Laplace transform with respect to  $t$  yields the ordinary differential equation

$$\chi \bar{\sigma}_{11}'' - s \bar{\sigma}_{11} = 0, \tag{2.380}$$

where  $\bar{\sigma}_{11}$  is the transform of  $\sigma_{11}$ ,  $s$  is the transformation parameter, and the prime denotes the derivative with respect to  $x$ . This equation has to be solved with respect to the transformed boundary conditions. This yields

$$\bar{\sigma}_{11}(x, s) = -p_i \frac{\cosh(\sqrt{s/\chi} x)}{s \cosh(\sqrt{s/\chi} L)}. \tag{2.381}$$

Integrating the strains with respect to the fixities at the sliding planes yields the displacement vector  $(u_x, u_y, u_z)$ , and this also holds for the Laplace transforms. The transform of the only non-zero displacement  $u_x(x, t)$  becomes

$$\bar{u}_x(x, s) = -\frac{p_i}{E} \left(1 - \frac{2\nu^2}{1 - \nu}\right) \frac{\sinh(\sqrt{s/\chi} x)}{s \sqrt{s/\chi} \cosh(\sqrt{s/\chi} L)}. \tag{2.382}$$

The entire solution may now be obtained from the transforms of stress  $\sigma_{11}$  and x-displacement. The numerical inversion scheme outlined in the introductory section may easily be applied to give the required values of  $\sigma_{11}(x, t)$  and  $u_x(x, t)$ .

## 2.8 Thermomechanics

Temperature changes cause thermal strains affecting the mechanical load. The formal solution of the subsequent examples always proceeds in two steps: first to solve for the temperature, and then to evaluate stresses, strains, and displacements. Various ideas already outlined in previous sections will appear again.

### 2.8.1 An Elastic Beam Deforms Due to an Instant Temperature Change

The domain is a rectangular beam of length  $L = 1$  m extending along the positive x-axis. It has three faces located on the coordinate planes and is discretized by  $20 \times 2 \times 2$  cubic elements. The solid material has been selected elastic with Poisson's ratio  $\nu = 0.25$ , Young's modulus  $E = 25,000$  MPa, zero heat capacity, and thermal expansion  $\alpha = 3 \times 10^{-5}$  1/K. Gravity is neglected via zero material density. The face  $x = 0$  is free, all other faces of the beam are sliding planes. The simulation starts from the initial temperature  $T_0 = 0^\circ\text{C}$  and comprises one time step applying an instant temperature change with temperature  $T_1 = 1^\circ\text{C}$  at  $x = L$  and zero temperature  $T_0$  at  $x = 0$ .

The formal solution proceeds in two steps, first to solve for the temperature distribution  $T(x)$  and then to evaluate stresses, strains, and displacements (Fig. 2.23).

The Laplace equation is the governing equation describing the steady-state temperature distribution. It reads

$$\frac{d^2T}{dx^2} = 0 \tag{2.383}$$

for 1D heat flow along the x-axis, hence, the temperature distribution is given by

$$T(x) = (T_1 - T_0) \frac{x}{L} + T_0. \tag{2.384}$$

For the closed form solution of the mechanical problem note, that due to the simulation setup, the entire system is free of shear and the principal axes coincide with the coordinate axes. The constitutive equations relate the strains  $\epsilon_{11}, \epsilon_{22}, \epsilon_{33}$ , (in x-, y-,

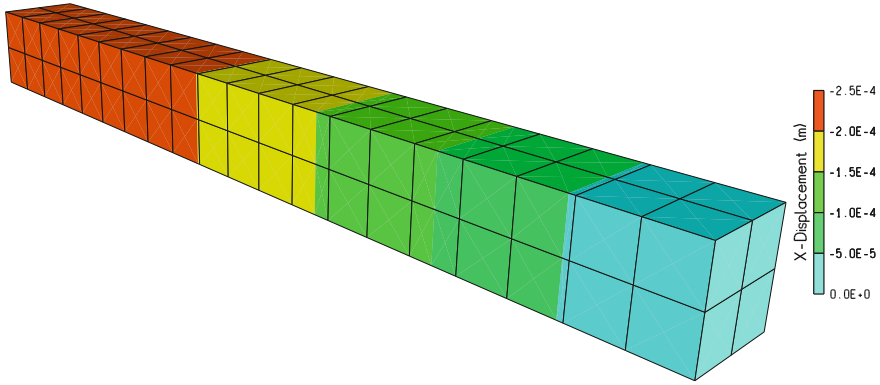


**Fig. 2.23** X-Displacements

and z-direction, respectively) and the associated stresses  $\sigma_{11}$ ,  $\sigma_{22}$ , and  $\sigma_{33}$  via

$$\begin{aligned}
 \epsilon_{11} - \alpha(T(x) - T_0) &= \frac{1}{E}[\sigma_{11} - \nu(\sigma_{22} + \sigma_{33})], \\
 \epsilon_{22} - \alpha(T(x) - T_0) &= \frac{1}{E}[\sigma_{22} - \nu(\sigma_{11} + \sigma_{33})], \\
 \epsilon_{33} - \alpha(T(x) - T_0) &= \frac{1}{E}[\sigma_{33} - \nu(\sigma_{11} + \sigma_{22})].
 \end{aligned}
 \tag{2.385}$$

Due to the setup the x-direction is free of stress, y- and z-direction are free of strain, therefore,

$$\begin{aligned}
 \sigma_{11} &= 0, \\
 \epsilon_{22} = \epsilon_{33} &= 0.
 \end{aligned}
 \tag{2.386}$$

Hence, due to the change in temperature, the remaining non-zero stresses and strains become

$$\begin{aligned}
 \sigma_{22} &= -\alpha \frac{E}{1 - \nu} (T(x) - T_0), \\
 \sigma_{33} &= -\alpha \frac{E}{1 - \nu} (T(x) - T_0), \\
 \epsilon_{11} &= \alpha \frac{1 + \nu}{1 - \nu} (T(x) - T_0).
 \end{aligned}
 \tag{2.387}$$

Integrating the strains with respect to the fixities at the sliding planes yields the displacement vector  $(u_x, u_y, u_z)$

$$\begin{aligned}
 u_x(x) &= \alpha \frac{1 + \nu}{1 - \nu} \frac{T_1 - T_0}{2L} (x^2 - L^2), \\
 u_y &= u_z = 0.
 \end{aligned}
 \tag{2.388}$$

### 2.8.2 An Elastic Square Deforms Due to an Instant Temperature Change

The domain represents the unit square  $[0, 1] \times [0, 1]$  in the x-y-plane. It has three faces located on the coordinate planes and is discretized by  $5 \times 5 \times 2$  equally sized hexahedral elements. The solid material has been selected elastic with Poisson's ratio  $\nu = 0.25$ , Young's modulus  $E = 25,000$  MPa, zero heat capacity, and thermal expansion  $\alpha = 4 \times 10^{-5}$  1/K. Gravity is neglected via zero material density. Top and bottom as well as the lateral faces on the coordinate planes are sliding planes. The simulation starts from the initial temperature  $T_0 = 0^\circ\text{C}$  and comprises one time step applying an instant temperature change to  $T_1 = 1^\circ\text{C}$  at the bottom of the domain.

The formal solution proceeds in two steps, first to solve for the temperature distribution and then to evaluate stresses, strains, and displacements. However, due to the setup the temperature change has constant value  $T_1 - T_0$  throughout the entire domain, and we will focus on the mechanical aspects of the problem.

Due to the simulation setup the entire system is free of shear and the principal axes coincide with the coordinate axes. The constitutive equations relate the strains  $\epsilon_{11}$ ,  $\epsilon_{22}$ ,  $\epsilon_{33}$ , (in x-, y-, and z-direction, respectively) and the associated stresses  $\sigma_{11}$ ,  $\sigma_{22}$ ,  $\sigma_{33}$  via

$$\begin{aligned}
 \epsilon_{11} - \alpha(T_1 - T_0) &= \frac{1}{E} [\sigma_{11} - \nu(\sigma_{22} + \sigma_{33})] = 0, \\
 \epsilon_{22} - \alpha(T_1 - T_0) &= \frac{1}{E} [\sigma_{22} - \nu(\sigma_{11} + \sigma_{33})] = 0, \\
 \epsilon_{33} - \alpha(T_1 - T_0) &= \frac{1}{E} [\sigma_{33} - \nu(\sigma_{11} + \sigma_{22})] = 0.
 \end{aligned}
 \tag{2.389}$$

Due to the setup x- and y-direction are free of stress, and the z-direction is free of strain, therefore,

$$\begin{aligned}
 \sigma_{11} &= \sigma_{22} = 0, \\
 \epsilon_{33} &= 0.
 \end{aligned}
 \tag{2.390}$$

Hence, due to the change in temperature from  $T_0$  to  $T_1$  the remaining non-zero strains and stresses become

$$\begin{aligned}
 \sigma_{33} &= -\alpha(T_1 - T_0) E, \\
 \epsilon_{11} = \epsilon_{22} &= (1 + \nu) \alpha(T_1 - T_0).
 \end{aligned}
 \tag{2.391}$$

Integrating the strains with respect to the fixities at the sliding planes yields the displacement vector  $(u_x, u_y, u_z)$

$$\begin{aligned} u_x(x) &= (1 + \nu) \alpha (T_1 - T_0) x, \\ u_y(y) &= (1 + \nu) \alpha (T_1 - T_0) y, \\ u_z &= 0. \end{aligned} \tag{2.392}$$

### 2.8.3 An Elastic Cube Deforms Due to an Instant Temperature Change

The domain is a cube with an edge size of 1 m. It has three faces located on the coordinate planes and is discretized by  $4 \times 4 \times 4$  cubic elements. The solid material has been selected elastic with Poisson's ratio  $\nu = 0.25$ , Young's modulus  $E = 25,000$  MPa, zero heat capacity, and thermal expansion  $\alpha = 5 \times 10^{-5}$  1/K. Gravity is neglected via zero material density. The faces on the coordinate planes are sliding planes. The simulation starts from the initial temperature  $T_0 = 0^\circ\text{C}$  and comprises one time step applying an instant temperature change to  $T_1 = -40^\circ\text{C}$  at the top of the domain.

The formal solution proceeds in two steps, first to solve for the temperature distribution and then to evaluate stresses, strains, and displacements. However, due to the setup the temperature change has constant value  $T_1 - T_0$  throughout the entire domain, and we will focus on the mechanical aspects of the problem.

Due to the simulation setup the entire system is free of shear, and the principal axes coincide with the coordinate axes.

$$\sigma_{11} = \sigma_{22} = \sigma_{33} = 0 \tag{2.393}$$

are the principal stresses in x-, y-, and z-direction, respectively. The constitutive equations yield for the associated strains  $\epsilon_{11}$ ,  $\epsilon_{22}$ , and  $\epsilon_{33}$

$$\begin{aligned} \epsilon_{11} - \alpha(T_1 - T_0) &= \frac{1}{E}[\sigma_{11} - \nu(\sigma_{22} + \sigma_{33})] = 0, \\ \epsilon_{22} - \alpha(T_1 - T_0) &= \frac{1}{E}[\sigma_{22} - \nu(\sigma_{11} + \sigma_{33})] = 0, \\ \epsilon_{33} - \alpha(T_1 - T_0) &= \frac{1}{E}[\sigma_{33} - \nu(\sigma_{11} + \sigma_{22})] = 0. \end{aligned} \tag{2.394}$$

Therefore, due to the change in temperature from  $T_0$  to  $T_1$  the strains become

$$\epsilon_{11} = \epsilon_{22} = \epsilon_{33} = \alpha(T_1 - T_0). \tag{2.395}$$

Integrating the strains with respect to the fixities at the coordinate planes yields the displacement vector  $(u_x, u_y, u_z)$

$$\begin{aligned}
u_x(x) &= \alpha (T_1 - T_0) x, \\
u_y(y) &= \alpha (T_1 - T_0) y, \\
u_z(z) &= \alpha (T_1 - T_0) z.
\end{aligned}
\tag{2.396}$$

### ***2.8.4 An Elastic Cuboid Undergoes Load Due to Gravity and Instant Temperature Change***

The domain is a cuboid of height  $H = 30$  m and edges parallel to the x-y-z coordinate axes. It is discretized by an irregular mesh of hexahedral elements. The cuboid is represented by four groups of elastic materials, where each has been assigned density  $\rho = 2038.736$  kg/m<sup>3</sup>, Poisson's ratio  $\nu = 0.25$ , Young's modulus  $E = 5,000$  MPa, zero heat capacity, and thermal expansion  $\alpha = 5 \times 10^{-6}$  1/K. Gravity is applied in negative z-direction,  $g = 9.81$  m/s<sup>2</sup> is the magnitude of gravity. The bottom and the lateral faces are sliding planes, the top face is free. The simulation starts from the initial temperature  $T_0 = 10^\circ\text{C}$  and comprises one time step applying an instant temperature change with temperature  $T_1 = 4^\circ\text{C}$  at the top ( $z = H$ ) and temperature  $T_0$  at  $z = 0$ .

The formal solution proceeds in two steps, first to solve for the temperature distribution  $T(x)$  and then to evaluate stresses, strains, and displacements.

The Laplace equation is the governing equation describing the steady-state temperature distribution. It reads

$$\frac{d^2T}{dz^2} = 0 \tag{2.397}$$

for 1D heat flow along the z-axis, hence the temperature distribution is given by

$$T(z) = (T_1 - T_0) \frac{z}{H} + T_0. \tag{2.398}$$

Next we focus on the closed form solution of the mechanical problem. Let  $\sigma$  denote the stress tensor. The equation of mechanical equilibrium

$$0 = \nabla \cdot \sigma - (0, 0, \rho g) \tag{2.399}$$

is satisfied by zero shear, if the horizontal stresses  $\sigma_{11}$  and  $\sigma_{22}$  are functions of  $z$  only and the vertical stress  $\sigma_{33}$  satisfies

$$\frac{d\sigma_{33}}{dz} = \rho g. \tag{2.400}$$

The face  $z = H$  is free, hence, integration gives

$$\sigma_{33} = \rho(-g)(H - z). \tag{2.401}$$

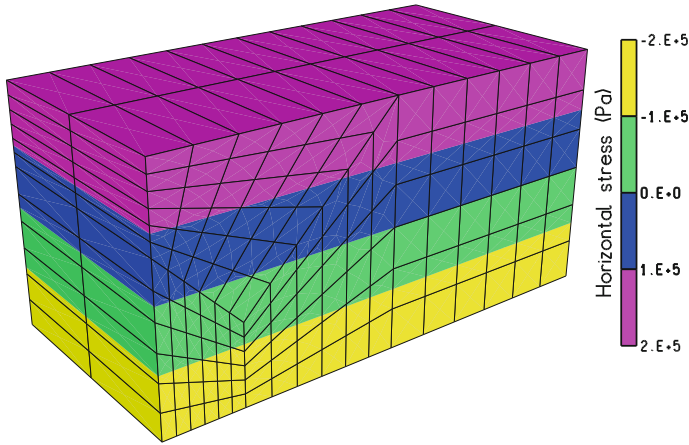


**Fig. 2.24** Horizontal stress

Due to the simulation setup there is no horizontal displacement anywhere, hence, for the horizontal strains

$$\epsilon_{11} = \epsilon_{22} = 0. \quad (2.402)$$

Then, with principal axes equal to coordinate axes, the constitutive equations give

$$\begin{aligned} \epsilon_{11} - \alpha(T(z) - T_0) &= \frac{1}{E}[\sigma_{11} - \nu(\sigma_{22} + \sigma_{33})], \\ \epsilon_{22} - \alpha(T(z) - T_0) &= \frac{1}{E}[\sigma_{22} - \nu(\sigma_{11} + \sigma_{33})], \\ \epsilon_{33} - \alpha(T(z) - T_0) &= \frac{1}{E}[\sigma_{33} - \nu(\sigma_{11} + \sigma_{22})]. \end{aligned} \quad (2.403)$$

Solving for  $\sigma_{11}$ ,  $\sigma_{22}$ , (Fig. 2.24) and the vertical strain  $\epsilon_{33}$  yields

$$\begin{aligned} \sigma_{11} = \sigma_{22} &= -\alpha \frac{E}{1-\nu} (T_1 - T_0) \frac{z}{H} + \frac{\nu}{1-\nu} \rho(-g)(H-z), \\ \epsilon_{33} &= \frac{1+\nu}{1-\nu} \alpha (T_1 - T_0) \frac{z}{H} + \left(1 - \frac{2\nu^2}{1-\nu}\right) \frac{1}{E} \rho(-g)(H-z) \end{aligned} \quad (2.404)$$

in terms of the vertical coordinate. Integrating the strains with respect to the fixities at the sliding planes yields the displacement vector  $(u_x, u_y, u_z)$

$$\begin{aligned} u_x = u_y &= 0, \\ u_z(z) &= \frac{1+\nu}{1-\nu} \alpha (T_1 - T_0) \frac{z^2}{2H} + \left(1 - \frac{2\nu^2}{1-\nu}\right) \frac{1}{E} \rho(-g) \left(zH - \frac{1}{2}z^2\right). \end{aligned} \quad (2.405)$$

### 2.8.5 An Elastic Beam Deforms Due to a Transient Temperature Change. Temperature Boundary Conditions are Time-Dependent and of 1st Kind

The domain is a rectangular beam of length  $L = 1$  m extending along the positive  $x$ -axis. It has three faces located on the coordinate planes and is discretized by hexahedral elements with section  $0 \leq x \leq 0.6L$  composed of  $10 \times 1 \times 1$  and section  $0.6L \leq x \leq L$  composed of  $60 \times 1 \times 1$  elements. The solid material has been selected elastic with Poisson's ratio  $\nu = 0.25$ , Young's modulus  $E = 25,000$  MPa, and density  $\rho = 2,000$  kg/m<sup>3</sup>. Thermal conductivity  $\lambda = 2.7$  W/(m · K), heat capacity  $c = 0.45$  J/(kg · K), and thermal expansion  $\alpha = 3 \times 10^{-4}$  1/K have been assigned. Gravity is neglected via explicit assignment. The face  $x = 0$  is free, all other faces of the beam are sliding planes. Zero temperature has been specified at the face  $x = 0$ , the temperature  $T_1 \cdot t$  ( $T_1 = 1$  °C/s) increases linearly with time  $t$ , it is applied at the face  $x = L$  for times  $t > 0$ . Starting from zero initial temperature the simulation evaluates the transient temperature distribution  $T(x, t)$  as well as stresses, strains, and displacements with output after 5 and 10 s.

The heat conduction equation is the governing equation describing the transient temperature distribution. It reads

$$\rho c \frac{\partial T}{\partial t} = \lambda \nabla \cdot \nabla T. \quad (2.406)$$

Introducing the notation

$$\chi = \frac{\lambda}{\rho c} \quad (2.407)$$

the present 1D problem is governed by the parabolic equation

$$\frac{1}{\chi} \frac{\partial T}{\partial t} = \frac{\partial^2 T}{\partial x^2}, \quad (2.408)$$

the initial condition

$$T(x, 0) = 0 \quad \text{for } 0 \leq x \leq L, \quad (2.409)$$

and the boundary conditions imposed at the beam ends

$$\begin{aligned} T(0, t) &= 0 & \text{for } t > 0, \\ T(L, t) &= T_1 \cdot t & \text{for } t > 0. \end{aligned} \quad (2.410)$$

We will shown next that the solution of the mechanical problem may be obtained in terms of the temperature distribution.

For the closed form solution of the mechanical problem note, that due to the simulation setup, the entire system is free of shear and the principal axes coincide with the coordinate axes. The constitutive equations relate the strains  $\epsilon_{11}$ ,  $\epsilon_{22}$ ,  $\epsilon_{33}$ ,

(in x-, y-, and z-direction, respectively) and the associated stresses  $\sigma_{11}$ ,  $\sigma_{22}$ , and  $\sigma_{33}$  via

$$\begin{aligned}\epsilon_{11} - \alpha T(x, t) &= \frac{1}{E}[\sigma_{11} - \nu(\sigma_{22} + \sigma_{33})], \\ \epsilon_{22} - \alpha T(x, t) &= \frac{1}{E}[\sigma_{22} - \nu(\sigma_{11} + \sigma_{33})], \\ \epsilon_{33} - \alpha T(x, t) &= \frac{1}{E}[\sigma_{33} - \nu(\sigma_{11} + \sigma_{22})].\end{aligned}\tag{2.411}$$

Due to the setup the x-direction is free of stress, y- and z-direction are free of strain, therefore,

$$\begin{aligned}\sigma_{11} &= 0, \\ \epsilon_{22} = \epsilon_{33} &= 0.\end{aligned}\tag{2.412}$$

Hence, due to the change in temperature, the remaining non-zero stresses and strains become

$$\begin{aligned}\sigma_{22} = \sigma_{33} &= -\alpha \frac{E}{1 - \nu} T(x, t), \\ \epsilon_{11} &= \alpha \frac{1 + \nu}{1 - \nu} T(x, t).\end{aligned}\tag{2.413}$$

Integrating the strains with respect to the fixities at the sliding planes yields the displacement vector ( $u_x, u_y, u_z$ )

$$\begin{aligned}u_x(x) &= \alpha \frac{1 + \nu}{1 - \nu} \int_L^x T(x', t) dx', \\ u_y = u_z &= 0.\end{aligned}\tag{2.414}$$

Once that the temperature distribution  $T(x, t)$  has been found, the entire solution of the thermomechanical problem may thus be obtained. It is therefore sufficient to solve the 1D heat conduction equation with respect to the imposed initial and boundary conditions cited above.

Applying the Laplace transform with respect to time  $t$  yields the ordinary differential equation

$$\chi \bar{T}'' - s \bar{T} = 0,\tag{2.415}$$

where  $\bar{T}$  is the transform of  $T(x, t)$ , the prime denotes the derivative with respect to  $x$ , and  $s$  is the transformation parameter. This equation has to be solved with respect to the transformed boundary conditions. This yields the transform of the temperature

$$\bar{T}(x, s) = T_1 \frac{\sinh(\sqrt{s/\chi} x)}{s^2 \sinh(\sqrt{s/\chi} L)}, \quad (2.416)$$

and the transform of the only non-zero displacement  $u_x(x, t)$  becomes

$$\bar{u}_x(x, s) = \alpha \frac{1 + \nu}{1 - \nu} T_1 \frac{\cosh(\sqrt{s/\chi} x) - \cosh(\sqrt{s/\chi} L)}{s^2 \sqrt{s/\chi} \sinh(\sqrt{s/\chi} L)}. \quad (2.417)$$

The entire solution may now be obtained from the transforms of temperature and  $x$ -displacement. The numerical inversion scheme outlined in the introductory section may easily be applied to give the required values of temperature  $T(x, t)$  and the entire mechanical load.

### ***2.8.6 Elastic Beams Deform Due to a Transient Temperature Change. Temperature Boundary Conditions are Time-Dependent and of 2nd Kind***

The domain is composed of two beams in parallel (Beam1 and Beam2) extending along the positive  $x$ -axis, each  $L = 25$  m long and subdivided into  $25 \times 1 \times 1$  cubic elements. The solid material has been selected elastic with Poisson's ratio  $\nu = 0.25$ , Young's modulus  $E = 25,000$  MPa, and density  $\rho = 2,000$  kg/m<sup>3</sup>. Thermal conductivity  $\lambda = 1.1574074$  W/(m · K), thermal expansion  $\alpha = 3 \times 10^{-4}$  1/K, and heat capacities  $c_1 = 0.01$  J/(kg · K) and  $c_2 = 0.02$  J/(kg · K) have been assigned to Beam1 and Beam2, respectively. Gravity is neglected via explicit assignment. The faces  $x = L$  are free, all other faces of the beams are sliding planes. No-flow boundary conditions prevail at the  $x = 0$  m faces. A specific heat flow is prescribed at  $x = L$  for times  $t > 0$ . It acts as heat source to the domain and increases linearly with time via  $q_{th1} \cdot t$ , where  $q_{th1} = 0.385802$  W/(d · m<sup>2</sup>) has been assumed. Starting from zero initial temperature the simulation evaluates the transient temperature distributions as well as stresses, strains, and displacements with output after 0.045 and 0.09 days (Figs. 2.25 and 2.26).

The formal solution proceeds in two steps, first to solve for the temperature distributions and then to evaluate stresses, strains, and displacements.

Let  $c$  denote any of  $c_1$  or  $c_2$ . The heat conduction equation is the governing equation describing the transient temperature distribution. It reads

$$\rho c \frac{\partial T}{\partial t} = \lambda \nabla \cdot \nabla T. \quad (2.418)$$

Introducing the notation

$$\chi = \frac{\lambda}{\rho c} \quad (2.419)$$

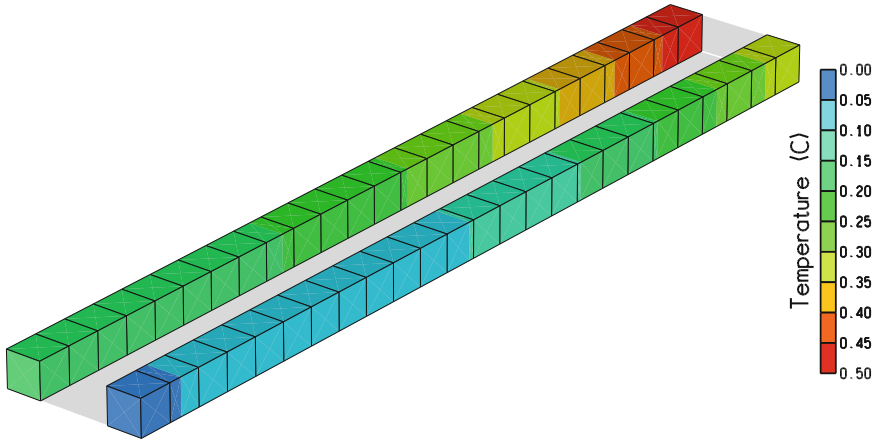


Fig. 2.25 Temperature distributions after 0.09 days

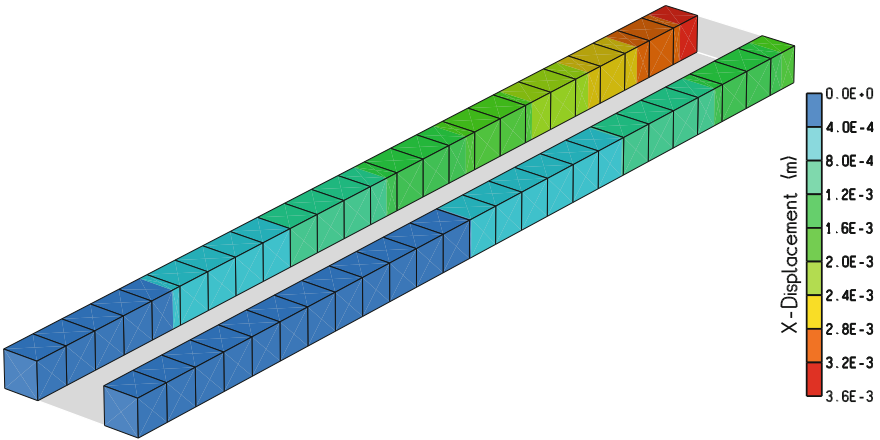


Fig. 2.26 X-Displacements after 0.09 days

the present 1D problems are governed by the parabolic equation

$$\frac{1}{\chi} \frac{\partial T}{\partial t} = \frac{\partial^2 T}{\partial x^2}, \tag{2.420}$$

the initial condition

$$T(x, 0) = 0 \quad \text{for } 0 \leq x \leq L, \tag{2.421}$$

and the boundary conditions

$$\begin{aligned}\frac{\partial T}{\partial x}(0, t) &= 0 & \text{for } t > 0, \\ \lambda \frac{\partial T}{\partial x}(L, t) &= q_{th1} \cdot t & \text{for } t > 0.\end{aligned}\tag{2.422}$$

The closed form solution of the above problem is given by Carslaw and Jaeger [3], who arrive at the series representation

$$T(x, t) = \frac{8q_{th1}\sqrt{\chi t^3}}{\lambda} \sum_{n=0}^{\infty} \left[ i^3 \operatorname{erfc} \frac{(2n+1)L-x}{2\sqrt{\chi t}} + i^3 \operatorname{erfc} \frac{(2n+1)L+x}{2\sqrt{\chi t}} \right]\tag{2.423}$$

where  $i^3 \operatorname{erfc}$  denotes the third repeated integral of the complementary error function. See [4] for its numerical evaluation.

For the closed form solution of the mechanical problem note, that due to simulation setup, the entire system is free of shear and the principal axes coincide with the coordinate axes. The constitutive equations relate the strains  $\epsilon_{11}$ ,  $\epsilon_{22}$ ,  $\epsilon_{33}$ , (in  $x$ -,  $y$ -, and  $z$ -direction, respectively) and the associated stresses  $\sigma_{11}$ ,  $\sigma_{22}$ , and  $\sigma_{33}$  via

$$\begin{aligned}\epsilon_{11} - \alpha T(x, t) &= \frac{1}{E} [\sigma_{11} - \nu(\sigma_{22} + \sigma_{33})], \\ \epsilon_{22} - \alpha T(x, t) &= \frac{1}{E} [\sigma_{22} - \nu(\sigma_{11} + \sigma_{33})], \\ \epsilon_{33} - \alpha T(x, t) &= \frac{1}{E} [\sigma_{33} - \nu(\sigma_{11} + \sigma_{22})].\end{aligned}\tag{2.424}$$

Due to the setup the  $x$ -direction is free of stress,  $y$ - and  $z$ -direction are free of strain, therefore,

$$\begin{aligned}\sigma_{11} &= 0, \\ \epsilon_{22} &= \epsilon_{33} = 0.\end{aligned}\tag{2.425}$$

Hence, due to the temperature change  $T(x, t)$ , the remaining non-zero stresses and strains become

$$\begin{aligned}\sigma_{22} &= -\alpha \frac{E}{1-\nu} T(x, t), \\ \sigma_{33} &= -\alpha \frac{E}{1-\nu} T(x, t), \\ \epsilon_{11} &= \alpha \frac{1+\nu}{1-\nu} T(x, t).\end{aligned}\tag{2.426}$$

Integrating the strains with respect to the fixities at the sliding planes yields the displacement vector  $(u_x, u_y, u_z)$

$$u_z = u_y = 0,\tag{2.427}$$

$$u_x(x) = \alpha \frac{1 + \nu}{1 - \nu} \frac{16q_{th1}\chi t^2}{\lambda} \cdot \sum_{n=0}^{\infty} \left[ i^4 \operatorname{erfc} \frac{(2n+1)L-x}{2\sqrt{\chi t}} - i^4 \operatorname{erfc} \frac{(2n+1)L+x}{2\sqrt{\chi t}} \right],$$

where  $i^4 \operatorname{erfc}$  denotes the 4th repeated integral of the complementary error function. See [4] for its numerical evaluation.

### 2.8.7 Stresses Relax in a Cube of Norton Material Undergoing an Instant Temperature Change

The domain is a single cube with edge size  $L = 1$  m located in the first octant. It has three faces located on the coordinate planes and is discretized by  $2 \times 2 \times 2$  cubic elements. The cube is represented by a Norton material. Poisson's ratio  $\nu = 0.27$ , Young's modulus  $E = 25,000$  MPa, zero heat capacity, and thermal expansion  $\alpha = 4 \times 10^{-5}$  1/K have been assigned, gravity is neglected via zero material density. Various additional parameters are involved in the rheological behaviour, details are given below. Faces on the coordinate planes and the top face are sliding planes. The simulation starts from an initial setup free of load and an initial temperature  $T_0 = 27^\circ\text{C}$ . It applies an instant temperature change to  $T_1 = 47^\circ\text{C}$  at the top of the domain and evaluates stresses, strains, and displacements through time with output after 0.5 and 2 days.

Let  $\sigma$  denote the stress tensor,  $\mathbf{I}$  the unit tensor,

$$\sigma^D = \sigma - \frac{\operatorname{tr}\sigma}{3} \mathbf{I} \quad (2.428)$$

the stress deviator, and

$$\sigma_{\text{eff}} = \sqrt{\frac{3}{2} \sum_{i=1}^3 \sum_{j=1}^3 \sigma_{ij}^D \sigma_{ji}^D} \quad (2.429)$$

the v. Mises or effective stress. The rheological model involved yields the fundamental stress/strain relationships as a system of differential equations for the creep strains

$$\frac{\partial \epsilon^{cr}}{\partial t} = \frac{3}{2} \frac{\sigma^D}{\sigma_{\text{eff}}} (N \sigma_{\text{eff}}^n) \quad (2.430)$$

and the total strains

$$\epsilon^{tot} = \epsilon^{th} + \epsilon^{el} + \epsilon^{cr}, \quad (2.431)$$

where  $\epsilon^{th}$  denotes the thermal strains and  $\epsilon^{el}$  the elastic strains via Hooke's law. Both equations have to be solved with respect to the imposed initial and boundary conditions.

For the present example the behaviour of the Norton material is specified with the aid of the parameters

$$\begin{aligned} n &= 5, \\ N(T) &= A \exp\left(-\frac{Q}{RT}\right), \end{aligned} \quad (2.432)$$

where  $R = 8.31441 \text{ J}/(\text{mol} \cdot \text{K})$  is the gas constant,  $T$  is the absolute temperature, and experimental data obtained from rock salt yield

$$\begin{aligned} A &= 0.18 \text{ 1}/(\text{d} \cdot \text{MPa}^5), \\ Q &= 54,000 \text{ J/mol}. \end{aligned} \quad (2.433)$$

Note that day is required as unit of time and stresses have to be in MPa.

Due to the example setup the principal axes are identical to the coordinate axes and the vertical stress is the only non-zero element of the stress tensor. Therefore,

$$\boldsymbol{\sigma} = \begin{pmatrix} 0 & 0 & 0 \\ 0 & 0 & 0 \\ 0 & 0 & \sigma_{33} \end{pmatrix}. \quad (2.434)$$

the trace of  $\boldsymbol{\sigma}$

$$\text{tr} \boldsymbol{\sigma} = \sigma_{33}, \quad (2.435)$$

the stress deviator

$$\boldsymbol{\sigma}^D = \frac{\sigma_{33}}{3} \begin{pmatrix} -1 & 0 & 0 \\ 0 & -1 & 0 \\ 0 & 0 & 2 \end{pmatrix}, \quad (2.436)$$

the v. Mises or effective stress

$$\sigma_{\text{eff}} = |\sigma_{33}| \frac{1}{3} \sqrt{3/2} \sqrt{1^2 + 1^2 + 2^2} = |\sigma_{33}|, \quad (2.437)$$

and the time derivative of the creep strains

$$\frac{\partial \boldsymbol{\epsilon}^{cr}}{\partial t} = \frac{N(T_1)}{2} \sigma_{33}^5 \begin{pmatrix} -1 & 0 & 0 \\ 0 & -1 & 0 \\ 0 & 0 & 2 \end{pmatrix}. \quad (2.438)$$

The entire domain is initially free of creep strains. Hence, integrating with respect to time  $t$  the creep strains become

$$\epsilon^{cr} = \frac{N(T_1)}{2} \begin{pmatrix} -1 & 0 & 0 \\ 0 & -1 & 0 \\ 0 & 0 & 2 \end{pmatrix} \int_0^t \sigma_{33}^5 dt. \quad (2.439)$$

Due to the simulation setup the thermal strains read

$$\epsilon^{th} = \alpha(T_1 - T_0) \begin{pmatrix} 1 & 0 & 0 \\ 0 & 1 & 0 \\ 0 & 0 & 1 \end{pmatrix}, \quad (2.440)$$

and the elastic strains are obtained from the stress  $\sigma$  via Hooke's law.

$$\epsilon^{el} = \frac{\sigma_{33}}{E} \begin{pmatrix} -\nu & 0 & 0 \\ 0 & -\nu & 0 \\ 0 & 0 & 1 \end{pmatrix}. \quad (2.441)$$

The total strains in terms of  $\sigma_{33}$  and the displacements ( $u_x, u_y, u_z$ ) read

$$\begin{aligned} \epsilon^{tot} = \epsilon^{th} + \epsilon^{el} + \epsilon^{cr} &= \begin{pmatrix} \partial u_x / \partial x & 0 & 0 \\ 0 & \partial u_y / \partial y & 0 \\ 0 & 0 & \partial u_z / \partial z \end{pmatrix} \\ &= \alpha(T_1 - T_0) \begin{pmatrix} 1 & 0 & 0 \\ 0 & 1 & 0 \\ 0 & 0 & 1 \end{pmatrix} \\ &\quad + \frac{\sigma_{33}}{E} \begin{pmatrix} -\nu & 0 & 0 \\ 0 & -\nu & 0 \\ 0 & 0 & 1 \end{pmatrix} \\ &\quad + \frac{N(T_1)}{2} \begin{pmatrix} -1 & 0 & 0 \\ 0 & -1 & 0 \\ 0 & 0 & 2 \end{pmatrix} \cdot \int_0^t \sigma_{33}^5 dt. \end{aligned} \quad (2.442)$$

Due to the simulation setup

$$\epsilon_{33}^{tot} = \frac{\partial u_z}{\partial z} = 0 \quad (2.443)$$

is the specified zero strain along the z-axis. Then

$$-\alpha(T_1 - T_0) = \frac{1}{E} \sigma_{33} + N(T_1) \int_0^t \sigma_{33}^5 dt. \quad (2.444)$$

This integral equation is transformed into the ordinary differential equation

$$0 = \frac{1}{E} \frac{d\sigma_{33}}{dt} + N(T_1) \sigma_{33}^5. \quad (2.445)$$

Separation of variables and integration yields

$$\sigma_{33}(t) = \frac{-E\alpha(T_1 - T_0)}{\sqrt[4]{4E^5[\alpha(T_1 - T_0)]^4 N(T_1) t + 1}}, \quad (2.446)$$

and the strains  $\partial u_x/\partial x$  and  $\partial u_y/\partial y$  are obtained in terms of  $\sigma_{33}(t)$

$$\begin{aligned} \epsilon_{11}^{tot}(t) &= \frac{\partial u_x}{\partial x} = \frac{3}{2}\alpha(T_1 - T_0) + \frac{1 - 2\nu}{2E}\sigma_{33}(t), \\ \epsilon_{22}^{tot}(t) &= \frac{\partial u_y}{\partial y} = \frac{3}{2}\alpha(T_1 - T_0) + \frac{1 - 2\nu}{2E}\sigma_{33}(t). \end{aligned} \quad (2.447)$$

Integrating the strains with respect to the specified fixities yields the displacement vector  $(u_x, u_y, u_z)$  in terms of  $\sigma_{33}(t)$  derived above

$$\begin{aligned} u_x(x, t) &= x \left[ \frac{3}{2}\alpha(T_1 - T_0) + \frac{1 - 2\nu}{2E}\sigma_{33}(t) \right], \\ u_y(y, t) &= y \left[ \frac{3}{2}\alpha(T_1 - T_0) + \frac{1 - 2\nu}{2E}\sigma_{33}(t) \right], \\ u_z(z, t) &= 0. \end{aligned} \quad (2.448)$$

## 2.9 Thermo-Hydro-Mechanical Coupling

Both, the presence of a liquid pressure as well as temperature changes affect the mechanical behaviour of the porous matrix; we present a steady-state and a transient problem. The underlying theory may be found in the references cited above.

### 2.9.1 A Permeable Elastic Cuboid Deforms Due to Gravity, Internal Liquid Pressure, and Instant Temperature Change

The domain is a cuboid of height  $H = 30$  m and edges parallel to the x-y-z coordinate axes. It is discretized by an irregular mesh of hexahedral elements. The cuboid is represented by four groups of elastic materials, where each has been assigned density  $\rho_s = 2038.736$  kg/m<sup>3</sup>, Poisson's ratio  $\nu = 0.25$ , Young's modulus  $E = 10,000$  MPa, thermal expansion  $\alpha = 3 \times 10^{-6}$  1/K, zero heat capacity, zero porosity, and Biot number equal one. Liquid density is  $\rho_l = 1019.368$  kg/m<sup>3</sup>, gravity is applied in negative z-direction,  $g = 9.81$  m/s<sup>2</sup> is the magnitude of gravity. Zero pressure is applied at the top face  $z = H$ . This face is free, all other faces are sliding planes. The simulation starts from the initial temperature  $T_0 = 0^\circ\text{C}$  and comprises one time step applying an instant temperature increase to  $T_1 = 2.5^\circ\text{C}$  throughout the entire

domain. The simulation evaluates the pressure distribution, the temperature, and the mechanical load.

The formal solution proceeds in three steps, first to solve for the temperature, next to evaluate the pressure distribution  $p(z)$ , and finally to determine stresses, strains and displacements. However, due to the setup the temperature change has constant value  $T_1 - T_0$  throughout the entire domain, and we will focus on the hydromechanical aspects of the problem.

The simulation setup employs a prescribed zero pressure at the top ( $z = H$ ), therefore the pressure distribution is hydrostatic, does not depend on the coordinates  $x$  and  $y$  and is given by

$$p(z) = \rho_l g (H - z). \quad (2.449)$$

For the closed form solution of the mechanical problem let  $\boldsymbol{\sigma}$  denote the stress tensor and  $\mathbf{I}$  the unit tensor. Employing Biot's simplified theory (i.e. Biot number equal one) the equation of mechanical equilibrium reads

$$0 = \nabla \cdot (\boldsymbol{\sigma} - p \mathbf{I}) - (0, 0, \rho_s g). \quad (2.450)$$

It is satisfied by zero shear, if pressure  $p$  and the horizontal stresses  $\sigma_{11}$  and  $\sigma_{22}$  are functions of the vertical coordinate  $z$  only and the vertical stress  $\sigma_{33}$  satisfies

$$\frac{d\sigma_{33}}{dz} = \rho_s g + \frac{dp}{dz} = (\rho_s - \rho_l) g. \quad (2.451)$$

The face  $z = H$  is free, hence, integration gives

$$\sigma_{33} = (\rho_s - \rho_l) (-g) (H - z). \quad (2.452)$$

Due to the simulation setup there is no horizontal displacement anywhere, hence, for the horizontal strains

$$\epsilon_{11} = \epsilon_{22} = 0. \quad (2.453)$$

Then, with principal axes equal to coordinate axes, the constitutive equations give

$$\begin{aligned} \epsilon_{11} - \alpha(T_1 - T_0) &= \frac{1}{E}[\sigma_{11} - \nu(\sigma_{22} + \sigma_{33})], \\ \epsilon_{22} - \alpha(T_1 - T_0) &= \frac{1}{E}[\sigma_{22} - \nu(\sigma_{11} + \sigma_{33})], \\ \epsilon_{33} - \alpha(T_1 - T_0) &= \frac{1}{E}[\sigma_{33} - \nu(\sigma_{11} + \sigma_{22})]. \end{aligned} \quad (2.454)$$

Solving for  $\sigma_{11}$ ,  $\sigma_{22}$ , and the vertical strain  $\epsilon_{33}$  yields

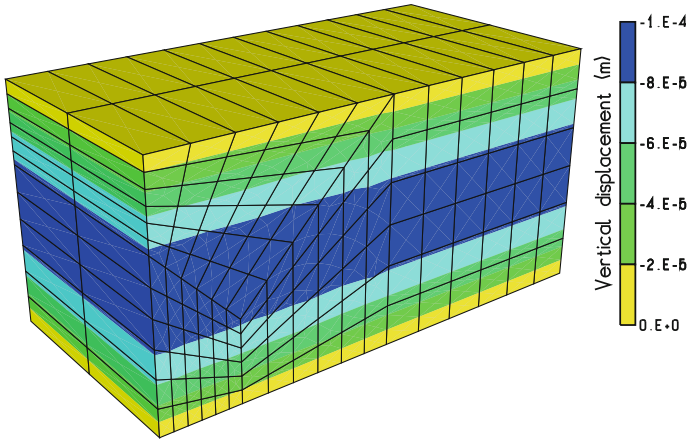


Fig. 2.27 Vertical displacements

$$\sigma_{11} = \sigma_{22} = -\alpha \frac{E}{1-\nu} (T_1 - T_0) + \frac{\nu}{1-\nu} (\rho_s - \rho_l)(-g)(H - z), \quad (2.455)$$

$$\epsilon_{33} = \frac{1+\nu}{1-\nu} \alpha (T_1 - T_0) + \left(1 - \frac{2\nu^2}{1-\nu}\right) \frac{1}{E} (\rho_s - \rho_l)(-g)(H - z)$$

in terms of the vertical coordinate. Integrating the strains with respect to the fixities at the sliding planes yields the displacement vector  $(u_x, u_y, u_z)$  (Fig. 2.27).

$$\begin{aligned} u_x &= u_y = 0, \\ u_z(z) &= \frac{1+\nu}{1-\nu} \alpha (T_1 - T_0) z \\ &\quad + \left(1 - \frac{2\nu^2}{1-\nu}\right) \frac{1}{E} (\rho_s - \rho_l)(-g) \left(zH - \frac{1}{2}z^2\right). \end{aligned} \quad (2.456)$$

### 2.9.2 A Permeable Elastic Beam Deforms Due to Cooling Liquid Injection

The domain is a rectangular beam of length  $L = 10\text{m}$  extending along the positive  $x$ -axis. It is discretized by  $100 \times 1 \times 1$  equally sized hexahedral elements. The solid material has been selected elastic with Poisson's ratio  $\nu = 0.25$ , Young's modulus  $E = 5 \times 10^9 \text{Pa}$ , thermal expansion  $\alpha = 1 \times 10^{-6} \text{1/K}$ , and Biot number equal one. An isotropic permeability  $k = 10^{-11} \text{m}^2$  and porosity  $\phi = 0.1$  is assumed for the material. The liquid is incompressible and has viscosity  $\mu = 1 \text{mPa} \cdot \text{s}$ . Densities, heat capacities, and thermal conductivities of liquid and solid grain are given below (Table 2.4), gravity has explicitly been neglected.

**Table 2.4** Example overview

	Liquid	Solid
Density	$\rho_l = 1000 \text{ kg/m}^3$	$\rho_s = 2000 \text{ kg/m}^3$
Specific heat capacity	$c_l = 1100 \text{ J/(kg} \cdot \text{K)}$	$c_s = 250 \text{ J/(kg} \cdot \text{K)}$
Thermal conductivity	$\lambda_l = 10 \text{ W/(m} \cdot \text{K)}$	$\lambda_s = 50 \text{ W/(m} \cdot \text{K)}$

The face  $x = L$  is free, all other faces of the beam are sliding planes. Pressure  $p_0 = 10^5 \text{ Pa}$  at the liquid inlet ( $x = 0 \text{ m}$ ) and zero pressure the liquid outlet ( $x = L$ ) generate steady-state 1D flow along the  $x$ -axis. At the liquid inlet a constant temperature  $T_0 = -10^\circ\text{C}$  is specified for times  $t > 0$ . Starting from zero initial temperature the simulation evaluates the transient temperature distribution  $T(x, t)$  as well as stresses, strains, and displacements with output after 10,000 and 20,000 s.

The formal solution proceeds in three steps, first to solve for pressure  $p(x)$  and specific discharge  $q$ , next to evaluate the temperature distribution  $T(x, t)$ , and finally to determine stresses, strains, and displacements (Figs. 2.28 and 2.29).

For incompressible liquids Darcy’s law and continuity equation yield the Laplace equation as the governing equation describing the steady-state pressure distribution. It reads

$$\frac{d^2 p}{dx^2} = 0 \tag{2.457}$$

for 1D flow along the  $x$ -axis, hence, the pressure is given by

$$p(x) = p_0 \left(1 - \frac{x}{L}\right), \tag{2.458}$$

and the specific discharge  $q$  is obtained by Darcy’s law

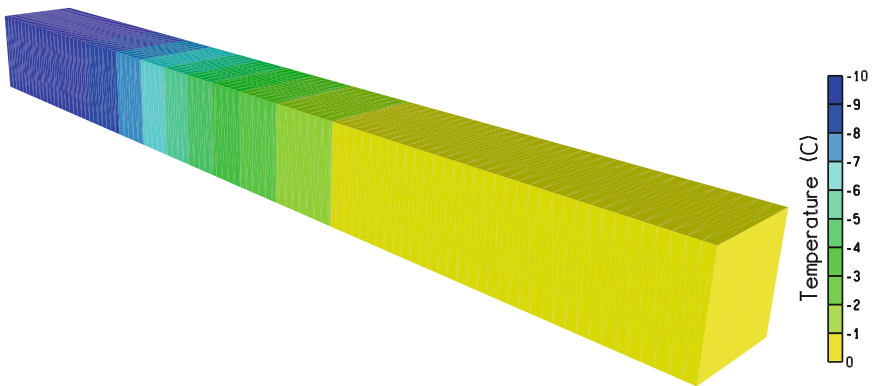


**Fig. 2.28** Temperature distribution after 20,000 s

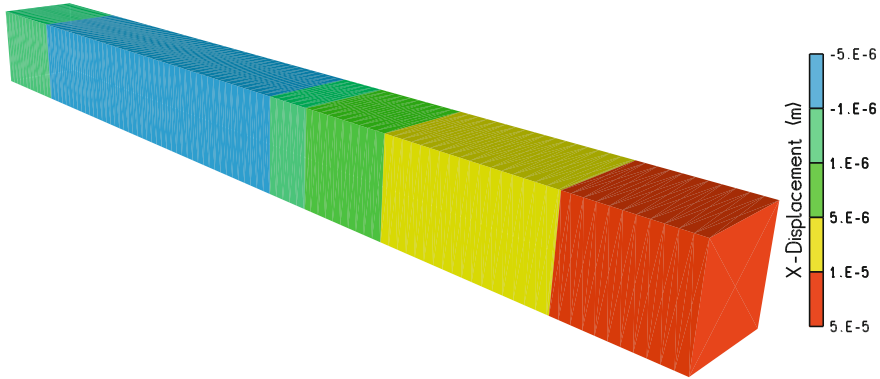


**Fig. 2.29** X-Displacements after 20,000 s

$$q = \frac{k}{\mu} \frac{p_0}{L}. \quad (2.459)$$

We will next focus on the closed form solution of the heat transport problem. Based on the setup of the present example the heat transport equation reads

$$(\phi\rho_l c_l + (1-\phi)\rho_s c_s) \frac{\partial T}{\partial t} + (\phi\rho_l c_l) \frac{q}{\phi} \frac{\partial T}{\partial x} = (\phi\lambda_l + (1-\phi)\lambda_s) \frac{\partial^2 T}{\partial x^2}. \quad (2.460)$$

Introducing the notation

$$w = \frac{\phi\rho_l c_l}{\phi\rho_l c_l + (1-\phi)\rho_s c_s} \frac{q}{\phi}, \quad (2.461)$$

$$\chi = \frac{\phi\lambda_l + (1-\phi)\lambda_s}{\phi\rho_l c_l + (1-\phi)\rho_s c_s},$$

the heat transport equation becomes

$$\frac{\partial T}{\partial t} + w \frac{\partial T}{\partial x} = \chi \frac{\partial^2 T}{\partial x^2}. \quad (2.462)$$

Due to free outflow at  $x = L$  the formal problem is to determine the solution  $T(x, t)$  of the above heat transport equation subject to the initial condition

$$T(x, 0) = 0 \quad \text{for } x > 0, \quad (2.463)$$

and the boundary conditions

$$\begin{aligned} T(0, t) &= T_0 \quad \text{for } t > 0, \\ \lim_{x \rightarrow \infty} T(x, t) &= 0 \quad \text{for } t > 0. \end{aligned} \quad (2.464)$$

Applying the Laplace transform with respect to  $t$  yields the ordinary differential equation

$$\chi \bar{T}'' - w \bar{T}' - s \bar{T} = 0, \quad (2.465)$$

where  $\bar{T}$  is the transform of  $T$ ,  $s$  is the transformation parameter, and the prime denotes the derivative with respect to  $x$ . This equation has to be solved with respect to the transformed boundary conditions. This yields

$$\bar{T}(x, s) = \frac{T_0}{s} \exp \left[ x \left( \frac{w}{2\chi} - \sqrt{\left(\frac{w}{2\chi}\right)^2 + \frac{s}{\chi}} \right) \right]. \quad (2.466)$$

The temperature distribution  $T(x, t)$  may now be obtained from their transform, Churchill [7] outlines how to proceed with the aid of operational calculus.

For the mechanical aspects of the problem we assume that the temperature distribution  $T(x, t)$  is already known from the above. Let  $\sigma$  denote the stress tensor and  $\mathbf{I}$  the unit tensor. Employing Biot's simplified theory (i.e. Biot number equal one) the equation of mechanical equilibrium reads

$$0 = \nabla \cdot (\sigma - p \mathbf{I}). \quad (2.467)$$

It is satisfied by zero shear, if the stresses  $\sigma_{22}$  and  $\sigma_{33}$  are functions of  $x$  only and the stress  $\sigma_{11}$  satisfies

$$\frac{\partial}{\partial x} (\sigma_{11} - p) = 0. \quad (2.468)$$

The face  $x = L$  is free of load, hence, integration gives

$$\sigma_{11} = p(x) = p_0 \left(1 - \frac{x}{L}\right). \quad (2.469)$$

With principal axes equal to coordinate axes, the constitutive equations give for the strains

$$\begin{aligned} \epsilon_{11} - \alpha T(x, t) &= \frac{1}{E} [\sigma_{11} - \nu(\sigma_{22} + \sigma_{33})], \\ \epsilon_{22} - \alpha T(x, t) &= \frac{1}{E} [\sigma_{22} - \nu(\sigma_{11} + \sigma_{33})], \\ \epsilon_{33} - \alpha T(x, t) &= \frac{1}{E} [\sigma_{33} - \nu(\sigma_{11} + \sigma_{22})]. \end{aligned} \quad (2.470)$$

By the problem setup there is

$$\epsilon_{22} = \epsilon_{33} = 0 \quad (2.471)$$

due to the y- and z-fixities along the front, rear, top, and bottom of the beam. In terms of pressure  $p(x)$  and temperature  $T(x, t)$  the remaining non-zero stresses and strains become

$$\begin{aligned} \sigma_{22} = \sigma_{33} &= \frac{1}{1-\nu} [\nu p(x) - \alpha ET(x, t)], \\ \epsilon_{11} &= \left(1 - \frac{2\nu^2}{1-\nu}\right) \frac{p(x)}{E} + \frac{1+\nu}{1-\nu} \alpha T(x, t). \end{aligned} \tag{2.472}$$

Integrating the strains with respect to the fixities at the sliding planes yields the displacement vector  $(u_x, u_y, u_z)$ . The only non-zero displacement  $u_x(x, t)$  becomes

$$u_x(x, t) = \left(1 - \frac{2\nu^2}{1-\nu}\right) \frac{p_0}{E} \left(x - \frac{x^2}{2L}\right) + \frac{1+\nu}{1-\nu} \alpha \int_0^x T(x', t) dx'. \tag{2.473}$$

The already known Laplace transform  $\bar{T}(x, s)$  of the temperature serves to evaluate the last integral over the temperature distribution. We have for the transformed integral

$$\begin{aligned} L \left\{ \int_0^x T(x', t) dx' \right\} &= \int_0^x \bar{T}(x', s) dx' \\ &= \frac{T_0}{s} \frac{\exp \left\{ x \left( \frac{w}{2\chi} - \sqrt{\left(\frac{w}{2\chi}\right)^2 + \frac{s}{\chi}} \right) \right\} - 1}{\frac{w}{2\chi} - \sqrt{\left(\frac{w}{2\chi}\right)^2 + \frac{s}{\chi}}}, \end{aligned} \tag{2.474}$$

and the last expression, as well as the Laplace transform of the temperature itself, are well suited for numerical inversion. The numerical inversion scheme outlined in the introductory section may easily be applied to give the required values of the temperature  $T(x, t)$  and the entire mechanical load (Fig. 2.29).

## References

1. K. S. Crumb. Numerical inversion of laplace transforms using a fourier series approximation. *J. Asso. Comp. Mech.*, 23(1):89–96, 1976.
2. J. R. MacDonald. Accelerated convergence, divergence, iteration, extrapolation, and curve fitting. *J. Appl. Phys.*, 10:3034–3041, 1964.
3. H. S. Carslaw and J. C. Jaeger. *Conduction of heat in solids*. Oxford University Press, London, 2nd edition, 1959.
4. W. Gautschi. Repeated integrals of the coerror function. *ACM Trans. Math. Software*, 3:301–302, 1977.
5. R. A. Freeze and J. A. Cherry. *Groundwater*. Prentice-Hall, Englewood Cliffs, New Jersey, 1979.
6. J. C. Jaeger and N. G. W. Cook. *Fundamentals of Rock Mechanics*. Chapman, London, 3rd edition, 1971.
7. R. V. Churchill. *Operational Mathematics*. McGraw-Hill Book Company, New York, 2nd edition, 1958.

8. F. J. Leij and J. H. Dane. Analytical solutions of the one-dimensional advection equation and two- or three-dimensional dispersion equation. *Water Resources Research*, 26(7):1475–1482, 1990.
9. M. Abramowitz and I. A. Stegun. *Handbook of Mathematical Functions*. Dover, New York, 10th edition, 1972.
10. J. Bear. *Dynamics of Fluids in Porous Media*. Elsevier, New York, 1972.
11. M. A. Biot. General theory of three-dimensional consolidation. *J. Appl. Phys.*, 12:155–164, 1941.
12. O. Kolditz, H. Shao, U.-J. Goerke, and W. Wang (eds). *Thermo-hydro-mechanical-chemical processes in fractured porous media*. Springer, Heidelberg, 2012.

# **Part II**

## **Single Processes**

# Chapter 3

## Groundwater Flow—Theis’ Revisited

Wenkui He

### 3.1 Problem Definition

Theis’ Problem describes the transient lowering of the water table caused by a pumping well. In this section, Theis’ Problem is simulated for a homogeneous, isotropic, confined aquifer numerically in 1.5D, 2D, 2.5D and 3D. The parameters for the simulations can be found in Table 3.1. In all the four cases, different processes i.e. groundwater flow processes and liquid flow processes are applied for the simulation in order to evaluate the plausibility of the model approaches GROUNDWATER\_FLOW and LIQUID\_FLOW in OGS. The governing equation for groundwater flow process in a confined aquifer is Eq. (3.1) with the primary variable hydraulic head, whereas that for liquid flow process is Eq. (3.2) with pressure as its primary variable.

$$S_s \frac{\partial h}{\partial t} = \nabla \cdot (K \cdot \nabla h) + q \quad (3.1)$$

$$\frac{S_s}{\rho g} \frac{\partial p}{\partial t} = \nabla \cdot \left( \frac{\kappa}{\mu} \cdot \nabla p \right) + q \quad (3.2)$$

### 3.2 Theis’ 1.5D and 2.5D

For the simulation of Theis’ problem in 1.5D and 2.5D, axisymmetric coordinate system is applied. For 1.5D a one dimensional line mesh is applied, whereas for 2.5D a two dimensional mesh with a width of 1 m is applied (see Fig. 3.1a, a scale

---

W. He (✉)  
Helmholtz Centre for Environmental Research UFZ, Permoserstr. 15,  
04318 Leipzig, Germany  
e-mail: Wenkui.He@ufz.de

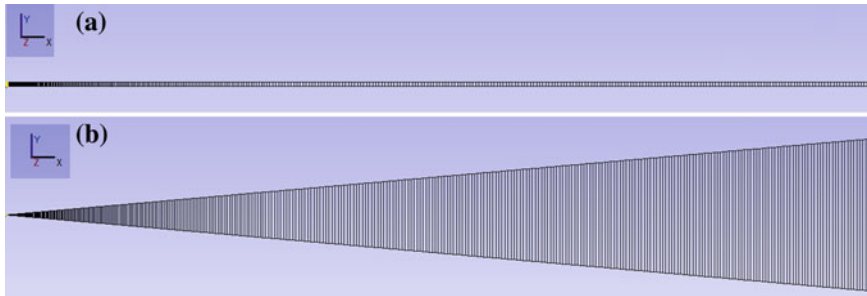


**Fig. 3.1** The mesh implemented. **a** 2D Mesh for Theis' 2.5D; **b** 2D Mesh for Theis' 2D

factor of 5 is taken for the y-direction). In the case of two dimensional groundwater flow process, Eq. (3.1) is transformed into Eq. (3.3).

$$S_s \frac{\partial h}{\partial t} = \frac{1}{r} \frac{\partial}{\partial r} (K_r r \frac{\partial h}{\partial r}) + \frac{\partial}{\partial z} (K_z \frac{\partial h}{\partial z}) + q \tag{3.3}$$

A hydraulic head of 0 m is given for the whole domain as the initial condition for the numerical simulations. Since the aquifer should be infinite in radial extent in order to fulfill the assumption required by the Theis' solutions, a relatively huge study area length of 1,000 m is applied. The hydraulic head at the end of radial extent is set as 0 m as the boundary condition.

Since discharge is evenly distributed around the whole surface area of the well (which can be seen as a cylinder), the source term (with the distribution type `CONSTANT_NEUMANN`) applied for Theis' 2.5D is calculated as follows ('1' in the formula represents the length of the 2D mesh in y-direction, i.e. 1 m):

$$q = \frac{Q}{2\pi r_w \cdot 1} = -7.393E - 3(\text{m} \cdot \text{s}^{-1})$$

In the case of Theis' 1.5D, the whole well is abstractly represented by a single point, hence both the radius and the depth of the well are regarded as 1 m. The discharge

**Table 3.1** Parameters and their values applied for Theis' problem

Parameter	Symbol	Value	Unit
Pumping rate	Q	1.4158E-2	m <sup>3</sup> /s
Hydraulic conductivity	K	9.2903E-4	m/s
Intrinsic permeability	κ	1.2391E-10	m <sup>2</sup>
Storage coefficient	S	1E-3	–
Specific storage	S <sub>s</sub>	1E-3	1/m
Well radius	r <sub>w</sub>	0.3048	m
Study area length	r <sub>b</sub>	1,000	m

**Table 3.2** The density and dynamic viscosity of water at 10 °C

Parameter	Symbol	Value	Unit
Density of water (10 °C)	$\rho$	999.7026	$\text{Kg}\cdot\text{m}^{-3}$
Viscosity of water (10 °C)	$\mu$	1.308E-03	$\text{Pa}\cdot\text{s}$

rate is thereby calculated by:

$$q = \frac{Q}{2\pi \cdot 1 \cdot 1} = -2.253E - 3(\text{m} \cdot \text{s}^{-1})$$

It is worth to mention that in the model approach GROUNDWATER\_FLOW, the value implemented for the key word PERMEABILITY\_TENSOR in OGS should be the value of hydraulic conductivity, i.e.

$$K = 9.2903E - 4(\text{m} \cdot \text{s}^{-1})$$

whereas the value implemented for the key word STORAGE should be the specific storage, i.e.

$$S_s = 1E - 3(\text{m}^{-1})$$

However, in the model approach LIQUID\_FLOW, the value used for the key word PERMEABILITY\_TENSOR is the intrinsic permeability, which is calculated as follows by using the value of hydraulic conductivity as well as the density and dynamic viscosity of water at 10 °C (see Table 3.2).

$$\kappa = \frac{K\mu}{\rho g} = 1.2391E - 10(\text{m}^2)$$

Whereas the value implemented for the key word STORAGE should be the whole parameter term on the left hand side of Eq. (3.2), i.e.

$$\frac{S_s}{\rho g} = 1.02E - 7(\text{Pa}^{-1})$$

Additionally, in the model approach LIQUID\_FLOW the influence of gravity is considered. Hence the geometries and meshes for both Theis' 1.5D and Theis' 2D are built in x-y plane instead of x-z plane to avoid the influence of gravity.

### 3.3 Theis' 2D

The governing equation system for groundwater flow process in 2D is

$$S \frac{\partial h}{\partial t} = T \left( \frac{\partial^2 h}{\partial x^2} + \frac{\partial^2 h}{\partial y^2} \right) + q \quad (3.4)$$

**Table 3.3** Summary of the model concepts for Theis' problem

Dimension	1.5D	2D	2.5D	3D
Geometry				
Concept	Radial symmetry	Axisymmetry		
Key word	\$AXISYMMETRY	–	\$AXISYMMETRY	–

or

$$S_s \frac{\partial h}{\partial t} = K \left( \frac{\partial^2 h}{\partial x^2} + \frac{\partial^2 h}{\partial y^2} \right) + q \quad (3.5)$$

In order to compare the simulation results of 2D approach with other approaches, the same parameter values, initial conditions and boundary conditions are applied for the Theis' 2D. A cake-shaped triangle geometry is chosen for the 2D approach (see Fig. 3.1b), in which the pumping well is set at the left vertex of the triangle. Since the angle of the left vertex is set as  $10^\circ$ , the source term is calculated as follows:

$$Q_1 = \frac{10}{360} Q = 3.9329E - 4 (\text{m}^3 \cdot \text{s}^{-1})$$

### 3.4 Theis' 3D

Based on the 2D mesh shown in Fig. 3.1b, a 3D mesh is generated by extruding the mesh elements into 3D. The 3D mesh is consist of one layer with a thickness of 1 m. Similarly, the parameters used in Theis' 2D are applied for Theis' 3D. Since the model approach LIQUID\_FLOW considers the gravity of the liquid, there is a pressure difference between the upper surface and the bottom surface. Hence the average value of the upper surface and the bottom surface is taken to compare with the results from Theis' 1.5D, Theis' 2D and Theis' 2.5D. A summary of the model concepts, implemented geometries and their related key words in OGS are listed in Table 3.3.

### 3.5 Results

All the simulations are performed for a duration of 10 days with varying time step lengths ranging from  $10E-5$  to 0.9 d. The time series of the hydraulic head drawdown at a distance of 9.639 m from the well are extracted from the simulation results of all the eight cases, and are shown in Fig. 3.2 together with the analytical solutions. The calculation of the analytical solutions can be found in the work of Srivastava et al. [1]. 'GF' in the graphic represents the simulations with model

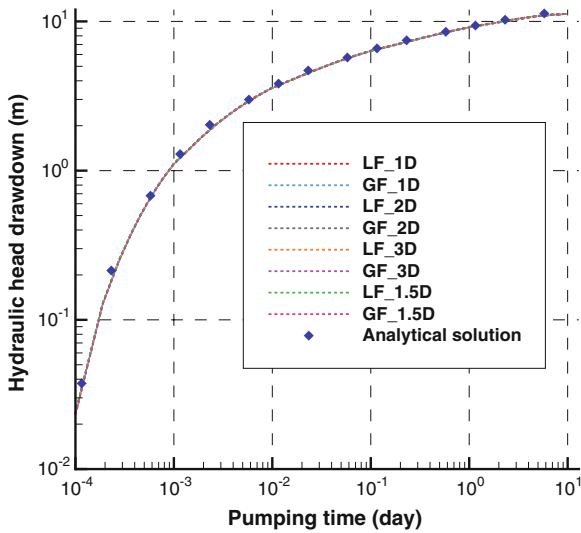


Fig. 3.2 Calculated drawdowns at a distance of 9.639 m from the well

approach GROUNDWATER\_FLOW, whereas ‘LF’ represents LIQUID\_FLOW. We can find that all the numerical results obtained with different model approaches are coincident with each other and agree well with the analytical solutions. Additionally, the distribution of the hydraulic head at the end of the simulation time for the 1D as well as 3D mesh are demonstrated in Figs. 3.3 and 3.4, respectively.

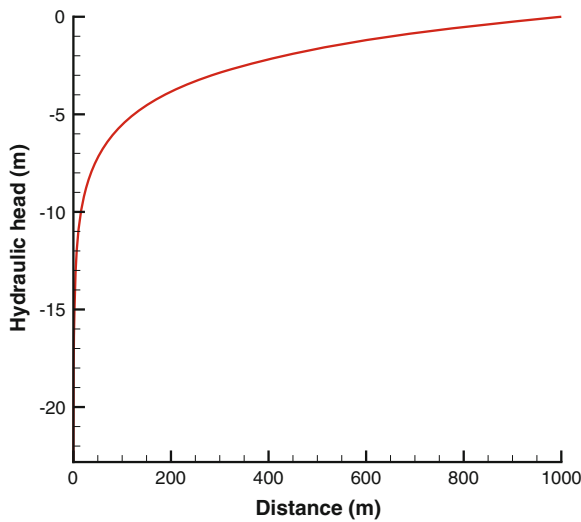
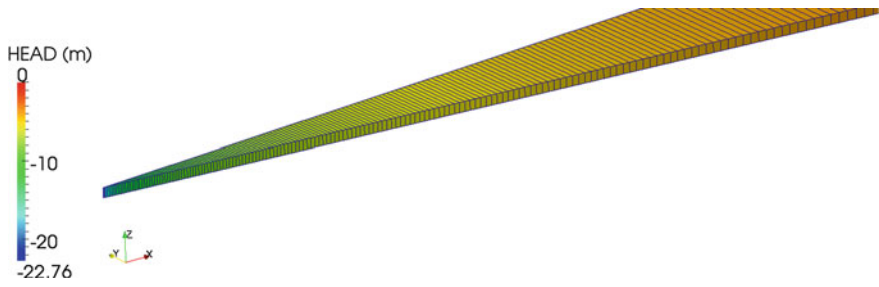


Fig. 3.3 Distribution of the hydraulic head at the end of the simulation time (1D)



**Fig. 3.4** Distribution of the hydraulic head at the end of the simulation time (3D)

In order to show the 3D mesh in Fig. 3.4 clearly, a scale factor of 5 is taken for the z-direction.

## Reference

1. R. Srivastava and A. Guzman-Guzman. Practical approximations of the well function. *Ground Water*, 36(5):844–848, 1998.

# Chapter 4

## Richards Flow

Thomas Kalbacher, Xi Chen, Ying Dai, Jürgen Hesser, Xuerui Wang and Wenqing Wang

Introduced by Richards [1], the Richards' equation is used to mathematically describe water movement in the unsaturated zone. Theoretically, the equation is also a sort of simplification of the two-phase flow equations of water-air processes in porous media under the constant gas pressure condition. By considering the water pressure as the primary variable, the equation takes form

$$-\phi \rho_w \frac{\partial S}{\partial p_c} \frac{\partial p_w}{\partial t} + \nabla \cdot \left( \rho_w \frac{k_{rel} \mathbf{k}}{\mu_w} (\nabla p_w - \rho_w \mathbf{g}) \right) = Q_w \quad (4.1)$$

where  $\phi$  is porosity,  $t$  is time,  $\rho_w$  is the liquid density,  $\mu_w$  is the liquid viscosity,  $p_c$  is the capillary pressure with  $p_c = -p_w$ ,  $p_w$  is the water pressure,  $S$  is the water saturation,  $\mathbf{g}$  is gravity acceleration vector,  $Q_w$  is the source term,  $k_{rel}$  is the relative permeability and  $\mathbf{k}$  is the intrinsic permeability which is related to the hydraulic conductivity  $\mathbf{K}$  with

$$\mathbf{k} = \frac{\mu_w}{\rho_w \mathbf{g}} \mathbf{K} \quad (4.2)$$

In this chapter, the finite element solution of the Richards' equations is compared with the semi-analytical one.

### 4.1 Comparison with Differential Transform Method (DTM)

Xi Chen, Wenqing Wang and Ying Dai

The concept of differential transformation method was first proposed by Zhou [4], which uses Taylor series for the solution of differential equations in the form of a

---

T. Kalbacher (✉) · X. Chen · Y. Dai · J. Hesser · X. Wang · W. Wang  
Helmholtz Centre for Environmental Research UFZ, Permoserstr. 15,  
D-04318 Leipzig, Germany  
e-mail: Thomas.Kalbacher@ufz.de

polynomial. For an arbitrary  $f(x)$ , it can be expanded in Talyor series at a specific point, say  $x_0$  as

$$f(x) = \sum_{k=0}^{\infty} \frac{(x - x_0)^k}{k!} \left[ \frac{d^k f}{d x^k} \right]_{x=x_0} \tag{4.3}$$

The differential transform of  $f(x)$  is defined as

$$F(x) = \left[ \frac{d^k f}{d x^k} \right]_{x=x_0} \tag{4.4}$$

Consequently, its inverse transform is given as

$$f(x) = \sum_{k=0}^{\infty} \frac{(x - x_0)^k}{k!} F(x) \tag{4.5}$$

Table 4.1 lists the basic properties of the differential transform method (DTM). Herewith, we apply the DTM to the Richards’ equation with van Genuchten [2] water retention model to derive a semi-analytic solution. For this purpose, we consider the saturation as the primary variable, and the Richards’ equation can be written as

$$\frac{\partial S}{\partial t} - \nabla \cdot \left( \rho_w \frac{k_{rel} \mathbf{k}}{\mu_w} (\nabla p_c + \rho_w \mathbf{g}) \right) = Q_w \tag{4.6}$$

With the Mualem–van Genuchten parameterization [2, 3] the capillary pressure can be described as

$$p_c = \frac{\rho_w g}{\alpha} \left[ S_{eff}^{-1/m} - 1 \right]^{1/n} \tag{4.7}$$

where  $\alpha$  [1/m] is a conceptualized parameter related to the air entry pressure,  $n$  is a dimensionless pore size distribution index and  $m = 1 - (1/n)$ . These parameters are usually used to fit the saturation dependent curves of capillary pressure and hydraulic

**Table 4.1** Properties of DTM

Original function	Transformed function
$y(x) = g(x) \pm h(x)$	$Y(k) = G(k) \pm H(k)$
$y(x) = ag(x)$	$Y(k) = aG(k)$
$y(x) = \frac{d^m g(x)}{d x^m}$	$Y(k) = \frac{(k + m)!}{k!} G(k + m)$
$y(x) = 1$	$Y(k) = \delta(k)$
$y(x) = x$	$Y(k) = \delta(k - 1)$
$y(x) = x^m$	$Y(k) = \delta(k - m)$
$y(x) = g(x) h(x)$	$Y(k) = \sum_{m=0}^k H(m)G(k - m)$

conductivity to experimental data. The relative permeability can be given as

$$k_{rel} = S_{eff}^{1/2} \left[ 1 - (1 - S_{eff}^{1/m})^m \right]^2 \tag{4.8}$$

The effective saturation is

$$S_{eff} = \frac{S - S_r}{S_{max} - S_r} \tag{4.9}$$

with  $S_{max}$  and  $S_r$  as the maximum and residual saturation.

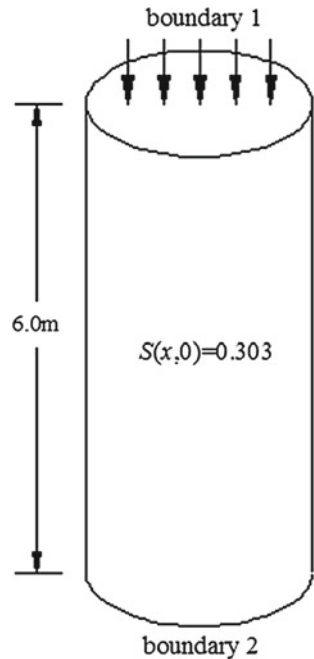
The example is a one-dimensional infiltration problem based on an experiment conducted by Abeele et al. [5].

Figure 4.1 shows the setup of the problem. The domain is a 6 m long cylinder with a diameter of 3 m. A constant infiltration of  $2.314 \times 10^{-6}$  m/s is applied on the top of the domain, while on the bottom the saturation is assumed to be 0.33. The initial saturation is 0.33 too. The domain is assumed to have a homogeneous material distribution, and all material parameters are listed in Table 4.2.

Inspired by the concept presented in [6], we employ an intermediate variable  $\zeta$  for the variable of Eq. (4.3) to enhance the convergence of the Taylor series, which is

$$\zeta = \tanh(a(x - b + ct)) \tag{4.10}$$

**Fig. 4.1** Computational domain of the numerical model



**Table 4.2** Material properties

Symbol	Parameter	Value	Unit
$\phi$	Porosity	0.33	–
$k_s$	Saturated permeability	2.95e-13	m <sup>2</sup>
$S_r$	Residual water saturation	0.0	–
$S_{max}$	Maximum water saturation	1.0	–
$\alpha$	van Genuchten parameter	1.43	1/m
$n$	van Genuchten parameter	1.506	–

where  $a$ ,  $b$  and  $c$  are parameters to be determined by initial and boundary conditions. Consequently, the saturation function  $S(\zeta)$  is approximated by the Talyor series as

$$S(\zeta) = \sum_{k=0}^{\infty} \frac{(\zeta - \zeta_0)^k}{k!} \left[ \frac{d^k f(\zeta)}{d \zeta^k} \right]_{\zeta=\zeta_0} \quad (4.11)$$

where  $\zeta_0$  is the initial value. In this example, the first order of the DTM is adopted, which leads to an approximation of the saturation as

$$S(\zeta) = S(\zeta_0) + \bar{S}(0)(\zeta - \zeta_0) \quad (4.12)$$

Applying the initial condition, the boundary condition with a constant saturation of 0.33 at the bottom, and the infiltration boundary condition of 2.314e-6 m/s at the top to Eq.(4.12) with the intermediate variable defined in Eq.(4.10), we get three equations with three unknowns of  $a$ ,  $b$  and  $c$ . Solving the derived three equation, the parameters in Eq.(4.10) are obtained as

$$a = 19.8, b = 5.99, c = 2.314e - 6/(0.33(1 - 0.303)) \quad (4.13)$$

Finally, a semi-analytical solution to this example is derived by applying the obtained parameters:

$$S(x, t) = 0.303 + 0.697(\tanh(a(x - b + ct)) + 1)/2 \quad (4.14)$$

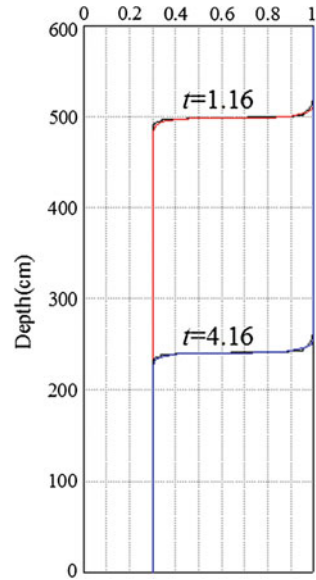
The solution is compared against the numerical result obtained by OGS (Fig. 4.2).

## 4.2 Undrained Heating

Xuerui Wang and Jürgen Hesser

The main purpose of this chapter is the numerical analysis of temperature effects on pore water pressure in unsaturated porous medium by consideration of coupled thermo-hydraulic (TH) processes using RICHARDS\_FLOW approach in OGS. Under thermal loading, the increase of temperature leads to anexpansion of pore

**Fig. 4.2** Comparison between OGS solution and semi-analytical solution (solid line represents the OGS solution)



fluids. Due to undrained condition this expansion can cause an increase of pore pressure as well as an increase of the degree of water saturation. Moreover, the increase of temperature can also lead to a decrease of fluid viscosity. Under undrained conditions, the thermal expansion, characterized by the thermal expansion coefficient is defined as:

$$\alpha_l = \frac{-1}{\rho_0} \left( \frac{\partial \rho_l}{\partial T} \right) \tag{4.15}$$

where  $\rho_0$  is initial liquid density,  $\rho_l$  is actual liquid density,  $T$  is temperature. The effect of the thermal expansion on pore pressure is considered as an additional term. This term is multiplied by the partial derivatives of temperature  $T$  with respect to time  $t$  in the Richards equation:

$$\phi \rho_w \frac{\partial S}{\partial p_c} \frac{\partial p_c}{\partial t} + \phi S \frac{\partial \rho_w}{\partial T} \frac{\partial T}{\partial t} + \nabla \cdot \left( \rho_w \frac{k_{rel} \mathbf{k}}{\mu_w} (\nabla p_w - \rho_w \mathbf{g}) \right) = Q_w \tag{4.16}$$

In order to evaluate the plausibility of using the RICHARDS\_FLOW model, three reference calculations of heating an undrained and saturated sample have been carried out. The first two reference calculations consider the same heating test. The only difference is that one is using RICHARDS\_FLOW, the other considers the LIQUID\_FLOW model. In the third reference calculation, the advection effects were neglected to compare the results with the analytical solution. Finally the simulation of an unsaturated heating test using the RICHARDS\_FLOW model was carried out.

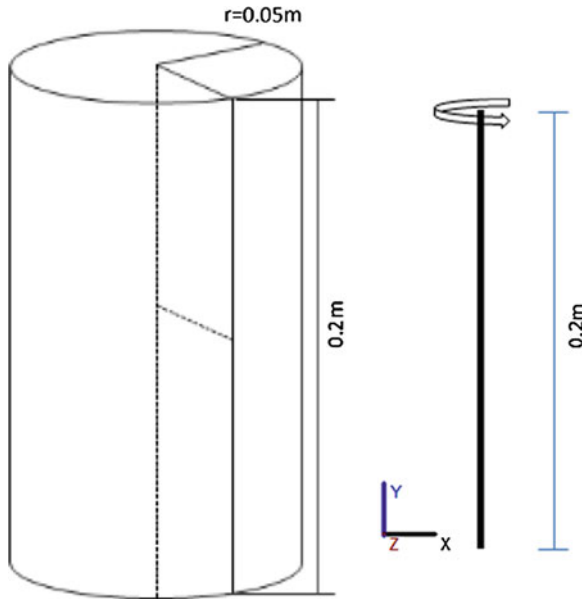


**Fig. 4.3** Geometry and dimension of the core sample (*left*) and the 1D calculation model (*right*)

### 4.2.1 Definition (1D)

In this example an undrained heating test on a cylindrical core sample (Fig. 4.3, left) is numerically simulated. Due to the axisymmetric situation and the assumption of homogeneous and isotropic material properties, a one-dimensional model

**Table 4.3** Model parameters

Symbol	Parameter	Value	Unit
<i>Porous medium</i>			
$\rho_s$	Density	2700.0	$\text{kg} \cdot \text{m}^{-3}$
$S_s$	Specific storage	$4.4 \cdot 10^{-10}$	$\text{Pa}^{-1}$
$k$	Permeability	$3.5 \cdot 10^{-20}$	$\text{m}^2 \cdot \text{s}^{-1}$
$\phi$	Porosity	14	%
$\alpha_s$	Thermal expansion's coefficient	$4.5 \cdot 10^{-5}$	$\text{K}^{-1}$
$\lambda_s$	Thermal conductivity	2.0	$\text{W} \cdot \text{m}^{-1} \cdot \text{K}^{-1}$
$c^s$	Specific heat capacity	800	$\text{J} \cdot \text{kg}^{-1} \cdot \text{K}^{-1}$
<i>Fluid</i>			
$\rho_l$	Density	991	$\text{kg} \cdot \text{m}^{-3}$
$c_l$	Specific heat capacity of water	4280	$\text{J} \cdot \text{kg}^{-1} \cdot \text{K}^{-1}$
$\lambda_l$	Thermal conductivity of water	0.6	$\text{W} \cdot \text{m}^{-1} \cdot \text{K}^{-1}$
$\nu$	Water viscosity	0.001	$\text{Pa} \cdot \text{s}$

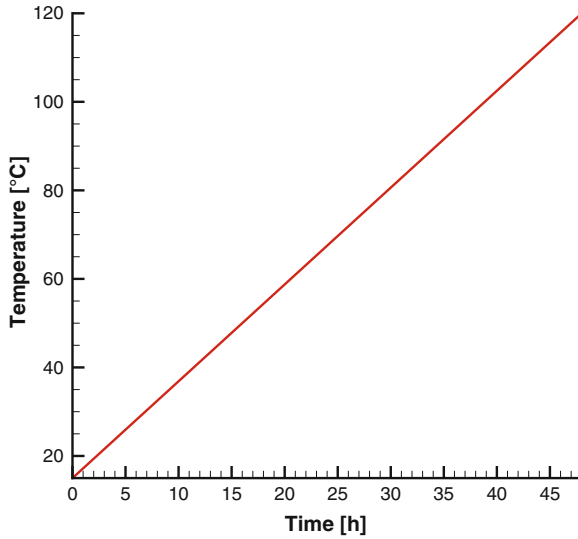


**Fig. 4.4** Temperature increase at the *bottom*

(Fig. 4.3, right) has been set up with 10 elements in the direction of the rotation axis. The model parameters are listed in Table 4.3. The initial temperature of the whole model was set to 15 °C. The boundary conditions are characterized with no flux boundary. The temperature increases at the bottom from initial 15 to 120 °C (Fig. 4.4) within 2 days. The calculations include 48 times steps, each with a length of 1 h.

### 4.2.2 Heating a Saturated Sample

Within the reference calculations using RICHARDS\_FLOW or LIQUID\_FLOW, the initial pore pressure was set to 1 MPa to ensure a full saturated initial condition. In the calculation using LIQUID\_FLOW only the water phase has been considered and the model remains always in full saturated state. Based on the calculation results (Fig. 4.5), it can be observed that the temperature increase induced a significant pore pressure increase from 1 to almost 9 MPa. Because of the advection effects the increase of pore pressure is nonlinear despite the linear increase of temperature with time. In the simulation using RICHARDS\_FLOW the relationship between capillary pressure and water saturation is given by the Mualem–van Genuchten function. In this case the pore size distribution index  $m$  is assumed with 0.52 belonging to the typical value range of opalinus clay. Moreover, the air entry pressure is considered as constant with 10 MPa. Theoretically, in the case of full saturation the calculated results using RICHARDS\_FLOW model should be identical with the results using

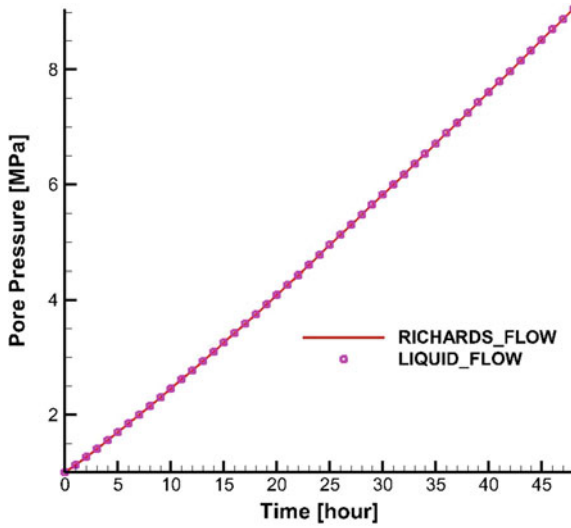


Fig. 4.5 Comparison of the calculated pore pressure evolution using RICHARDS\_FLOW model with the results using LIQUID\_FLOW model

LIQUID\_FLOW. A the results comparison (Fig. 4.5) shows that the results from the two different models are congruent. In the third reference calculation the advection effects are neglected with the assumption that permeability converges to 0. Equation 4.16 shows a linear dependency of the pore pressure with the temperature, when saturation is constant to 1 and the Laplace term is always equal to 0. Thus, an increase

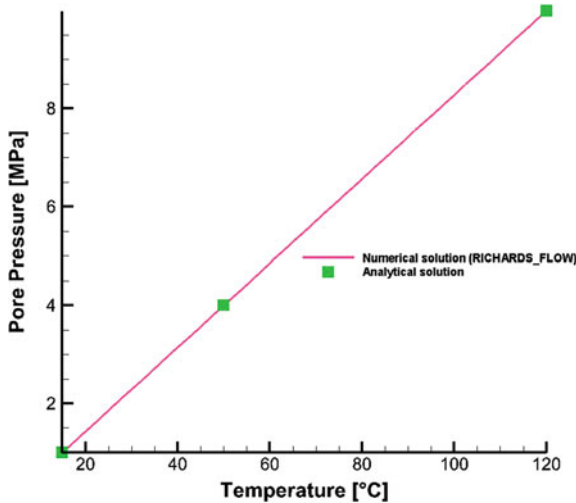


Fig. 4.6 Pore pressure evolution as a function of temperature

in pore pressure of about 8.99 MPa can be analytically calculated when the temperature rises from 15 to 120°C. With the results in Fig. 4.6, it can be observed that pore pressure increases linearly with the rise in temperature, and these values match with analytical results very well.

### 4.2.3 Heating an Unsaturated Sample

Based on a RICHARDS\_FLOW benchmark model of OGS, a numerical simulation of undrained heating in an unsaturated sample has been carried out. Using the

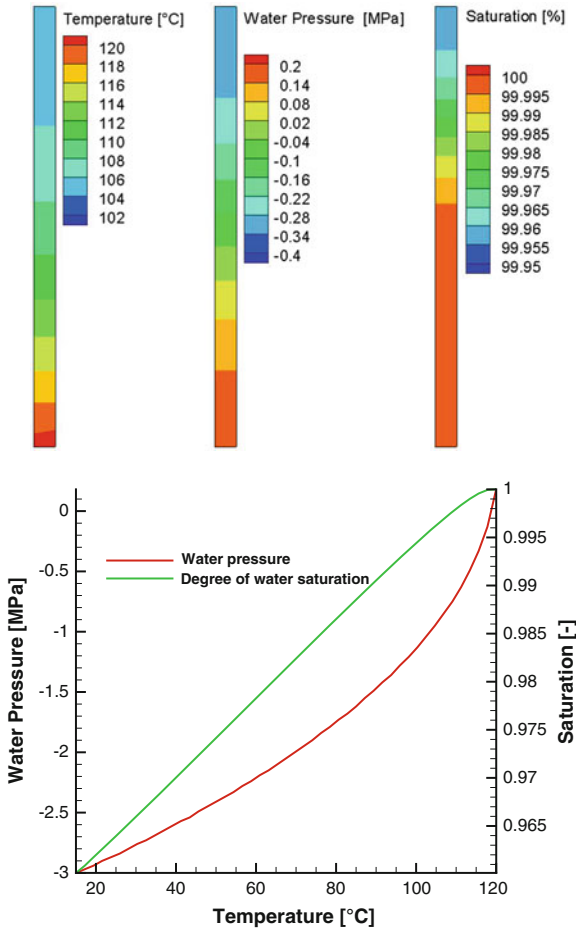


Fig. 4.7 Distribution of temperature (left) water pressure (middle) water saturation (right) at the end of simulation (top) and calculated water pressure and saturation at the bottom of model in comparison with temperature (bottom)

Mualem–van Genuchten function, the initial capillary pressure was set to 3 MPa to ensure that the initial saturation is equal to 96 %. The main purpose of this benchmark model is to analyze the thermal induced expansion of pore water by using RICHARDS\_FLOW model. Therefore, thermal expansion of solid and the vapor effects by none isothermal conditions are neglected.

#### 4.2.4 Results

Figure 4.7 (top) shows the calculated distribution of temperature, water pressure and degree of water saturation within this model at  $t = 48$  h. During heating, temperature as well as pore pressure increase gradually. The highest water pressure is 0.175 MPa and is found at the bottom where the temperature is highest. The lowest water pressure is equal to  $-0.33$  MPa and located at the top, where the temperature is lowest. With the increase of temperature, the degree of saturation rises from 96 % to full saturation in parts of the sample. The increase of water pressure and saturation degree indicates a pore water expansion which is caused by the heating. Figure 4.7 (bottom) illustrates the development of pore pressure and water saturation as a function of temperature at the bottom. Here, it can be observed that saturation increases almost linear with the increase of temperature until full saturation. It can also be seen that the pore pressure rises faster at a higher saturation degree.

## References

1. L.A. Richards. Capillary conduction of liquids through porous mediums. *Physics A-J Gen. Appl. Phys.*, 1(1):318–333, 1931.
2. M.T. VanGenuchten and P.J. Wierenga. Mass-transfer studies in sorbing porous-media. 1. Analytical solutions. *Soil Sci. Soc. Am. J.*, 40(4):473–480, 1976.
3. Y. Mualem. New model for predicting hydraulic conductivity of unsaturated porous-media. *Water Resour. Res.*, 12(3):513–522, 1976.
4. J.K. Zhou. *Differential transformation and its applications for electrical circuits*. Huazhong University Press, 1986.
5. W.V. Abeele M.L. Wheeler and B.W. Burton. Geohydrology of bandelier tuff. *Los Alamos National Laboratory report*, LA-8962-MS, 1981.
6. H. S. Carslaw and J. C. Jaeger. *Conduction of heat in solids*. Oxford University Press, London, 2nd edition, 1959.

# Chapter 5

## Multi-Componential Fluid Flow

Ashok Singh

This chapter deals with mathematical modeling of multi-componential fluid flow and transport processes in a porous media. Compare to flow of a pure fluid, interaction of multi-componential fluid flow with other processes is very complex due to the variability of material parameters due to change in pressure, temperature and composition. Numerical simulation helps to understand such complex interaction is arisen from process coupling or variability in the material parameters. Numerical simulation also helps for making a precise prediction the consequences of fluid injection/extraction associated with subsurface. The present modeling is useful for computational investigation of industrial and fundamental problems of mass, momentum and heat transfer through porous media.

### 5.1 Basic Equations

This section is concerned with derivation of governing equations for multi-componential fluid flow and transport processes in a porous media. A porous media can be considered as a two-phase system which solid phase is immobile and isotropic material. And the mobile phase is a mixture of different pure fluids filled in the pores of solid skeleton. In this derivation, the concept of Representative Elementary Volume (REV—measurement over a smallest volume represents the whole two phase system) is adopted. In the continuum mechanism, REV concept neglects that a matter is made of atoms. The size of this REV is restricted by inequality  $\lambda \leq l \leq L$  which provides definition of the Knudsen number  $K_n = \frac{\lambda}{l}$ .  $\lambda$  is the average mean free path between two molecules and  $l$  is the characteristic length (e.g., diameter of pores).

---

A. Singh (✉)

University of Southern Denmark, Campusvej 55, 5230 Odense M, Denmark  
e-mail: asi@iti.sdu.dk

### 5.1.1 Mass Balance Equation

The mass balance equation of a multi-componential fluid flowing with velocity,  $\mathbf{v}$ , in a porous media is given by

$$\frac{\partial (n\rho^f)}{\partial t} + \nabla \cdot (\rho^f n\mathbf{v}) = n\rho^f Q_\rho^f \quad (5.1)$$

Here,  $\mathbf{v} = \sum_k \omega_k^f \mathbf{v}_k$  is the averaged velocity shared by each component (Bear [1]).  $t$  is time, superscript  $f$  stands for fluid phase, subscript  $k$  stands for component.  $\omega_k^f$  is the mass fraction of  $k$ th components in the mixture,  $\rho^f$  is mixture density,  $\mathbf{k}$  is permeability,  $n$  is porosity,  $\mu$  is viscosity,  $\mathbf{g}$  is gravity vector and  $Q_\rho^f$  is fluid source/sink term.

According to Helmig [2], sum of the diffusive fluid flux over all components is zero. And the Darcy's law is used for the advective fluid flux,  $F_a$ .

$$F_a = \rho^f \mathbf{w} = \rho^f n\mathbf{v} = -\frac{\rho^f \mathbf{k}}{\mu} \cdot (\nabla p - \rho^f \mathbf{g}) \quad (5.2)$$

Equation (5.1) is expanded in following form

$$n\beta^f \rho^f \frac{\partial p}{\partial t} - n\alpha_T^f \rho^f \frac{\partial T}{\partial t} + \sum_k n\rho^f \gamma_k \frac{\partial \omega_k^f}{\partial t} + \nabla \cdot [\rho^f \mathbf{w}] = n\rho^f Q_\rho^f \quad (5.3)$$

Here, thermal expansivity  $\alpha_T^f = -\frac{1}{\rho^f} \left( \frac{\partial \rho^f}{\partial T} \right)_{p, \omega_k^f}$ , fluid compressibility  $\beta^f = \frac{1}{\rho^f} \left( \frac{\partial \rho^f}{\partial p} \right)_{T, \omega_k^f}$  and solutal expansivity  $\gamma_k = \frac{1}{\rho^f} \left( \frac{\partial \rho^f}{\partial \omega_k^f} \right)_{p, T, \omega_i^f}$ ;  $i \neq k$ .

### 5.1.2 Fractional Mass Transport Equation

Consider a reaction which affects mass fraction of  $k$ th chemical component in fluid and solid phases. Rate of this reaction,  $R^\gamma$ , can be decomposed into zero order and 1st order rates.

$$R^\gamma = \underbrace{R_{(0)}^\gamma}_{\text{zero order}} + \underbrace{R_{(1)}^\gamma}_{\text{1st order}}; \gamma = f, s \quad (5.4)$$

The zero order rate is equivalent to the source/sink term, i.e.  $R_{(0)}^\gamma = \rho^\gamma Q^\gamma$ . Whereas, according to the decay process, 1st order rate is given by relation  $R_{(1)}^\gamma = -\lambda \rho^\gamma \omega_k^\gamma$ . Choosing the dispersive mass flux in terms of mass fraction, the mass transport

equation of the  $k$ th component for fluid and solid phases are given by

$$\frac{\partial (n\rho^f \omega_k^f)}{\partial t} + \nabla \cdot (\mathbf{w}\rho^f \omega_k^f) - \nabla \cdot (n\rho^f D_{ij} \cdot \nabla \omega_k^f) = -n\lambda\rho^f \omega_k^f + n\rho^f Q_\omega^f \quad (5.5)$$

and

$$\frac{\partial [(1-n)\rho^s \omega_k^s]}{\partial t} = -(1-n)\lambda\rho^s \omega_k^s + (1-n)\rho^s Q_\omega^s \quad (5.6)$$

The mass fraction of  $k$ th chemical component in mixture ( $\omega_k^f = \frac{m_k^f}{m^f}$ ) and solid ( $\omega_k^s = \frac{m_k^s}{m^s}$ ) phases are related via sorption law i.e.,  $\omega_k^s = f(\omega_k^f)\omega_k^f$ . With considering sorption process, the convective form of the fractional mass transport equation is given by

$$\begin{aligned} n\rho^f R_1 \frac{\partial \omega_k^f}{\partial t} + \rho^f \mathbf{w} \cdot \nabla \omega_k^f - \nabla \cdot (n\rho^f D_{ij} \cdot \nabla \omega_k^f) \\ + \omega_k^f \rho^f (n\rho^f Q_\rho^f - nR_0\lambda) = n\rho^f Q_\omega^f + (1-n)Q_\omega^s \end{aligned} \quad (5.7)$$

The retardation coefficient,  $R_0$ , and its derivative,  $R_1$ , are given by

$$R_0 = 1 + \frac{1-n}{n} \frac{\rho^s}{\rho^f} f(\omega_k^f); \quad \text{and} \quad R_1 = 1 + \frac{1-n}{n} \frac{\rho^s}{\rho^f} \frac{\partial [f(\omega_k^f)\omega_k^f]}{\partial \omega_k^f}$$

The coefficients of hydrodynamic-dispersion tensor are given by

$$D_{ij} = \tau D \delta_{ij} + \alpha_t |\mathbf{v}| \delta_{ij} + (\alpha_l - \alpha_t) \frac{\mathbf{v}_i \mathbf{v}_j}{|\mathbf{v}|}$$

Here,  $\delta_{ij}$  is Kronecker delta,  $\tau$  is tortuosity,  $D$  is diffusion coefficient,  $\alpha_t$  and  $\alpha_l$  are transverse- and longitudinal- dispersivity, respectively.

### 5.1.3 Heat Transport Equation

Consider an open system with a fluid which internal energy is  $e^f$  and density is  $\rho^f$ . According to the first law of thermodynamics, energy balance equation for this system is expressed as

$$\rho^f \frac{De^f}{Dt} + \nabla \cdot \mathbf{i}^f + e^f \rho^f Q_\rho^f = \tau_{ij} \frac{\partial v_i}{\partial x_j} \quad (5.8)$$

where,  $e^f \rho^f Q_\rho^f$  is amount of internal energy associated with fluid source/sink term,  $Q_\rho^f$ , and  $\mathbf{i}^f$  is the fluid heat conduction flux vector. The stress tensor,  $\tau_{ij} \frac{\partial v_i}{\partial x_j}$ , can be

decomposed into pressure term,  $p\nabla \cdot \mathbf{v}$ , and viscous term,  $\mathbf{v} \cdot \nabla p$ .

$$\rho^f \frac{De^f}{Dt} + \nabla \cdot \mathbf{i}^f + e^f \rho^f Q_\rho^f = \mathbf{v} \cdot \nabla p - p\nabla \cdot \mathbf{v} \quad (5.9)$$

For a thermodynamically open system, enthalpy,  $h^f$ , is preferred over internal energy,  $e^f$ . Hence, Eq.(5.9) is being transformed in terms of fluid enthalpy with using the mass balance equation.

$$p\nabla \cdot \mathbf{v} = -\frac{p}{\rho^f} \frac{D\rho^f}{Dt} + pQ_\rho^f = \rho^f \frac{D\left(\frac{p}{\rho^f}\right)}{Dt} - \frac{Dp}{Dt} + pQ_\rho^f \quad (5.10)$$

Replacing the pressure term in the Eq.(5.9) by using Eq.(5.10) and relation,  $h^f = e^f + \frac{p}{\rho^f}$ , we have

$$\rho^f \frac{Dh^f}{Dt} + \nabla \cdot \mathbf{i}^f = \mathbf{v} \cdot \nabla p + \frac{Dp}{Dt} - h^f \rho^f Q_\rho^f \quad (5.11)$$

The energy balance equation for solid phase in terms of the internal energy,  $e^s$ , is given by

$$\rho^s \frac{De^s}{Dt} + \nabla \cdot \mathbf{i}^s = Q_e^s \quad (5.12)$$

Replace the total derivative in Eqs. (5.11) and (5.12) with following thermodynamical relations.

$$\begin{aligned} \frac{Dh^f}{Dt} &= \left( \frac{1}{\rho^f} - \frac{\alpha_T^f T^f}{\rho^f} \right) \frac{Dp}{Dt} + c_p^f \frac{DT^f}{Dt} \\ \frac{De^s}{Dt} &= c_v^s \frac{DT^s}{Dt} \end{aligned} \quad (5.13)$$

The heat transport equation for fluid and solid phases in terms of respective phase temperature are

$$\rho^f c_p^f \frac{DT^f}{Dt} + \nabla \cdot \mathbf{i}^f = \mathbf{v} \cdot \nabla p + \alpha_T^f T^f \frac{Dp}{Dt} - h^f \rho^f Q_\rho^f \quad (5.14)$$

and

$$\rho^s c_v^s \frac{\partial T^s}{\partial t} + \nabla \cdot \mathbf{i}^s = Q_e^s \quad (5.15)$$

Under the thermal equilibrium ( $T^f \cong T^s = T$ ), total energy conservation equation is preferred which is obtained by averaging the Eqs. (5.14) and (5.15) over fluid and solid phases.

**Table 5.1** Approximation of material parameters for a mixture

$\frac{1}{\rho^f} = \sum_k \frac{\omega_k^f}{\rho_k^f}$	$\rho_k^f = \frac{pM_k}{z_k(p, T)RT}$
$\beta^f = \sum_k \frac{v_k}{v} \beta_k^f$	$\beta_k^f = -\frac{1}{v} \left( \frac{\partial v}{\partial p} \right)_{T, \omega_k^f}$
$\alpha_T^f = \sum_k \frac{v_k}{v} \alpha_{Tk}^f$	$\alpha_{Tk}^f = \frac{1}{v} \left( \frac{\partial v}{\partial p} \right)_{p, \omega_k^f}$
$\frac{1}{\mu} = \sum_k \frac{\omega_k^f}{\mu_k(\rho_k^f, T)}$	$\mu_k(\rho_k^f, T) = \mu_k^0(T) + \Delta\mu_k(\rho_k^f, T) + \Delta_c\mu_k(\rho_k^f, T)$
$\frac{1}{\kappa^f} = \sum_k \frac{\omega_k^f}{\kappa_k^f(\rho_k^f, T)}$	$\kappa_k^f(\rho_k^f, T) = \kappa_k^0(T) + \Delta\kappa_k(\rho_k^f, T) + \Delta_c\kappa_k(\rho_k^f, T)$
$c_p^f = \sum_k \omega_k^f c_{pk}^f(\rho_k^f, T)$	$c_{pk}^f(\delta, \tau) = -\tau^2 (\phi_{\tau\tau}^0 + \phi_{\tau\tau}) + \frac{(1 + \delta\phi_\delta - \delta\tau\phi_{\delta\tau})^2}{1 + 2\delta\phi_\delta + \delta^2\phi_{\delta\delta}}$
$D_{ij} = \frac{0.00143T^{1.75}}{p\sqrt{\frac{2M_iM_j}{M_i+M_j}} \left[ \Sigma_{V_{di}}^{\frac{1}{3}} + \Sigma_{V_{dj}}^{\frac{1}{3}} \right]}$	

$$\begin{aligned}
& (\rho c_p)_{eff} \frac{\partial T}{\partial t} + c_p^f \rho^f n \mathbf{v} \cdot \nabla T - \nabla \cdot [\kappa_{eff} \cdot \nabla T] \\
& = n \alpha_T^f T \frac{\partial p}{\partial t} + n \mathbf{v} \cdot \nabla p - \alpha_T^f T n \mathbf{v} \cdot \nabla p + c_p^f (T - T_0) n \rho^f Q_\rho^f + Q_T \quad (5.16)
\end{aligned}$$

Here,  $Q_T = Q_e$ , and heat conduction flux can be represented according to the Fourier's law.

$$\mathbf{i}^\gamma = -\kappa^\gamma \cdot \nabla T \quad (5.17)$$

where  $\kappa_{eff}$ , is the effective thermal conductivity tensor of the porous media, with coordinates defined as  $\kappa_{eff} = (1 - n)\kappa^s + n\kappa^f$ .  $(\rho c_p)_{eff}$  is the effective heat capacity of the porous medium defined by  $(\rho c_p)_{eff} = (1 - n)\rho^s c_v^s + n\rho^f c_p^f$ . Here, specific heat capacity and thermal conductivity of the fluid mixture are given in Table 5.1.

### 5.1.4 Equation of State

Tsai and Chen [3] presented the volume translated Peng-Robinson equation of state (VTPR-EoS). In this EoS, molar volume,  $v_k$ , is corrected by the translated volume,  $c$ . The translated volume is difference in molar volume obtained by experimental and computation at the reduced temperature  $T_r = T/T_c$ . Because of this translation, VTPR-EoS approximates the fluid parameters for liquids, gases and supercritical states.

$$p = \frac{RT}{(v_k + c - b)} - \frac{a(T)}{(v_k + c)(v_k + c + b) + b(v_k + c - b)} \quad (5.18)$$

Here,  $R$  is universal gas constant.  $a$  and  $b$  are attraction and repulsion parameter, respectively.

$$a(T) = 0.4572 \frac{R^2 T_c^2}{p_c} [1 + M_0(1 - T_r) + N_0(1 - T_r)(0.7 - T_r)]^2$$

$$M_0 = 0.2047 + 0.8354\omega_a - 0.1847\omega_a^2 + 0.1667\omega_a^3 - 0.0988\omega_a^4$$

$$b = 0.077796 \frac{RT_c}{p_c}$$

$$c = \frac{RT_c}{p_c} \left[ k_1 + k_2 \left(1 - T_r^{2/3}\right) + k_3 \left(1 - T_r^{2/3}\right)^2 \right]$$

$$k_1 = 0.00185 + 0.00438\omega_a + 0.36322\omega_a^2 - 0.90831\omega_a^3 + 0.55885\omega_a^4$$

$$k_2 = -0.00542 - 0.51112k_3 + 0.04533k_3^2 + 0.07447k_3^3 - 0.03831k_3^4$$

Here,  $p_c$  is critical pressure,  $T_c$  is critical temperature and  $\omega_a$  is acentric parameter. Required parameters for VTPR-EoS are given in Table 5.2. A cubic equation based on VTPR-EoS is obtained by setting  $v_k = z_k RT p$ , in Eq. (5.18).

$$z^3 + Pz^2 + Qz + r = 0$$

$$P = B - 1 + 3C$$

$$Q = -3B^2 + 3C^2 + 2BC - 2B - 2C + A$$

$$r = B^3 + C^3 + B^2 - C^2 + BC^2 - 3CB^2 - 2BC + CA - AB \quad (5.19)$$

Here,  $A = \frac{ap}{RT}$ ,  $B = \frac{bp}{RT}$  and  $C = \frac{cp}{RT}$ . The cubic equation can be easily solved using either Newton-Raphson iteration or analytical method for super compressibility

**Table 5.2** Constants of the pure fluid

	CO <sub>2</sub>	CH <sub>4</sub>	N <sub>2</sub>	H <sub>2</sub> O	Unit
$\rho_c$	467.6	162.66	314.0	322	kg m <sup>-3</sup>
$T_c$	304.13	190.55	126.20	647.096	K
$p_c$	7,377,300	459,920	338,300	22,064,000	Pa
$M$	44.01	16.04	28.013	18.015	kg kmol <sup>-1</sup>
$\omega_a$	0.22491	0.011	0.039	0.344	–
$V_d$	26.9	25.14	18.5	–	m <sup>3</sup> kmol <sup>-1</sup>
$N_0$	0.11333	0.08248	0.09967	0.1156	–
$M_0$	0.3849	0.2138	0.0185	0.4756	–
$k_3$	0.28996	0.20978	0.24086	0.0471	–

factor,  $z_k = z_k(p, T)$ . According to the **Katz** chart, at temperature below to critical point cubic equation has only one real root representing the existence of a single phase. Otherwise, it has two real roots. The maximum root represents gas state, whereas, minimum root represents either liquid or supercritical state.

### 5.1.4.1 PVT Derivatives

Two important derivatives, i.e.  $\frac{\partial v_k}{\partial p}$  and  $\frac{\partial v_k}{\partial T}$  are prerequisite to find other fluid and thermal parameters (particularly,  $\beta_k^f$  and  $\alpha_{T,k}^f$ ). In this section, we provide expression for these derivative deriving from Eq. (5.18).

$$\left(\frac{\partial v_k}{\partial T}\right)_{p,\omega_k} = \frac{F - \frac{da}{dT}E}{F + 2pEH - 2RTH + a}$$

$$\left(\frac{\partial v_k}{\partial p}\right)_{T,\omega_k} = \frac{EF}{pF + 2pEH - 2RTH + a}$$

with,  $F = (v_k + c)(v_k + c + b) + b(v_k + c - b)$ ,  $E = v_k + c - b$ , and  $H = v_k + c + b$

$$\left(\frac{da}{dT}\right) = -0.4572 \frac{R^2 T_c}{p_c} 2a_0 [1 + M(1 - T_r) + N(1 - T_r)(0.7 - T_r)]$$

Here,  $a_0 = M_0 + N_0(1.0 - T_r) + N_0(0.7 - T_r)$ .

### 5.1.4.2 Amagat's Mixing Rule

According to the rule, the molar volume of a mixture is the sum of its component's partial volumes, i.e.  $v = \sum_k v_k$ . This mixing rule with the real gas law, we have

$pv = \sum_k z_k(p, T)RT$ . The expression for mixture density is given by

$$\frac{1}{\rho^f} = \sum_k \frac{\omega_k^f}{\rho_k^f}$$

From above relation, expression for the salute expansivity is obtained as

$$\gamma_k = \left(\frac{1}{\rho^f} \frac{\partial \rho^f}{\partial \omega_k^f}\right)_{p,T,\omega_i^f} = -\frac{\rho_k^f}{\rho^f}; \quad i \neq k$$

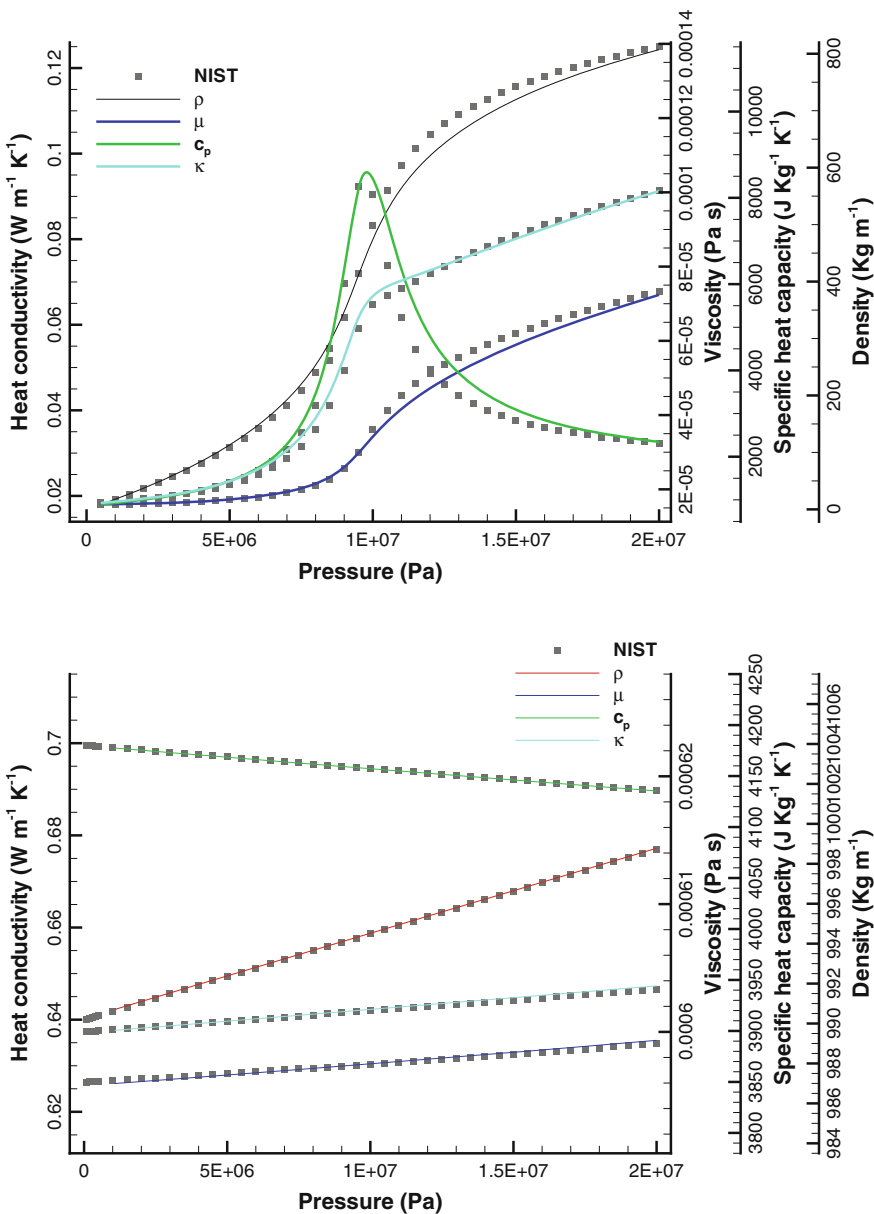


Fig. 5.1 Comparison of carbon dioxide (left) and water (right) parameters with NIST data for pressure from  $1.0 \times 10^5$  Pa to  $2.0 \times 10^7$  Pa at 318.15 K

### 5.1.4.3 Material Functions for Mixture

We computed density, viscosity, heat conductivity and specific heat capacity for pure fluids according the expression given in the Table 5.1. Figure 5.1 shows that the computed parameters are in close agreement with corresponding data from the National Institute of Standards and Technology (NIST).

## 5.2 Examples

### 5.2.1 Tracer Test

Tracer is used to characterize the fluid flow through the reservoirs and for estimation of medium parameters. For example, in oil and gas industries (also in hydrology) it is used for indicate mean flow velocity, residual saturation, dispersivities, and etc. For the transport of a contaminant through a porous medium, Genuchten and Alves [4] provided one dimensional analytical solution which is as follow.

$$\begin{aligned} \omega^f(x, 0 < t \leq t_0) &= \omega_i^f + (\omega_0^f - \omega_i^f)A(x, t) \\ \omega^f(x, t \geq t_0) &= \omega_i^f + (\omega_0^f + \omega_i^f)A(x, t) - \omega_0^f A(x, t - t_0) \end{aligned} \quad (5.20)$$

with

$$A(x, t) = 0.5\text{erfc} \left[ \frac{nR_0x - vt}{\sqrt{4n\tau R_0Dt}} \right] + 0.5\text{erfc} \left[ \frac{nR_0x + vt}{\sqrt{4n\tau R_0Dt}} \right] \exp \left( \frac{vx}{n\tau D} \right)$$

To consider sorption process in the mass transport, the sorption law can be adapted, e.g. Henry’s law. Extent to which sorption process affects the tracer transport is accounted by the retardation factor,  $R_0$ . Here,  $D$  is the binary diffusion coefficient,  $\omega_0^f$  is the mass fraction of the tracer chemical is used for pulse,  $t_0$ , injection.



Fig. 5.2 Conceptual model geometry

**Table 5.3** Model properties and material parameters

Parameter	Symbol	Value	Unit
Length	$L$	1,000	m
Area	$A$	1	m <sup>2</sup>
Tortuosity	$\tau$	1.0	–
Porosity	$n$	0.1	–
Intrinsic permeability	$k$	$1.0 \times 10^{-14}$	m <sup>2</sup>
Fluid density	$\rho^f$	30	kg m <sup>-3</sup>
Solid density	$\rho^s$	2,000	kg m <sup>-3</sup>
Dynamic viscosity	$\mu$	$1.0 \times 10^{-5}$	Pa s
Diffusion coefficient	$D$	$1.0 \times 10^{-6}$	m <sup>2</sup> s <sup>-1</sup>
Sorption coefficient	$K_D$	$1.0 \times 10^{-4}$	m <sup>3</sup> kg <sup>-1</sup>
Initial pressure	$p_0$	$1.01325 \times 10^5$	Pa
Constant temperature	$T_0$	318.15	K
Tracer injection rate	$q_m$	0.82946592	kg per day
Pulse injection time	$t_0$	10	day

### 5.2.1.1 Definition

Problem of tracer transport in one-dimensional porous column is considered. The pores of the solid skeleton are completely filled with water at a constant pressure and temperature. The tracer chemical is injected from the inlet within short time and computed the tracer breakthrough curve (time evolution of tracer mass fraction) at two different points located at 5 and 10m from the inlet (see Fig. 5.2). System properties and material parameters used in the simulation (porous medium as well as of fluid and solid phases) are summarized in Table 5.3.

### 5.2.1.2 Model Geometry and Conditions

- Geometry: The porous column is 1,000 m long in x-direction. Inlet and outlet are located at  $x = 0$  and 1,000m, respectively.
- IC: At a constant temperature, 318.15 K, we assume that the pores of solid skeleton are occupied by water at pressure of  $1.01325 \times 10^5$  Pa.
- BC: Free boundary condition for pressure and tracer mass fraction is prescribed at the outlet boundary. At the inlet, mass fraction of tracer chemical  $\omega_0^f = 1$  during pulse tracer injection then altered by free boundary condition.
- ST: From the inlet, the tracer chemical is introduced with rate of 0.83 kg per day for 10 days.

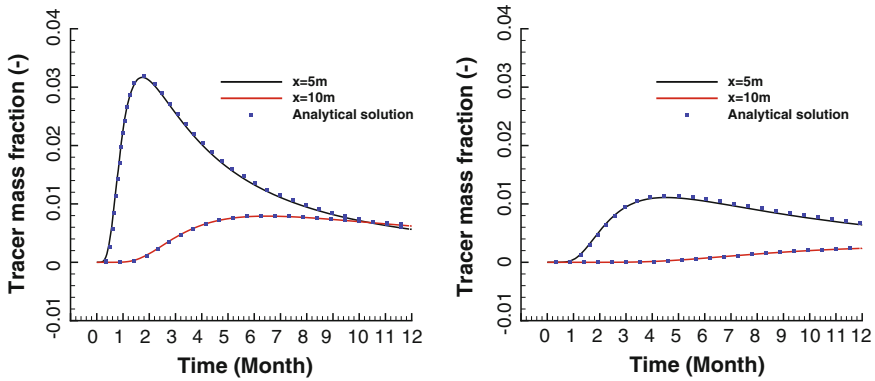


Fig. 5.3 Comparison of analytical and finite element solution

### 5.2.1.3 Numerical Solution

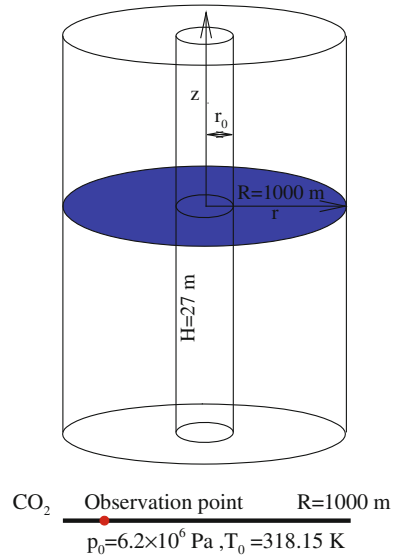
For numerical simulation, the numerical module ‘Multi Componential Flow’ embedded in OGS simulator is utilized. This module solves coupled system of mass balance and fractional mass transport equations in monolithic way for pressure and mass fraction of the tracer chemical. For non-linear iterations, it uses the Picard linearization method. Numerical solution is stabilized with mass lumping method. The model geometry is shown in Fig. 5.2 which is discretized into 1,001 line elements. To capture a sharp tracer concentration gradient, a variable spatial step size, i.e.  $\Delta x = 0.000925289$  m is chosen close to the inlet and it is increased to 10 m far away from it. One year of the reservoir behavior has been simulated using a constant time step size of one day.

Figure 5.3a, b show the tracer breakthrough curves at the observation points. In Fig. 5.3a, sorption process is not included, however, Fig. 5.3b clearly showing that sorption process retards the mass transport significantly. The present finite element solution is in close agreement with the analytical solution, i.e. Eq. (5.20).

### 5.2.2 Bottom Hole Pressure

Well control is a technique prevalent in oil and natural gas industries for well drilling or fluid injection. In this technique, hydrostatic pressure (fluid column) is maintained with formation pressure to avoid influx into well. So understanding of the different pressure is important, particularly, Well Head Pressure (WHP) and Bottom Hole Pressure (BHP). Hence, in this benchmark, BHP is simulated with simplified geometry using multi-componential fluid flow approach.

The model geometry is shown in Fig. 5.4. This uses axisymmetric concept to simplify the model, i.e. one-dimensional porous column in r-direction which pores are occupied with water at pressure  $6.2 \times 10^6$  Pa and temperature 318.15 K.

**Fig. 5.4** Benchmark setup**Table 5.4** Model parameters and geometrical information

Parameter	Symbol	Value	Unit
Radius	$R$	1,000	m
Height	$H$	27	m
Well radius	$r_0$	0.1	m
Porosity	$n$	0.25	–
Permeability	$k$	$4.6 \times 10^{-14}$	$\text{m}^2$
Density	$\rho^f$	Table 5.1	$\text{kg m}^{-3}$
Viscosity	$\mu$	Table 5.1	Pa s
Diffusion coefficient	$D$	Table 5.1	$\text{m}^2 \text{ s}^{-1}$
Mass injection rate	$q_m(t)$	Fig. 5.5	$\text{kg s}^{-1}$
Time step	$\Delta t$	10	h
Simulation time	$t$	19,170	h

From the left point, time dependent injection rate is assigned for  $\text{CO}_2$  injection. Required parameters for this numerical simulation are given in Table 5.4. Pressure evolution during injection operation is computed to show that measured pressure data (from real site) could be reproduced by numerical simulation.

### 5.2.2.1 System Geometry and Conditions

- Geometry: The porous column is 1,000 m long in the  $r$ -direction. The inlet and outlet are located at  $r = 0.1$  and  $r = 1,000 \text{ m}$ , respectively.

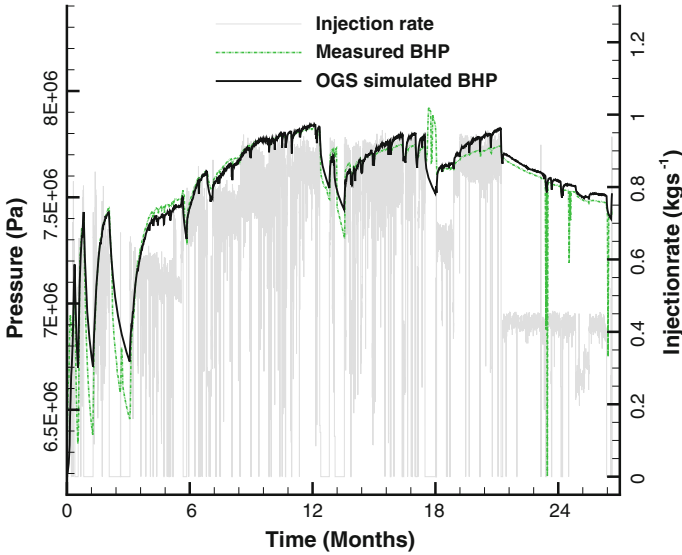


Fig. 5.5 BHP evolution at  $r = 23$  m distance from the  $\text{CO}_2$  injection point

- IC: The pores of the solid skeleton are occupied by water at pressure of  $6.2 \times 10^6$  Pa and temperature of 318.15 K.
- ST: A time dependent mass source term is assigned at the inlet (see Fig. 5.4) for  $\text{CO}_2$  injection.

5.2.2.2 Numerical Solution

The geometrical model consists 1,001 line elements. To capture the sharp pressure gradient close to the inlet, the spatial step size is refined to  $\Delta r = 0.000925289$  m whereas far from the injection point it is 10 m. The numerical simulation for 19,170 h has been performed using a constant time step size of ten hours. In Fig. 5.5, the pressure evolution is presented which is observed at  $r = 23$  m from the injection point.

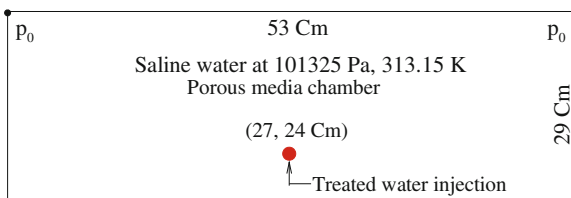


Fig. 5.6 Semantic of the original experimental

### 5.2.3 Plume Migration

Treated wastewater disposal into saline aquifers can rise up to the surface. Due to this, saline aquifers generally are overlain by treated water layers. To make decision for using these layers as a potable drinking water source or not, investigation about plume rising become important. Usually, plume moves away from its source because of density contrast and widens because of entrainment of the surrounding fluid at its edges. Experimental (see Fig. 5.6) investigation of buoyant plume movement is presented by Brakefield [5].

#### 5.2.3.1 Definition

Geometry of the problem is shown in Fig. 5.6. This two-dimensional plane is assumed a isotropic porous media which pores are completely filled with saltwater at a pressure of  $1.01325 \times 10^5$  Pa. Mass rate for treated water (lighter than saltwater) injection is assigned at the injection point. The density of the treated water varies linear with mass fraction, i.e.  $\rho_w^f = \rho_{w0}^f(1 + \gamma_w \omega_w^f)$ . The density of saltwater is used for reference density  $\rho_{w0}^f = 1,019 \text{ kg m}^{-3}$ .

#### 5.2.3.2 Model Geometry and Conditions

- Geometry: The considered plane is 56 cm long and 29 cm high in  $x$  and  $z$ -directions, respectively. From the point (27, 24 cm), treated water is injected.
- IC: At constant temperature, 313.15 K, we assume that the pores of solid skeleton are occupied by saltwater at pressure of  $1.01325 \times 10^5$  Pa.
- BC: At the top left and top right point, pressure  $p_0 = 1.01325 \times 10^5$  Pa is assigned. Elsewhere, free boundary conditions for pressure and treated water mass fraction are prescribed.
- ST: A 60 ml volume of treated water is injected by syringe into saltwater for 41 s (Table 5.5).

#### 5.2.3.3 Numerical Solution

The model geometry is discretized into 24,591 quad elements. For numerical simulation, the numerical module ‘multi componential flow’ is utilized. This solves coupled system of mass balance and fractional mass transport equations in monolithic way for pressure and mass fraction of treated water. For accuracy, a very fine mesh is used in the region of plume rising. 2,671 s of plume rising have been simulated using a constant time step size of ten seconds. For non-linear iterations, the Picard linearization method is applied with the mass lumping method for numerical stabilization. Figure 5.7 shows the development of treated water plume simulated by SUTRA and SEWAT simulators along with the present finite element solution. It is found that plume distribution patter from each simulator is very similar at all-time steps.

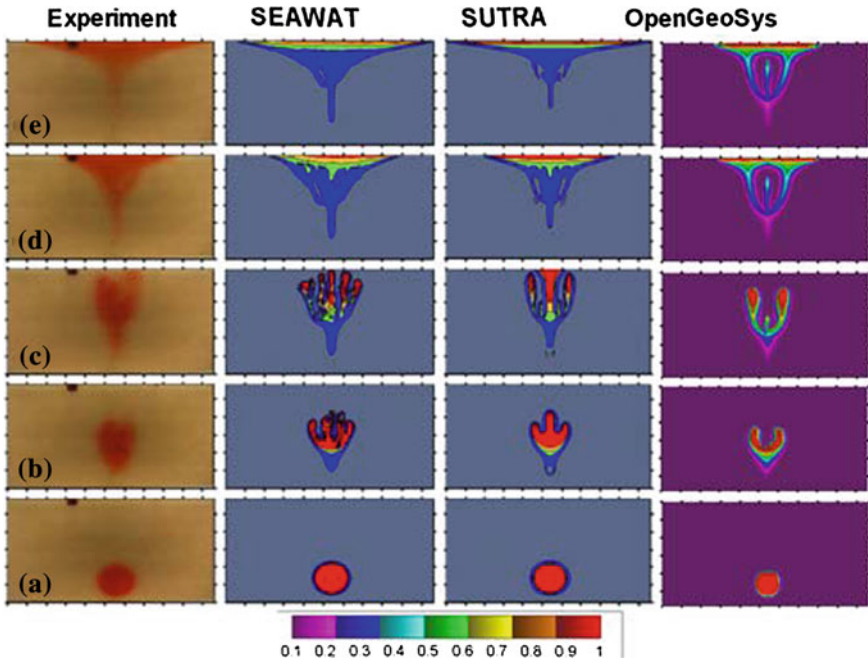


**Fig. 5.7** Evolution of treated water plume at **a** 27; **b** 369; **c** 685; **d** 1,385; **e** 2,631 s after injection completed

**Table 5.5** Simulation parameters

Parameter	Symbol	Value	Unit
Plane area	$L \times H$	$0.56 \times 0.29$	$\text{cm}^2$
Densities	$\rho_w^f, \rho_s^f$	$1.0 \times 10^3, 1.019 \times 10^3$	$\text{kg m}^{-3}$
Dynamic viscosity	$\mu$	0.001	$\text{Pa s}$
Salution expansivity	$\gamma_w$	-0.01865	-
Compressibility	$\beta^f$	0.0	$\text{Pa}^{-1}$
Porosity	$n$	0.39	-
Intrinsic permeability	$k$	$1.120795 \times 10^{-9}$	$\text{m}^2$
Diffusion coefficient	$D$	$1.477 \times 10^{-9}$	$\text{m}^2 \text{s}^{-1}$
Dispersivity coefficient	$\alpha_l, \alpha_t$	0.0005, 0.00005	m
Simulation time	$t$	2,671	s
Injection time	$t_{inj}$	41	s
Time step	$\Delta t$	10	s
Mass injection rate	$q_m$	0.032831	$\text{kg s}^{-1}$

### 5.2.4 CO<sub>2</sub> Leakage Through Abandoned Well

Leakage is a way for fluid to escape from storage. Leakage of geological stored CO<sub>2</sub> through natural occurring faults and fractures would have different fatal effects on the nearby environment. So, numerical modeling of the CO<sub>2</sub> leakage is an useful tool for understanding the leakage mechanism. Its understanding helps to estimate fraction of the stored CO<sub>2</sub> that can be retained in a suitable storage for a sufficiently long period of time. In CO<sub>2</sub> capture and storage technology is associated with pressure pulse that move away from the injection point and it is quicker compare to the front of advancing CO<sub>2</sub>. The pressure pulse forces the saline water to leak via naturally occurred fractures or existing abandoned well. And CO<sub>2</sub> arrives at the leaky point late and buoyancy assists CO<sub>2</sub> leakage and opposes the saline water leakage. The leakage rate is measured in terms of the non-dimensional leakage rate defined by

$$\text{Non-dimensional leakage rate} = \frac{\text{Fluid flux through observation point}}{\text{CO}_2 \text{ injection rate}} \quad (5.21)$$

The problem of the advective spreading of CO<sub>2</sub> into an aquifer already addressed by Ebigbo et al. [6]. However, they used multi-phase fluid flow approach with assumptions (i) the CO<sub>2</sub> and the brine are two separate and immiscible phases (ii) capillary pressure is negligible. These assumptions help to obtain the similar result using compositional fluid flow approach with neglecting the diffusion-dispersion part of mass transport. We used theirs results in this benchmark for code validation. In this study, we used data from *MUFTE* and *ELSA* simulators

- *ELSA* code uniquely addresses the challenge of providing quantitative estimation of fluid distribution and leakage rate.
- This problem is came in existence by developer of *MUFTE* code.

#### 5.2.4.1 Definition

The problem of CO<sub>2</sub> leakage is modeled using a two-dimensional plane consisting two layers separated by an aquitard. The bottom layer is considered as CO<sub>2</sub> storage and top layer for freshwater body. Both layers share a common hydraulic parameters. To be computationally efficient, the aquitard is omitted from numerical simulation. At a constant temperature, the pores of the solid skeleton of both layers are filled with water at the hydrostatic pressure condition. In the vicinity of the injection point, an inclined fracture is incorporated. The non-dimensional leakage rate is defined in Eq. (5.21) measured at the observation point located at the midpoint of the fracture. The computed CO<sub>2</sub> leakage rate is compared with similar result from *ELSA* and *MUFTE* simulators.

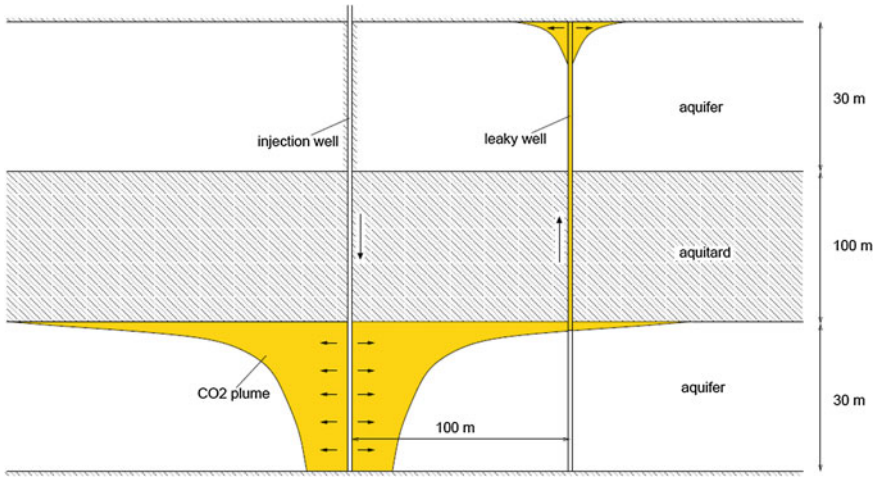


Fig. 5.8 Leakage scenario [6]

### 5.2.4.2 Model Geometry and Conditions

- Geometry: A 1,000 m long and 160 m high plane located between 2,860–3,000 m deep to earth surface. This consists two layers each 30 m thick and a 100 m thick aquitard. The CO<sub>2</sub> injection and observation points are located at (0, -2,970 m) and (100, -2,920 m), respectively.
- IC: At constant temperature, 318.15 K, pores of both layers are filled completely with water under hydrostatic pressure condition  $\frac{dp}{dz} = 10,251.45 \text{ Pa m}^{-1}$  with reference depth of 2,840 m.
- BC: At both lateral boundaries, hydrostatic pressure similar to initial condition is assigned. No flow condition is prescribed at top and bottom boundaries.
- ST: CO<sub>2</sub> injection rate is 8.87 kg s<sup>-1</sup> for 18 months.

### 5.2.4.3 Numerical Solution

The layers (see Fig. 5.8) are discretized into 15,231 triangular whereas the fracture is discretized into 52 line elements. The triangular element closed to fracture are densely distributed is. Within the multi-componential approach, the coupled system of flow and transport equations is solved numerically using monolithic approach for primary variables, i.e. pressure and mass fraction of water and CO<sub>2</sub>. Generalized single step scheme is used for time discretization with time step  $\Delta t = 1 \text{ Day}$ . For non-linear iterations the Picard linearization method is applied with the mass lumping method for numerical stabilization. Negligence of diffusion-dispersion makes difficult to achieve the desired convergence, but using available techniques (*SUPG*, *FTC*, or *MASS LUMPING*) we simulate this benchmark problem (Table 5.6).

Figure 5.9 shows the non-dimensional leakage rate of CO<sub>2</sub>. To simulate the problem, OGS uses multi-componential fluid flow approach, whereas, other two

**Table 5.6** Simulation parameters

Parameter	Symbol	Value	Unit
CO <sub>2</sub> , water density	$\rho_c^f, \rho_w^f$	479,1045	kg m <sup>-3</sup>
CO <sub>2</sub> , water viscosity	$\mu_c, \mu_w$	0.3950, $2.535 \times 10^{-4}$	Pa s
Diffusion	D	0.0	m <sup>2</sup> s <sup>-1</sup>
Aquifer permeability	$k_a$	$2.0 \times 10^{-14}$	m <sup>2</sup>
Fracture permeability	$k_f$	$1.0 \times 10^{-12}$	m <sup>2</sup>
Porosity	$n$	0.15	
Aquifer depth	$h$	2,840–3,000	m
Aquifer, aquitard thickness	$\Delta h$	30,100	m
Injection rate	$q_m$	8.87	kg s <sup>-1</sup>
Simulation time	$t$	18	Month

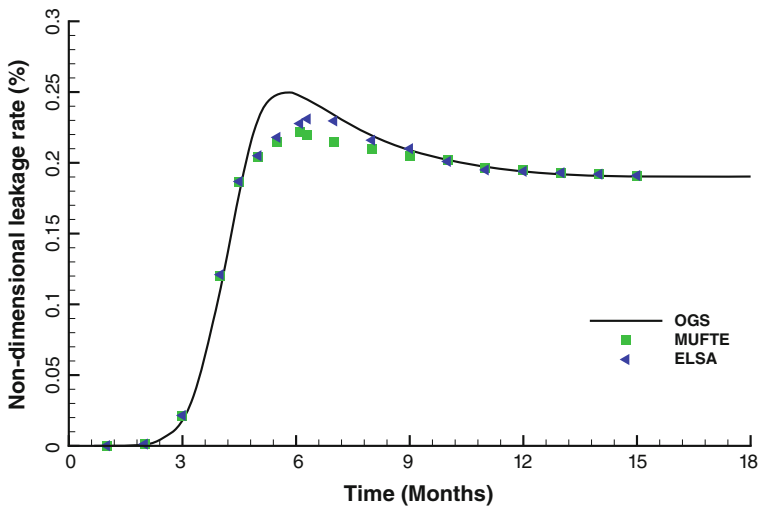


**Fig. 5.9** Comparison of computed leakage rate from three different simulators

simulators were used the multi-phase fluid flow approach. This benchmark state that CO<sub>2</sub> leakage rate from both approaches are in close agreement under assumption made earlier in this benchmark.

### 5.2.5 Thermo-Chemical Energy Storage

For a given reaction, amount of product(s) and reactant(s) are varied with reaction time. It also releases/absorbs certain amount of thermal energy, i.e. reaction enthalpy. Therefore, we present numerical modeling approach for investigation of interphase mass and heat transfer.

Consider a CaO bed which pore is filled with  $N_2$  gas. On introduction of water vapor, CaO reacts with water produces  $Ca(OH)_2$  and releases heat ( $\Delta h$ ). This system can be considered as a two-phase system which solid phase is composed by CaO and  $Ca(OH)_2$  and gas phase is a mixture of water vapor and  $N_2$ . The reaction rate of this system is modelled with a trigonometric function such that the solid density evolution is sinusoidal (amplitude  $a$ , angular frequency  $f$ )

$$\dot{\rho}^s(t) = af \cos(ft) \quad (5.22)$$

From this reaction rate, the following composition relations can be derived analytically for solid phase and water vapor densities:

$$\rho^s(t) = \rho_0^s + a \sin(ft), \quad \rho^g(t) = \rho_0^g + a \sin(ft) \quad (5.23)$$

$$\rho_V(t) = \rho_{V0} + a \sin(ft), \quad \omega_V(t) = \frac{\rho_V(t)}{\rho^g(t)} \quad (5.24)$$

Here, s and g stand for solid and gas phase. The heat transport equation for this system is governed by

$$\left[ (1-n)\rho^s c_p^s + n\rho^g c_p^g \right] \frac{\partial T}{\partial t} - n \frac{\partial p}{\partial t} = (1-n)\Delta h \frac{\partial \rho^s}{\partial t} \quad (5.25)$$

To obtain the analytical solution of Eq. (5.25), we assumed that  $\Delta h \rightarrow \infty$  and solid and gas phases are in thermodynamical equilibrium. If the gases are ideal and mixing is according to the Amagat's rule, we find

$$\frac{1}{M} = \sum_i \frac{\omega_i}{M_i}, \quad \beta_p = \frac{1}{p}, \quad \alpha_T = -\frac{1}{T}, \quad \gamma_i = -\frac{\rho_i}{\rho} \quad (5.26)$$

$$\frac{1}{\rho^g} = \sum_i \frac{\omega_i}{\rho_i}, \quad p = \sum_i \frac{RT\rho^g \omega_i}{M_i}; \quad i = V, N \quad (5.27)$$

Here, V and N stand for water vapor and nitrogen. Taking time derivative of gas density function in Eq. (5.27), we have

$$\frac{\partial p}{\partial t} = \sum_i \frac{RT\omega_i}{M_i} \frac{\partial \rho^g}{\partial t} + \sum_i \frac{R\rho^g \omega_i}{M_i} \frac{\partial T}{\partial t} + \sum_i \frac{RT\rho^g}{M_i} \frac{\partial \omega_i}{\partial t} \quad (5.28)$$

Again time derivative of pressure function of Eq. (5.27) and considering  $N_2$  is no-reactive ( $\dot{\rho}^s = \dot{\rho}_V = \dot{\rho}$ ), we find

$$\frac{\partial p}{\partial t} = \sum_i \frac{RT}{M_i} \frac{\partial \rho_i}{\partial t} + \sum_i \frac{R\rho^g \omega_i}{M_i} \frac{\partial T}{\partial t} \quad (5.29)$$

the energy balance thus reads

$$\left[ (1-n)\rho^s c_p^s + n\rho^g \left( c_p^g - \frac{R}{M} \right) \right] \frac{\partial T}{\partial t} = (1-n) \frac{\partial \rho^s}{\partial t} \left( \Delta h - \frac{nTR}{M_V} \right) \quad (5.30)$$

If  $\delta = \frac{nR}{M_V c_p^s}$ , integration yields

$$\frac{nRT}{M_V} = \Delta h - \left( \Delta h - \frac{nRT_0}{M_V} \right) \left( \frac{(1-n)\rho^s c_p^s + n\rho^g \left( c_p^g - \frac{R}{M} \right)}{(1-n)\rho_0^s c_{p0}^s + n\rho_0^g \left( c_{p0}^g - \frac{R}{M_0} \right)} \right)^{-\delta} \quad (5.31)$$

### 5.2.5.1 Definition

In this example, the behavior of the model when mass transfer occurs between the phases is verified. Consider a closed off system similar to the one described in the previous example. The porous body is filled with a mixture of nitrogen and water vapor modelled as ideal gasses.

### 5.2.5.2 Model Geometry and Conditions

- Geometry: Water vapor is introduced from inlet of a 10 cm long bed of CaO.
- IC: Pores are filled with  $N_2$  ( $\omega_N = 0.5$ ) at  $p_0 = 1.0 \times 10^5$  Pa and  $T_0 = 400$  K.
- BC: No flow condition is prescribed at inlet and outlet boundaries.
- ST: Injection rate for water vapor  $1 \times 10^{-10}$  kg  $\cdot$  s $^{-1}$  is assigned for one second.

### 5.2.5.3 Numerical Solution

The exemplary parameter set is listed in Table 5.7. The values are chosen such that temperature changes due to mass transfer are visible in both phases. The numerical

**Table 5.7** Simulation parameters

Parameter	Symbol	Value	Unit
Length	$L$	10	cm
Area	$A$	0.0314	m <sup>2</sup>
Heat conductivity	$\kappa^s$	0.4	W $\cdot$ m <sup>-1</sup> $\cdot$ K <sup>-1</sup>
Permeability	$k$	$6.94 \times 10^{-14}$	m <sup>2</sup>
Self-diffusion coefficient	$D_0$	$9.5 \times 10^{-5}$	m <sup>2</sup> $\cdot$ s <sup>-1</sup>
Dispersivity	$\alpha_l, \alpha_t$	0.1, 0.01	m
Heat of reaction	$\Delta h$	$5.0 \times 10^5$	J $\cdot$ kg <sup>-1</sup>
Time step	$\Delta t$	0.001	s
Simulation time	$t$	1.0	s

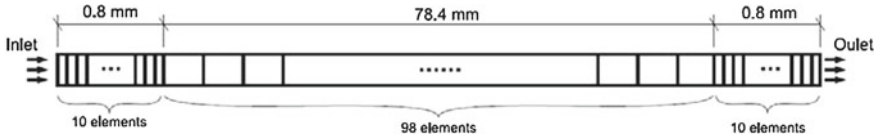


Fig. 5.10 Model setup

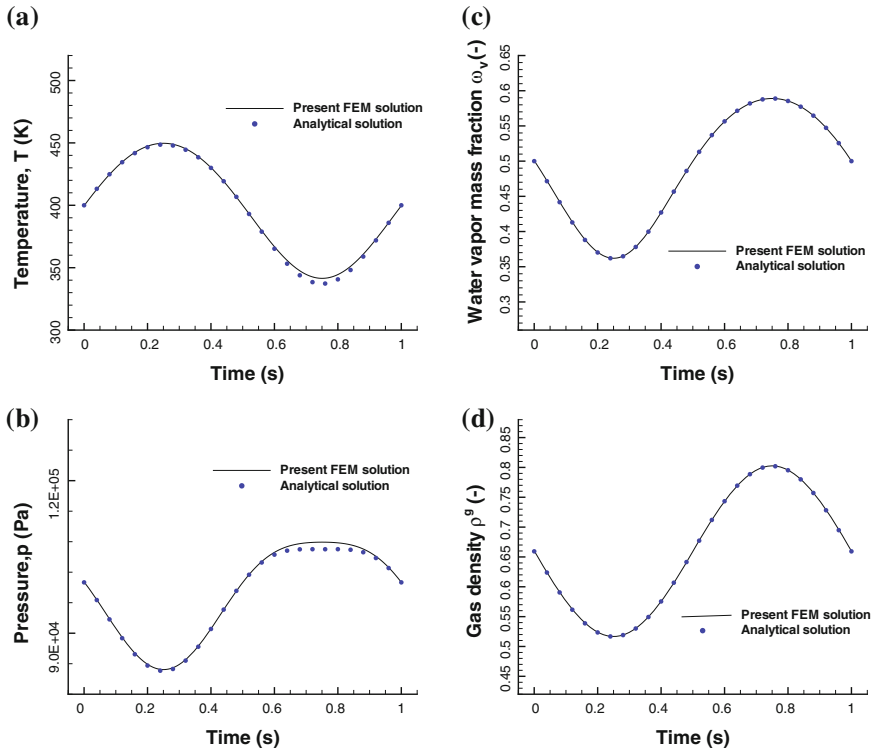


Fig. 5.11 Comparison of present FEM solution with the analytical solutions of **a** temperature; **b** pressure; **c** water vapor mass fraction; **d** gas density

model was run with the Multi Componential Flow numerical module with a very high number for  $\Delta h$ . A time step size of 0.001 s was chosen for a time interval of 1 s. One dimensional line elements were used for its spatial discretisation (Fig. 5.10).

The model correctly reproduced the conditions of thermal equilibrium. During the initial stage of the reaction the gas loses mass while the solid (not shown) gains that amount of mass. During the back reaction the opposite effect occurs. An equally good match is obtained for the temperature profiles (Fig. 5.11a). If no heat of reaction is released, the gas simply cools down as its density and pressure drop. The solid phase follows this trend due to the very low density chosen here for demonstration purposes. In the gas pressure profiles this switch of sign can be observed as well

**Table 5.8** Parameter values for interphase mass transfer verification

$n$ (-)	$\rho^s$ ( $\text{kg} \cdot \text{m}^{-3}$ )	$\rho_0^g$ ( $\text{kg} \cdot \text{m}^{-3}$ )	$c_p^g$ ( $\text{J} \cdot \text{kg}^{-1} \cdot \text{K}^{-1}$ )	$c_p^s$ ( $\text{J} \cdot \text{kg}^{-1} \cdot \text{K}^{-1}$ )
0.7	1.0	0.659	1,000	1,000
$T_0$ (K)	$f$ (Hz)	$a$ ( $\text{kg} \cdot \text{m}^{-3}$ )	$\omega_{V0}$ (-)	$M_0$ ( $\text{kmol} \cdot \text{kg}^{-1}$ )
400	$2\pi$	0.1	0.5	21.919

along with an increasingly non-sinusoidal trend in the pressure profile (Fig. 5.11b). The numerically obtained water vapor mass fraction and gas density are compared well with the analytical solution (Fig. 5.11c, d and Table 5.8).

## References

1. J. Bear. *Dynamics of Fluids in Porous Media*. Elsevier, New York, 1972.
2. R. Helmig. *Multiphase Flow and Transport Processes in the Subsurface*. Springer, 1997.
3. J.C. Tsai and Y.P. Chen. Application of a volume translated peng-robinson equation of state on vapor liquid equilibrium calculations. *Fluid Phase Equilib*, 145:193–215, 1998.
4. M.Th. van Genuchten and W.J. Alves. Alvesanalytical solutions of the one-dimensional convective-dispersive solute transport equation. Technical report, U.S. Department of Agriculture, Washington, DC, Technical bulletin no. 1661, 1982.
5. L.K. Brakefield. Physical and numerical modeling of buoyant groundwater plumes. Technical report, Auburn University, Alabama, USA, Thesis, 2008.
6. A. Ebigbo, H. Class, and R. Helmig. Co2 leakage through an abandoned well: problem oriented benchmarks. *Comput Geosci*, 11:103–115, 2007.

# Chapter 6

## Random Walk Particle Tracking

Yuanyuan Sun, Chan-Hee Park, Geraldine Pichot and Joshua Taron

The classical advection-dispersion equation of a conservative solute in porous media can be written as [1]

$$\frac{\partial C}{\partial t} = -\nabla \cdot (\mathbf{v}C) + \nabla \cdot (D\nabla C) \quad (6.1)$$

where  $C$  is the concentration ( $\text{kg m}^{-3}$ ),  $\mathbf{v}$  is the pore velocity vector ( $\text{m s}^{-1}$ ),  $D$  is the hydrodynamic dispersion tensor ( $\text{m}^2 \text{s}^{-1}$ ),  $t$  is time (s) and  $\nabla$  is the differential operator.

The random walk particle tracking (RWPT) method is issued from stochastic physics. The stochastic differential equation is [2]

$$x(t_i) = x(t_{i-1}) + \mathbf{v}(x(t_{i-1}))\Delta t + Z\sqrt{2D(x(t_{i-1}))\Delta t} \quad (6.2)$$

where  $x$  is the coordinate of the particle location,  $\Delta t$  is the time step, and  $Z$  is a random number whose mean is zero and variance is unity.

It has been shown that this equation is equivalent to an equation that is slightly different from the advection-dispersion Eq. (6.1). To be equivalent to Eq. (6.1), the modified velocity [3] and dispersion tensor [1] are expressed as

---

Y. Sun (✉)  
Chinese Research Academy of Environmental Sciences CRAES, 8 Dayangfang BeiYuan Road,  
Beijing 100012, China  
e-mail: sunyuanyuan@aliyun.com

C.-H. Park  
Korea Institute of Geoscience and Mineral Resources (KIGAM), Daejeon, Republic of Korea

J. Taron  
United States Geological Survey (USGS), Reston, VA, USA

G. Pichot  
Inria Rennes-Bretagne Atlantique Research Centre, Campus de Beaulieu, 35042 Rennes Cedex,  
France  
e-mail: Geraldine.Pichot@inria.fr

© Springer International Publishing Switzerland 2015

O. Kolditz et al. (eds.), *Thermo-Hydro-Mechanical-Chemical Processes in Fractured Porous Media: Modelling and Benchmarking*, Terrestrial Environmental Sciences, DOI 10.1007/978-3-319-11894-9\_6

$$\mathbf{v}_i^* = \mathbf{v}_i + \sum_{j=1}^3 \frac{\partial D_{ij}}{\partial x_j} \quad (6.3)$$

$$D_{ij} = \alpha_T |\mathbf{v}| \delta_{ij} + (\alpha_L - \alpha_T) \frac{\mathbf{v}_i \mathbf{v}_j}{|\mathbf{v}|} + D_{ii}^d \quad (6.4)$$

where  $\delta_{ij}$  is the Kronecker symbol,  $\alpha_L$  is the longitudinal dispersion length,  $\alpha_T$  is the transverse dispersion length,  $D_{ij}^d$  is the tensor of molecular diffusion coefficient, and  $\mathbf{v}_i$  is the component of the mean pore velocity in the  $i$ th direction.

The equivalent stochastic differential equation to Eq. (6.1) in three-dimensional problems can be written as [4–6]

$$\begin{aligned} x_{t+\Delta t} &= x_t + \left( \mathbf{v}_x(x_t, y_t, z_t, t) + \frac{\partial D_{xx}}{\partial x} + \frac{\partial D_{xy}}{\partial y} + \frac{\partial D_{xz}}{\partial z} \right) \Delta t \\ &\quad + \sqrt{2D_{xx}\Delta t}Z_1 + \sqrt{2D_{xy}\Delta t}Z_2 + \sqrt{2D_{xz}\Delta t}Z_3 \\ y_{t+\Delta t} &= y_t + \left( \mathbf{v}_y(x_t, y_t, z_t, t) + \frac{\partial D_{yx}}{\partial x} + \frac{\partial D_{yy}}{\partial y} + \frac{\partial D_{yz}}{\partial z} \right) \Delta t \\ &\quad + \sqrt{2D_{yx}\Delta t}Z_1 + \sqrt{2D_{yy}\Delta t}Z_2 + \sqrt{2D_{yz}\Delta t}Z_3 \\ z_{t+\Delta t} &= z_t + \left( \mathbf{v}_z(x_t, y_t, z_t, t) + \frac{\partial D_{zx}}{\partial x} + \frac{\partial D_{zy}}{\partial y} + \frac{\partial D_{zz}}{\partial z} \right) \Delta t \\ &\quad + \sqrt{2D_{zx}\Delta t}Z_1 + \sqrt{2D_{zy}\Delta t}Z_2 + \sqrt{2D_{zz}\Delta t}Z_3 \end{aligned} \quad (6.5)$$

where  $x$ ,  $y$ , and  $z$  are the coordinates of the particle location,  $\Delta t$  is the time step, and  $Z_i$  is a random number whose mean is zero and variance is unity.

In Eq. (6.5), the spatial derivatives of the dispersion coefficients are introduced from the modified velocity [3]. Together with Eq. (6.4), the spatial derivatives of the dispersion coefficients can be expressed as a function of the derivatives of velocity. Note that to obtain the derivatives of velocity, velocity has to be continuous mathematically. To this end, we interpolate velocity at any location in an element from the known velocity at the element nodes.

Since the proposed RWPT method makes use of the FEM for velocity estimation, the derivative of velocity within each element is computed as in Fig. 6.1 and written as

$$\begin{aligned} \frac{\partial \mathbf{v}_x}{\partial x} &= \frac{\mathbf{v}(x_R) - \mathbf{v}(x_L)}{l_x}; & \frac{\partial \mathbf{v}_y}{\partial y} &= \frac{\mathbf{v}(y_U) - \mathbf{v}(y_D)}{l_y}; & \frac{\partial \mathbf{v}_z}{\partial z} &= \frac{\mathbf{v}(z_N) - \mathbf{v}(z_S)}{l_z} \\ \frac{\partial \mathbf{v}_x}{\partial y} &= \frac{\partial \mathbf{v}_x}{\partial z} = \frac{\partial \mathbf{v}_y}{\partial z} = \frac{\partial \mathbf{v}_y}{\partial x} = \frac{\partial \mathbf{v}_z}{\partial x} = \frac{\partial \mathbf{v}_z}{\partial y} \simeq 0 \end{aligned} \quad (6.6)$$

where  $x_L$  and  $x_R$  are intersection points of the element edges with a line parallel to the global  $x$  axis at which velocities are  $\mathbf{v}(x_L)$  and  $\mathbf{v}(x_R)$ ,  $y_D$  and  $y_U$  are intersection points of the element edges from down to up with a line parallel to the global  $y$  axis at which velocities are  $\mathbf{v}(y_D)$  and  $\mathbf{v}(y_U)$ ,  $z_S$  and  $z_N$  are the intersection points of the element edges from south to north with a line parallel to the global  $z$  axis at which velocities are  $\mathbf{v}(z_S)$  and  $\mathbf{v}(z_N)$ , and  $l_x$ ,  $l_y$ , and  $l_z$  are the length of each intersection line, respectively.

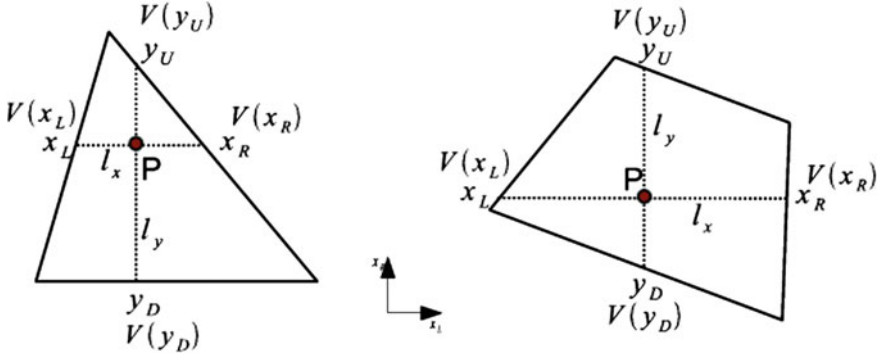


**Fig. 6.1** Spatial derivatives of velocity for a particle in triangular and quadrilateral elements ( $V$  is velocity)

Thus, the derivatives of the dispersion coefficients are as follows [7]

$$\begin{aligned}
 \frac{\partial D_{xx}}{\partial x} &= \mathbf{v}_x \frac{\partial \mathbf{v}_x}{\partial x} \left[ \alpha_L \left( \frac{2}{\mathbf{v}} - \frac{\mathbf{v}_z^2}{\mathbf{v}^3} \right) - \alpha_T \frac{\mathbf{v}_y^2 + \mathbf{v}_z^2}{\mathbf{v}^3} \right] \\
 \frac{\partial D_{xy}}{\partial y} &= (\alpha_L - \alpha_T) \left[ \frac{\partial \mathbf{v}_y}{\partial y} \frac{\mathbf{v}_x}{\mathbf{v}} - \frac{\mathbf{v}_x \mathbf{v}_y^2}{\mathbf{v}^3} \frac{\partial \mathbf{v}_y}{\partial y} \right] \\
 \frac{\partial D_{xz}}{\partial z} &= (\alpha_L - \alpha_T) \left[ \frac{\partial \mathbf{v}_z}{\partial z} \frac{\mathbf{v}_x}{\mathbf{v}} - \frac{\mathbf{v}_x \mathbf{v}_z^2}{\mathbf{v}^3} \frac{\partial \mathbf{v}_z}{\partial z} \right] \\
 \frac{\partial D_{yy}}{\partial y} &= \mathbf{v}_y \frac{\partial \mathbf{v}_y}{\partial y} \left[ \alpha_L \left( \frac{2}{\mathbf{v}} - \frac{\mathbf{v}_z^2}{\mathbf{v}^3} \right) - \alpha_T \frac{\mathbf{v}_x^2 + \mathbf{v}_z^2}{\mathbf{v}^3} \right] \\
 \frac{\partial D_{yx}}{\partial x} &= (\alpha_L - \alpha_T) \left[ \frac{\partial \mathbf{v}_x}{\partial x} \frac{\mathbf{v}_y}{\mathbf{v}} - \frac{\mathbf{v}_y \mathbf{v}_x^2}{\mathbf{v}^3} \frac{\partial \mathbf{v}_x}{\partial x} \right] \\
 \frac{\partial D_{yz}}{\partial z} &= (\alpha_L - \alpha_T) \left[ \frac{\partial \mathbf{v}_z}{\partial z} \frac{\mathbf{v}_y}{\mathbf{v}} - \frac{\mathbf{v}_y \mathbf{v}_z^2}{\mathbf{v}^3} \frac{\partial \mathbf{v}_z}{\partial z} \right] \\
 \frac{\partial D_{zz}}{\partial z} &= \mathbf{v}_z \frac{\partial \mathbf{v}_z}{\partial z} \left[ \alpha_L \left( \frac{2}{\mathbf{v}} - \frac{\mathbf{v}_z^2}{\mathbf{v}^3} \right) - \alpha_T \frac{\mathbf{v}_x^2 + \mathbf{v}_y^2}{\mathbf{v}^3} \right] \\
 \frac{\partial D_{zx}}{\partial x} &= (\alpha_L - \alpha_T) \left[ \frac{\partial \mathbf{v}_x}{\partial x} \frac{\mathbf{v}_z}{\mathbf{v}} - \frac{\mathbf{v}_z \mathbf{v}_x^2}{\mathbf{v}^3} \frac{\partial \mathbf{v}_x}{\partial x} \right] \\
 \frac{\partial D_{zy}}{\partial y} &= (\alpha_L - \alpha_T) \left[ \frac{\partial \mathbf{v}_y}{\partial y} \frac{\mathbf{v}_z}{\mathbf{v}} - \frac{\mathbf{v}_z \mathbf{v}_y^2}{\mathbf{v}^3} \frac{\partial \mathbf{v}_y}{\partial y} \right]
 \end{aligned} \tag{6.7}$$

Because velocity is not derivable at the interface of two adjacent elements in a nonuniform flow, computing dispersion coefficient derivatives by using a finite element approach would yield erroneous values [7]. To prevent these errors, a particle is coded to have information of an element index and the velocity estimation is continuous even at the elemental boundaries in this method. Thus, the derivatives of dispersion coefficients will be computed accordingly. This is an improved approach from the work by Hoteit et al. [7].

## 6.1 Particle Tracking in Porous Medium

### 6.1.1 Particle Tracking in Porous Medium: 1D Case Study

#### 6.1.1.1 Definition

A one-dimensional homogeneous aquifer is chosen to simulate a soil column experiment conducted by Harter et al. [8]. In the experiment, a constant flow rate was established, 2.5 pore volumes NaCl—tap water solution and 2.5 pore volumes *Cryptosporidium parvum* solution ( $1 \times 10^5$  oocysts per mL) were injected respectively, the outflow was continuously collected. Figure 6.2 shows the schematic description of the experiment.

NaCl—tap water solution is used as a tracer, which experiences only advection and dispersion. The *Cryptosporidium parvum* can be classified as a biological colloid. Colloids moving in porous media experience advection, dispersion, sorption-desorption, and filtration.

#### 6.1.1.2 Analytical Solution

For the one-dimensional transport including sorption-desorption and filtration through a homogeneous medium the following differential equation is applied

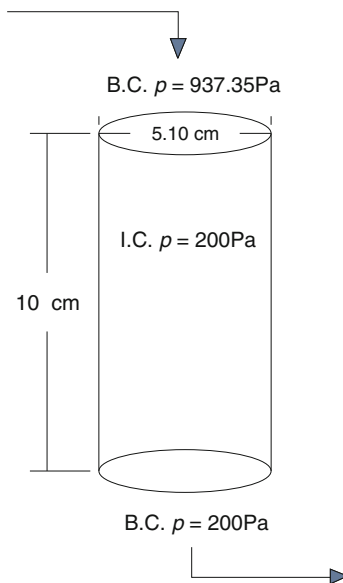


Fig. 6.2 Schematic of soil column experiment

$$\frac{\partial C}{\partial t} + \frac{\rho_b}{n} \frac{\partial C_S}{\partial t} = v\alpha_L \frac{\partial^2 C}{\partial x^2} - v\left(\frac{\partial C}{\partial x} + \lambda C\right) \quad (6.8)$$

where  $C$  is dissolved concentration ( $\text{kg m}^{-3}$ ),  $C_S$  is sorbed concentration ( $\text{kg kg}^{-1}$ ),  $t$  is time (s),  $\rho_b$  is bulk density ( $\text{kg m}^{-3}$ ),  $n$  is porosity ( $-$ ),  $v$  is velocity ( $\text{m s}^{-1}$ ),  $\alpha_L$  is longitudinal dispersivity (m),  $x$  is distance (m), and  $\lambda$  is filtration coefficient ( $\text{m}^{-1}$ ).

The instantaneous, linear sorption model assumes that

$$C_S = K_d C \quad (6.9)$$

where  $K_d$  is the partitioning coefficient ( $\text{m}^3 \text{kg}^{-1}$ ). The retardation coefficient  $R$  is

$$R = 1 + \frac{\rho_b}{n} K_d \quad (6.10)$$

The dispersion coefficient in the  $x$ -direction  $D_{xx}$  ( $\text{m}^2 \text{s}^{-1}$ ) is

$$D_{xx} = v\alpha_L \quad (6.11)$$

The analytical solution for a pulse input is [9]:

$$C = \frac{1}{2} C_0 \left[ \exp\left(\frac{vx(1-\gamma)}{2D_{xx}}\right) \text{erfc}\left(\frac{x-v\gamma t/R}{2\sqrt{D_{xx}t/R}}\right) + \exp\left(\frac{vx(1+\gamma)}{2D_{xx}}\right) \text{erfc}\left(\frac{x+v\gamma t/R}{2\sqrt{D_{xx}t/R}}\right) \right] \quad (6.12)$$

for  $t \in (0, \tau)$ , (injection time from 0 to  $\tau$ )

$$C = \frac{1}{2} C_0 \left[ \exp\left(\frac{vx(1-\gamma)}{2D_{xx}}\right) \text{erfc}\left(\frac{x-v\gamma t/R}{2\sqrt{D_{xx}t/R}}\right) + \exp\left(\frac{vx(1+\gamma)}{2D_{xx}}\right) \text{erfc}\left(\frac{x+v\gamma t/R}{2\sqrt{D_{xx}t/R}}\right) - \exp\left(\frac{vx(1-\gamma)}{2D_{xx}}\right) \text{erfc}\left(\frac{x-v\gamma(t-\tau)/R}{2\sqrt{D_{xx}(t-\tau)/R}}\right) - \exp\left(\frac{vx(1+\gamma)}{2D_{xx}}\right) \text{erfc}\left(\frac{x+v\gamma(t-\tau)/R}{2\sqrt{D_{xx}(t-\tau)/R}}\right) \right] \quad (6.13)$$

for  $t \in (\tau, \infty)$ , where

$$\gamma = \sqrt{1 + 4v\lambda R D_{xx}/v^2} \quad (6.14)$$

### 6.1.1.3 Numerical Solution

The calculation area is simplified to a line with the length of 0.1 m. For the numerical model 100 elements and 101 nodes are included. Head gradient is set by giving two constant pressures at both left and right boundaries to establish a uniform velocity field with the value of  $7.1 \text{ m d}^{-1}$ .

The number of pore volume ( $x$ -axis) is calculated by

$$P_V = \frac{vt}{L} \quad (6.15)$$

where  $v$  is the seepage velocity,  $L$  is the length of the soil column. Considering the Courant number, the time step size is set by assigning  $P_V$  to 0.01. In the simulation, 100 particles per time steps are loaded near the left boundary for 250 time steps.

The filtration process is described by using the filtration coefficient. The sorption-desorption process is described by the two-rate model from Johnson et al. [10]. In the two-rate model, desorption is governed by two different rate coefficients

$$N/N_0 = Ae^{-k_1t} + (1 - A)e^{-k_2t} \quad (6.16)$$

where  $N$  is the number of particles remaining on the medium at time  $t$ ,  $N_0$  is the initial number of particles on the medium at the time of initial sorption,  $A$  is a weighting factor, and  $k_1$  and  $k_2$  are the fast and slow sorption rate coefficient, respectively. Relevant parameters are listed in Table 6.1.

### 6.1.1.4 Results

The tracer experiences only advection and dispersion, which means in Eq.(6.8),  $C_S = 0$ ,  $\lambda = 0$ . The results of RWPT simulation for the distribution of concentration over time are compared to those of measured value from the experiment by Harter, the analytical solution, and the OGS simulation with the mass transport method.

**Table 6.1** Model parameters for the column experiment

Symbol	Parameter	Value	Unit
$k$	Permeability	$1.114476 \times 10^{-11}$	$\text{m}^2$
$\alpha_L$	Longitudinal dispersivity	0.005	m
$n$	Porosity(tracer)	0.5	—
$n$	Porosity(colloid)	0.42	—
$A$	Weighting factor	0.9	—
$k_1$	Fast sorption rate coefficient	0.1	—
$k_2$	Slow sorption rate coefficient	0.001	—
$\lambda$	Filtration coefficient	5.2	$\text{m}^{-1}$

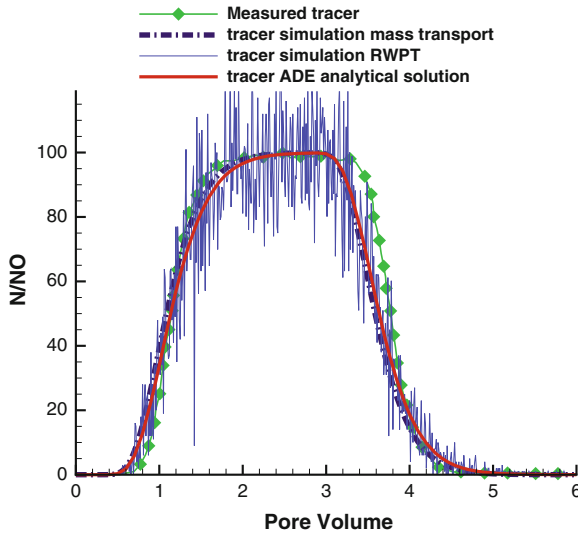


Fig. 6.3 Tracer transport with advection and dispersion

The comparison results are shown in Fig. 6.3, where the green curve is the measured value, the dashed black curve is the simulation result operated with FEM, the blue curve is the RWPT simulation result, and the red curve is the analytical solution.

In the colloid transport simulation, the number of particles leaving the right boundary is counted each time step. The number is then converted to concentration in order to obtain the corresponding breakthrough curve over time. The comparison with the

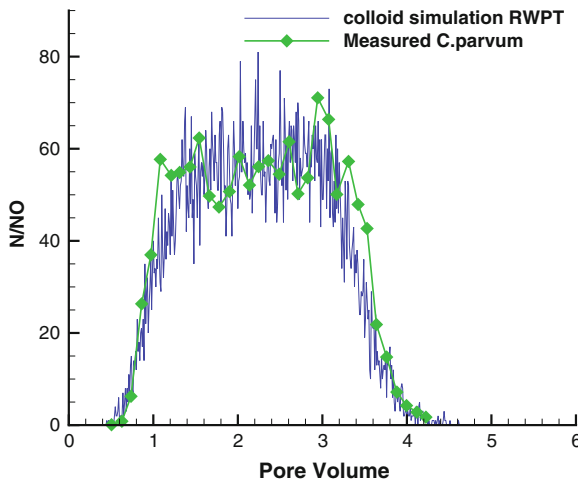


Fig. 6.4 Colloid transport with sorption-desorption and decay

measured value from Harter’s experiment is shown in Fig. 6.4, where the green curve is the measured value, and the blue curve is the RWPT simulation result. No analytical solution is available in this kind of situation.

### 6.1.2 Particle Tracking in Porous Medium: 2D Case Study

#### 6.1.2.1 Definition

A two-dimensional homogeneous aquifer is chosen to verify advective dispersive transport. The dimension of the model domain is 184 m by 64 m where the uniform velocity field is held constant in the  $x$  direction (Fig. 6.5).

#### 6.1.2.2 Analytical Solution

The stated problem can be solved with an analytical solution provided by Ogata et al. [11].

$$C(x, y, t) = \frac{C_0 A}{4\pi t \sqrt{D_{xx} + D_{yy}}} \exp \left[ -\frac{(x - x_0)^2}{4D_{xx}t} - \frac{(y - y_0)^2}{4D_{yy}t} \right] \quad (6.17)$$

where  $C_0$  is the initial concentration.

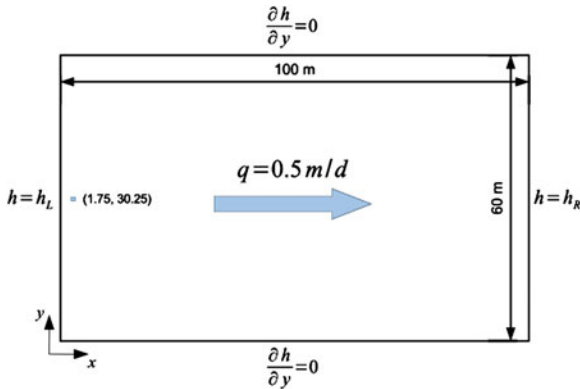


Fig. 6.5 Schematic of 2D homogeneous model

### 6.1.2.3 Numerical Solution

The domain is discretized with quadrilateral elements of 0.5 m by 0.5 m. The same grid density is also used for converting particle distributions to element concentrations. The head gradient of one in the  $x$  direction is set by assigning two constant boundary conditions along both the left and right sides, thus obtaining the uniform velocity field with the value of  $0.5 \text{ m d}^{-1}$ .

The initial source load is applied to an area with dimensions of 0.1 m by 0.1 m to have an initial concentration of  $C_0 = 1 \text{ kg m}^{-3}$ . The material properties for this model setup are given in Table 6.2.

### 6.1.2.4 Results

Transport results of the RWPT method compared with the analytical solution at 20, 40, and 60 days are provided in Fig. 6.6. The solid line is the analytical solution, the dotted line is the RWPT result. Contour lines are shown for  $C = 2.6e^{-4}$ ,  $1.6e^{-4}$ ,  $1.0e^{-4}$ , and  $4e^{-5}$ . The number of particles used for this simulation is 50,000. This is significantly less than the number of particles reported by Hassan et al. [12], who stated that up to 2.5 million particles were necessary to achieve smoothness of the solution due to oscillations around the contours. As the oscillations observed here for the method proposed are smaller than reported by Hassan et al. [12], the proposed method allows a dramatic reduction of around two orders of magnitude in the number of particles required for a smooth solution.

**Table 6.2** Material properties for 2D homogeneous medium

Symbol	Parameter	Value	Unit
$k$	Permeability	$1.114 \times 10^{-11}$	$\text{m}^2$
$\alpha_L$	Longitudinal dispersivity	0.1	m
$\alpha_T$	Transverse dispersivity	0.1	m

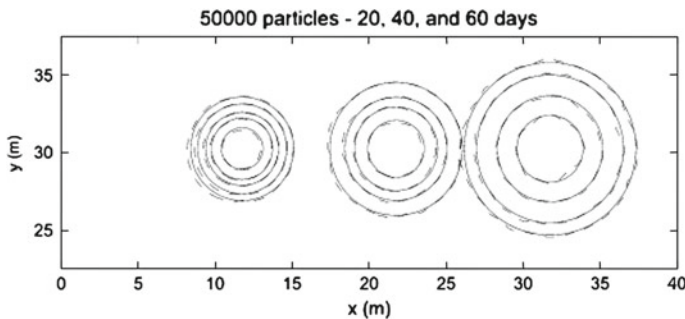


**Fig. 6.6** Transport results of the 2D RWPT method compared with analytical solution

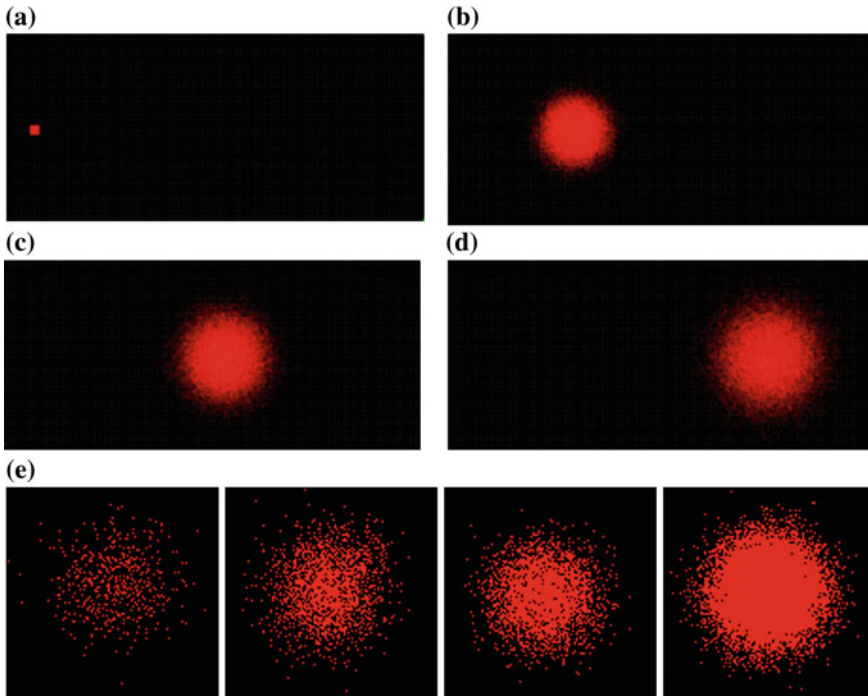


**Fig. 6.7** Particle clouds at different days. **a** Day 0. **b** Day 20. **c** Day 60. **d** Day 60. **e** Day 60 for each particle resolution

In addition, different numbers of particles are used to solve the same problem, producing several different particle clouds as shown in Fig. 6.7. Figure 6.7a–d show the particle clouds of 50,000 particles at 0, 20, 40, and 60 days, Fig. 6.7e shows particle clouds of 1,000, 5,000, 10,000, and 50,000 particles at 60 days.

### 6.1.3 Particle Tracking in Porous Medium: 3D Case Study

#### 6.1.3.1 Definition

A three-dimensional homogeneous cube is chosen to verify advective dispersive transport. The side length of the cube model domain is 100m. The velocity field is held constant in the diagonal direction from the bottom left to top right (Fig. 6.8).

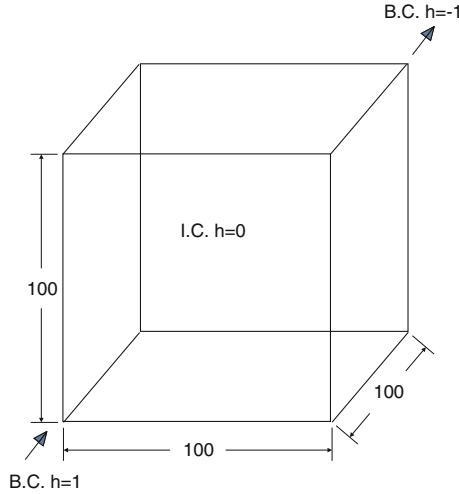


Fig. 6.8 Schematic of 3D homogeneous model

### 6.1.3.2 Analytical Solution

The stated problem can be solved with an analytical solution provided by Ogata et al. [11].

$$C(x, y, z, t) = \frac{C_0 \mathbf{v}}{8 (\pi t)^{3/2} \sqrt{D_{xx} D_{yy} D_{zz}}} \times \exp \left[ -\frac{(x - x_0)^2}{4D_{xx}t} - \frac{(y - y_0)^2}{4D_{yy}t} - \frac{(z - z_0)^2}{4D_{zz}t} \right] \quad (6.18)$$

where  $C_0$  is the initial concentration.

### 6.1.3.3 Numerical Solution

The domain is discretized with tetrahedral elements. The same grid density is used for converting particle distributions to element concentrations. The head gradient is set by assigning two constant boundary conditions on the diagonal joint points.

The initial source load is applied to an area close to the bottom left of the domain with an initial concentration of  $C_0 = 1 \text{ kg m}^{-3}$ . The material properties for this model setup are given in Table 6.3.

**Table 6.3** Material properties for 3D homogeneous medium

Symbol	Parameter	Value	Unit
$k$	Permeability	$6.0804 \times 10^{-10}$	$\text{m}^2$
$\alpha_L$	Longitudinal dispersivity	0.005	m
$\alpha_T$	Transverse dispersivity	0.005	m
$n$	Porosity	0.2	—

### 6.1.3.4 Results

The advection-dispersion of the particles pulse across the cube is shown in Fig. 6.9. At the beginning, particles are assembled together as they were released from positions that are very close to each other. As the particles moving along with the flow, they disperse and form a spherical surface-shaped cloud. When the particles move to the center of the cube, the area of the spherical surface-shaped cloud reach to the maximum. After particles across the center of the cube, as the flow-paths begin to converge, the shape of the particle cloud change to a funnel-shaped curved surface. Particles move along the diagonal line have the bigger velocities and shorter pathlines so they reach to the top right corner of the cube earlier than other particles.

The number of particles that pass the top right corner of the cube is counted at every time step in order to generate the concentration breakthrough curve. The result

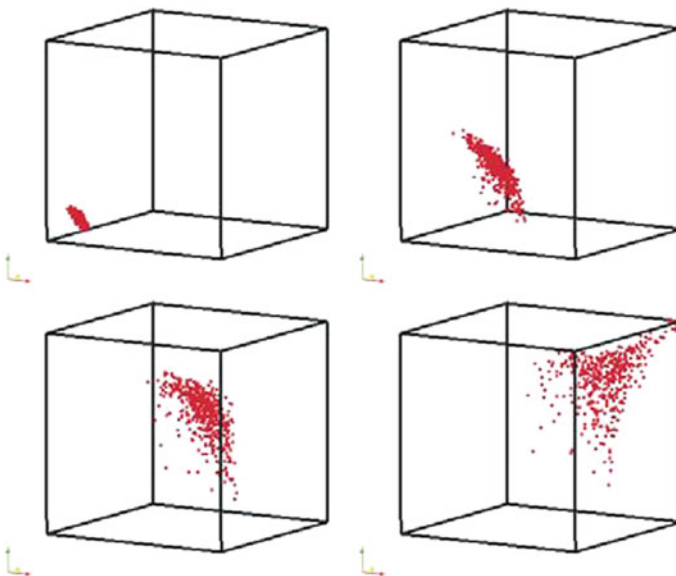


**Fig. 6.9** Particle clouds in the *cube*

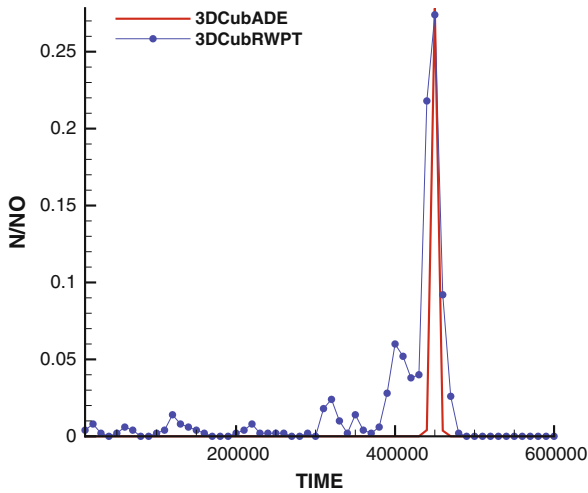


**Fig. 6.10** Transport results of the 3D RWPT method compared with analytical solution

of RWPT simulation for the distribution of concentration over time is compared to the analytical solution. The comparison results are shown in Fig. 6.10, where the blue curve is the RWPT simulation result, and the red curve is the analytical solution. The shape of the breakthrough curve is classical and similar to 1D and 2D simulations. With a relatively large number of particles the problem of fluctuations in concentration calculation can be overcome.

This benchmark shows that the proposed RWPT method can describe the fluid flow and solute transport in more details comparing to the traditional finite element method. With the post-processing programming one can observe the visualized results of the movement of every single particle at any time step, and the development of the particle cloud over time. While with the traditional finite element method one can only get the result of concentration distribution.

## 6.2 Particle Tracking in Pore Scale

Physical observations and theoretical treatments of flow in porous media are usually associated with three different length scales: pore-, local-, and field-scales. Dominant processes and governing equations may vary with scales. In this benchmark, efforts are taken in order to simulate solute transport in pore scale in a simplified manner. The governing equation adopted here is the groundwater flow equation based on Darcy's law.

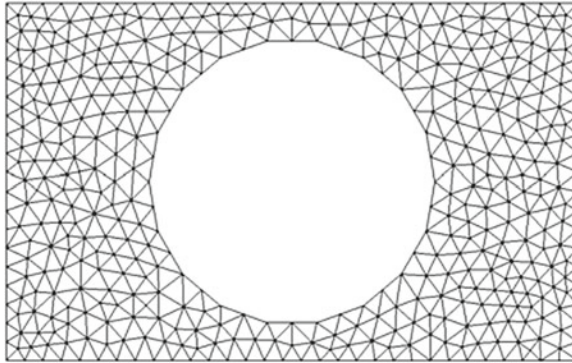


**Fig. 6.11** Mesh of 2D box with one grain inside

## 6.2.1 Particle Tracking in Pore Scale: 2D Case Study

### 6.2.1.1 Definition

To simulate particles moving in pore scale space, first the problem is simplified into a two-dimensional case which is a box with only one grain inside. The calculation area is a rectangular space with a circle in the middle, the void between the circle and the rectangular is the calculation domain and discretized by triangle mesh (Fig. 6.11).

### 6.2.1.2 Numerical Solution

Firstly, the proposed RWPT method in this model is testified by assign constant hydraulic head to the left and right boundaries (Dirichlet boundary condition), and no-flow boundary conditions to the top and bottom boundaries. Particles are released from a line that is close to the left boundary. Relative parameters are listed in Table 6.4.

### 6.2.1.3 Results

The particles are moving in the pore space according to the velocity field. Particle cloud develops over time is show in Fig. 6.12. The shape of the particle cloud is a

**Table 6.4** Material properties for 2D pore scale model with one grain inside—advective

Symbol	Parameter	Value	Unit
$k$	Permeability	$1 \times 10^{-10}$	$\text{m}^2$
$D_d$	Diffusion coefficient	0.0	$\text{m}^2 \text{s}^{-1}$
$n$	Porosity	1.0	—

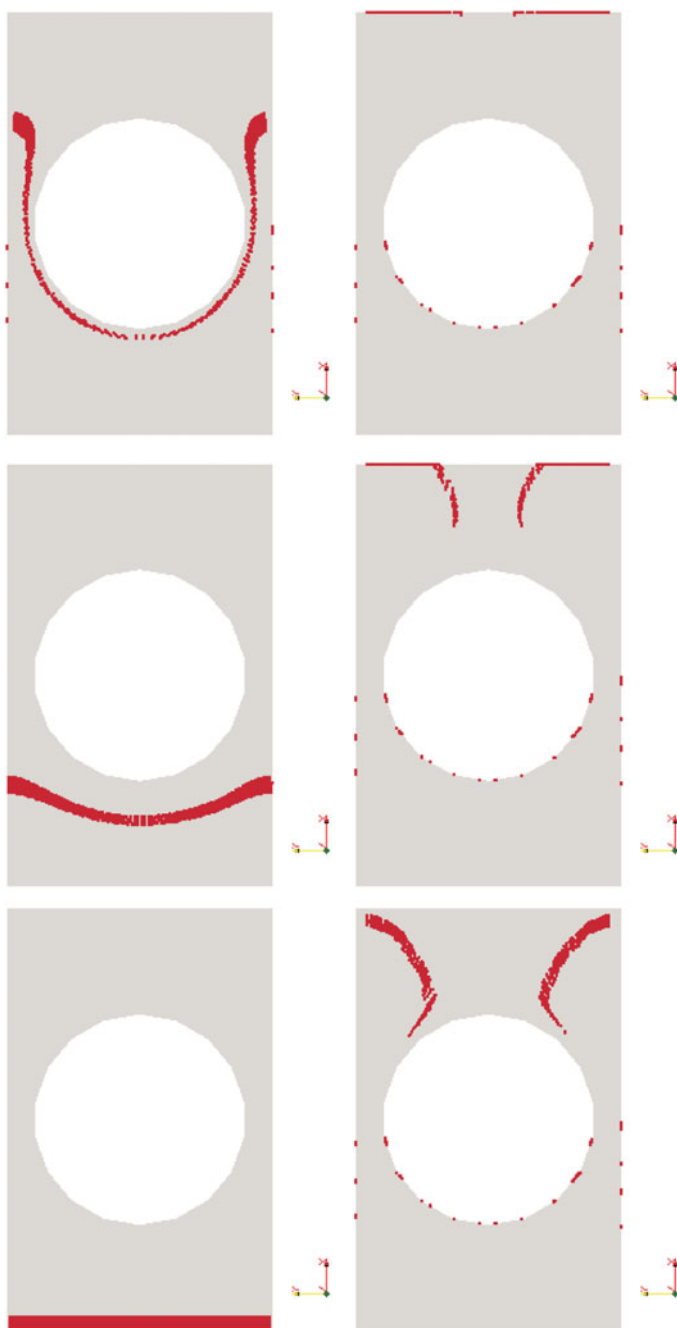


Fig. 6.12 Particles advect in *rectangular* domain with one grain

straight line in the beginning, and then is curved a little as it getting closer to the grain. The velocities in the area surrounding the grain are very small that particles in this area are moving very slowly. When a particle hit the surface of the grain or the boundary of the box, it will be captured. Particles pass through the throats between the grain and the box are accelerated as the velocities in these throats are large. After passing through the throats, particles spread to form an arc and move on to the right side boundary. In the zone that is behind the grain no particles are observed because the flow velocity is relatively small and dispersion is not considered in this benchmark.

#### 6.2.1.4 Discussion 1

If there is no flow in this domain, and the molecular diffusion coefficient is increased, then the movements of the particles are dominated by the molecular diffusion process. Relative parameters are listed in Table 6.5.

Particles are released from a line that is close to the left boundary. As there is no flow, particles are moving randomly in the pore space. Particle cloud develops over time is show in Fig. 6.13. Some of the particles attach to the surface of the grain or the boundary of the box. The molecular diffusion coefficient is relative to temperature. This benchmark is aimed to achieve the effect that particles are moving differently when temperature changes.

#### 6.2.1.5 Discussion 2

Next, the number of grains in the box is increased from one to six. The void between the circles and the rectangular is the calculation domain and discretized by triangle mesh (Fig. 6.14). Dirichlet boundary conditions are set by assign constant hydraulic head to the left and right boundaries. No-flow boundary conditions are set to the top and bottom boundaries. Particles are released from a line that is close to the left boundary. Relative parameters are unchanged as listed in Table 6.4.

Particle cloud develops over time is show in Fig. 6.15. Note that in this benchmark, released particles are displayed in the color of blue. When a particle hits the boundary and gets attached, it turns to red. But in the next time step, the attached particle still has the chance to detach and move again. It is clear that this benchmark is not a simple combination of six single grains, because they can affect each other. The velocity

**Table 6.5** Material properties for 2D pore scale model with one grain inside—diffusive

Symbol	Parameter	Value	Unit
$k$	Permeability	$1 \times 10^{-10}$	$\text{m}^2$
$D_d$	Diffusion coefficient	$1 \times 10^{-8}$	$\text{m}^2 \text{s}^{-1}$
$n$	Porosity	1.0	—

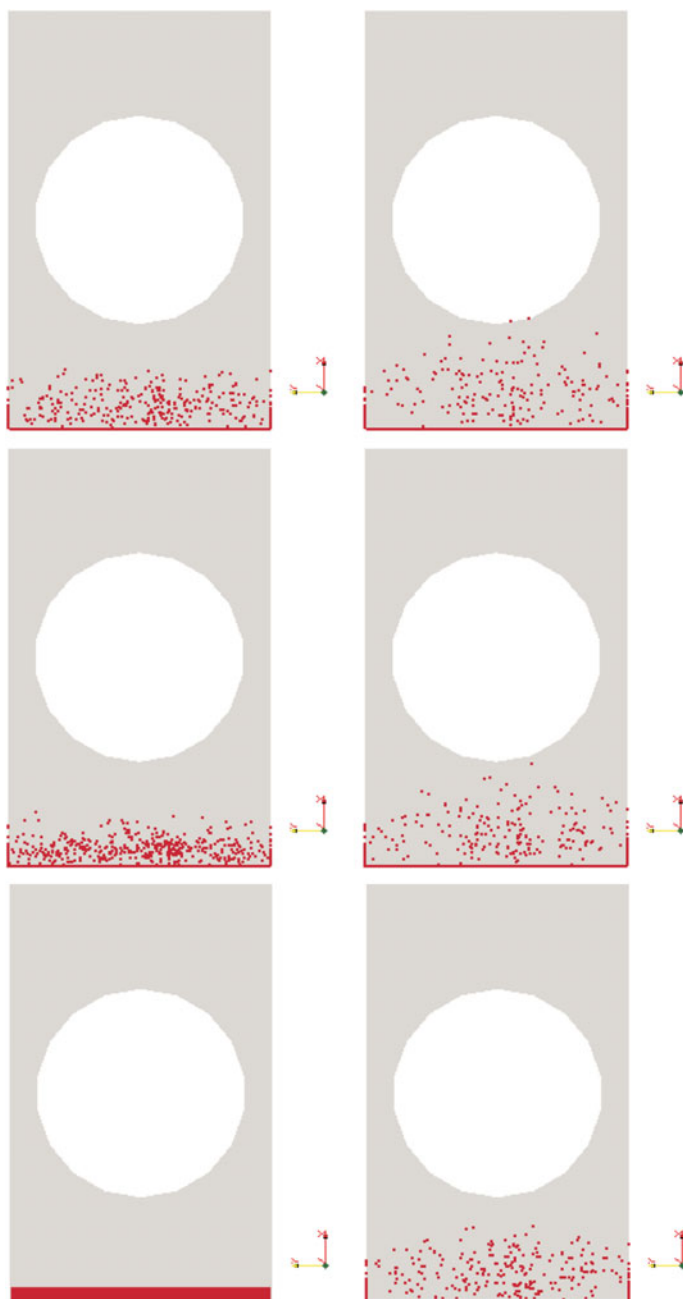


**Fig. 6.13** Particles diffuse in *rectangular* domain with one grain

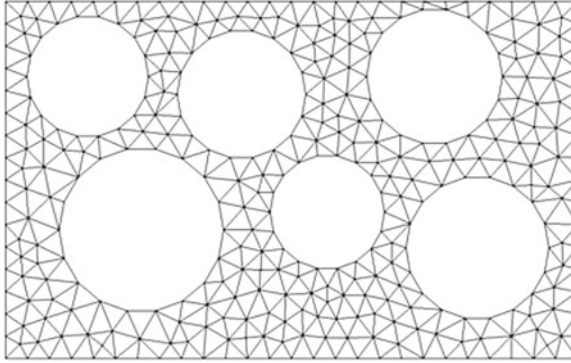


**Fig. 6.14** Mesh of 2D box with several grains inside

field in this case is with more complexity thus the particle cloud is complicated. But the particle cloud development obeys the same trend as in the single grain case.

### 6.2.1.6 Discussion 3

If the grain (circle) is discretized inside (Fig. 6.16), then particles attached to the surface of the grain can go into the grain and diffuse inside. Different porosity and permeability coefficient are given to grains and the pore space. Note that the different colors here represent materials with different properties. Dirichlet boundary conditions are set by assign constant hydraulic head to the left and right boundaries. No-flow boundary conditions are set to the top and bottom boundaries. Particles are released from a line that is close to the left boundary. Relative parameters are listed in Table 6.6.

Particle cloud develops over time is show in Fig. 6.17. The particles in the pore space are moving according to the velocity field. Note that there's no flow inside of the grains, only molecular diffusion. Particles that hit the surface of the grains can go into the grains and move inside. Their movements are because of molecular diffusion thus are random.

## 6.2.2 Particle Tracking in Pore Scale: 3D Case Study

### 6.2.2.1 Definition

Similar to the 2D case study, the problem is first simplified into a three-dimensional case with only one grain in a box. The calculation area is a cube space with a sphere in the center, the void space between the sphere and the cube is the calculation domain and discretized by tetrahedral mesh (Fig. 6.18).

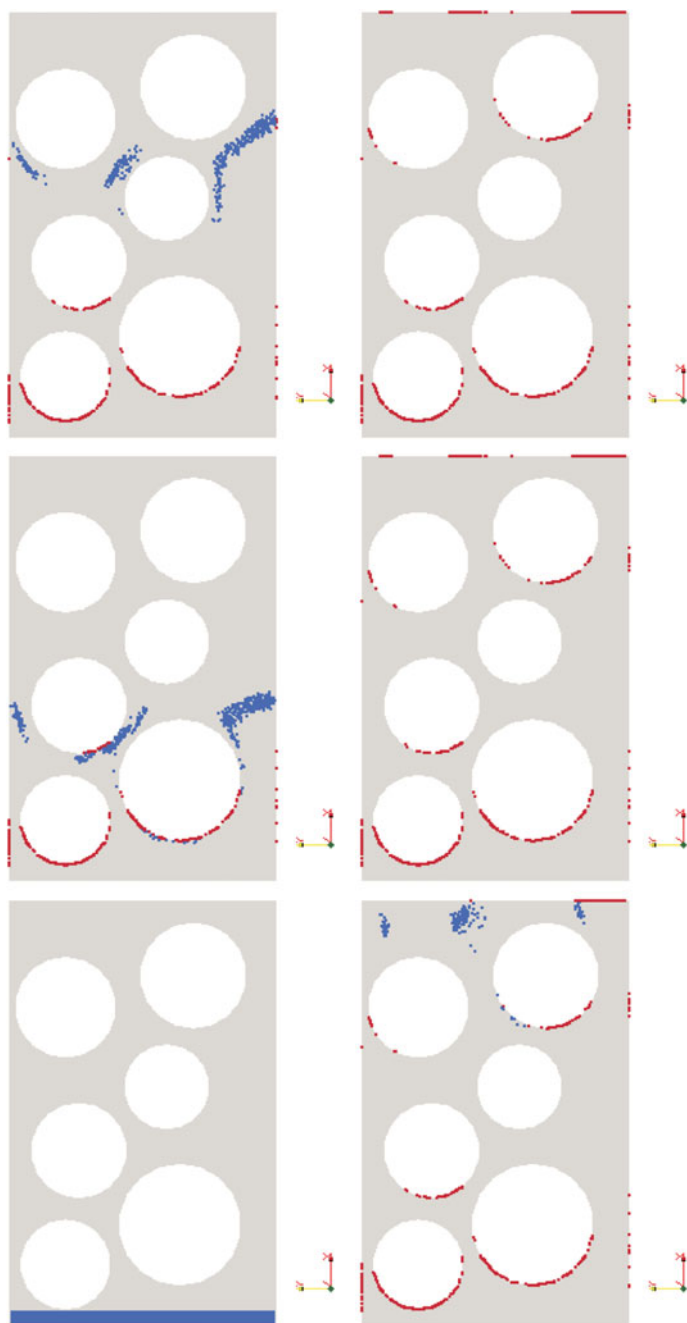
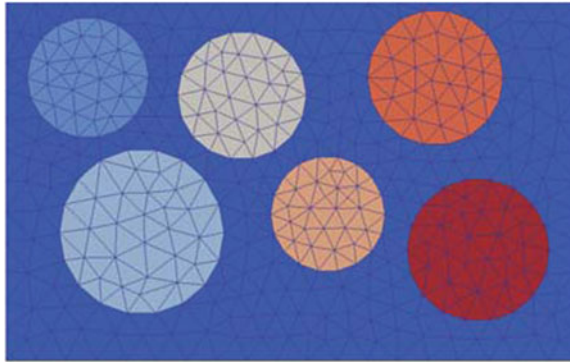


Fig. 6.15 Particles transport in *rectangular* domain with several grains



**Fig. 6.16** Mesh of 2D *box* with meshed grains inside

**Table 6.6** Material properties for 2D pore scale model with six meshed grains inside

Symbol	Parameter	Value	Unit
$k$	Permeability (pore space)	$1 \times 10^{-10}$	$\text{m}^2$
$k$	Permeability (grains)	$1 \times 10^{-12}$	$\text{m}^2$
$D_d$	Diffusion coefficient	$1 \times 10^{-15}$	$\text{m}^2 \text{s}^{-1}$
$n$	Porosity (pore space)	1.0	—
$n$	Porosity (grains)	0.1	—

### 6.2.2.2 Numerical Solution

The proposed RWPT method in this model is testified by assign constant hydraulic head to the left surface and right surface boundaries (Dirichlet boundary condition), and no-flow boundary conditions to the top, bottom, front, and back surface boundaries. Particles are released from a surface that is close and parallel to the left surface boundary. Relative parameters are listed in Table 6.7.

### 6.2.2.3 Results

The particles are moving in the pore space according to the velocity field. Particle cloud develops over time is show in Fig. 6.19. The shape of the particle cloud is a plain surface in the beginning, then is curved a little as it getting closer to the grain. The velocities in the area surrounding the grain is very small that particles in this area are moving very slowly. When a particle hit the surface of the grain or the box, it will be attached. In the zone that is behind the grain no particles are observed because the flow velocity is relatively small that no turbulence is happened in that zone.

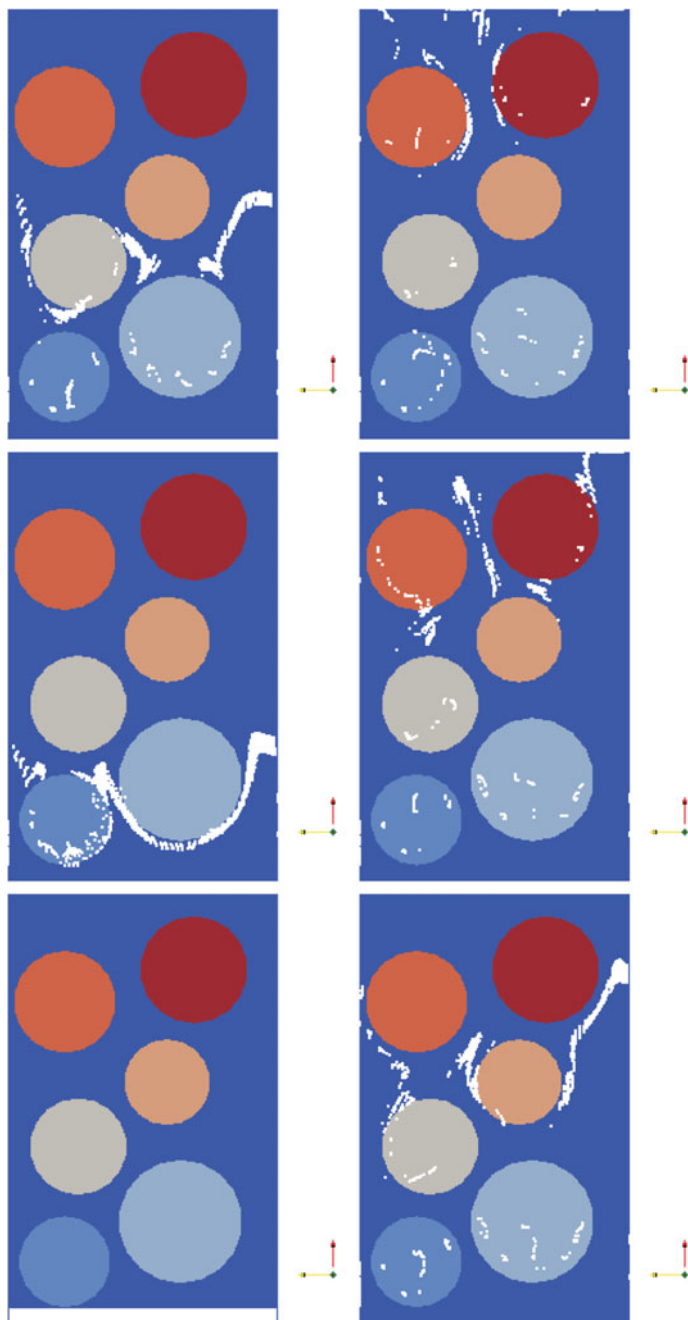


**Fig. 6.17** Particles transport in *rectangular* domain with several meshed grains

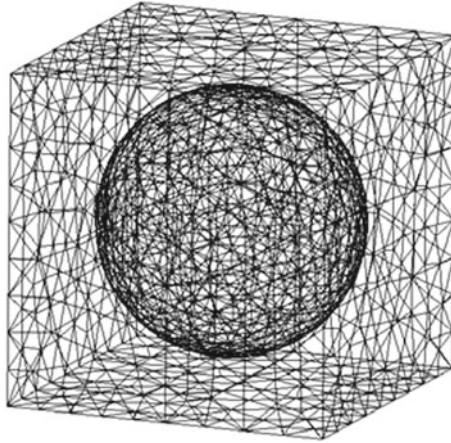


**Fig. 6.18** Mesh of 3D *box* with one grain inside

**Table 6.7** Material properties for 3D pore scale model with one grain inside

Symbol	Parameter	Value	Unit
$k$	Permeability	$1 \times 10^{-10}$	$\text{m}^2$
$D$	Diffusion coefficient	$1 \times 10^{-15}$	$\text{m}^2 \text{s}^{-1}$
$n$	Porosity	1.0	—

### 6.3 Particle Tracking with Different Flow Processes

The accuracy of the velocity field calculation is crucial to the precision of the RWPT method. In groundwater flow simulation, the velocity field is determined by the hydraulic head or pressure difference according to Darcy's law. However, when the velocity is higher, inertial effects can be significant and need for consideration; the non-linear impact of the pressure difference to the velocity can be described by Forchheimer flow. The proposed RWPT method is capable to be adopted with different flow processes since the displacements of the particles are calculated according to the velocity field, regardless of how it is obtained.

#### 6.3.1 Forchheimer Term

Modeling groundwater flow in porous media typically makes use of Darcy's law and equation of mass conservation to establish the groundwater flow equation. For low velocity flows, Darcy's law gives a good description of the flows and thus a number of linear forms have been developed [13, 14]. However, there are circumstances when the velocities are high that discrepancies occur between the experimental observations and simulation results obtained according to Darcy's law.

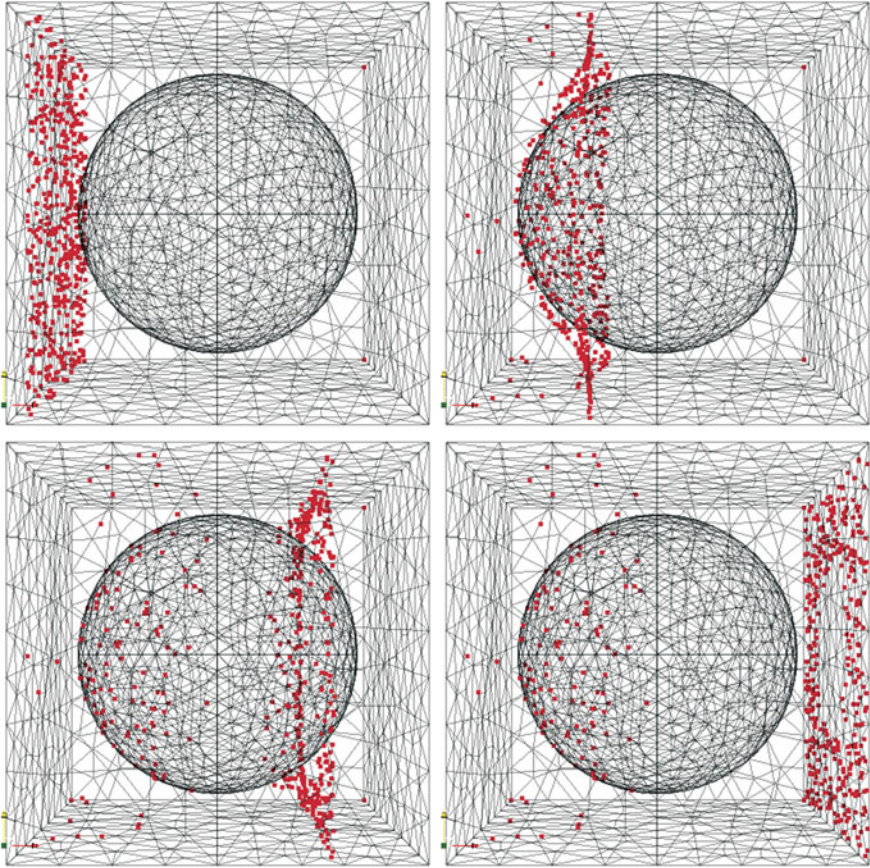


**Fig. 6.19** Particles advect in *cube* domain with one grain

Forchheimer flow describes the non-linear form of fluid flow in porous media in a scale that is smaller than the macro-scale domain size and larger than the micro-scale pore size. It is an extension of the Darcy’s law when the viscous forces do not prevail over the inertial forces. A kinetic effect is considered and expressed as an additive term in the description of pressure difference. The classic form of Forchheimer term is written as [15]

$$-\nabla P = \frac{\mu}{k} \mathbf{q} + \beta \rho |\mathbf{q}| \mathbf{q} \tag{6.19}$$

where  $\mu[MT^{-1}L^{-1}]$  is the dynamic viscosity of water,  $k[L^2]$  is intrinsic permeability,  $\mathbf{q}[LT^{-1}]$  is Forchheimer velocity vector,  $\beta[L^{-1}]$  is Forchheimer coefficient, and  $\rho[ML^{-3}]$  is density of water.

The Forchheimer coefficient  $\beta$  is also known as non-Darcy coefficient. Several approaches have been applied to obtain the value of  $\beta$  [16–18]. The formulae are

normally defined for certain flow conditions. There is no general agreement on the nature of this coefficient. Some of the approaches are based on empirical results and some on fundamental characterizations of the porous media. Parameters involved in the calculation of  $\beta$  include permeability, as well as porosity, and tortuosity in some cases.

### 6.3.2 Forchheimer Flow in 1D Porous Medium

The 1D homogeneous porous medium benchmark (see Sect. 6.1.1 for description) is adopted in order to compare different behaviors of flow under Darcy and Forchheimer regimes, and their influence on solute transport performance which is simulated with particle tracking.

#### 6.3.2.1 Governing Equations

If we consider the hydraulic head  $h = \frac{p}{\rho g} + z$ , where  $z[L]$  is elevation head, and neglect the gravitational effect, then the Forchheimer equation (6.19) can be written as

$$-\nabla h = \frac{1}{K} \mathbf{q} + \frac{\beta}{g} |\mathbf{q}| \mathbf{q} \quad (6.20)$$

where  $K [LT^{-1}]$  is hydraulic conductivity and  $K = \frac{k \rho g}{\mu}$ . In the OGS simulation of Forchheimer flow,  $\frac{1}{K}$  is referred to as  $a_1$  and  $\frac{\beta}{g}$  as  $a_2$ , and they are used as coefficients for the calculation.

$$-\nabla h = a_1 \mathbf{q} + a_2 |\mathbf{q}| \mathbf{q} \quad (6.21)$$

The equation of mass conservation that describes the groundwater flow without source term can be formed as

$$-\nabla \mathbf{q} = S_s \frac{\partial h}{\partial t} \quad (6.22)$$

where  $S_s [L^{-1}]$  is the storativity (volumetric specific storage),  $t [T]$  is time.

In 1D case, Eqs. (6.21) and (6.22) can be rewritten as

$$-\frac{\partial h}{\partial x} = a_1 q + a_2 q^2 \quad (6.23)$$

$$S_s \frac{\partial h}{\partial t} + \frac{\partial q}{\partial x} = 0 \quad (6.24)$$

### 6.3.2.2 Steady State Flow with Dirichlet Boundary Condition

For the steady state flow, constant hydraulic heads are set at the inlet and outlet boundaries. Relevant parameters for the flow are listed in Table 6.8.

Forchheimer velocity can be calculated from Eq. (6.23) that

$$q = \frac{-a_1 + \sqrt{a_1^2 - 4a_2 \frac{\partial h}{\partial x}}}{2a_2} \quad (6.25)$$

Darcy velocity can be obtained from Eq. (6.23) by assign  $a_2 = 0$ .

Simulation results of hydraulic head distribution and the comparison of Forchheimer velocity and Darcy velocity are shown in Fig. 6.20.

The proposed RWPT method makes use of the velocities obtained from the flow process, regardless of the flow regimes. 25,000 particles are injected at the inlet boundary for 2.5 pore volume ( $P_V = vt/L$ ,  $v = q/n$ ) to simulate non-reactive solute transport with slug input in 1D steady state flow under Forchheimer and Darcy regimes respectively. Parameters for the simulation of solute transport are listed in Table 6.9. Note that particles experience not only advection and hydrodynamic dispersion, but decay and retardation processes as well in this case. Detailed description for these processes is referred to in Sect. 6.1.1.

Figure 6.21 shows the simulation result of concentration breakthrough curve at  $x = 0.1$  m. Note that in RWPT method, the concentration is represented by the number of particles.

**Table 6.8** Model parameters for the column experiment—steady state flow

Symbol	Parameter	Value	Unit
$h_{in}$	Hydraulic head(inlet)	0.09555	m
$h_{out}$	Hydraulic head(outlet)	0.02038	m
$L$	Column length	0.1	m
$k$	Intrinsic Permeability	$1.114476 \times 10^{-11}$	$m^2$
$K$	Hydraulic conductivity	$1.0933 \times 10^{-4}$	$ms^{-1}$
$S_s$	Volumetric specific storage	0.5	$m^{-1}$
$a_1$	OGS coefficient (equals to $K^{-1}$ )	$9.146612 \times 10^3$	$m^{-1}s$
$a_2$	OGS coefficient	$10^8$	$m^{-2}s^2$

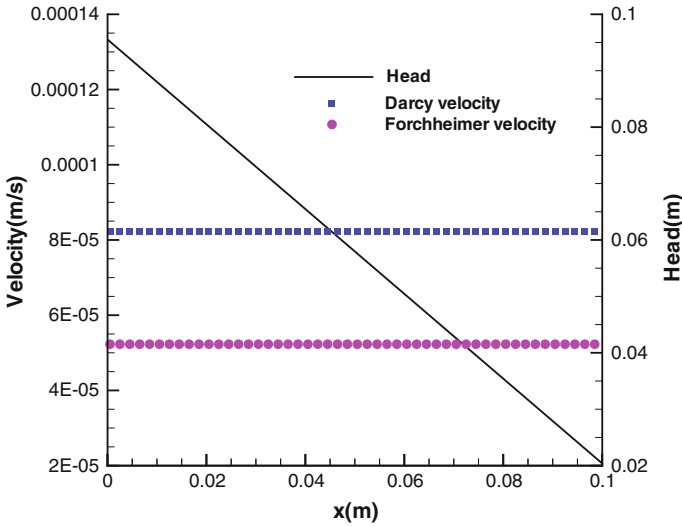


Fig. 6.20 Forchheimer velocity and Darcy velocity in 1D steady state flow

Table 6.9 Model parameters for the column experiment—solute transport

Symbol	Parameter	Value	Unit
$\alpha_L$	Longitudinal dispersivity	0.005	m
$n$	Porosity	0.42	—
$A$	Weighting factor	0.9	—
$k_1$	Fast sorption rate coefficient	0.1	—
$k_2$	Slow sorption rate coefficient	0.001	—
$\lambda$	Filtration coefficient	5.2	$m^{-1}$

### 6.3.2.3 Transient Flow with Dirichlet Boundary Condition

For unsteady, nonlinear flow in the 1D homogeneous porous medium, the same parameters are used as listed in Table 6.8. Simulation results of hydraulic head and velocity distributions under Forchheimer and Darcy regimes at  $t = 5.1, 10.2, 15.3, 20.4, 25.5, 30.6$  s are shown in Fig. 6.23.

Particles are injected at the inlet boundary for 2.5 pore volume ( $P_V = vt/L, v = q/n$ ) to simulate non-reactive advective-dispersive solute transport with slug input in 1D transient flow under Forchheimer and Darcy regimes respectively. Figure 6.22 shows the simulation result of concentration breakthrough curve at  $x = 0.1$  m. Note that in RWPT method, the concentration is represented by the number of particles.

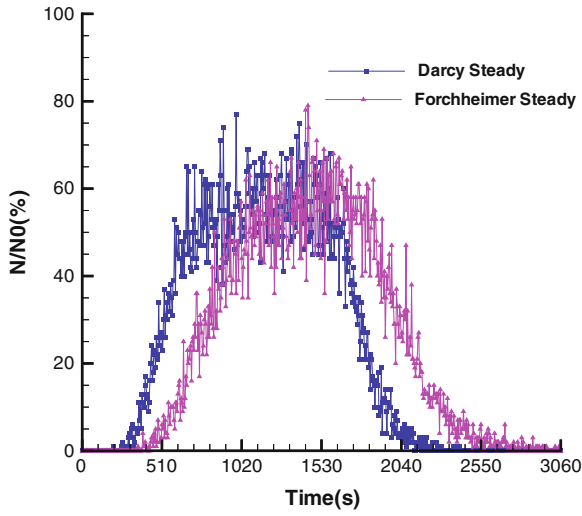


Fig. 6.21 Particle tracking under Forchheimer and Darcy regimes in 1D steady state flow

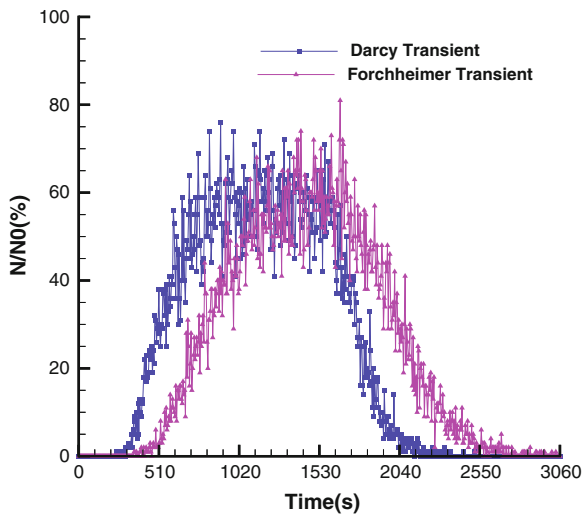
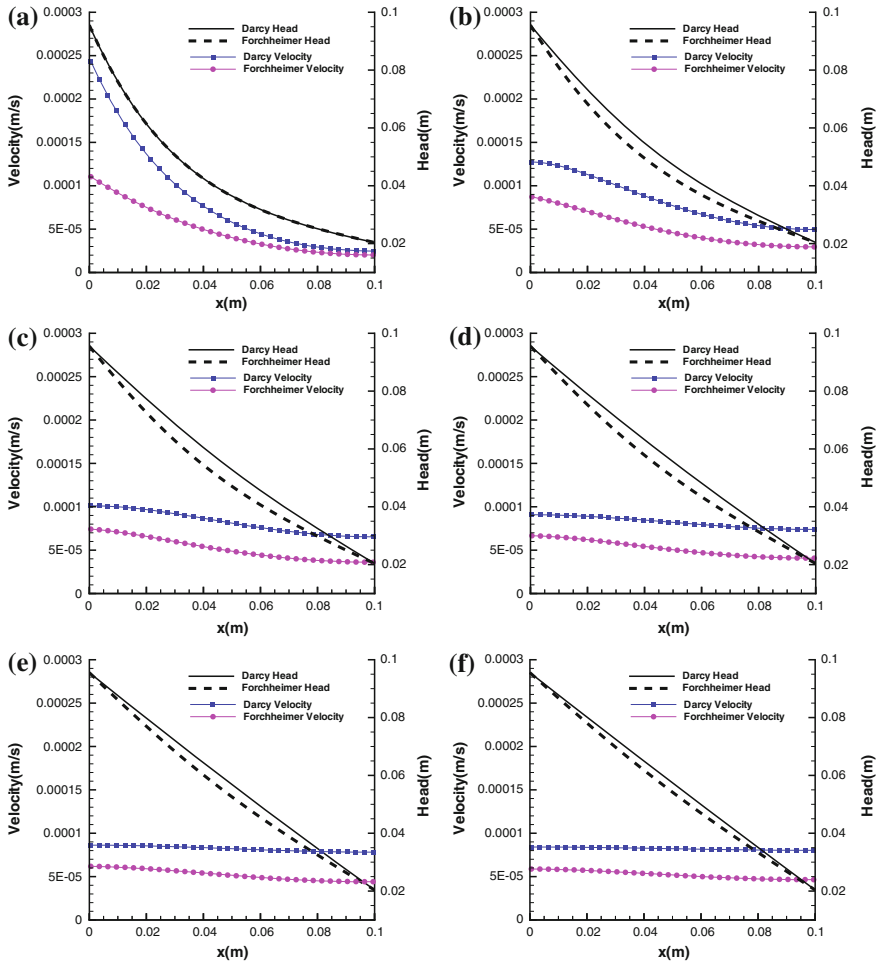


Fig. 6.22 Particle tracking under Forchheimer and Darcy regimes in 1D transient flow



**Fig. 6.23** Forchheimer velocity and Darcy velocity in 1D transient flow. **a**  $t = 5.1$  s. **b**  $t = 10.2$  s. **c**  $t = 15.3$  s. **d**  $t = 20.4$  s. **e**  $t = 25.5$  s. **f**  $t = 30.6$  s

### 6.3.3 Groundwater Flow Regimes

The applicability limits of Darcy’s and Forchheimer’s regimes of flow are of great interest. Ruth et al. [19] rearranged the Forchheimer equation (6.19) in the form

$$-\nabla P = \frac{\mu}{k} \mathbf{q} + \beta \rho |\mathbf{q}| \mathbf{q} = \frac{1}{k} \left( 1 + \frac{\beta k \rho \mathbf{q}}{\mu} \right) \mu \mathbf{q} = \frac{1}{k} (1 + F_o) \mu \mathbf{q} = \frac{\mu}{k_v} \mathbf{q} \quad (6.26)$$

and named  $F_o[-]$  as Forchheimer number, and  $k_v[L^2]$  as the velocity-dependent permeability. The Forchheimer number can be used as a criterion to indicate when the inertial force can prevail over the viscosity force. The velocity-dependent permeability shows that permeability can be treated as a velocity dependent parameter.

Apart from the Forchheimer number, another basic criterion to distinguish between these two regimes is the range of Reynolds number (Re), which is defined as the ratio of inertial forces to viscous forces and can be written as

$$Re = \frac{\rho \mathbf{q} L}{\mu} \quad (6.27)$$

where  $\rho[ML^{-3}]$  is the density of water,  $\mathbf{q}[LT^{-1}]$  is the specific discharge,  $L[L]$  is the characteristic linear dimension, and  $\mu[MT^{-1}L^{-1}]$  is the dynamic viscosity of water.

Darcy flow occurs at low Reynolds number, which means the dominant force in this situation is viscous force and the flow is comparatively smooth. In Forchheimer flow the inertial force prevails over the viscous force so the Reynolds number is high. The upper limit of Reynolds number in Darcy flow is considered to be coincided with the lower limit of Reynolds number in Forchheimer flow [17, 20–23].

## 6.4 Particle Tracking in Fractured Porous Media

Fractures may be defined through direct measurement or geo-statistical reproduction. In the benchmarks of this chapter, both methods will be utilized. Where fractures are directly measured, the methodology utilizes a laser profiler. Profiles (elevation measurements) are taken of each fracture surface and these are manipulated numerically. Point-wise fracture aperture is the difference between the top and bottom surfaces at corresponding locations. Statistically reproduced fractures reproduce roughness of the aperture (not each surface) in order to achieve a desired mean and standard deviation. The result is used directly as the fracture aperture in numerical simulations.

For a fracture represented by two parallel (planar) plates, permeability is a function of the fracture aperture by the cubic law,

$$k = \frac{b^2}{12} \quad (6.28)$$

For a uniformly fractured rock mass, the cubic law takes form as  $b^3/12s$ , where  $s$  is fracture spacing.

The aperture,  $b$ , however, represents only the mechanical state of the fracture. In reality, observed flow rates are dependent on the hydraulic state of the fracture. In other words, fracture roughness matters. We therefore distinguish two different apertures: the so-called “void” aperture,  $b_v$  and the “hydraulic” aperture,  $b_h$ . The void aperture is the mean geometrically measured distance between the two fracture surfaces, including only those points that are not in contact (as the name implies,

including only voids). The hydraulic aperture is a correction from this value ( $b_h \leq b_v$ ), with one possibility known as the geometric correction [24],

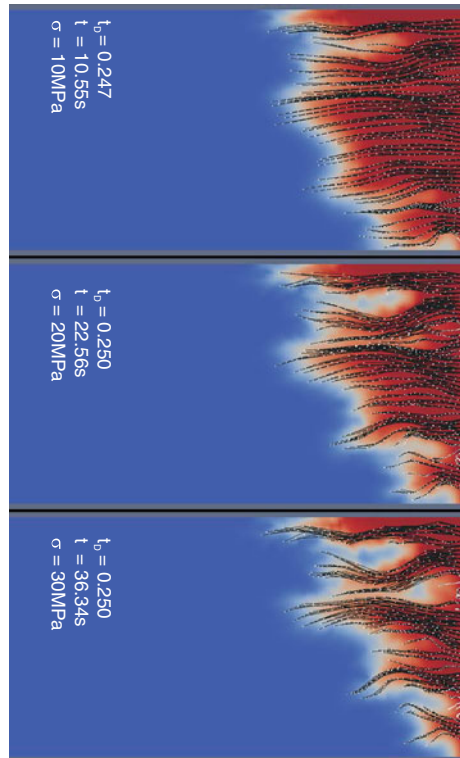
$$b_h^3 = \exp \langle \ln(k) \rangle = \exp(3 \langle \ln(b_v) \rangle) \tag{6.29}$$

where the angled brackets indicate that the mean is taken over the logarithm of the point-wise void aperture. Therefore, as an approximation to reality, the (effective) true permeability of a rough fracture is given by,

$$k = \frac{b_h^2}{12} \tag{6.30}$$

In what follows, we use this permeability to approximate behavior of the fracture and to generate an analytical solution for (qualitative) comparison to simulations within rough fractures, where permeability occurs point-wise (and mechanically) as  $k_i = b_i^2/12$ . Therefore, this is an *effective permeability*, and shall be used as an attempt to approximate (or provide reference to) true flow behavior in a rough fracture from a single bulk property.

**Fig. 6.24** RWPT versus ADE at different stress states. Two separate simulations are conducted and overlay one another. Particle pathlines (*black*) and particles (*white*) are illustrated, and overlay contours (*red* = higher concentration) generated from the ADE simulation



### 6.4.1 Uncertainty in Flow, Preferential Flow

To examine changes to flow characteristics, we utilize two alternate forms of mass transport: the classical advection-dispersion equation (ADE) and random walk particle tracking (Fig. 6.24). The RWPT simulator within OGS is modified to allow a continuous source of particles (numerically approximate to a Neumann concentration boundary) for comparison with results from ADE simulations. For comparison, dispersion is not allowed within the RWPT simulation: particles are only advected with the flow. Therefore, particles represent the 50% concentration breakthrough if particles are imagined as concentrations. The plot for each stress state is shown at a different absolute time, but each corresponds to the same dimensionless time,  $t_D = v \cdot t/L$ , where  $t$  is current time and  $L$  is total flow length, with  $v$  calculated from the mean  $b_h$ . Therefore, if  $b_h$  is a good approximation of behavior, the concentration advance in each plot should be approximately of the same extent. Note that this is true, but also that the increasing tendency for preferential flow with stress lends to increasingly less uniform concentration advance: with increasing stress, a given point in the geometry will record strongly different behavior than its neighbors.

## References

1. J. Bear. *Hydraulics of groundwater*. McGraw-Hill, New York, 1979.
2. K. Ito. On stochastic differential equations. *American Mathematical Society*, 4:289–302, 1951.
3. W. Kinzelbach. *Groundwater Modelling*. Elsevier, Amsterdam, 1986.
4. A.F.B. Tompson and L.W. Gelhar. Numerical simulation of solute transport in three-dimensional, randomly heterogeneous porous media. *Water Resour. Res.*, 26(10):2541–2562, 1990.
5. E.M. LaBolle, G.E. Fogg, and A.F.B. Tompson. Random-walk simulation of transport in heterogeneous porous media: Local mass-conservation problem and implementation methods. *Water Resour. Res.*, 32(3):583–593, 1996.
6. W. Kinzelbach. The random-walk method in pollutant transport simulation. *NATO ASI Ser. Ser. (C224)*:227–246, 1988.
7. H. Hoteit, R. Mose, A. Younes, F. Lehmann, and Ph. Ackerer. Three-dimensional modeling of mass transfer in porous media using the mixed hybrid finite elements and the random-walk methods. *Mathe. Geology*, 34(4):435–456, 2002.
8. T. Harter and S. Wagner. Colloid transport and filtration of *Cryptosporidium parvum* in sandy soils and aquifer sediments. *Environ. Sci. Technol.*, 34:62–70, 2000.
9. M. van Genuchten. Analytical solutions for chemical transport with simultaneous adsorption, zero-order production and first order decay. *Jour. of Hydrol.*, 49:213–233, 1981.
10. W.P. Johnson, K.A. Blue, and B.E. Logan. Modeling bacterial detachment during transport through porous media as a residence-time-dependent process. *Water Resour. Res.*, 31:2649–2658, 1995.
11. A. Ogata and R.B. Banks. A solution of the differential equation of longitudinal dispersion in porous media. Technical report, USGS, Washington, D.C., 1961.
12. A.E. Hassan and M.M. Mohamed. On using particle tracking methods to simulate transport in single-continuum and dual continua porous media. *Jour. of Hydrol.*, 275:242–260, 2003.
13. S. Whitaker. Advances in theory of fluid motion in porous media. *Ind. Eng. Chem.*, 61(12):14–28, 1969.

14. F.A.L. Dullien and M.I.S. Azzam. Flow rate - pressure gradient measurements in periodically nonuniform capillary tubes. *A. I. Ch. E. J.*, 19:222–229, 1973.
15. P. Forchheimer. *Wasserbewegung durch Boden*. Zeitschrift des Vereines Deutscher Ingenieur, 1901.
16. S. Ergun and A. A. Orning. Fluid flow through randomly packed columns and fluidized beds. *Ind. & Engng. Chem.*, 41(6):1179–1184, 1949.
17. T.H. Chilton and A.P. Colburn. Pressure drop in packed tubes. *Ind. & Engng. Chem.*, 23(8):913–919, 1931.
18. M. Balhoff, A. Mikelic, and M. Wheeler. Polynomial filtration laws for low reynolds number flows through porous media. *Transport in Porous Media*, 81:35–60, 2010.
19. D.W. Ruth and H. Ma. On the derivation of the forchheimer equation by means of the averaging theorem. *Transport in Porous Media*, 7:255–264, 1992.
20. G.H. Fancher and J.A. Lewis. Flow of simple fluids through porous materials. *Ind. & Engng. Chem.*, 25(10):1139–1147, 1933.
21. L. Jr. Green and P. Duwez. Fluid flow through porous metals. *J. Appl. Mech.*, pages 39–45, 1951.
22. S. Ergun. Fluid flow through packed columns. *Chem. Engng. Prog.*, 48(2):89–94, 1952.
23. S.M. Hassanizadeh and W.G. Gray. High velocity flow in porous media. *Transport Porous Media*, 2:521–531, 1987.
24. A.R. Piggott and D. Elsworth. Laboratory assessment of the equivalent apertures of a rock fracture. *Geophysical Research Letters*, 20(13):1387–1390, 1993.

# Chapter 7

## Mechanical Processes

Thomas Nagel and Norbert Böttcher

### 7.1 Theory and Implementation

This section introduces benchmarks to verify the implementation of a pressure boundary condition for mechanical processes. A traction boundary condition is given as

$$[[\mathbf{t}]] = 0 \quad \rightarrow \quad \mathbf{t} = \boldsymbol{\sigma} \mathbf{n} = \bar{\mathbf{t}} \quad \forall \mathbf{x} \in \partial\Omega_t \quad (7.1)$$

where the traction  $\bar{\mathbf{t}}$  is applied on  $\partial\Omega_t$  ( $\partial\Omega_t \cap \partial\Omega_u = \emptyset$  and  $\partial\Omega_t \cup \partial\Omega_u = \partial\Omega$ ) and  $\mathbf{n}$  is the unit outward normal vector on  $\partial\Omega_t$ .

A pressure load is defined by

$$\mathbf{t}_p = p \mathbf{n} \quad (7.2)$$

For the RHS of the weak form of the momentum balance we thus find

$$\int_{\partial\Omega_t} \mathbf{t} \cdot \delta \mathbf{u} d\Gamma = \int_{\partial\Omega_t} p \mathbf{n} \cdot \delta \mathbf{u} d\Gamma \quad (7.3)$$

With  $N^a$  as the displacement shape function at node  $a$  and the vector of nodal displacements  $\tilde{\mathbf{u}}^a$  the FE approximation

$$\mathbf{u} \approx \hat{\mathbf{u}} = \sum_{n_n} N^a \tilde{\mathbf{u}}^a = \mathbf{N} \tilde{\mathbf{u}} \quad (7.4)$$

---

T. Nagel (✉) · N. Böttcher  
Helmholtz Centre for Environmental Research UFZ, Permoserstr. 15,  
04318 Leipzig, Germany  
e-mail: Thomas.Nagel@ufz.de

is introduced. Considering the arbitrary nature of the virtual displacements, the discretised form of the external virtual work by surface tractions provides the nodal force vector for a finite element:

$$\mathbf{f}_p = \int_{\partial\Omega_t} p \mathbf{N}^T \mathbf{n} d\Gamma \quad (7.5)$$

The switch from global ( $\mathbf{x}$ ) to local ( $\boldsymbol{\xi}$ ,  $\xi_i \in [-1, 1]$ ) coordinates of the integration domain yields with  $\det J = |\partial x_i / \partial \xi_j|$

$$\mathbf{f}_p = \int_{\partial\Omega_\xi} p(\boldsymbol{\xi}) \mathbf{N}^T(\boldsymbol{\xi}) \mathbf{n}(\boldsymbol{\xi}) \det J d\Gamma_\xi \quad (7.6)$$

The surface normal vector of the element becomes (Fig. 7.1)

$$\mathbf{n}(\boldsymbol{\xi}) = \frac{\frac{\partial \mathbf{x}}{\partial \xi_1} \times \frac{\partial \mathbf{x}}{\partial \xi_2}}{\left| \frac{\partial \mathbf{x}}{\partial \xi_1} \times \frac{\partial \mathbf{x}}{\partial \xi_2} \right|} = \frac{\mathbf{g}_1 \times \mathbf{g}_2}{|\mathbf{g}_1 \times \mathbf{g}_2|} \quad (7.7)$$

In the current implementation, normal vector and surface area are evaluated on the undeformed geometry only. The pressure load is thus conservative and not following the (infinitesimal) deformation of the boundary contour. Further details can be found in [1].

Finally, for the determination of the forces at a particular node  $a$ , the contributions from all connected elements  $e_c$  will have to be assembled:

$$\mathbf{f}^a = \bigoplus_{e_c} \mathbf{f}_p^a \quad (7.8)$$

## 7.2 Deformation of a Steel Tubing

### 7.2.1 Analytical Solution—Linear Elasticity

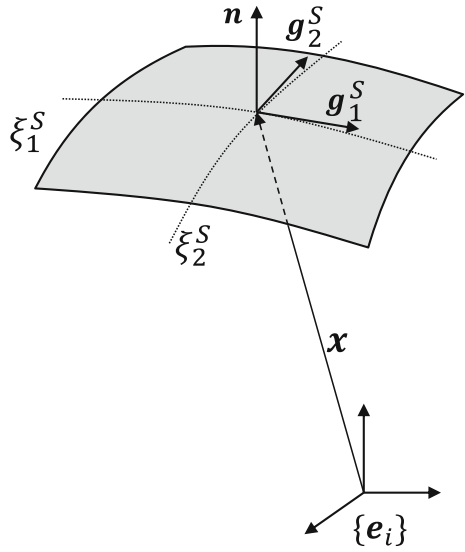
The pressure boundary condition was verified by simulating a ring under plane strain conditions and a sphere. In both cases, the pressure was prescribed on the inner and outer surfaces and the material was modelled as linearly elastic. The quasistatic balance of linear momentum

$$\operatorname{div} \boldsymbol{\sigma} = \mathbf{0} \quad (7.9)$$

and Hooke's law

$$\boldsymbol{\sigma} = \lambda(\operatorname{tr} \boldsymbol{\epsilon}) \mathbf{I} + 2\mu \boldsymbol{\epsilon} \quad (7.10)$$

**Fig. 7.1** Surface coordinates and surface normal for the integration of the pressure boundary condition



therefore constitute the governing equations with the Lamé constants  $\lambda$  and  $\mu$ .

The *tube* example can be solved analytically in cylindrical coordinates (radius  $r$ , polar angle  $\varphi$ , axial coordinate  $z$ ). With the use of the metric tensor having the covariant coordinates

$$g_{ij} = \text{diag}(1, r^2, 1) \tag{7.11}$$

and by considering plane strain conditions as well as rotational symmetry of both load and kinematics, the differential equation

$$0 = \left[ \frac{1}{r} (r u_r)_{,r} \right]_{,r} \tag{7.12}$$

can be found for the radial displacements. Along with the boundary conditions at the inner and outer surfaces

$$\sigma_{rr}(r = R_i) = -p_i \quad \text{and} \quad \sigma_{rr}(r = R_a) = -p_a \tag{7.13}$$

integration of the differential equation and substitution of the result into Hooke's law yields the stresses

$$\sigma_{rr} = \frac{p_i R_i^2 - p_a R_a^2}{R_a^2 - R_i^2} - \frac{(p_i - p_a) R_a^2 R_i^2}{(R_a^2 - R_i^2) r^2} \quad (7.14)$$

$$\sigma_{\varphi\varphi} = \frac{p_i R_i^2 - p_a R_a^2}{R_a^2 - R_i^2} + \frac{(p_i - p_a) R_a^2 R_i^2}{(R_a^2 - R_i^2) r^2} \quad (7.15)$$

$$\sigma_{zz} = \frac{\lambda(p_a R_a^2 - p_i R_i^2)}{(\lambda + \mu)(R_i^2 - R_a^2)} = \frac{2\nu(p_a R_a^2 - p_i R_i^2)}{(R_i^2 - R_a^2)} \quad (7.16)$$

The radial displacement follow as

$$u_r = \frac{R_i^2 p_i (1 + \nu) r}{E(R_i^2 - R_a^2)} \left[ \left( \frac{p_a}{p_i} \left( \frac{R_a}{R_i} \right)^2 - 1 \right) (1 - 2\nu) + \left( \frac{p_a}{p_i} - 1 \right) \left( \frac{R_a}{r} \right)^2 \right] \quad (7.17)$$

## 7.2.2 Numerical Solution

This benchmark investigates the strength of seamless cold drawn tubes, specifically standard tubes according to DIN EN 10305. The specific object of interest is a tube with an inner diameter of 2 mm and a wall thickness of 1 mm. According to the DIN standard, the maximum allowed internal pressure of that tube is 522 bar. To investigate principal stresses and the deformation of the tube cross section, the exact solutions (7.14)–(7.17) are compared against numerical approximations obtained using OpenGeoSys. The aim of the comparison is the verification of the implemented pressure boundary condition as well as the linear elastic material models.

Shape and size of the tube cross section are displayed in Fig. 7.2a. Due to symmetry, the finite element discretization considers only a quarter of the full circle (Fig. 7.2b). As boundary conditions, the peak pressure of  $p_{in} = 52.2$  MPa is applied at the inner wall, while atmospheric pressure of  $p_{out} = 0.1$  MPa is applied from outside. Symmetry boundary conditions are applied at the remaining surfaces. The tube

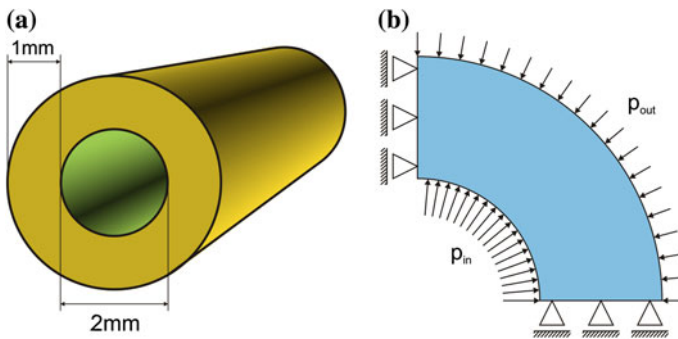


**Fig. 7.2** Schematic view and boundary conditions of the tube model. **a** Cross section of the tubing. **b** Model concept and boundary conditions

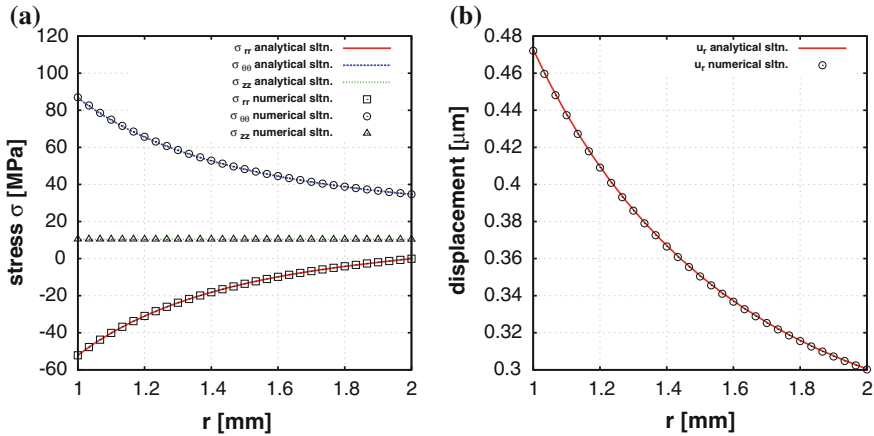


**Fig. 7.3** Stress distribution and radial displacement along the tube radius. Comparison of exact solutions and numerical approximations. **a** Stress distribution. **b** Radial displacement

is made of E235, a steel with a yield stress of  $\sigma_F = 300$  MPa and a *Young's* modulus of  $E = 210$  GPa. The *Poisson's* ratio is assumed to be  $\nu = 0.3$ . For the numerical solution, the tube cross section was discretized into 480 quadrilateral elements with biquadratic shape functions.

In Fig. 7.3a, the principal stresses within the tube's wall are plotted. The figure shows both the exact solutions and the numerical approximations. The third principal stress corresponds to the normal stress in the radial direction ( $\sigma_{rr}$ ) and approaches the pressure of 52.2 MPa at the inner boundary, while it drops down to atmospheric pressure at the outer edge of the domain (see also Fig. 7.4). Since we consider plane strain conditions, the displacement in  $z$  direction is suppressed and the second principal stress, corresponding to  $\sigma_{zz}$ , is constant over the whole cross section according to (7.16). Under the present conditions, the maximum principal stress occurs in the circumferential direction ( $\sigma_{\theta\theta}$ ) at the inner edge of the tube and amounts to about 85 MPa, which is less than 30% of the yield stress of that material.

### 7.3 Deformation of a Thick-Walled, Hollow Sphere

#### 7.3.1 Analytical Solution—Linear Elasticity

The *sphere* example can be solved analytically in spherical coordinates (radius  $r$ , azimuthal angle  $\theta \in [0, 2\pi)$ , polar angle  $\varphi \in [0, \pi]$ ). With the use of the metric tensor having the covariant coordinates

$$g_{ij} = \text{diag}(1, r^2 \sin^2 \varphi, r^2) \tag{7.18}$$

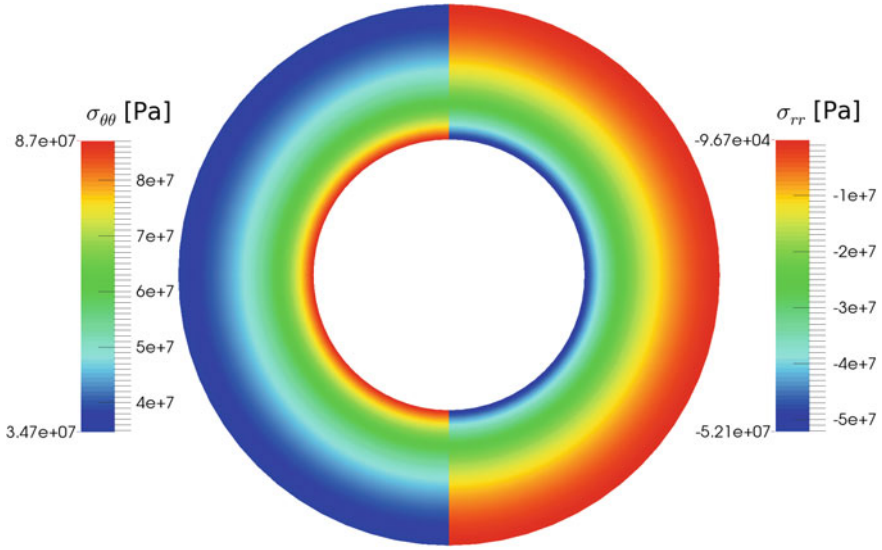


**Fig. 7.4** Circumferential (*left*) and radial (*right*) stress at the cross section of the tube

and by considering spherical symmetry of both load and kinematics, the differential equation

$$0 = u_{r,rr} + \frac{2}{r}u_{r,r} - \frac{2}{r^2}u_r \tag{7.19}$$

can be found for the radial displacements. Along with the boundary conditions

$$\sigma_{rr}(r = R_i) = -p_i \quad \text{and} \quad \sigma_{rr}(r = R_a) = -p_a \tag{7.20}$$

the differential equation can be solved. Substitution of the result into Hooke’s law yields the stresses

$$\sigma_{rr} = \frac{p_a R_a^3 - p_i R_i^3}{R_i^3 - R_a^3} - \frac{R_a^3 R_i^3 (p_a - p_i)}{(R_i^3 - R_a^3)r^3} \tag{7.21}$$

$$\sigma_{\varphi\varphi} = \sigma_{\theta\theta} = \frac{p_a R_a^3 - p_i R_i^3}{R_i^3 - R_a^3} + \frac{R_a^3 R_i^3 (p_a - p_i)}{2(R_i^3 - R_a^3)r^3} \tag{7.22}$$

The radial displacement follows as

$$u_r = \frac{R_i^3 p_i r}{E(R_i^3 - R_a^3)} \left[ \left( \frac{p_a}{p_i} \left( \frac{R_a}{R_i} \right)^3 - 1 \right) (1 - 2\nu) + \left( \frac{p_a}{p_i} - 1 \right) \frac{1 + \nu}{2} \left( \frac{R_a}{r} \right)^3 \right] \quad (7.23)$$

### 7.3.2 Numerical Solution—Linear Elasticity

In 1654, *Otto von Guericke*, the mayor of Magdeburg (Germany) at that time, performed a famous experiment to show the effects of air pressure and to prove the existence of the atmosphere. He took two hollow copper hemispheres, put them together against each other and evacuated them using a piston pump. Afterwards, the hemispheres stuck together only by virtue of the surrounding air pressure. Even two teams of 15 horses were unable to separate both hemispheres (see Fig. 7.5).

In this benchmark test, the stresses and strains inside the copper shells caused by the pressure difference between its inside and outside will be investigated.



**Fig. 7.5** Historical engraving of the *Magdeburg hemispheres* experiment performed by *Otto von Guericke* in 1654. Source Wikipedia

The investigated hollow sphere has a diameter of 45 cm, the thickness of the shell is 5 cm (the wall thickness was slightly increased compared to *von Guericke's* prototype to clearly observe the non-linear distribution of the stresses). Copper has a *Young's* modulus of  $E = 125 \text{ GPa}$  and a *Poisson's* ratio of  $\nu = 0.35$ . The pressure inside the sphere is assumed to be  $p_{in} = 1 \text{ kPa}$  (which is just a guess of the magnitude of a vacuum that could be produced in 1654) and the outside pressure is set to atmospheric levels ( $p_{out} = 1.01325 \text{ bar}$ ). Using cylindrical coordinates and taking advantage of symmetry, it is sufficient to reduce the model geometry to a 2D representation of a 90° slice of the sphere (see Fig. 7.6b). The geometry is represented by 980 quadrilateral elements with biquadratic shape functions.

Radial and circumferential stresses in the hollow sphere are plotted in Fig. 7.7a. The radial stress approaches both inner and outer boundary conditions:  $\sigma_{rr} = -1 \cdot 10^{-3} \text{ MPa}$  on the inside and  $\sigma_{rr} = -1 \cdot 10^{-1} \text{ MPa}$  on the outside edge of the sphere.

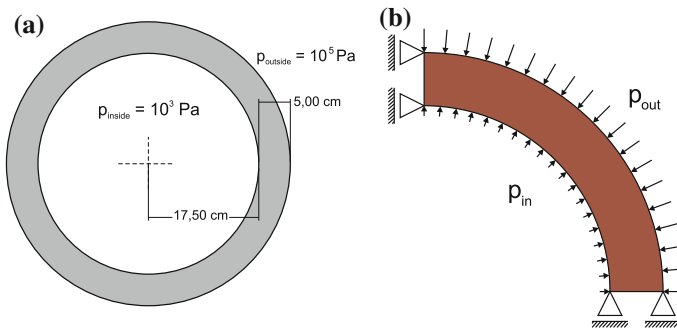


**Fig. 7.6** Schematic view and boundary conditions for the linear elastic deformation of a sphere. **a** Schematic view. **b** Model domain and boundary conditions

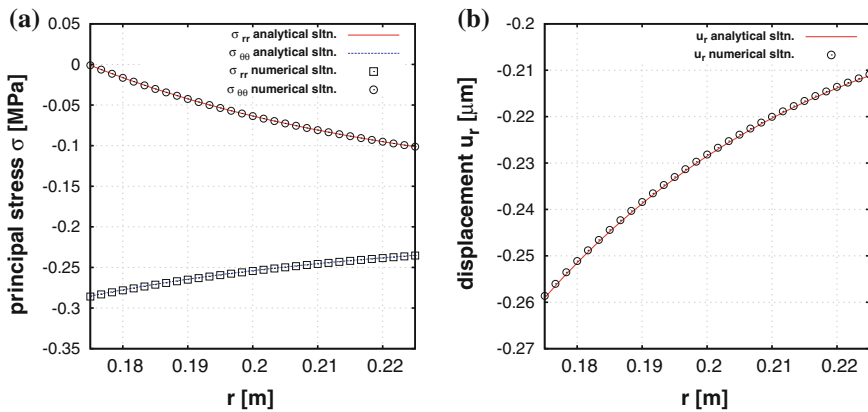


**Fig. 7.7** Principal stresses and radial displacement along the sphere wall. Comparison of exact solutions and numerical approximations. **a** Principal stresses. **b** Radial displacement

The maximum circumferential compressive stress exists at the inside edge of the sphere with about  $-0.285$  MPa, which is far below the yield stress of copper. The radial displacement of the casing ranges from  $-0.26$   $\mu\text{m}$  at the inside to  $-0.21$   $\mu\text{m}$  at the outside of the sphere (see Fig. 7.7b).

### 7.3.3 Analytical Solution—Elastoplasticity

Now an elasto-plastic material model without hardening is considered for the case of a thick-walled sphere under internal pressure only:

$$\sigma_{rr}(r = R_i) = -p \quad \text{and} \quad \sigma_{rr}(r = R_a) = 0$$

From Eqs. (7.21) and (7.22), the elastic solution in this case follows as

$$\sigma_{rr} = \frac{pR_i^3}{R_a^3 - R_i^3} \left[ 1 - \left( \frac{R_a}{r} \right)^3 \right] \quad (7.24)$$

$$\sigma_{\varphi\varphi} = \sigma_{\theta\theta} = \frac{pR_i^3}{R_a^3 - R_i^3} \left[ 1 + \frac{1}{2} \left( \frac{R_a}{r} \right)^3 \right] \quad (7.25)$$

With the definition of the deviatoric stress

$$\boldsymbol{\sigma}^D = \boldsymbol{\sigma} - \frac{1}{3}(\boldsymbol{\sigma} : \mathbf{I})\mathbf{I} \quad (7.26)$$

and the yield stress  $\sigma_F$ , the von Mises yield function is given as

$$\varphi = \frac{1}{2} \boldsymbol{\sigma}^D : \boldsymbol{\sigma}^D - \frac{1}{3} \sigma_F^2 = 0 \quad (7.27)$$

Substituting the physical tensor coordinates of the elastic solution into the yield condition produces

$$\sigma_F = \sigma_{\varphi\varphi} - \sigma_{rr} = \frac{3}{2} \frac{pR_i^3}{R_a^3 - R_i^3} \left( \frac{R_a}{r} \right)^3 \quad (7.28)$$

for the yield stress which, for a given  $p$ , has its maximum at  $r = R_i$ . Thus, the minimum pressure  $p_{\min}^{\text{pl}}$  to achieve plastic deformation is

$$p_{\min}^{\text{pl}} = \frac{2}{3} \sigma_F \left[ 1 - \left( \frac{R_i}{R_a} \right)^3 \right] \quad (7.29)$$

For  $p^{\text{pl}} > p_{\min}^{\text{pl}}$ , the plastic zone will grow to the radius  $r_p \in [R_i, R_a]$ . In the interval  $r \in [r_p, R_a]$  we use the elastic solution together with the boundary and yield conditions

$$\sigma_{\varphi\varphi}(r = r_p) - \sigma_{rr}(r = r_p) = \sigma_F \quad \text{and} \quad \sigma_{rr}(r = R_a) = 0 \quad (7.30)$$

to find the stresses in the elastic region as

$$\sigma_{rr} = \frac{2}{3}\sigma_F \left[ \left( \frac{r_p}{R_a} \right)^3 - \left( \frac{r_p}{r} \right)^3 \right] \quad (7.31)$$

$$\sigma_{\varphi\varphi} = \sigma_{\theta\theta} = \frac{2}{3}\sigma_F \left[ \left( \frac{r_p}{R_a} \right)^3 + \frac{1}{2} \left( \frac{r_p}{r} \right)^3 \right] \quad (7.32)$$

while the radial displacement follows as

$$u_r = \frac{2\sigma_F}{3E} \left( \frac{r_p}{R_a} \right)^3 r \left[ (1 - 2\nu) + \frac{1 + \nu}{2} \left( \frac{R_a}{r} \right)^3 \right] \quad (7.33)$$

To obtain the stress distribution in the inner (plastic) region  $r \in [R_i, r_p]$  we use the linear momentum balance in the radial direction together with the yield condition. Integration of the resulting differential equation produces

$$\sigma_{rr} = 2\sigma_F \ln r + C_3 \quad (7.34)$$

where  $C_3$  is found from the stress continuity condition with respect to the elastic component  $\sigma_{rr}(r = r_p - 0) = \sigma_{rr}(r = r_p + 0)$

$$\sigma_{rr} = 2\sigma_F \ln \frac{r}{r_p} + \frac{2}{3}\sigma_F \left[ \left( \frac{r_p}{R_a} \right)^3 - 1 \right] \quad (7.35)$$

$$\sigma_{\varphi\varphi} = \sigma_{\theta\theta} = 2\sigma_F \ln \frac{r}{r_p} + \frac{2}{3}\sigma_F \left[ \left( \frac{r_p}{R_a} \right)^3 + \frac{1}{2} \right] \quad (7.36)$$

With the boundary condition  $\sigma_{rr}(r = R_i) = -p^{\text{pl}}$  we find the pressure necessary to plastify the material in the region  $r \in [R_i, r_p]$ :

$$p^{\text{pl}} = 2\sigma_F \ln \frac{r_p}{R_i} + \frac{2}{3}\sigma_F \left[ 1 - \left( \frac{r_p}{R_a} \right)^3 \right] \quad (7.37)$$

To compute the radial displacements in the plastic region the associated flow rule is considered:

$$\dot{\epsilon}^{\text{pl}} = \dot{\lambda} \frac{\partial \varphi}{\partial \sigma} \quad (7.38)$$

Especially for the von Mises yield surface, we find

$$\dot{\epsilon}^{\text{pl}} = \dot{\lambda} \boldsymbol{\sigma}^D \quad (7.39)$$

With the additive decomposition of the strains, Hooke's law in the plastic region reads

$$\boldsymbol{\sigma} = \lambda(\mathbf{I} : \boldsymbol{\epsilon}^{\text{el}})\mathbf{I} + 2\mu\boldsymbol{\epsilon}^{\text{el}} \quad (7.40)$$

$$= \lambda[\mathbf{I} : (\boldsymbol{\epsilon} - \boldsymbol{\epsilon}^{\text{pl}})]\mathbf{I} + 2\mu(\boldsymbol{\epsilon} - \boldsymbol{\epsilon}^{\text{pl}}) \quad (7.41)$$

Taking the trace of that equation leads, in conjunction with  $\text{tr } \dot{\epsilon}^{\text{pl}} = 0$ , to

$$\text{tr } \boldsymbol{\sigma} = (3\lambda + 2\mu)\text{tr } \boldsymbol{\epsilon} \quad (7.42)$$

Substitution of the known stress distributions in the plastic region yields the following differential equation:

$$u_{r,r} + 2\frac{u_r}{r} = \frac{(1-2\nu)\sigma_F}{E} \left[ 6 \ln \frac{r}{r_p} + 2 \left( \frac{r_p}{R_a} \right)^3 \right] \quad (7.43)$$

Upon integration together with the continuity requirement to the elastic solution at  $r = r_p$ , the final solution is

$$u_r = \frac{2(1-2\nu)\sigma_F}{3E} r \left[ \frac{3(1-\nu)}{2(1-2\nu)} \left( \frac{r_p}{r} \right)^3 - 1 + \left( \frac{r_p}{R_a} \right)^3 + 3 \ln \left( \frac{r}{r_p} \right) \right] \quad (7.44)$$

If the pressure is now decreased back to zero, residual stresses will remain. Subtraction of the elastic solution with  $p = p^{\text{pl}}$  from the elastoplastic solution in both regions yields the residual stresses upon unloading.

$$\sigma_{rr}(p^{\text{pl}}) = \frac{pR_i^3}{R_a^3 - R_i^3} \left[ 1 - \left( \frac{R_a}{r} \right)^3 \right] = \frac{2}{3}\sigma_F \frac{p^{\text{pl}}}{p_{\text{min}}^{\text{pl}}} \left[ \left( \frac{R_i}{R_a} \right)^3 - \left( \frac{R_i}{r} \right)^3 \right] \quad (7.45)$$

$$\sigma_{\varphi\varphi} = \sigma_{\theta\theta} = \frac{pR_i^3}{R_a^3 - R_i^3} \left[ 1 + \frac{1}{2} \left( \frac{R_a}{r} \right)^3 \right] = \frac{2}{3}\sigma_F \frac{p^{\text{pl}}}{p_{\text{min}}^{\text{pl}}} \left[ \left( \frac{R_i}{R_a} \right)^3 + \frac{1}{2} \left( \frac{R_i}{r} \right)^3 \right] \quad (7.46)$$

### 7.3.4 Numerical Solution—Elastoplastic Deformation of a Sphere

For the numerical solution of the elastoplastic sphere problem we use the same model geometry as in the previous section. Geometry and boundary conditions are displayed in Fig. 7.6b. In contrast to the previous example, the pressure outside of the sphere is now disregarded ( $p_{\text{out}} = 0$ ).

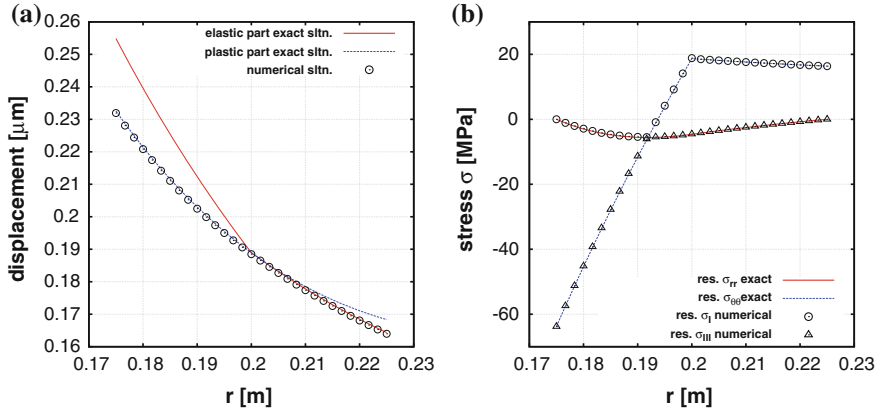


**Fig. 7.8** Schematic and finite-element discretization of the sphere model. **a** Radial displacements. **b** Principal residual stresses

The maximum pressure inside the sphere is chosen such that the radius of the plastic zone  $r_p$  will extend to the middle of the sphere's wall, i.e.

$$r_p = 0.5(R_i + R_a) = 0.2 \quad (7.47)$$

Setting the yield stress of copper to  $\sigma_F = 200$  MPa, we obtain the required pressure to plastify the sphere from  $R_i$  up to  $r_p$  from Eq.(7.37) to be  $p^{pl} = 93.102$  MPa. Therefore, the inner boundary pressure is increased linearly up to that critical pressure. Once  $p_{pl}$  is reached, the pressure declines to zero at the same rate.

As expected, the critical pressure  $p_{pl}$  caused a plastic deformation on the inner half of the spherical shell. Equations (7.33) and (7.44) can be used to determine the radial displacement of the shell. In Fig. 7.8a, the red and blue lines show the analytical solutions of elastic and plastic parts of the radial displacement when the inner pressure equals the critical pressure  $p_{pl}$ . Note that the elastic and plastic solutions are valid only for  $r_p \leq r \leq R_a$  and  $R_i \leq r \leq r_p$ , respectively. The numerical solution, indicated by black circles in the diagram, follows this distinction accurately. Upon unloading, residual stresses become apparent. In Fig. 7.8b, the residual principal stresses are shown. The circumferential residual stress is tensile on the outside of the spherical shell, compressive on the inside.

## 7.4 Deformation of an Artificial Salt Cavern

### 7.4.1 Linear Elastic Material

This example shows a large subterranean salt cavern for gas storage purposes. The cavern is man-made and has a volume of about  $2.4 \cdot 10^6$  m<sup>3</sup>. Those caverns are

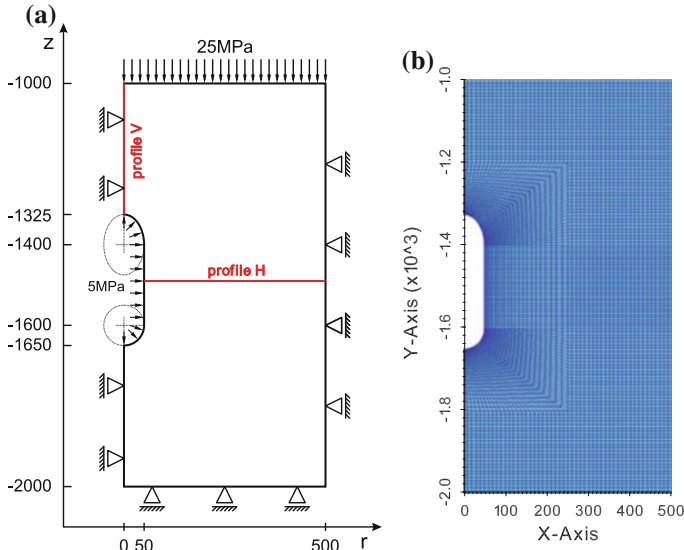


**Fig. 7.9** Geometry and boundary conditions (a) and finite element mesh (b) of the model cavern for the linear elastic material case

usually built in large salt domes as storage facilities for large amounts of fossil fuels or chemical products.

The model geometry is a column with a length of 1,000 m and a radius of 500 m, located at a depth of 1,000 m below the surface of earth. In the center of that domain, an excavation shaped like a pillar with rounded faces represents a simplified cavern (see Fig. 7.9a for detailed schematics). The overall length of the excavation is 325 m and the radius is 50 m. The model domain is described in cylindrical coordinates and is discretized by a two-dimensional finite element mesh (see Fig. 7.9b) consisting of 8,750 biquadratic quadrilateral elements, where smaller elements (with edge lengths of about 0.3 m) are located at the boundary of the cavern. OpenGeoSys is used to compute stress conditions and displacements within this model domain (Figs. 7.10, and 7.11).

Since the model domain is located at a depth of 1,000 m, the load of the overburden is given at the top of the domain by a stress of  $\sigma_{zz}^{\text{top}} = -25 \text{ MPa}$ . Inside the cavern, a gas resided at a constant pressure of  $p_{\text{cav}} = 5 \text{ MPa}$ . The outside boundary at  $r = 500 \text{ m}$  and the symmetry axis at  $r = 0 \text{ m}$  are fixed in radial direction, while the bottom of the domain at  $z = -2,000 \text{ m}$  is fixed in vertical direction.

For this simple test case, the behaviour of the host rock material is assumed to be linear elastic, with a *Young's* modulus of  $E = 14 \text{ GPa}$  and a *Poisson's* ratio of  $\nu = 0.3$ . In fact, this simple material model is not referring to realistic salt rock, its purpose is only to show the general behaviour of a cavern during gas storage

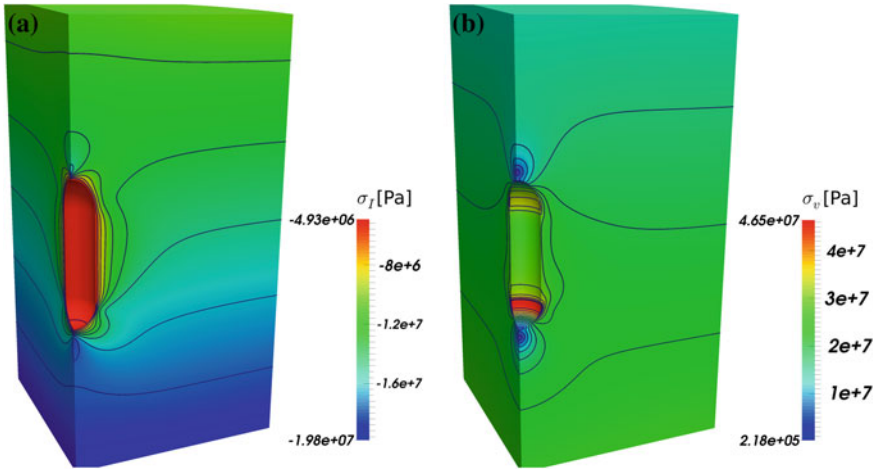


**Fig. 7.10** First principal stress  $\sigma_I$  (a) as well as *von Mises* equivalent stress  $\sigma_v$  (b) of the linear elastic cavern

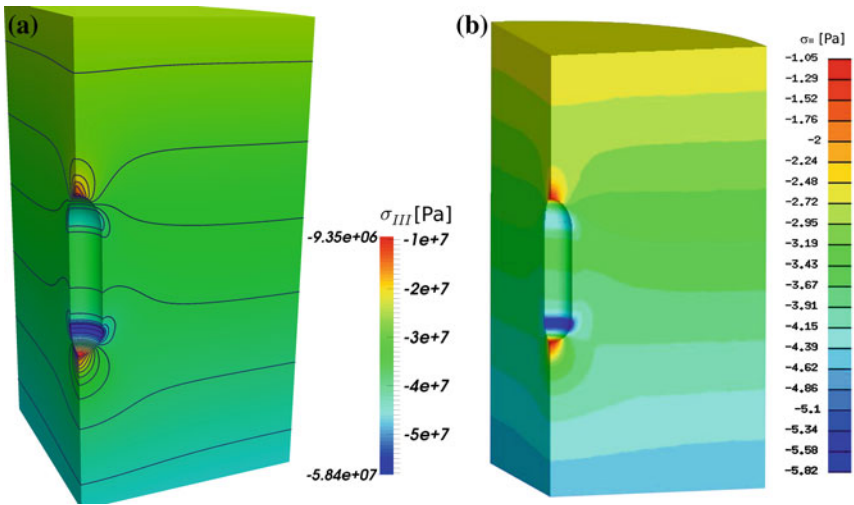


**Fig. 7.11** Comparison of third principal stress  $\sigma_{III}$  computed by OpenGeoSys (a) and by FEBio (b)

operations. In this case, the gas pressure inside the cavern is low, so that the cavern walls are displaced in negative  $r$  direction by a few centimeters, as can be seen in Fig. 7.12a. Due to its own weight and the top load, the top of the model domain is squeezed downwards by about  $u_z = -1.9$  m, see Fig. 7.12b.

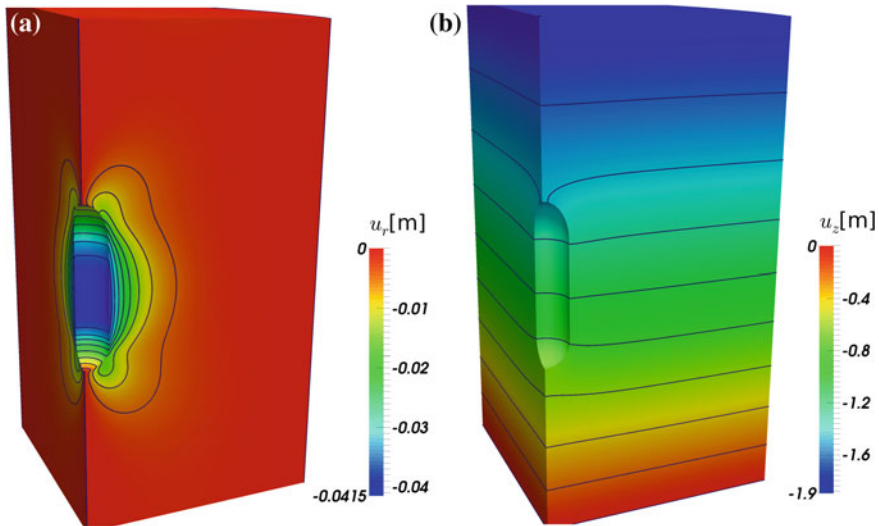


**Fig. 7.12** Displacement  $u_r$  in radial direction (a) and  $u_z$  in vertical direction (b) for linear elastic material behaviour

To validate the OpenGeoSys results, a model comparison against another FE simulator was made. Figure 7.11 shows the third principal stress distribution in the domain computed by OpenGeoSys and by FEBio [2]. Both plots show basically the same results, slight differences can be explained by a much coarser resolution of the mesh that was used for the FEBio simulation: the 3D mesh uses quarter symmetry and consists of 277105 nodes and 1563712 linear tetrahedral elements. The minimal edge length (located at the cavern wall) was about 1 m.

### 7.4.2 Elastoplastic Material

While the last example considered linear elastic material behaviour, this case investigates plastic deformation beyond an arbitrarily chosen yield stress of  $\sigma_F = 20$  MPa according to the *von Mises* plasticity model (Fig. 7.13). Otherwise, the model setup is identical to the last example. Due to the overburden load, the *von Mises* stress exceeds the critical yield stress at about the height of the cavern, as displayed in Fig. 7.14a. Due to the displacement constraints at the model boundary, plastic deformation predominantly occurs at the border of the cavern. The accumulated plastic strain can be seen in Fig. 7.14b. Therefore, displacements in the radial direction are larger compared to the elastic example (compare Figs. 7.12a and 7.15a).

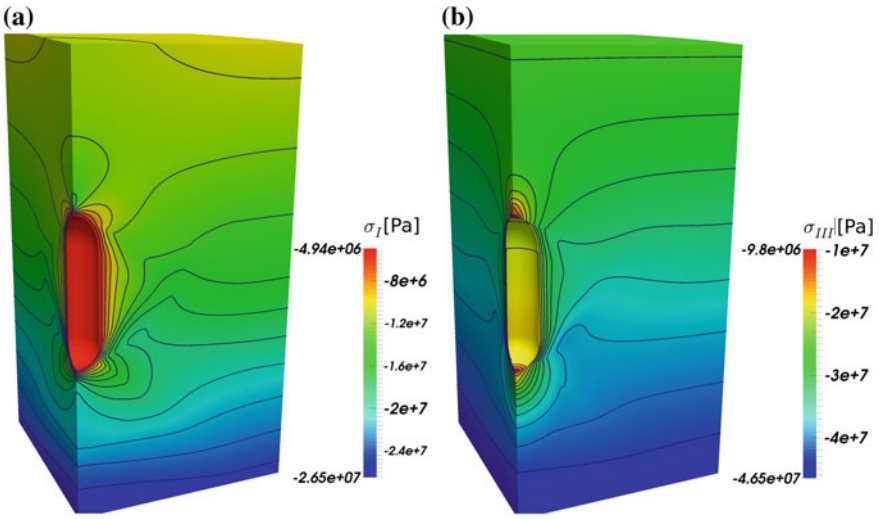


Fig. 7.13 First principal stress  $\sigma_I$  (a) and third principal stress  $\sigma_{III}$  (b) of the elastoplastic cavern

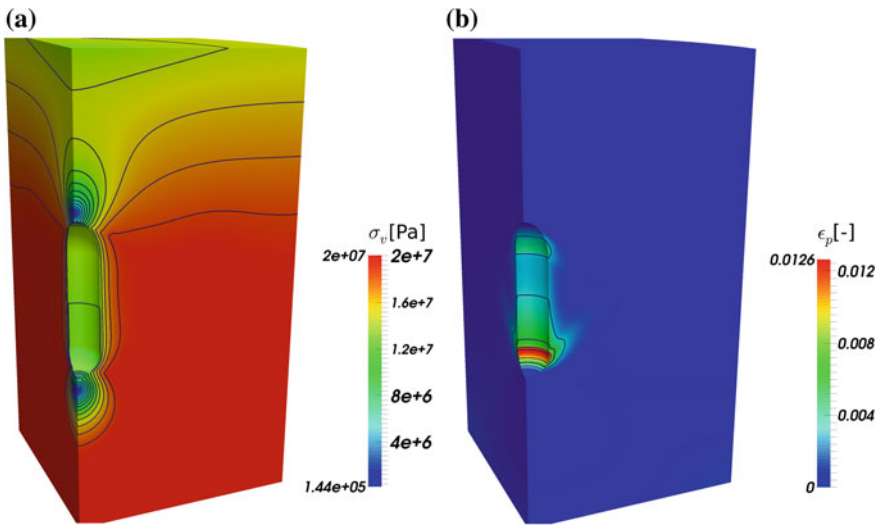
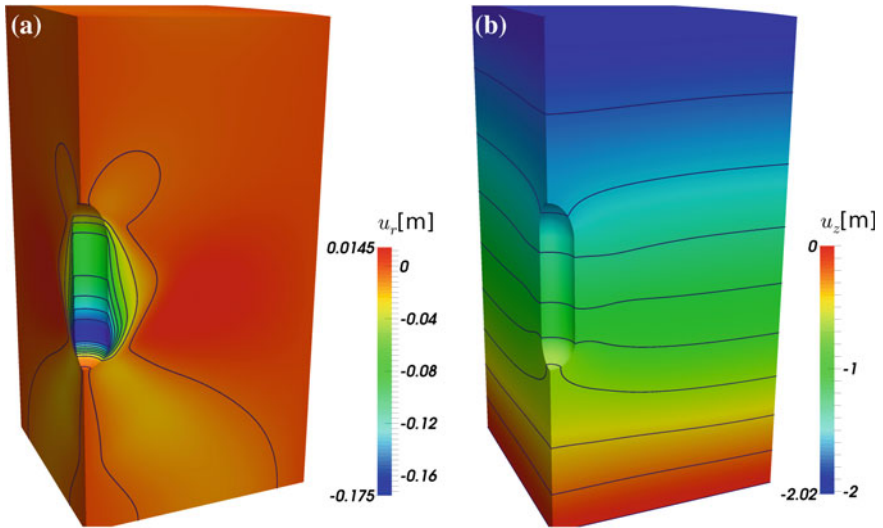


Fig. 7.14 von Mises equivalent stress  $\sigma_v$  (a) and accumulated plastic strain  $\epsilon_p$  (b) of the elastoplastic cavern



**Fig. 7.15** Displacement  $u_r$  in radial direction (a) and  $u_z$  in vertical direction (b) for a *von Mises* plasticity model

## References

1. O.C. Zienkiewicz, R.L. Taylor, and J.Z. Zhu. *The finite element method set*. Elsevier Butterworth-Heinemann, Oxford, 6 edition, 2005–2006.
2. Maas S.A., Ellis B.J., Ateshian G.A., and Weiss J.A. FEBio: Finite elements for biomechanics. *Journal of Biomechanical Engineering*, 134(1), 2012.

**Part III**  
**Coupled Processes**

# Chapter 8

## Density-Dependent Flow

Marc Walther, Leonard Stoeckl, Jens-Olaf Delfs and Thomas Graf

Density-driven flow still remains to be a demanding challenge for both, the user and the numerical model. Especially for real-world applications, e.g. regional scale case studies, or even smaller scale laboratory experiments, proper parametrization is an ambitious task, that is usually addressed by calibration. Additionally, when spatial heterogeneity is high, and forces to drive variable-density flow are strong, it may be hard to acquire convergence of the model. Yet, it is unavoidable to include density coupling for applications where changes of fluid parameters result in a variation of the flow conditions. Popular examples include seawater intrusion, or saltwater upcoming as a result from excessive pumping activity, or when fluid parameters vary due to changing boundary conditions, e.g. temperature change due to geothermal gradient, or atmospheric influence on shallow groundwater bodies.

Proper benchmarking is a necessary task to understand complex model behaviour and ensure correct model propagation capabilities. In the following, we present two benchmarks to proof applicabilities of OPENGEO SYS to simulate density-dependent flow. The examples include transient development of a freshwater lens and stability

---

M. Walther (✉)

Helmholtz Centre for Environmental Research UFZ, Permoserstr. 15,  
04318 Leipzig, Germany  
e-mail: Marc.Walther@ufz.de

J.-O. Delfs

Institute for Geosciences Geohydromodelling, Christian-Albrechts-Universität zu Kiel,  
Ludewig-Meyn-Straße 10, 24118 Kiel, Germany

L. Stoeckl

Federal Institute for Geosciences and Natural Resources (BGR),  
Stilleweg 2, 30655 Hannover, Germany

T. Graf

Institute of Fluid Mechanics and Environmental Physics in Civil Engineering,  
Leibniz Universität Hannover,  
Appelstraße 9a, 30167 Hannover, Germany

© Springer International Publishing Switzerland 2015

O. Kolditz et al. (eds.), *Thermo-Hydro-Mechanical-Chemical Processes in Fractured Porous Media: Modelling and Benchmarking*, Terrestrial Environmental Sciences,  
DOI 10.1007/978-3-319-11894-9\_8

for thermohaline convection. Relevant governing equations were given in the previous edition of the book [1] and are not repeated at this point.

## 8.1 Haline Setups

### 8.1.1 Development and Degregation of a Freshwater Lens

#### 8.1.1.1 Problem Description

This benchmark shows the capability of OPENGEO5YS to represent displacement of saline water due to an infiltration recharge process from top in a saturated, initially completely salinized domain. Experimental data from [2] is used to validate the shape in the development and degregation phase, and maximum penetration depth of the freshwater lens.

#### 8.1.1.2 Methods and Model Setup

The geometry of the physical model of [2] was a symmetrical trapezoid. The conceptual model for the numerical setup includes the left side of the real-world setup, dividing the model at the symmetry line to reduce computational burden (see Fig. 8.1). Table 8.1 shows simulation parameters.

The experiment was two-folded: (i) starting from an initial state of full salinization, a constant recharge  $q$  was applied on top of the domain until a steady state was reached at time  $t_1$ ; (ii) when the freshwater lens was fully evolved, recharge flux was stopped and the degregation of the lens was observed. The homogeneous, isotropic domain was set up using triangular elements with a mean edge length  $\Delta l \approx 3 \times 10^{-3}$  m. At right and bottom sides, boundary conditions (BCs) are Neumann 2nd-type NO-FLOW for flow and transport. On the top edge, a 2nd-type recharge rate was applied uniformly with  $q(0 < t \leq t_1) = 1.3 \times 10^{-5} \text{ m}\cdot\text{s}^{-1}$  and  $q(t > t_1) = 0$ . Mass transport

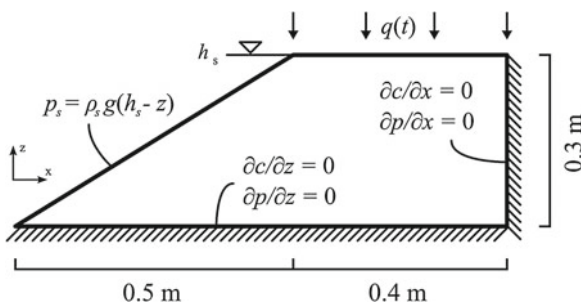


Fig. 8.1 Model domain and boundary conditions after [2] (not to scale)

**Table 8.1** Benchmark parameters for freshwater lens development

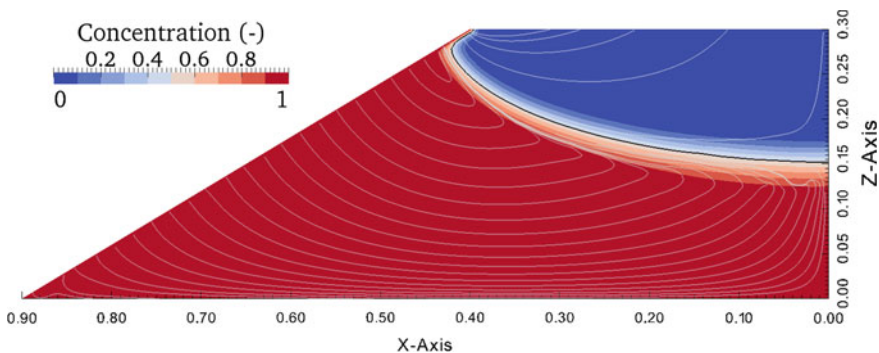
Parameter	Value
Saltwater head $h_s$ (m)	0.0
Porosity $\varphi$ (-)	0.39
Permeability $\kappa$ ( $m^2$ )	$4.601 \cdot 10^{-10}$
Dynamic viscosity $\mu$ ( $Pa \cdot s$ )	$1 \cdot 10^{-3}$
Specific storage $S_s$ (-)	$1 \cdot 10^{-4}$
Freshwater density $\rho_f$ ( $kg \cdot m^{-3}$ )	997
Saltwater density $\rho_s$ ( $kg \cdot m^{-3}$ )	1,021
Saltwater-freshwater density relation $\gamma_c$ (-)	0.02407
Longit./transv. dispersivity $\alpha_{l/t}$ (m)	$5 \cdot 10^{-3}/5 \cdot 10^{-4}$
Diffusion coefficient $D_m$ ( $m^2 \cdot s^{-1}$ )	$1 \cdot 10^{-9}$

BC on top was  $c = 0$  for  $0 < t \leq t_1$  and switched to no-flow for  $t > t_1$ . For the left, inclined edge, constant 1st-type linear pressure gradient  $p(z)$  and concentration BC  $c = c_s = 1$  were set.

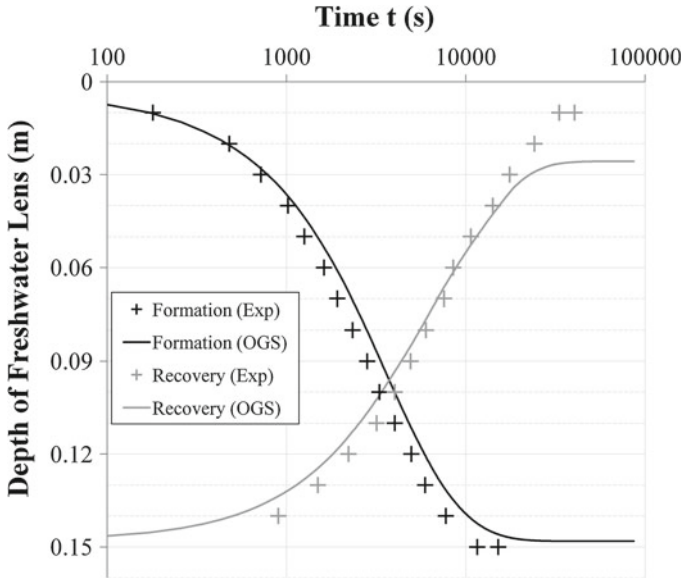
### 8.1.1.3 Results

Figure 8.2 shows the steady state flow regime at  $t_1$ . A stable freshwater lens evolved with a mixing zone visible at the interface between the fresh and saltwater. During evolution of the lens, recharge applied on top forced saltwater to retreat and flow out of the domain on the left boundary. Stream tracers show homogeneous flow paths with only small disturbance in the mixing zone.

On the right side, at the symmetrical line of the domain, the depth of the isoline of  $c = 0.5$  (black line in Fig. 8.2) is observed over time for formation and recovery of the lens. The results are compared to experimental data in Fig. 8.3. Generally, numer-



**Fig. 8.2** Concentration and flow paths for steady state of freshwater lens



**Fig. 8.3** Depth of freshwater lens (isoline  $c = 0.5$ ) at right edge of domain

ical results from OPENGEOsYS are in good accordance with laboratory observations. The temporal development of the formation and recovery, as well as total penetration depth of the freshwater lens are met with deviations in the range of  $\leq 1$  cm, which is likely below visual accuracy of laboratory observations. Small deviations only occur to the end of the recovery experiment, when differences between laboratory and numerical results slightly increase. Despite limited observation accuracy, deviations might also be due the interpolation technique used for data extraction of the visualization software ParaView.

## 8.2 Thermohaline Setups

### 8.2.1 Stability in Rayleigh Convection

#### 8.2.1.1 Problem Description and Introduction

This benchmark investigates the capability of OPENGEOsYS to delineate the boundary between diffusive and convective regimes in a thermohaline double-diffusive setup. The stability of a density-driven system can be defined by the Rayleigh Number  $Ra$  as

$$\text{Ra}_\Psi = \frac{\rho^f g \kappa}{\mu} \cdot \frac{\gamma_\Psi H \Delta\Psi}{D_{m,\Psi}} \quad (8.1)$$

with  $\Psi$  as an arbitrary system variable,  $\rho^f$  as fluid density,  $g$  as gravity constant,  $\kappa$  as permeability,  $\mu$  as dynamic viscosity,  $\gamma_\Psi$  as expansion coefficient due to change of  $\Psi$ ,  $H$  as height of the system,  $\Delta\Psi$  as difference of boundary conditions, and  $D_{m,\Psi}$  as molecular diffusivity of  $\Psi$ . Depending on the strength of the convective or diffusive part (denominator and numerator in Eq. 8.1, respectively), a convective or diffusive regime will evolve in a variable density system.

For a thermohaline system, where density is influenced by both, temperature  $T$  and concentration  $c$ , two Ra can be defined for heat and mass transport,  $\text{Ra}_T$  and  $\text{Ra}_c$  respectively, extending the regime characterization into a two-dimensional space. Nield [3] postulated several boundaries to distinguish between stable convective and diffusive regimes. For the simplest case, one can define the critical Rayleigh Number  $\text{Ra}'$  of the boundary as

$$\text{Ra}' = \text{Ra}_T + \text{Ra}_c = 4\pi^2 \quad (8.2)$$

Being able to define the stability of a system a priori may provide valuable information for contaminant migration without the need to set up a numerical model. Also, a thermohaline benchmark evaluates the robustness of a numerical modelling software, as double diffusive models tend to remain initially stable for a long time until a small disturbance fastly causes convective motion.

### 8.2.1.2 Methods and Model Setup

The model setup is a two-dimensional, homogeneous, vertical domain with a spatial discretization of  $\Delta x = \Delta z = 0.25$  m. The conceptual model, including boundary and initial conditions, is pictured in Fig. 8.4. Relevant model parameters are listed in Table 8.2. Time step sizes are controlled by an adaptive error-control method.

Horizontal bottom and top boundaries are defined as 1st-type boundary conditions for heat and mass transport, while  $\Delta T$  and  $\Delta c$  are defined in the way, that Ra will have a value close to  $\text{Ra}'$ . Vertical boundaries are defined as 2nd-type no-flow conditions. An initial linear gradient distribution is given for all primary variables, i.e. temperature, concentration, and pressure.

At point  $\text{P}_{\text{dist}}$ , a disturbance of 10 % (as deviation from the initial linear distribution of temperature and heat) provides a small initial instability. Assuming, the grid has a fine resolution, possible convection is therefore not initiated by numerical errors. The latter would depend on the model accuracy (including grid level, time stepping, solver convergence criteria etc.), thus being unrelated to the capabilities of the numerical model itself to solve the problem.

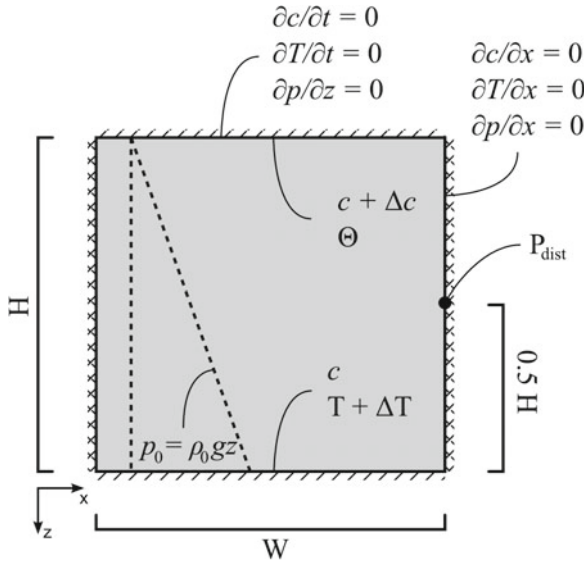


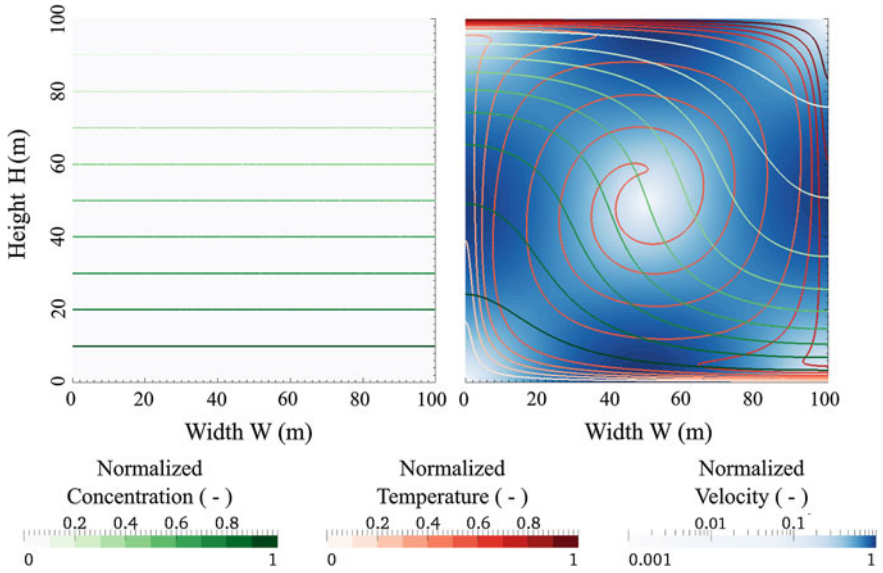
Fig. 8.4 Model domain and boundary conditions for thermohaline simulation

### 8.2.1.3 Results

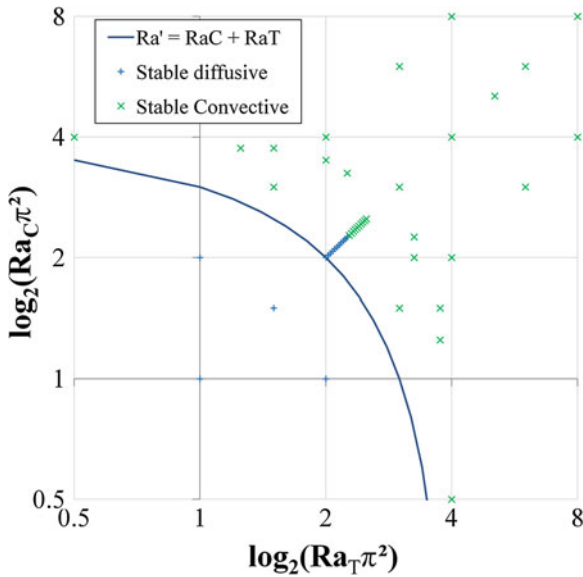
Figure 8.5 plots exemplary a stable diffusive and a stable convective regime. In the diffusive case, the initial disturbance disperses very fast showing no indication of any convective fluid motion; the transport is dominated by diffusion. In the convective case, the sign of the initial disturbance, i.e.  $\pm 10\%$ , decides the direction of the initiated convective flow; the transport is dominated by convection. Both exemplary simulations reach the stable state within a small number of time steps.

Table 8.2 Parameters used in thermohaline simulations

Parameter	Value
Density solid $\rho^s$ ( $\text{kg} \cdot \text{m}^{-3}$ )	2,650
Heat capacity solid $C_p^s$ ( $\text{J} \cdot \text{kg}^{-1} \cdot \text{K}^{-1}$ )	800
Thermal conductivity solid $\lambda^s$ ( $\text{W} \cdot \text{m}^{-1} \cdot \text{K}^{-1}$ )	1.5
Initial density fluid $\rho_0^f$ ( $\text{kg} \cdot \text{m}^{-3}$ )	1,000
Heat capacity fluid $C_p^f$ ( $\text{J} \cdot \text{kg}^{-1} \cdot \text{K}^{-1}$ )	4,184
Thermal conductivity fluid $\lambda^f$ ( $\text{W} \cdot \text{m}^{-1} \cdot \text{K}^{-1}$ )	0.5
Dynamic viscosity $\mu$ ( $\text{Pa} \cdot \text{s}$ )	0.0011
Permeability $\kappa$ ( $\text{m}^2$ )	$2.7 \cdot 10^{-12}$
Molecular diffusion coefficient $D_m$ ( $\text{m}^2 \cdot \text{s}^{-1}$ )	$1 \cdot 10^{-8}$
Porosity $\varphi$ (-)	0.3
Haline expansion coefficient $\gamma_c$ (-)	0.7
Thermal expansion coefficient $\gamma_T$ ( $\text{K}^{-1}$ )	-0.001



**Fig. 8.5** Distribution of normalized temperature, concentration, and velocity, exemplary given as steady states for  $Ra_T = Ra_c = 1\pi^2$  (a diffusive), and  $Ra_T = 6\pi^2$ ,  $Ra_c = 3\pi^2$  (b convective)



**Fig. 8.6** Boundary at critical Rayleigh number  $Ra'$  compared to simulation results

Figure 8.6 shows different states along the critical Rayleigh number  $Ra' = 4\pi^2$ . Simulation results are in close correlation with the theory. Stable diffusive regimes generally evolve for  $Ra < Ra'$ , and stable convective state can be observed for larger  $Ra$ . Small deviations can be found close to the critical Rayleigh number. For  $Ra_T = Ra_c$ , the conversion from a diffusive to a convective regime occurs between  $2.25\pi^2 < Ra_i < 2.275\pi^2$ .

## References

1. O. Kolditz, U. J. Görke, H. Shao, and W. Wang, editors. *Lecture Notes in Computational Science and Engineering 86: Thermo-Hydro-Mechanical-Chemical Processes in Fractured Porous Media*. Springer, Heidelberg, Dordrecht, London, New York, 1 edition, 2012.
2. Leonard Stoeckl and Georg Houben. Flow dynamics and age stratification of freshwater lenses: Experiments and modeling. *Journal of Hydrology*, 458–459:9–15, August 2012.
3. D.A. Nield and A. Bejan. *Convection in Porous Media*. Springer, 1999.

# Chapter 9

## Multiphase Flow and Transport with OGS-ECLIPSE

Wolf Tilmann Pfeiffer, Christof Beyer, Bastian Graupner  
and Sebastian Bauer

### 9.1 Introduction

For the combined simulation of multiphase flow and transport OpenGeoSys has been coupled with the ECLIPSE simulator package [1]. In this chapter we present the coupling principle of OGS with ECLIPSE as well as some test cases used to evaluate the functionality and the performance of the OGS-ECLIPSE simulator.

For the basic principles of multiphase flow and transport within a porous medium please refer to Chaps. 10 and 12 of [2].

The ECLIPSE simulator package consists of two simulators tailored specifically for different model scenarios. E100 is a black-oil simulator while E300 is a compositional simulator. Both simulators can use either a fully implicit or a IMPES (implicit pressure, explicit saturation) scheme for solving the partial differential equations. As a default E100 utilizes the fully implicit scheme while E300 uses the combined AIM (adaptive implicit method) approach in which the fully implicit and the IMPES scheme are used for different areas of the model domain simultaneously.

When combining OGS and ECLIPSE, each simulator handles individual processes (Fig. 9.1). ECLIPSE simulates the flow process while OGS provides the general framework for the ECLIPSE model and solves for all additional processes, i.e. mass transport, chemical reactions or heat transport. ECLIPSE and OGS each need a dedicated grid. Mesh consistency is mandatory between both simulators and non-neighbour connections are not supported. ECLIPSE uses the corner point gridding approach, thus the OGS mesh is limited to hexahedral elements. Because both grids

---

W.T. Pfeiffer (✉) · C. Beyer · S. Bauer  
Christian-Albrechts-Universität zu Kiel, Ludwig-Meyn-Str. 10, 24118 Kiel, Germany  
e-mail: wtp@gpi.uni-kiel.de

B. Graupner  
Eidgenössisches Nuklearsicherheitsinspektorat ENSI, Industriestrasse 19, 5200 Brugg,  
Switzerland

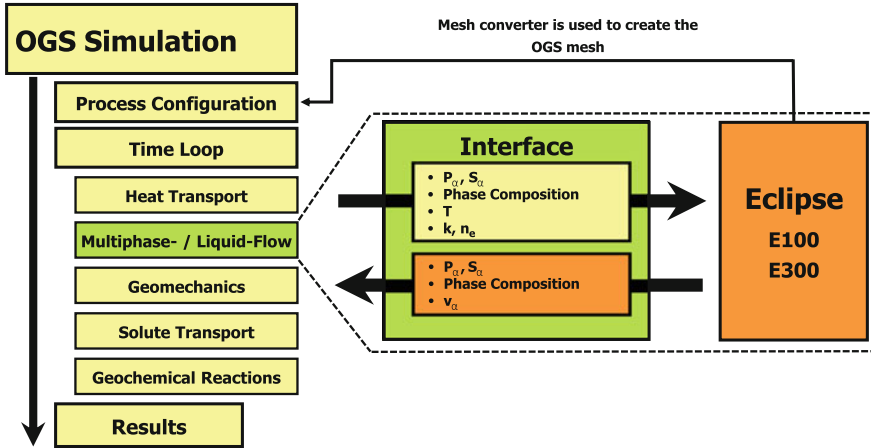


Fig. 9.1 Schematic overview of the OGS-ECLIPSE interface and its integration into the OGS process structure

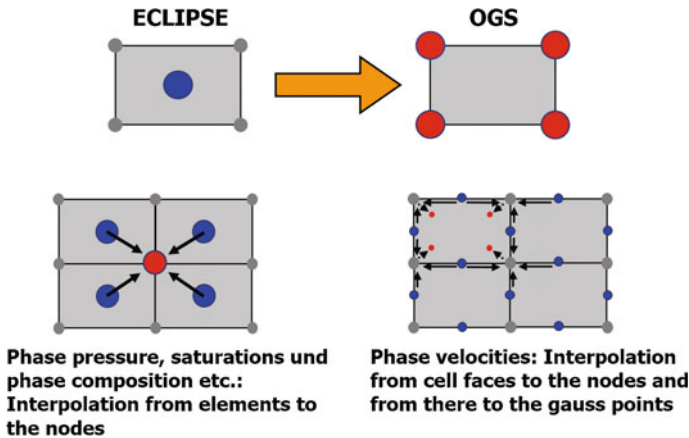


Fig. 9.2 Interpolation scheme used to transfer the data from ECLIPSE to OGS. The position of the data in ECLIPSE is depicted in blue, OGS in red

have to be identical, the OGS grid creation is automated by a grid conversion tool and based on the ECLIPSE grid.

Since both simulators work with different numerical schemes (OGS—Finite Elements, ECLIPSE—Finite Differences) the model data has to be converted between them (Fig. 9.2). For ECLIPSE the primary variables pressure and saturation are calculated in the grid block center, corresponding to the center of the elements. OGS calculates these variables at the nodes of the Finite-Element mesh, which are situated at the corner of the element. Pressure and saturation thus have to be interpolated from the element centers to the element corners to be available within the OGS data

structure. Phase velocities are calculated by ECLIPSE at the block faces, and therefore have to be converted to the element Gauss points. This is done by first interpolating the data to the element nodes and from there to the Gauss points. All data conversions are done using an inverse volume weighted interpolation scheme. Transferring the flow data of ECLIPSE to the correct position instead of recalculating it using the pressure distribution maintains a higher data precision. A detailed description of the OGS-ECLIPSE interface is given in [3]. As of OGS v5.5 the interface is capable of working with the ECLIPSE E100 simulator as well as the E300 simulator with the option CO2STORE enabled.

## 9.2 Test Cases

### 9.2.1 Two-Phase Flow with Two-Phase Transport

#### 9.2.1.1 Description

The first test case represents the injection of supercritical CO<sub>2</sub> into a deep aquifer initially fully saturated with brine. Additionally to multiphase flow, tracers are transported in both the gas and the water phase.

A quasi 2D model of 200 m length, 0.1 m width and a vertical thickness of 20 m is used to simulate the lateral and vertical spreading of the gas phase as well as the advance of the dissolved tracer fronts. The spatial discretization increases from  $dx = 0.5$  m at the injection side of the model to  $dx = 34$  m at the outer model boundary. The injection boundary is set to a constant influx of CO<sub>2</sub> (BC of 2nd kind) and a constant gas phase tracer concentration (BC of 1st kind). The outer model boundary is set to a constant pressure (BC of 1st kind). Initially a hydrostatic pressure distribution is present in the aquifer. The water tracer is introduced into the model by defining initial tracer concentrations of  $1 \text{ mol/m}^3_{\text{water}}$  at a vertical polyline at  $x = 14$  m, near the injection side of the model. An initial CO<sub>2</sub> saturation of 0.025 is assumed throughout the model. All additional parameters used in the simulation are shown in Table 9.1. Multiphase flow is simulated using ECLIPSE, component transport is simulated using OGS. A component in OGS (Process MASS\_TRANSPORT) can only be defined in one phase, i.e. for each component in each phase one mass transport process has to be defined. Constant fluid parameters such as fluid density and viscosity are assumed. Brooks and Corey formulations are used for both the  $k_r(S)$  and the  $p_c(S)$  functions [4].

#### 9.2.1.2 Results

The model results are shown in Fig. 9.3. Both an upward and a lateral spreading of the CO<sub>2</sub> phase can be observed. The lateral movement of the CO<sub>2</sub> phase is a result of

**Table 9.1** Model parameters

Parameter	Symbol	Value	Unit
Permeability	$K_x$	$2 \times 10^{-13}$	$m^2$
	$K_y$	$2 \times 10^{-13}$	$m^2$
	$K_z$	$2 \times 10^{-14}$	$m^2$
Porosity	$n$	0.2	–
CO <sub>2</sub> injection rate	$Q_{in}$	0.256	$m^3/s$
residual water saturation	$S_{w\ res}$	0.25	–
residual CO <sub>2</sub> saturation	$S_{CO_2\ res}$	0.0	–
Brooks and Corey exponent	$\lambda$	2	–
capillary entry pressure	$P_{c\ entry}$	0.05	bar
Density CO <sub>2</sub>	$\rho_{CO_2}$	675	$kg/m^3$
Density brine	$\rho_{water}$	1050	$kg/m^3$
Viscosity CO <sub>2</sub>	$\eta_{CO_2}$	$5.5 \times 10^{-5}$	$Pa \cdot s$
Viscosity brine	$\eta_{water}$	$5.1 \times 10^{-4}$	$Pa \cdot s$

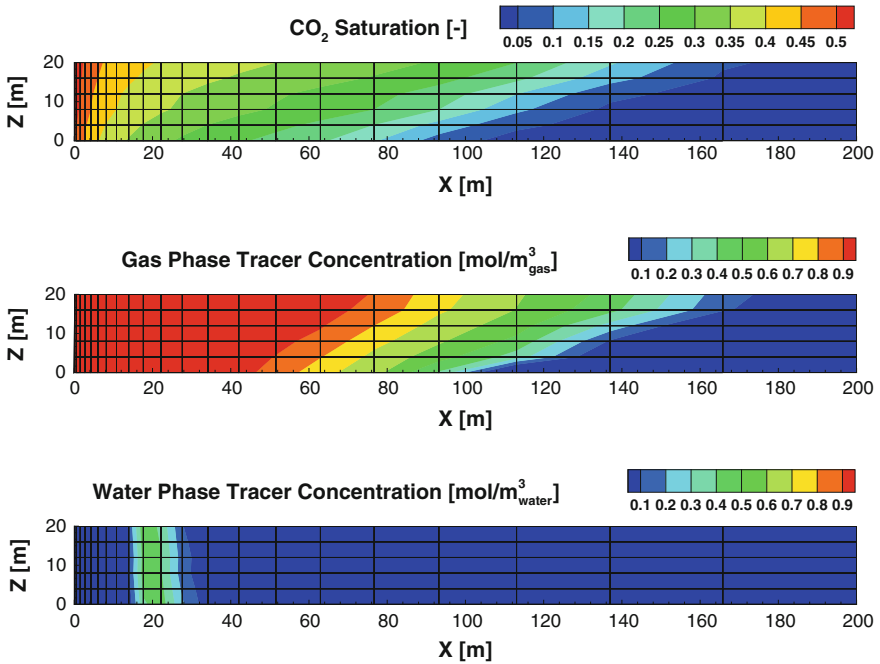


**Fig. 9.3** CO<sub>2</sub> saturation (*top*), gas phase tracer concentration (*middle*) and water phase tracer concentration after 50 days of injection

the injection induced pressure gradient from the injection well to the fixed pressure model boundary. The vertical movement of the  $\text{CO}_2$  is due to the gravitational sorting of the heavier water and the lighter  $\text{CO}_2$  gas phase. The advance of the gas phase tracer front corresponds to the movement of the  $\text{CO}_2$  phase. The initially present  $\text{CO}_2$  causes a smearing of the gas phase tracer front as a result of mixing the initially present tracer free  $\text{CO}_2$  gas with the tracer enriched injected  $\text{CO}_2$ . The water tracer only shows slight movement. This small displacement is a result of the water phase saturation approaching its residual saturation due to the injected  $\text{CO}_2$ , thus reducing the mobility of the water phase.

## 9.2.2 Gas Phase Partitioning

### 9.2.2.1 Description

The second test case resembles a static groundwater body in which a leakage of  $\text{CO}_2$  from a storage formation below the aquifer occurs.  $\text{CO}_2$  is added to the model in dissolved form. Because  $\text{CO}_2$  is added faster than it is transported away by diffusion,  $\text{CO}_2$  accumulates and eventually a  $\text{CO}_2$  phase will form. This benchmark tests the interaction of gas phase components between OGS and ECLIPSE.

The model is set up as a two phase model consisting of gas ( $\text{CO}_2$ ) and water of which initially only the water phase is present. Due to the dissolution of  $\text{CO}_2$  in the water phase, also mass transport is considered as a process. To simulate this test case a quasi 2D model of  $10\text{ m} \times 1\text{ m} \times 2\text{ m}$  is used. The model is discretized using 20 cells in x-direction and 5 cells in z-direction. An isotropic permeability of  $2 \times 10^{-13}\text{ m}^2$  and a porosity of 0.2 is assumed. The  $k_r(S)$  and  $p_c(S)$  relationships are described using linear functions. Effects of capillary trapping are neglected by defining the capillary entry pressure as  $p_{c\text{ entry}} = 0\text{ bar}$ . Upper and lower model boundaries are assumed to be closed, on the left and right model boundary constant hydrostatic pressure is assumed. The dissolved  $\text{CO}_2$  is introduced into the water phase at the bottom of the model domain by a constant source term of  $100\text{ mol}/(\text{s} \cdot \text{REV})$  and assumed to dissolve instantaneously. Since ECLIPSE uses an equilibrium approach to distribute the  $\text{CO}_2$  between the phases, increasing  $\text{CO}_2$  concentrations in the water phase eventually lead to out-gassing of the  $\text{CO}_2$  and thereby to the generation of a  $\text{CO}_2$  gas phase. The flow- and transport processes are handled by the E300 simulator with the fully-implicit scheme and the CO2STORE option while OGS is used to calculate the  $\text{CO}_2$  source term. When using the CO2STORE option, the fluid densities and viscosities are calculated by ECLIPSE. The  $\text{CO}_2$  density is determined using a modified Redlich and Kwong equation of state while the  $\text{CO}_2$  viscosity is calculated based on work by [5, 6]. Water density and viscosity are calculated using an analytical form presented by [1].

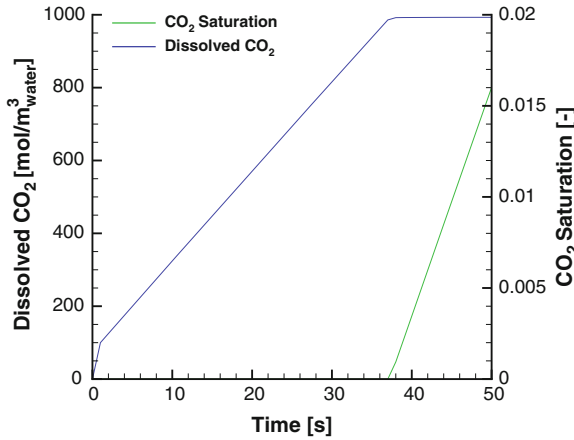


Fig. 9.4 Temporal evolution of the amount of dissolved CO<sub>2</sub> in water and the saturation of the CO<sub>2</sub> phase in the source zone

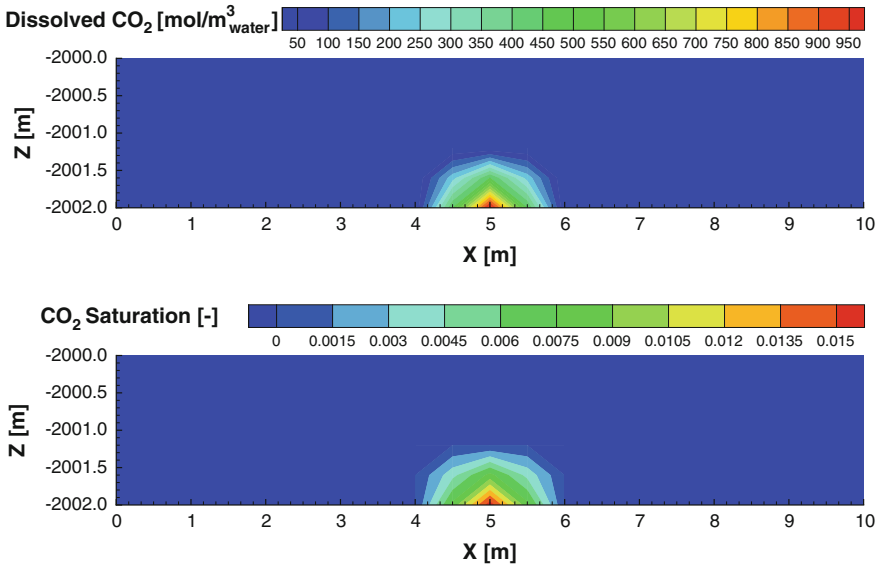


Fig. 9.5 Spatial distribution of the dissolved CO<sub>2</sub> concentration in water (top) and CO<sub>2</sub> phase generated (bottom) after 50s

### 9.2.2.2 Results

The results of the gas phase partitioning test case are shown in Figs. 9.4 and 9.5. The CO<sub>2</sub> is introduced into the model via the water phase which leads to an increasing CO<sub>2</sub> concentration in water. Once the maximum CO<sub>2</sub> solubility of about 1000 mol/m<sup>3</sup><sub>water</sub>

is reached within a cell, the gas saturation increases and a  $\text{CO}_2$  phase is generated (Fig. 9.4). From this time on the concentration of  $\text{CO}_2$  in the water phase stagnates at the maximum solubility and all additional  $\text{CO}_2$  is directly transferred into the gas phase. The timescale and the extent of the phase generation is a function of the leakage rate. In this case a strongly simplified scenario using a constant leakage rate of  $\text{CO}_2$  was assumed, which nevertheless shows the capability of both simulators to handle such gas phase generation problems.

## References

1. Schlumberger. *ECLIPSE reservoir simulation software v2012.1 - Technical Description Manual*. Schlumberger Ltd., 2012.
2. O. Kolditz, U. J. Görke, H. Shao, and W. Wang, editors. *Lecture Notes in Computational Science and Engineering 86: Thermo-Hydro-Mechanical-Chemical Processes in Fractured Porous Media*. Springer, Heidelberg, Dordrecht, London, New York, 1 edition, 2012.
3. B. J. Graupner, D. Li, and S. Bauer. The coupled simulator eclipse - opengeosys for the simulation of  $\text{CO}_2$  storage in saline formations. *Energy Procedia*, 4:3794–3800, 2011.
4. R. Brooks and A. Corey. *Hydrology Papers 3: Hydraulic Properties of Porous Media*. Colorado State University, Fort Collins, Colorado, 1964.
5. V. Vesovic, W. A. Wakeham, G. A. Olchowy, J. V. Sengers, J. T. R. Watson, and J. Millat. The transport properties of carbon dioxide. *Journal of Physical and Chemical Reference Data*, 19(3):763–808, 1990.
6. A. Fenghour, W. A. Wakeham, and V. Vesovic. The viscosity of carbon dioxide. *Journal of Physical and Chemical Reference Data*, 27(1):31–44, 1998.

# Chapter 10

## Coupled THM Processes

Fabien Magri, Jobst Maßmann, Wenqing Wang and Katharina Benisch

### 10.1 HM/THM Processes in a Faulted Aquifer

Hydro-Mechanical (HM) and transient Thermo-Hydro-Mechanical (THM) simulations in a faulted aquifer are presented. Both 2D and 3D scenarios are illustrated. OpenGeoSys (OGS) results are compared with those obtained using ABAQUS [1], a commercial finite element software with wide material modeling capability, including coupled hydraulic and mechanical processes in porous media. To some extent, the results comparison validates OGS numerical capabilities in solving 2D and 3D HM and THM problems.

#### 10.1.1 Definition

The model geometry is shown in Fig. 10.1. The model is a  $900 \times 900$  m cube including a 100 m thick storage aquifer embedded in a sedimentary fill. A 20 m wide fault with a dip angle of  $80^\circ$  cuts all units. The fault is conceptually modeled as an equivalent porous media, i.e. a unit made of solid elements with their own hydraulic and

---

F. Magri (✉)

Helmholtz Centre Potsdam, GFZ German Research Centre For Geosciences,  
Telegrafenberg, 14473 Potsdam, Germany  
e-mail: fabienma@gfz-potsdam.de

K. Benisch

Institute of Geosciences, Christian-Albrechts-Universität zu Kiel, Kiel, Germany

J. Maßmann

Federal Institute for Geosciences and Natural Resources BGR, Stilleweg 2,  
30655 Hannover, Germany

W. Wang

Helmholtz Centre for Environmental Research (UFZ), Permoserstr. 15,  
04318 Leipzig, Germany

© Springer International Publishing Switzerland 2015

O. Kolditz et al. (eds.), *Thermo-Hydro-Mechanical-Chemical Processes in Fractured Porous Media: Modelling and Benchmarking*, Terrestrial Environmental Sciences,  
DOI 10.1007/978-3-319-11894-9\_10

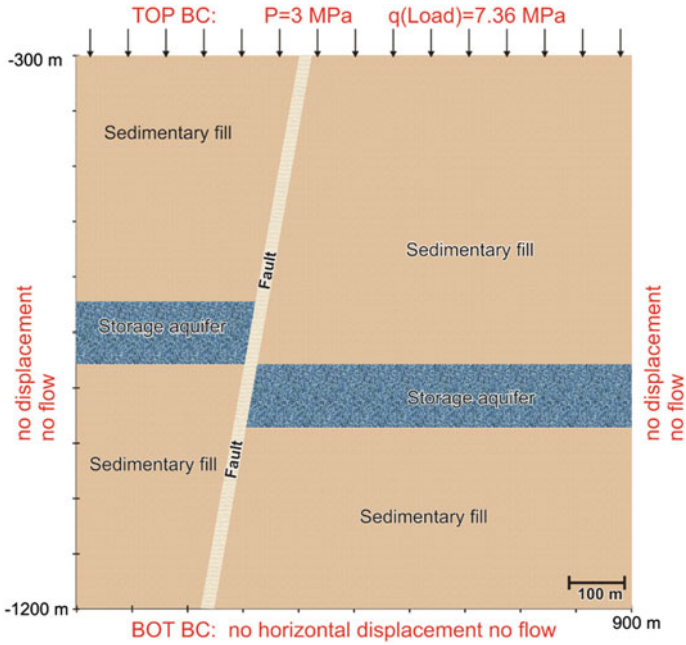


**Fig. 10.1** Model geometry displaying three different units (sedimentary fill, fault and storage aquifer) and the boundary conditions of the HM problem. In the 2D simulations, the vertical profile is referred to the XY reference frame (i.e. depth in the Y direction)

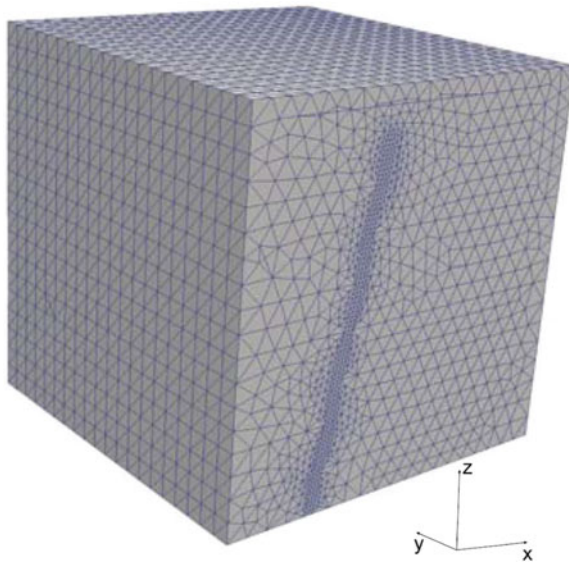


**Fig. 10.2** Example of 3D finite element mesh used for HM simulations (62,818 nodes and 359,566 tetrahedral elements) in OGS and ABAQUS

mechanical physical properties. Both ABAQUS and OGS numerical simulations use the same 3D mesh. For the HM case, the grid consists of 62,818 nodes and 359,566 tetrahedral elements. Elements near the fault are 10 m wide as shown in Fig. 10.2. For THM simulations instead, ABAQUS requires hexahedral elements. Here 30 m wide first order cubes (i.e. 8 nodes) are used to discretize the sedimentary fill, whereas in the fault the resolution is still 10 m.

### 10.1.2 Initial and Boundary Conditions

A hydrostatic pore pressure distribution is used to initialize the simulation. For simplicity zero stress field is set over the whole model. In the paragraph “Initial conditions effects”, a simulation importing a stress state as initial conditions is illustrated. Constant pore pressure ( $3 \times 10^6$  Pa) and stress ( $7.36 \times 10^6$  Pa load) are assumed as boundary conditions at the top. No flow is set on the remaining sides of the model. Null displacement conditions are applied normal to the vertical and bottom boundaries. A constant pressure of  $10^8$  Pa is set in the hanging wall aquifer (i.e. at the left side of the fault) in order to simulate the overpressure resulting from fluid injection. Though  $10^8$  Pa is not a realistic value it allows to test the software capabilities with regard to extreme pressures in a heterogeneous system.

### 10.1.3 Material Properties

Hydraulic and mechanical properties are given in Tables 10.1, 10.2 and 10.3, where each unit is considered isotropic and homogeneous. The fluid properties are: viscosity

**Table 10.1** Material properties of sedimentary fill

Property	Value	Unit
Density	2500	kg/m <sup>3</sup>
Young's modulus	$2.964 \times 10^{10}$	N/m <sup>2</sup>
Poisson's ratio	0.12	–
Permeability	$2 \times 10^{-16}$	m <sup>2</sup>
Storage coefficient	$8.63 \times 10^{-11}$	Pa <sup>-1</sup>
Porosity	0.04	–

**Table 10.2** Material properties of storage aquifer

Property	Value	Unit
Density	2200	kg/m <sup>3</sup>
Young's modulus	$1.44 \times 10^{10}$	N/m <sup>2</sup>
Poisson's ratio	0.20	–
Permeability	$1.5 \times 10^{-13}$	m <sup>2</sup>
Storage coefficient	$8.36 \times 10^{-11}$	Pa <sup>-1</sup>
Porosity	0.19	–

**Table 10.3** Material properties of fault

Property	Value	Unit
Density	2200	kg/m <sup>3</sup>
Young's modulus	$1.44 \times 10^{10}$	N/m <sup>2</sup>
Poisson's ratio	0.20	–
Permeability	$1.5 \times 10^{-12}$	m <sup>2</sup>
Storage coefficient	$1.96 \times 10^{-10}$	Pa <sup>-1</sup>
Porosity	0.19	–

$= 1 \times 10^{-3}$  Pa s, density= 998 kg m<sup>-3</sup>. Properties of the sedimentary fill and the storage aquifer represent sandstones according to data from the book by [2].

### 10.1.4 Results

The calculated 2D steady state pressure, pore fluid velocity, displacement and stress fields are illustrated and directly compared with the results obtained with ABAQUS in the following.

A pressure buildup induced by the highly pressurized hanging aquifer (Fig. 10.3) develops within the fault owing to its higher hydraulic permeability (Table 10.3). Con-

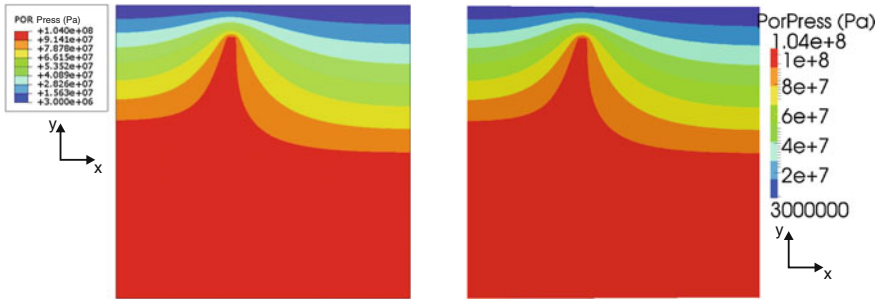


**Fig. 10.3** Pore pressure (Pa) distribution calculated with ABAQUS (left) and OGS (right)

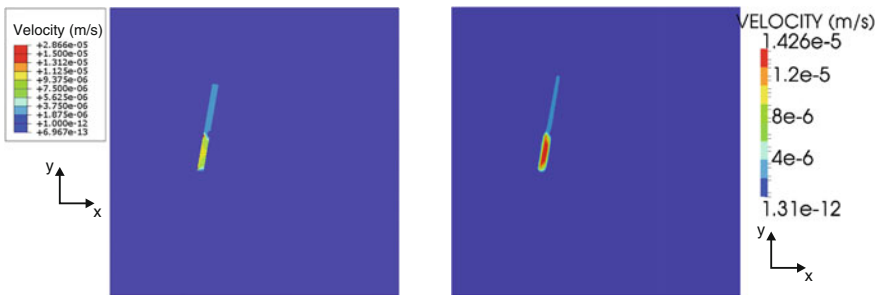


**Fig. 10.4** Pore fluid velocity (ms<sup>-1</sup>) calculated with ABAQUS (left) and OGS (right). Please note the different scales



Fig. 10.5 Displacement in the y direction (m) calculated with ABAQUS (left) and OGS (right)

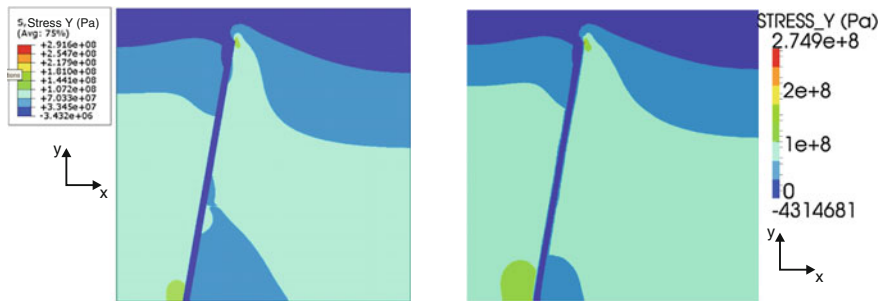
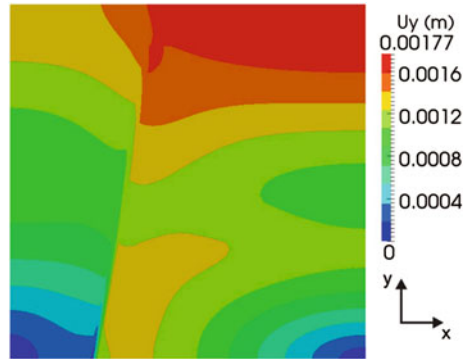


Fig. 10.6 Y component of the stress field (Pa) calculated ABAQUS (left) and OGS (right)

sequently, the fault acts as a preferential pathway for groundwater flow (Fig. 10.4). Deep seated fluids can flow therein at velocities ranging between  $4 \times 10^{-6}$  to  $1.4 \times 10^{-5}$  m/s (i.e. 0.3 to 1.2 m/day), the peak velocities being observed at the boundary between the storage aquifer and the fault zone. Owing to the no displacement conditions at the lateral and bottom boundaries, major structural deformations are observed within the sedimentary fill above the hanging storage aquifer (Fig. 10.5). The calculated uplift of the surface is 2.58 m, in good agreement with ABAQUS calculations. The sliding of the hanging wall occurs along the fault plane because of the differences in the material properties between the sedimentary fill and fault, in particular the density and the elastic properties. The physical properties contrast between the fault and surrounding sediments are also reflected in the calculated stress (Fig. 10.6). In general, the stress should increase roughly linear with depth due to the increase of lithostatic pressure with depth. Here, this trend is intensely perturbed by the fault. Jumps in stress magnitude at both the top and bottom interface of the fault may reach maximum values of several hundreds of MPa. Abrupt changes in stress magnitude also occur along the fault sides, as therein the stress reaches its minimal values.

**Fig. 10.7** Initial conditions effects: displacement in the y direction (m) calculated using initial stress and hydraulic pressure fields. The IC were derived a priori with a two time-steps simulation



### 10.1.5 Initial Conditions Effects

Here the stress and hydraulic pressure calculated with the previously described simulation are used as IC to verify whether or not the system is at hydro-mechanical equilibrium. If the mechanical equilibrium between the applied boundary conditions and the state of stress in the units has been reached, no displacement should be observed in this test case.

As a first test, a simulation is initialized with stress and hydraulic pressure fields that were calculated a priori with a two time-steps simulation. The vertical displacement is illustrated in Fig. 10.7. It can be seen that a vertical displacement exists though in the order of few millimeter (Fig. 10.7), suggesting that the stress field calculated with two time-steps is very close to mechanical equilibrium. An additional simulation initialized with stress and hydraulic pressure fields calculated with three iterations display no vertical displacement.

### 10.1.6 Temperature Effects THM Simulation

Here the results obtained from a transient Thermo-Hydro-Mechanical (THM) simulation are illustrated. Flow and mechanical boundary conditions are those pictured in Fig. 10.1. Additionally, a constant temperature of 17 and 44°C are set at the top and bottom boundaries, respectively, leading to a thermal gradient of 30 K/km.

**Table 10.4** Thermal properties of the solid and fluid used to simulate 2D and 3D THM problem

Layers	Specific heat capacity (J kg <sup>-1</sup> K <sup>-1</sup> )	Thermal conductivity (W m <sup>-1</sup> K <sup>-1</sup> )	Thermal expansion coefficient (K <sup>-1</sup> )
Solid	900	3	10 <sup>-5</sup>
Fluid	4,280	0.6	—

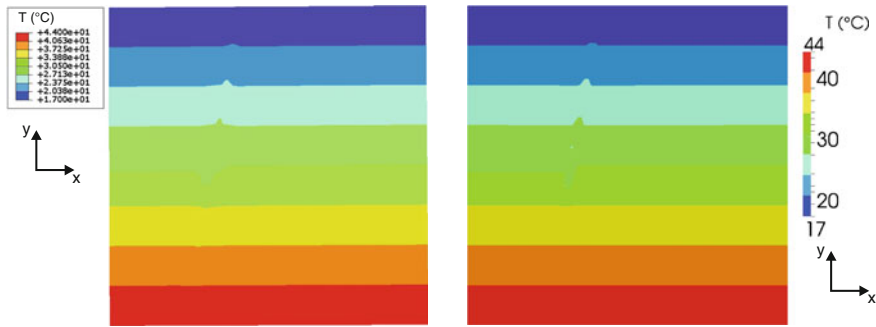


**Fig. 10.8** Temperature (°C) calculated with ABAQUS (*left*) and OGS (*right*). Temperature increase (decrease) can be observed in the fold as a result of fluid outflow from the storage aquifer into the fault

For simplicity, the whole model is homogeneous with respect to thermal properties (Table 10.4). The simulation is conducted for  $7.4 \times 10^7$  s (856 days) with a time step size of varying between  $10^5$  and  $10^6$  s (1 to 10 days). To ensure higher flow motion, the porosity of the sedimentary fill and fault are increased to 0.2 and 0.43 respectively. The other physical properties are those given in Tables 10.1, 10.2 and 10.3.

*Results of temperature* The hanging aquifer is saturated with fluid at 30°C approximately. Driven by the imposed pressure gradient, groundwater flows from the storage aquifer to the fault. As a result, fluid moving upward (downward) increases (decreases) the temperature within the fold, as illustrated by convex (concave) isotherms in Fig. 10.8.

### 10.1.6.1 3D Results

The same set of simulations has been run for the 3D cases. OGS results well compare to those obtained with ABAQUS which validates OGS capabilities in solving 3D pressure induced stress field (Figs. 10.9, 10.10, 10.11 and 10.12).

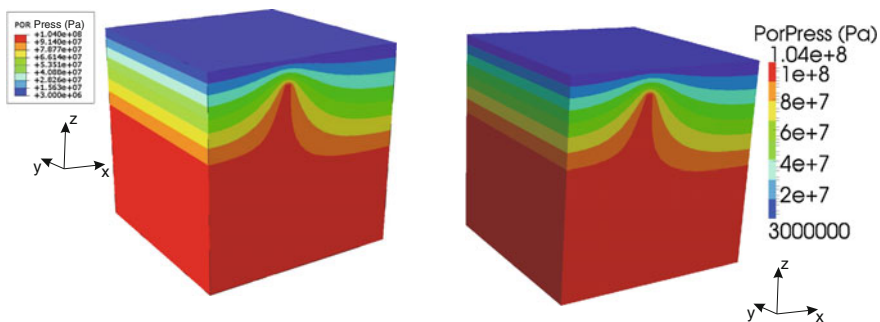


**Fig. 10.9** Pore pressure (Pa) distribution calculated with ABAQUS (*left*) and OGS (*right*)

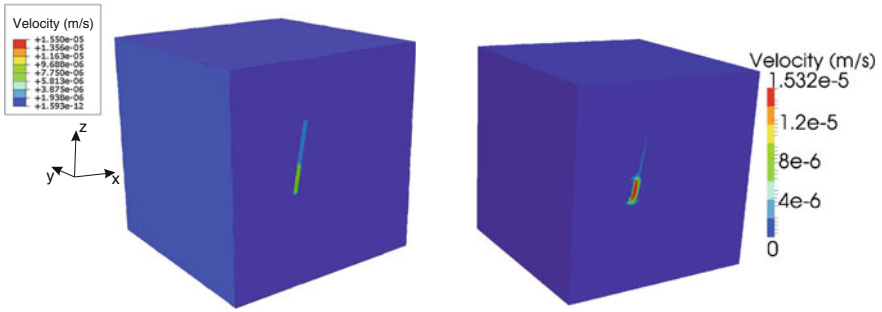


Fig. 10.10 Pore fluid velocity (m/s) calculated with ABAQUS (left) and OGS (right)

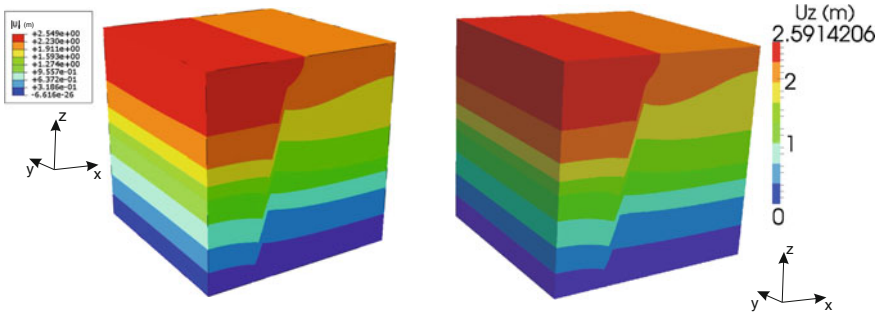


Fig. 10.11 Displacement (m) calculated with ABAQUS (left) and OGS (right)

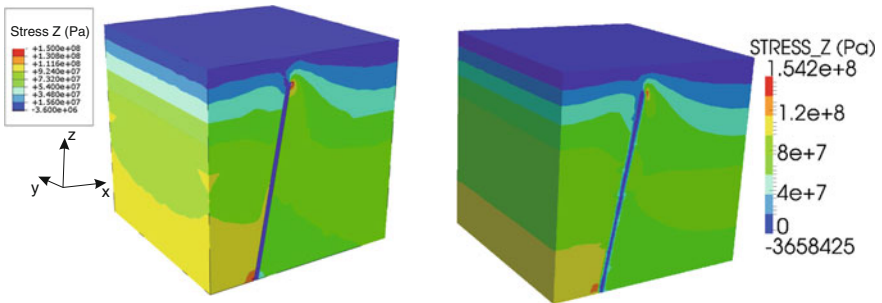
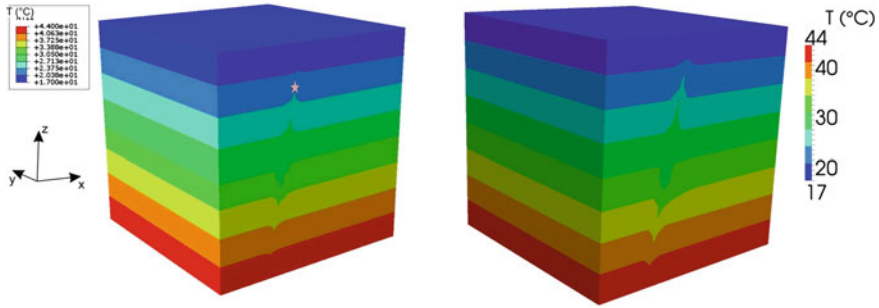
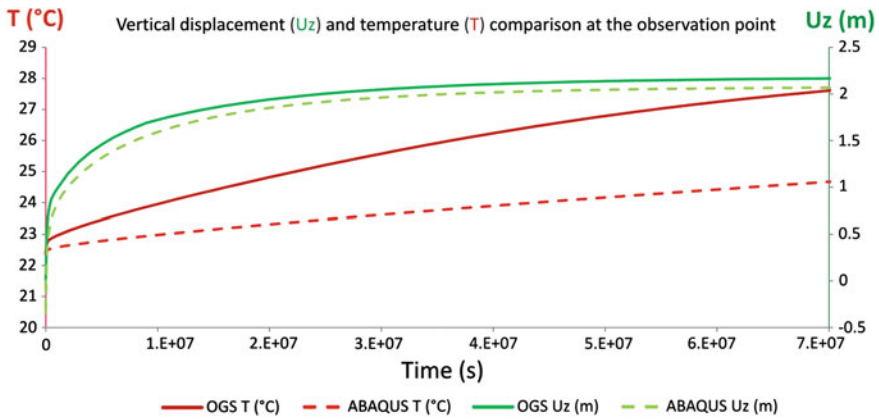


Fig. 10.12 Z component of the stress field (Pa) calculated with ABAQUS (left) and OGS (right)



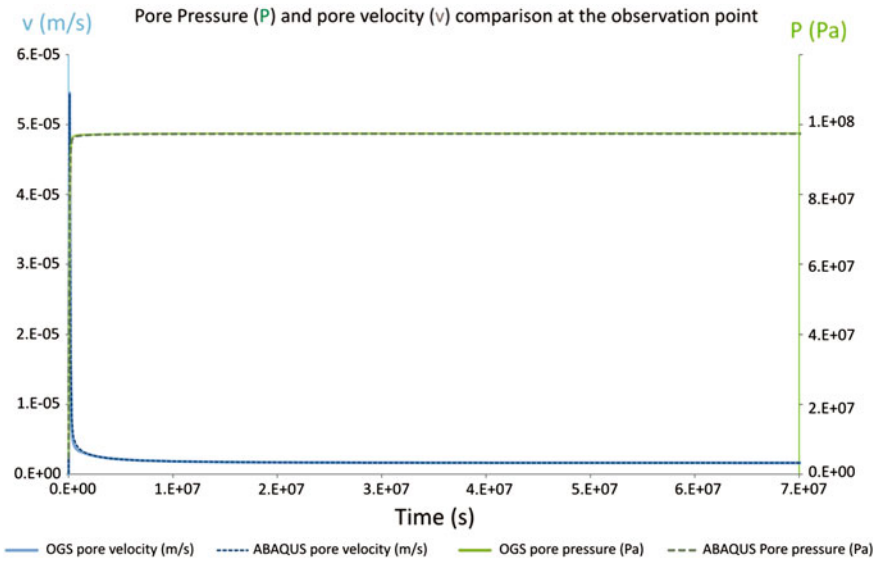
**Fig. 10.13** Temperature ( $^{\circ}\text{C}$ ) calculated at  $3 \times 10^7$  s with ABAQUS (left) and OGS (right). The star locates the observation point for the comparative graphs in Figs. 10.14 and 10.15



**Fig. 10.14** OGS and ABAQUS comparison: temporal trends at the observation point of the temperature ( $T$ , in  $^{\circ}\text{C}$  left axis) and vertical displacement ( $U_z$ , in m, right axis)

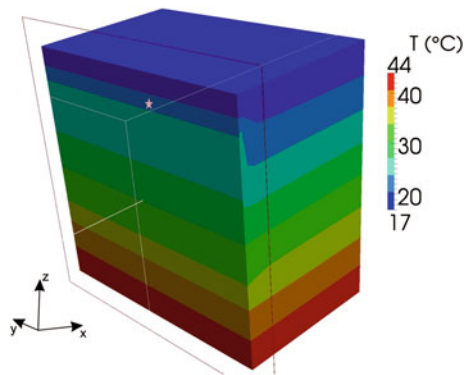
OGS and ABAQUS results are compared at an observation point (located with the star in Fig. 10.13) for the simulated period. The temporal trends of vertical displacement ( $U_z$ ) and temperature ( $T$ ) are illustrated in Fig. 10.14. It can be seen that whereas the vertical displacements calculated with both software match within the error allowance, heat transport in OGS is more vigorous. The observed differences can be explained as follow: In ABAQUS, the elastic part of the volumetric behavior is proportional to the logarithm of the pressure stress (Chap. 19.3.1. ABAQUS User’s manual [1]) whereas in OGS we assume that the elastic modulus are constant. Therefore the important fluid pressure modeled here will induce slightly different stress

and displacements. In ABAQUS porosity is strain dependent. In this problem, the calculated strain increases porosity in the fold as flow evolves. Increasing porosity values lead to higher heat storage which in turn slows down heat flow. By contrast, in OGS, porosity is constant during all the simulation. OGS and ABAQUS pore pressure and pore velocity perfectly fit (Fig. 10.15). Additionally, results are provided for an observation point located inside the model at the  $(x, y, z)$  coordinates  $(343, -540, -400)$  m (Fig. 10.16).



**Fig. 10.15** OGS and ABAQUS comparison: temporal trends pore velocity ( $v$  in m/s *left* axis) and pressure ( $P$ , in Pa, *right* axis), at the observation point in Fig. 10.13

**Fig. 10.16** Temperature ( $^{\circ}\text{C}$ ) calculated at  $3 \times 10^7$  s with: OGS. The *star* locates the observation point for the comparative graphs in Figs. 10.17 and 10.18



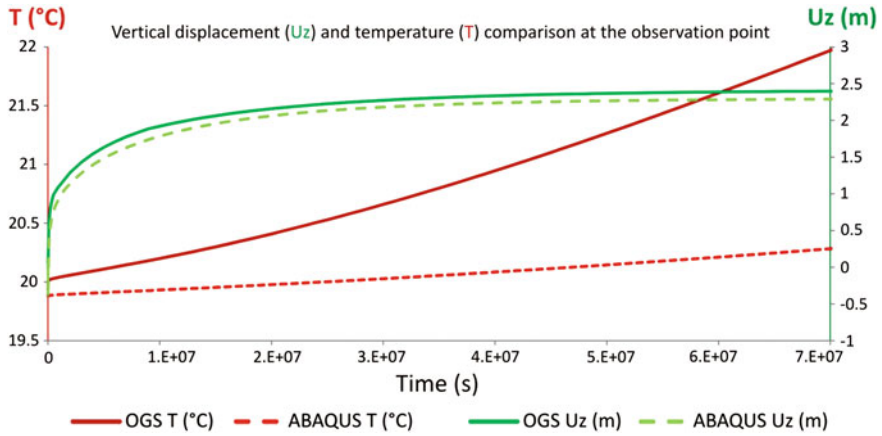


**Fig. 10.17** OGS and ABAQUS comparison: temporal trends of pore velocity ( $v$  in m/s *left axis*) and pressure ( $P$ , in Pa *right axis*) at the observation point in Fig. 10.16

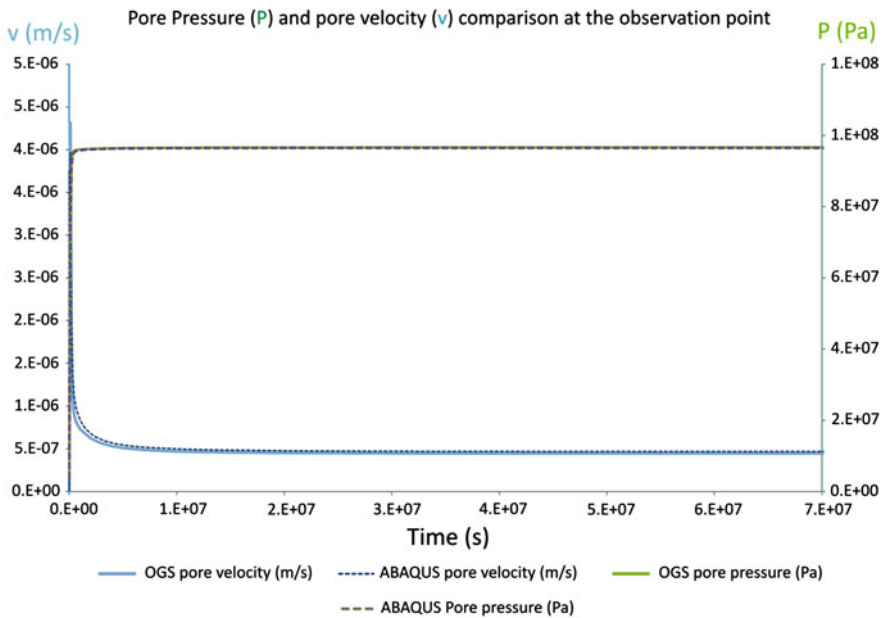


**Fig. 10.18** OGS and ABAQUS comparison: temporal trends of the temperature ( $T$ , in °C *left axis*) and vertical displacement ( $U_z$ , in m *right axis*) at the internal observation point in Fig. 10.16

## 10.2 Injection Induced Hydromechanical (HM) Processes

Katharina Benisch and Sebastian Bauer

### 10.2.1 Definition

Injection induced hydromechanical (HM) processes in a non-faulted reservoir are investigated in this benchmark. It aims at testing and verifying the implementation of coupled HM processes in OpenGeoSys as well as initial conditions, boundary conditions and source terms.

### 10.2.2 Solution

Flow and deformation processes are solved in a staggered scheme. One-way coupling is used to simulate the impact of fluid flow on deformation processes via the pore pressure. In a first step, pressure and stress initialization is simulated to calculate the pressure and stress distribution in the model domain. The initial pore pressure effect on the stress distribution is neglected to avoid initial displacement. In a second step, boundary conditions and source terms are added to the model to simulate a brine injection. The coupled HM process simulation is performed on a 2D and a 3D model, respectively.

### 10.2.3 Model Description

#### 10.2.3.1 Model Area and Parameters

The simulation model is shown in Fig. 10.19. It contains two geological formations, where the lower one (Domain 1) represents a saline aquifer of 6 m thickness which is used as injection formation in the following simulations. It is overlain by a 50 m thick cap rock with low permeability (Domain 0). Petrophysical parameters of both domains as well as the constant fluid properties are listed in Table 10.5.

#### 10.2.3.2 Pressure and Stress Initialization

Hydrostatic pore pressure gradient and total stress gradients in X-, Y- and Z-directions are initially given as listed in Table 10.6 assuming a compressive (negative) stress regime. Two different stress gradients are given for domains 0 and 1 resulting from

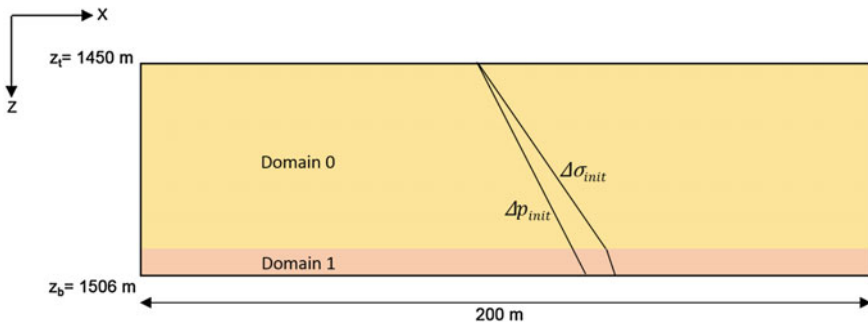


**Fig. 10.19** Setup of the 2D simulation model showing the two domains as well as the initial pressure and stress gradients

**Table 10.5** Fluid properties and petrophysical parameters

		Domain 0	Domain 1
Brine density $\rho_{br}$	( $\text{kg/m}^3$ )	1173	
Brine viscosity $\mu_{br}$	(Pas)	$1.252 \times 10^{-3}$	
Brine compressibility $\kappa_{br}$	( $\text{kPa}^{-1}$ )	0.0	
Intrinsic permeability K	( $\text{m}^2$ )	$3.0 \times 10^{-20}$	$3.0 \times 10^{-13}$
Porosity $\phi$	(—)	0.08	0.26
Solid density $\rho_s$	( $\text{kg/m}^3$ )	2,650	2,650
Young's modulus E	(kPa)	$10^9$	$10^9$
Poisson's ratio $\nu$	(—)	0.3	0.3

**Table 10.6** Initial pressure and stress gradients

		Domain 0	Domain 1
Pore pressure gradient $\Delta p$	(kPa)	11.5071	11.5071
Vertical effective stress gradient $\Delta \sigma'_{zz}$	(kPa)	-13.3302	-10.7221
Horizontal effective stress gradient $\Delta \sigma'_{xx,yy}$	(kPa)	-5.8779	-4.0533

different rock porosities (see Fig. 10.19 and Table 10.5). Figure 10.20a, b show the resulting initial pore pressure and effective stress distribution in the model domain. A displacement of zero is the result of no pore pressure or stress changes (Fig. 10.20c).

### 10.2.3.3 Injection Induced Deformation Processes

Flow and stress boundaries as well as a source term are added to the model (see Fig. 10.21) to simulate a brine injection. For the flow process, constant hydrostatic

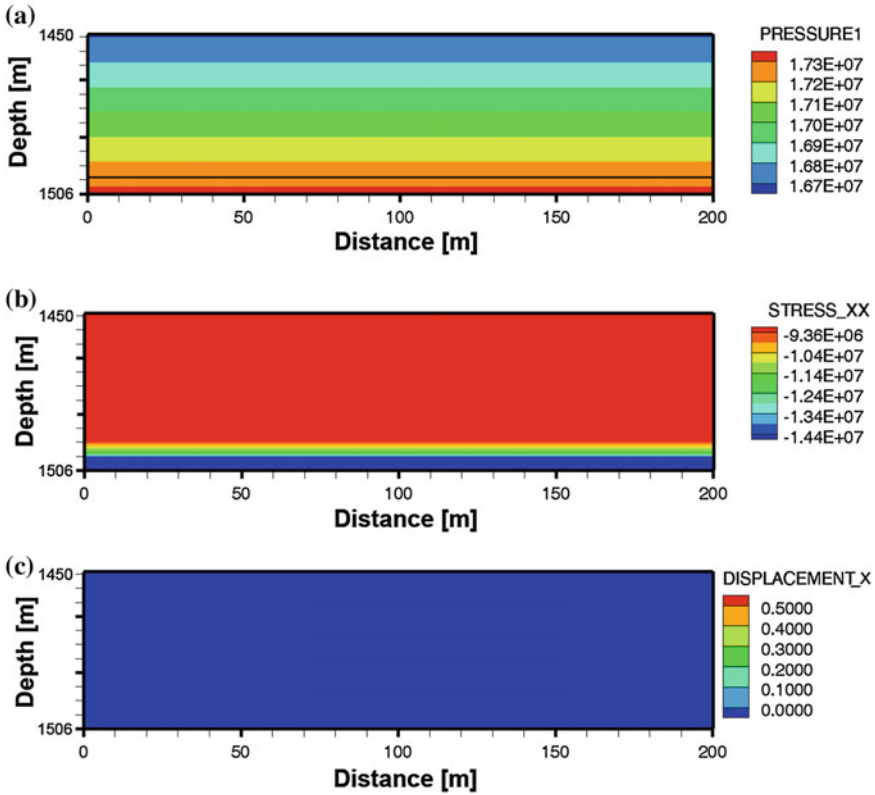


**Fig. 10.20** 2D initialization results. **a** Initial pore pressure, **b** initial effective stress field and **c** initial displacement

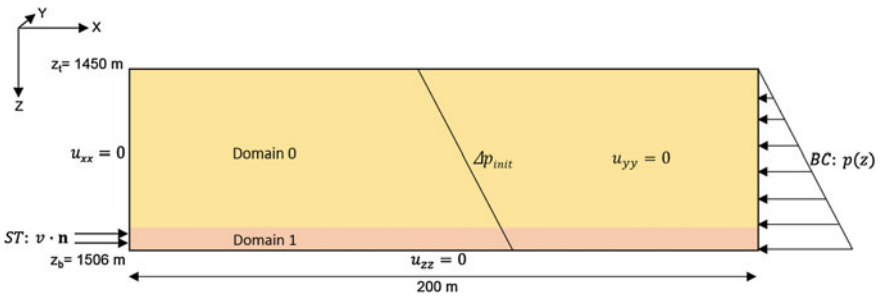


**Fig. 10.21** Model setup for brine injection scenario

pressure conditions are set at the right model boundary. Brine is injected at the left boundary of domain 1 using a constant source term of 1 m/day for 41 days. Displacement is set to zero at the model bottom ( $u_{zz} = 0$ ), at the left model boundary ( $u_{xx} = 0$ ), as well as within the model domain ( $u_{yy} = 0$ ) in case of the 3D model.

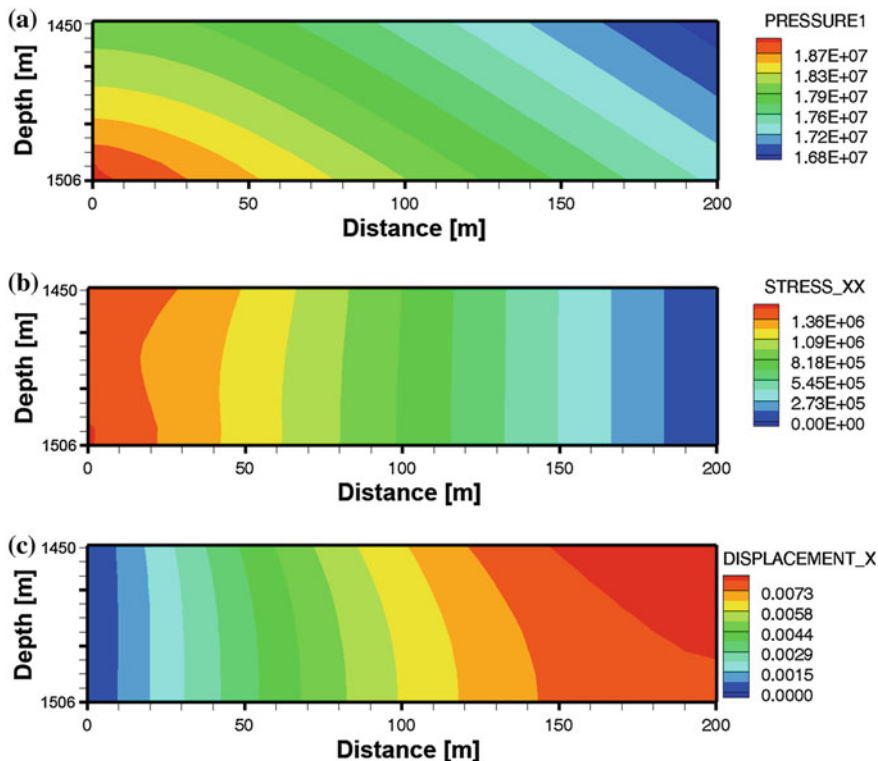


Fig. 10.22 2D results of the brine injection scenario after 41 days. **a** Pore pressure, **b** effective stress changes in X-direction and **c** displacement in X-direction

## 10.2.4 Results

### 10.2.4.1 2D Model

Figure 10.22 depicts the simulation results after 41 days. Due to the injection process, pressure increases by  $1.6 \times 10^6$  Pa (9%) near the injection well and propagates into the reservoir and also the cap rock (Fig. 10.22a) as no compressibility is incorporated in the model. The injection induced pressure increase leads to a positive effective stress change i.e. a dilatation of the rock and a displacement to the right model boundary across the whole model thickness (Fig. 10.22b, c). At the right model boundary, effective stress changes are zero as no pore pressure changes occur due to the constant pressure head boundary. The displacement in X-direction increases towards the model top because of the free moving boundary there.

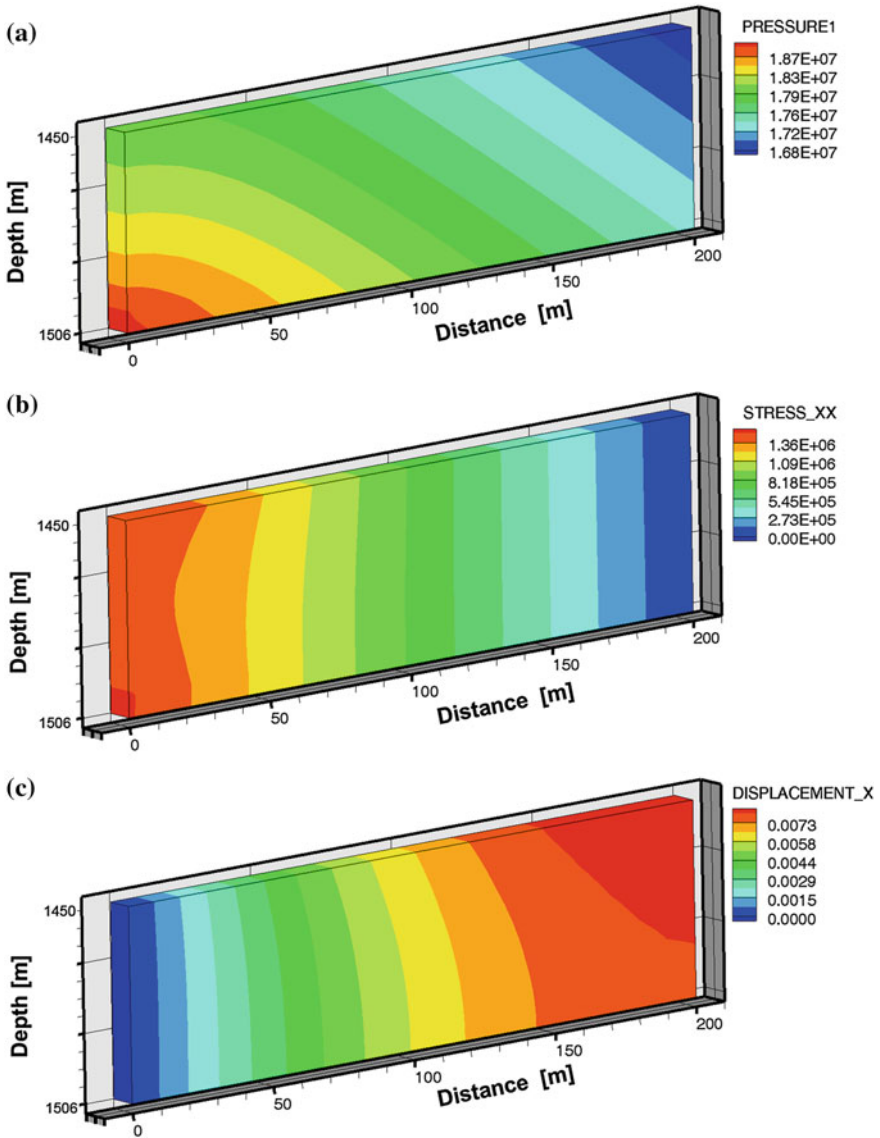
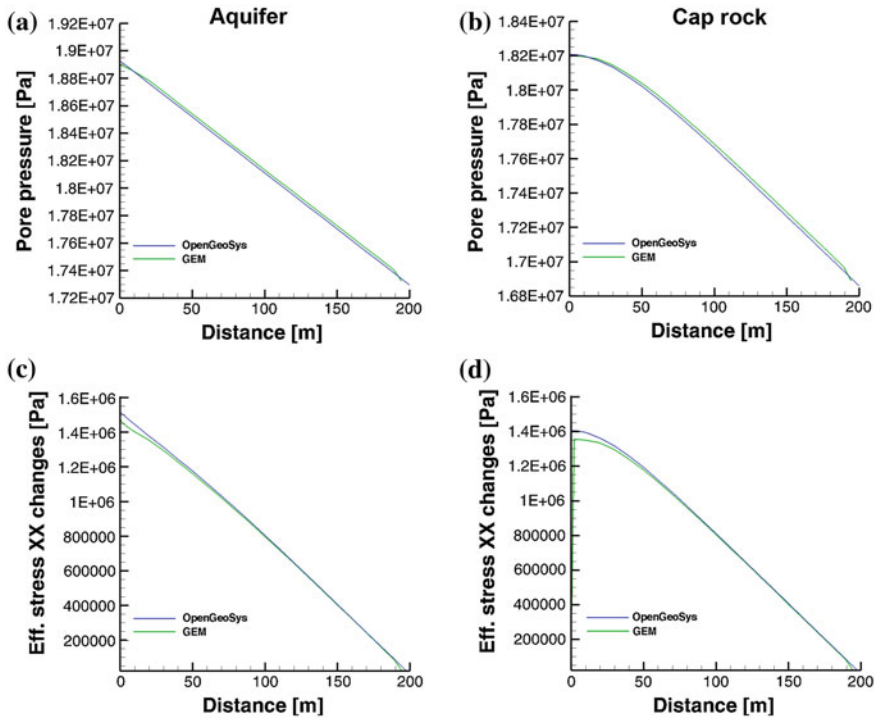


Fig. 10.23 3D simulation results after 41 days. **a** Pore pressure, **b** effective stress changes in X-direction and **c** displacement in X-direction

### 10.2.4.2 3D Model

The 2D model is extended to a 3D model by adding one cell of 1 m thickness in the Y-direction. The initial and boundary conditions as well as the source term are changed correspondingly to represent the model setup in Fig. 10.21. With that, the simulation results of the 3D model should agree with those of the 2D model.



**Fig. 10.24** Comparison of the simulation results of OpenGeoSys and GEM. **a** Pore pressure in the aquifer, **b** Pore pressure in the cap rock, **c** effective stress changes in the aquifer, **d** effective stress changes in the cap rock

The simulation results of pore pressure, effective stress changes and displacement in X-direction after 41 days are plotted in Fig. 10.23. It can be seen that the results fit the results of the 2D model (Fig. 10.22).

### 10.2.4.3 Code Comparison

The 3D simulation results of OpenGeoSys are compared to those calculated by the commercial compositional FD simulator GEM (©ComputerModellingGroup) to verify the HM coupling process in OpenGeoSys. The same model setup as well as spatial and time discretization are used for both numerical simulators.

The results of pore pressure and effective stress changes in the X-direction are compared for two profiles along the X-axis. One profile within the aquifer at 1503 m depth (Fig. 10.24a, c) and a second profile within the cap rock at 1463 m depth (Fig. 10.24b, d). Generally, the results of both simulators agree well for the presented test case. Only small differences can be seen for both pore pressure and effective stress. Comparing the pore pressures, there is a small shift between the profiles, which is due to the fact that GEM uses the finite difference method and OpenGeoSys

the finite element method and results therefore cannot be compared exactly at the same depth. At the injection well, OpenGeoSys calculates higher injection pressures than GEM, which may be caused by different methods of implementing source terms. As a result, the effective stress change at the injection well is higher for OpenGeoSys.

### 10.3 AnSichT THM Test Case

Jobst Maßmann (BGR), Sha Li (DBE-TEC), Michael Jobmann (DBE-TEC), Thomas Nowak (BGR)

In the framework of the AnSichT project a methodology for the safety analysis of a repository for high level radioactive waste in clay stone is developed [3]. Project partners are the DBE TECHNOLOGY, Gesellschaft für Anlagen- und Reaktorsicherheit (GRS) and the Federal Institute for Geosciences and Natural Resources (BGR).

One aspect of this project are numerical simulations with the objective of investigating the integrity of the geotechnical and geological barriers. To ensure the comparability of the different codes, a THM test case has been defined.

Considering the thermal expansion of the fluid and the solid phase, the conservation of fluid volume in a deformable porous media can be written as

$$\nabla \cdot \left( \frac{\mathbf{k}}{\mu} (-\nabla p + \rho^f \mathbf{g} \nabla z) \right) + S \frac{\partial p}{\partial t} - \phi \beta_T^f \frac{\partial T}{\partial t} - (\alpha - \phi) \beta_T^s \frac{\partial T}{\partial t} + \alpha \nabla \cdot \frac{\partial \mathbf{u}}{\partial t} = 0. \quad (10.1)$$

With the intrinsic permeability  $\mathbf{k}$ , the fluid viscosity  $\mu$ , the fluid pressure  $p$ , the fluid density  $\rho^f$ , the vector of gravity  $\mathbf{g}$ , the specific storage coefficient  $S$ , the porosity  $\phi$ , the cubic expansion of the fluid and the solid  $\beta_T^f$  and  $\beta_T^s$ , respectively, the temperature  $T$ , the Biot coefficient  $\alpha$  and the vector of displacements  $\mathbf{u}$ . The thermal fluid expansion can be defined by the derivative of fluid density with respect to the temperature:

$$\beta_T^f = \frac{\partial \rho^f}{\partial T} \frac{1}{\rho_0^f}. \quad (10.2)$$

Several linear and non-linear models are available in the applied computer codes.

#### 10.3.1 Definition

The test case is a 3-D THM problem, considering drilling and heating. This kind of test case was chosen with regard to the concept of borehole disposal of heat generating radioactive waste. The geometry is given by a square cuboid, whose

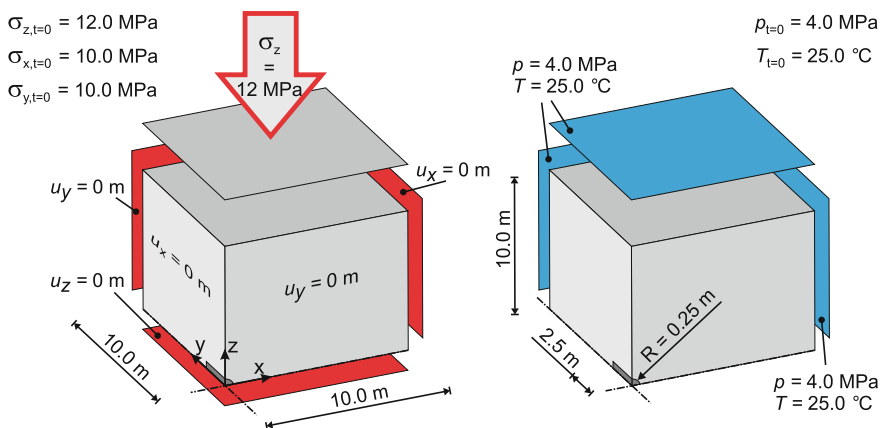


Fig. 10.25 Definition of the AnSicht THM test case

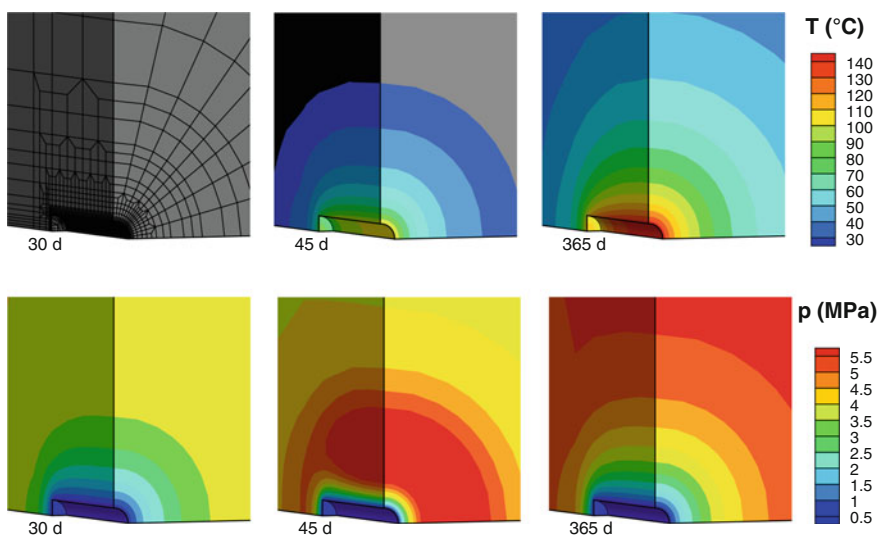


Fig. 10.26 Temperature ( $T$ ) and pore water pressure ( $p$ ) distributions at three different times calculated with OGS

sides measure 20.0 and 10.0 m, respectively. The centered borehole length is 2.5 m the diameter equals 0.5 m. The initial and boundary conditions are depicted at one quarter of the domain in Fig. 10.25. The drilling starts at  $t = 0.0$  d and is completed at  $t = 0.2$  d. Atmospheric pressure is assumed at the borehole. The heating period begins at  $t = 32$  d and is completed at  $t = 365$  d. The output variables are evaluated at 6 points along the  $x$ -axis. The material properties are listed in Table 10.7.

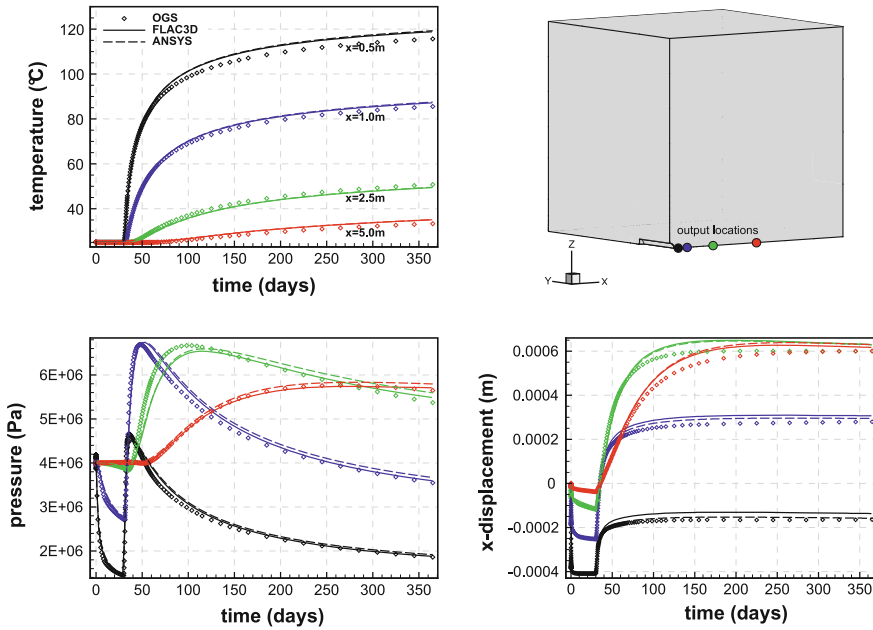


Fig. 10.27 Temperature ( $T$ ), water pressure ( $p$ ) and displacement ( $u_x$ ) distributions at three different output locations along the  $x$ -axis calculated with OGS, FLAC3D and ANSYS

Table 10.7 Material properties

Symbol	Parameter	Value	Unit
$\rho^s$	Density solid	2533.0	kg/m <sup>3</sup>
$\phi$	Porosity	0.1	—
$\mathbf{k}$	Intrinsic permeability	1.0e-19	m <sup>2</sup>
$E$	Young's modulus	4000.0	MPa
$\nu$	Poisson's ratio	0.35	—
$c^s$	Specific heat capacity solid	1254.74	J/(kg·K)
$\beta_T^s$	Cubic thermal expansion coefficient solid	3.0e-5	1/K
$\tau^s$	Heat conductivity solid	2.156	W/(m·K)
$\alpha$	Biot's coefficient	0.6	—
$\rho^f$	Density fluid	1200.0	kg/m <sup>3</sup>
$\mu$	Viscosity	1.5	mPa·s
$c^f$	Specific heat capacity fluid	4160.0	J/(kg·K)
$\beta_T^f$	Cubic thermal expansion coefficient fluid	6.0e-4	1/K
$\tau^f$	Heat conductivity fluid	0.6	W/(m·K)
$K^f$	Bulk modulus fluid	2000.0	MPa

### 10.3.2 Results

In Fig. 10.26 the distributions of temperature and pore water pressure at three points in time are depicted. 13 days after the heating has been initiated ( $t = 45$  d), a zone of increased pore pressure can be observed. This is caused by the thermal expansion of the fluid in a low permeable medium.

Results of three different numerical codes are presented in Fig. 10.27. ANSYS [4] and FLAC3D [5] are applied besides OGS. The temporal evolutions of the main variables are shown at four points along the x-axis. Only minor derivations can be observed, which are explainable by differences in the discretization and the modeling approach. For instance, advective heat transport is considered by OGS only.

## 10.4 Consolidation Under Two-Phase Flow Condition: Five Spot Example

Wenqing Wang

The example is based on a classic two-phase flow example for benchmark purpose [6], which describes a sort of water flooding process in porous media, and it is expended hereby with an elastic deformation.

Assuming that the density of the each phase is constant, the process can be described by the mass balance equations and the momentum balance equation. With the capillary pressure  $p^c$  and the non-wetting phase pressure  $p^{nw}$  as two primary variables, the mass balance equations are given as

$$n\rho^w \frac{\partial S^w}{\partial p^c} \frac{\partial p^c}{\partial t} - \nabla \cdot \left[ \rho^w \frac{\mathbf{k}k_{rel}^w}{\mu^w} (\nabla(p^{nw} - p^c) - \rho^w \mathbf{g}) \right] + S^w \rho^w \frac{\partial}{\partial t} \nabla \cdot \mathbf{u} = Q_w \quad (10.3)$$

$$-n\rho^{nw} \frac{\partial S^w}{\partial p^c} \frac{\partial p^c}{\partial t} + (1 - S^w)n \left( \frac{\partial \rho^{nw}}{\partial p^{nw}} \frac{\partial p^{nw}}{\partial t} + \frac{\partial \rho^{nw}}{\partial p^c} \frac{\partial p^c}{\partial t} \right) - \nabla \cdot \left[ \rho^{nw} \frac{\mathbf{k}k_{rel}^{nw}}{\mu^{nw}} (\nabla p^{nw} - \rho^{nw} \mathbf{g}) \right] + (1 - S^w)\rho^{nw} \frac{\partial}{\partial t} \nabla \cdot \mathbf{u} = Q_{nw} \quad (10.4)$$

where  $nw$  indicates the non-wetting phase,  $w$  indicates the wetting phase,  $S$  is saturation,  $\mathbf{u}$  is the displacement,  $n$  is the porosity,  $\rho$  denotes the density,  $Q$  denotes the source/sink term,  $\mathbf{k}$  is the intrinsic permeability,  $k_{rel}^w$  and  $k_{rel}^{nw}$  represents the relative permeability of phases,  $\mu$  denotes the viscosity, and  $\mathbf{g}$  is the vector of gravity.

While, the momentum balance equation takes the following form

$$\nabla \cdot (\boldsymbol{\sigma} - (p^{nw} - S^w p^c) \mathbf{I}) + \rho \mathbf{g} = 0 \quad (10.5)$$

where  $\boldsymbol{\sigma}$  is the effective stress of the porous medium, and  $\mathbf{I}$  is the identity tensor. The density of the porous medium is composed by three phases, two fluids and solids  $\rho = nS^w\rho^w + n(1 - S^w)\rho^{nw} + (1 - n)\rho^s$  with  $\rho^s$ , the solid density. The unknowns of the momentum equation is the displacement,  $\mathbf{u}$ , and which is solved via the constitutive law

$$\boldsymbol{\sigma} = \mathbb{C}\boldsymbol{\epsilon}$$

and the strain displacement relationship

$$\boldsymbol{\epsilon} = \left( (\nabla\mathbf{u})^T + \nabla\mathbf{u} \right) / 2$$

where  $\mathbb{C}$  is the stress strain tensor, and the subscript  $T$  means transpose.

Due to the symmetry, we take one quarter of the five spot example with a size of  $10 \times 10 \times 1 \text{ m}^3$ . The fluids that are assumed to be involved in the process are water (wetting phase) and hydrocarbon (non-wetting phase). The material parameters are given in Table 10.8. In the original definition of the problem, the capillary pressure is small and omitted. Since the capillary pressure is adopted as one of the primary variables in the present mass balance equations, we employ the van Genuchten model as

$$p^c = \frac{\rho^w g}{\alpha} \left[ S_{\text{eff}}^{-1/m_v} - 1 \right]^{1/n_v} \quad (10.6)$$

where  $\alpha$  [1/m] is a conceptualized parameter related to the air entry pressure,  $n_v$  is a dimensionless pore size distribution index and  $m_v = 1 - (1/n_v)$ , and  $S_{\text{eff}}$  is the effective saturation defined as

$$S_{\text{eff}} = \frac{S^w - S_r^w}{S_{\text{max}}^w - S_r^w} \quad (10.7)$$

with  $S_{\text{max}}^w$  and  $S_r^w$  as the maximum and residual saturation. In this example, we set  $m_v = 0.7$ ,  $S_{\text{max}}^w = 1$ ,  $S_r^w = 0$ , and  $\alpha = 0.37$ .

**Table 10.8** Material properties of five-spot example

Property	Value	Unit
Water density	1000	kg/m <sup>3</sup>
Hydrocarbons density	1000	kg/m <sup>3</sup>
Water viscosity	10 <sup>-3</sup>	Pa s
Hydrocarbons viscosity	4 × 10 <sup>-3</sup>	Pa s
Porosity	0.206	–
Intrinsic permeability	10 <sup>-13</sup>	m <sup>2</sup>
Relative permeability	$k_{rel}^w = (S^w)^2, k_{rel}^{nw} = (1 - S^w)^2$	–
Capillary-saturation relationship	van Genuchten	Pa
Young's modulus	3.5 × 10 <sup>10</sup>	Pa
Poisson ratio	0.3	–

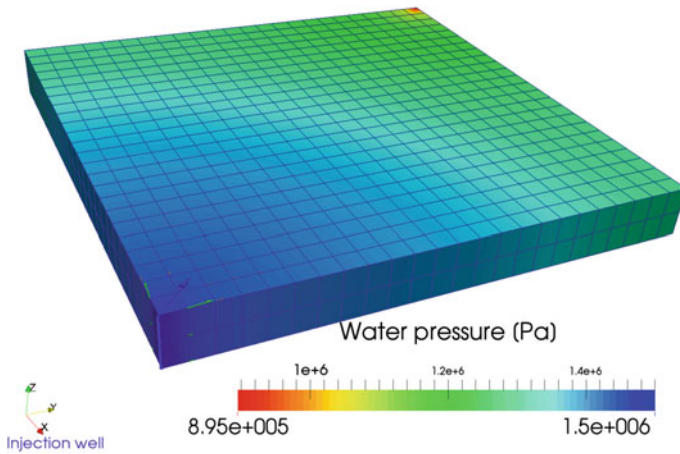


**Fig. 10.28** Mesh and water pressure distribution after 20 days

Initially, the capillary pressure is set to  $p_0^c = 105018 \text{ Pa}$  to represent a very small water saturation of 0.04, meanwhile the non-wetting phase pressure is given as  $p_0^{nw} = p_0^c \text{ Pa}$  to represent that there is no water pressure at the beginning of the injection/pumping. Besides, the initial effective stresses are all zero by omitting the gradational force.

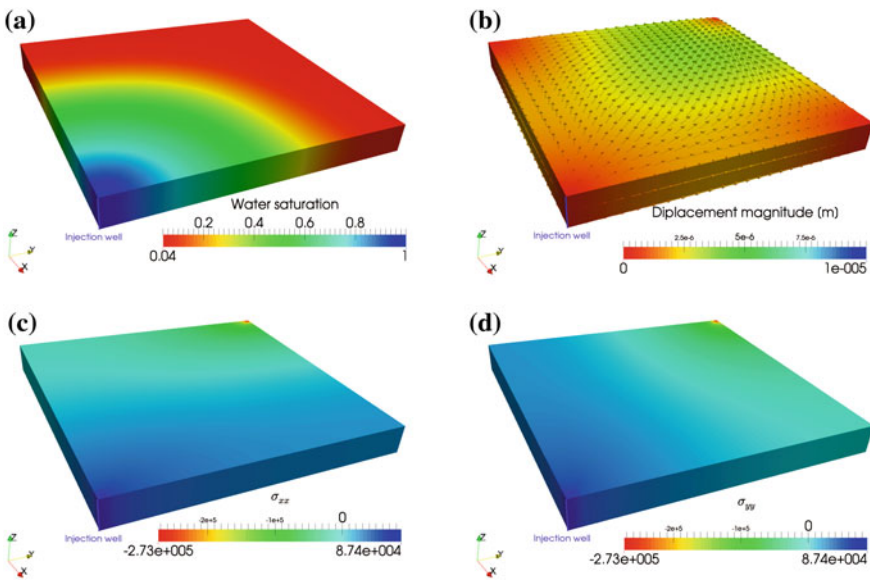


**Fig. 10.29** Variable distribution after 20 days' injection. **a** Water saturation, **b** Displacement magnitude, **c** Effective stress  $\sigma_{xx}$ , **d** Effective stress  $\sigma_{yy}$

At the injection corner, the boundary conditions are prescribed as  $p^c = 0$  and  $1.5 \times 10^6$  Pa, while at the pumping corner, the non-wetting phase pressure is  $10^6$  Pa. The displacement in the normal direction of all surface is restricted to zero. The time duration of the pumping is 20 days.

The domain is discretized into 1,151 hexahedral elements with 1,875 nodes, which is demonstrated in Fig. 10.28. Figure 10.28 also shows the calculated water pressure (calculated by  $p^{nw} - p^w$ ) distribution at 20 days.

After 20 days' injection, the distribution of other variables is shown in Fig. 10.29a, b, c and d respectively. Figure 10.29 prompts that there is tensile effective stresses increasing in the vicinity of the injection well. Since there is not any mechanical load applied to the domain, the changes of the effective stresses are caused by the changes of fluid pressures solely. We can see this hydraulic mechanical coupling more distinctively with the following variable profiles (Fig. 10.30), which are plotted along one horizontal edge of the domain that starts from the injection well.

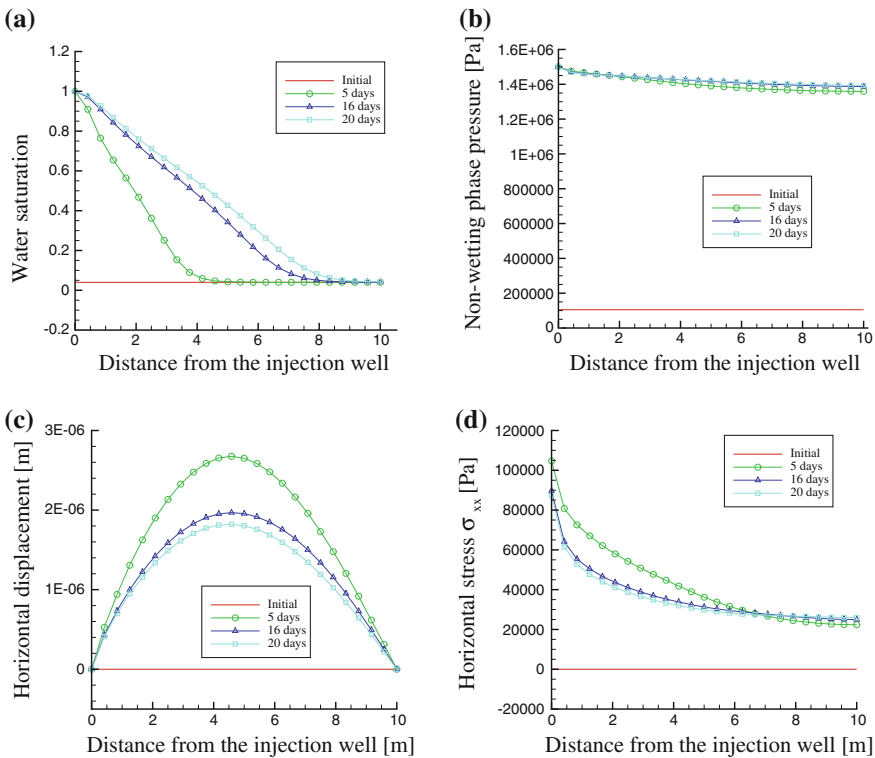


**Fig. 10.30** Profiles along one horizontal edge that starts from the injection well. **a** Water saturation, **b** Non-wetting phase pressure, **c** Horizontal displacement, **d** Effective stress  $\sigma_{xx}$

## References

1. Abaqus. Abaqus FEA. Technical report, Dassault Systèmes, 2007.
2. J. C. Jaeger, N. G. W. Cook, and R. W. Zimmerman. *Fundamentals of Rock Mechanics (4th Edition)*. John Wiley & Sons, 2007.
3. M. Jobmann. Methodik und Anwendungsbezug eines Sicherheits- und Nachweiskonzeptes für ein HAW-Endlager im Tonstein, ANSICHT. Jahresbericht 2012, DBE-Tec, 2013.
4. ANSYS Inc., Minnesota, USA. *ANSYS Mechanical, Help System, Mechanical APDL Documentation*. Release 14.5.7.
5. ITASCA Consultants, Minnesota, USA. *FLAC3D Manuals*, 3.1 edition, 2006.
6. K. Aziz and A. Settari. *Petroleum reservoir simulation*, volume 476. Applied Science Publishers London, 1979.

# Chapter 11

## Thermo-Mechanics: Stress-Induced Heating of Elastic Solids

Norihiro Watanabe, Guido Blöcher, Harald Milsch and Andreas Reinicke

### 11.1 Theory

This benchmark focuses on stress-induced heating in elastic solids. In the following, we briefly present governing equations relevant to this coupled thermal and mechanical processes. For details, readers are referred to [1, 2].

From the first law of thermodynamics, an energy balance equation of solid materials per unit volume can be expressed as [2]

$$\rho \frac{De}{Dt} + \nabla \cdot (-\lambda \nabla T) - \boldsymbol{\sigma} : \nabla \mathbf{v} = Q \quad (11.1)$$

with density  $\rho$ , specific internal energy  $e$ , thermal conductivity  $\lambda$ , absolute temperature  $T$ , the stress tensor  $\boldsymbol{\sigma}$ , the solid velocity  $\mathbf{v}$ , and the source and sink term  $Q$ .

The stress induced heating is revealed by expanding the first term in the left hand side (LHS) of the above equation. The term can be rewritten as

$$\rho \frac{De}{Dt} = \rho \frac{Dh}{Dt} + \frac{P}{\rho} \frac{D\rho}{Dt} - \frac{DP}{Dt} \quad (11.2)$$

by substituting the specific internal energy with

$$e = h - \frac{P}{\rho} \quad (11.3)$$

---

N. Watanabe (✉)

Helmholtz Centre for Environmental Research UFZ, Permoserstr. 15, 04318 Leipzig, Germany  
e-mail: Norihiro.Watanabe@ufz.de

G. Blöcher · H. Milsch · A. Reinicke

Helmholtz-Zentrum Potsdam - Deutsches GeoForschungsZentrum GFZ, 14473 Telegrafenberg, Potsdam

where  $h$  is specific enthalpy, and  $P = -1/3\sigma_{ii}$  is the hydrostatic part of the stress tensor. Utilizing the following thermodynamic relations

$$\left(\frac{\partial h}{\partial T}\right)_P = c_p \quad (11.4)$$

$$\left(\frac{\partial h}{\partial P}\right)_T = \frac{1}{\rho}(1 - \beta_T T) \quad (11.5)$$

with the specific heat at constant pressure  $c_p$  and the volumetric thermal expansion coefficient  $\beta_T$ , the differential of the specific enthalpy is expressed as

$$dh(P, T) = \left(\frac{\partial h}{\partial T}\right)_P dT + \left(\frac{\partial h}{\partial P}\right)_T dP = c_p dT + \frac{1}{\rho}(1 - \beta_T T)dP. \quad (11.6)$$

Therefore, the first term can be expanded as

$$\rho \frac{De}{Dt} = \rho c_p \frac{DT}{Dt} + \frac{P}{\rho} \frac{D\rho}{Dt} - \beta_T T \frac{DP}{Dt} \quad (11.7)$$

in which the last term in the right hand side (RHS) corresponds to the heat source induced by the pressurization. Using the expression and neglecting the mechanical work, the energy balance equation is rewritten as

$$\rho c_p \frac{DT}{Dt} - \beta_T T \frac{DP}{Dt} + \nabla \cdot (-\lambda \nabla T) = Q \quad (11.8)$$

which explicitly includes the stress-induced heat production. As one can see from the equation, temperature increase due to the pressurization depends on absolute temperature and the ratio of the thermal expansion coefficient to heat capacity of solids, i.e.  $\beta_T/(\rho c_p)$ . The latter is material dependent.

For isotropic linear elastic materials, the differential of the pressure can be substituted by

$$dP = -K_s d\bar{\epsilon}_e = -K_s (d\bar{\epsilon}_t - \beta_T dT) \quad (11.9)$$

where  $\bar{\epsilon}_e$  is the volumetric elastic strain,  $\bar{\epsilon}_t$  is the volumetric total strain, and  $K_s$  is the adiabatic bulk modulus (subscript  $s$  is conventionally used for adiabatic condition) given by

$$K_s = \frac{E}{3(1 - 2\nu)} \quad (11.10)$$

with Young's modulus  $E$  and Poisson's ratio  $\nu$ . Hence, the energy balance equation is formulated as

$$\rho c_p \frac{DT}{Dt} + \beta_T T K_s \left( \frac{D\bar{\epsilon}_t}{Dt} - \beta_T \frac{DT}{Dt} \right) + \nabla \cdot (-\lambda \nabla T) = Q \quad (11.11)$$

including the volumetric strain rate instead of the pressurization rate. Using the Grüneisen parameter [1]

$$\gamma = \frac{\beta_T K_s}{\rho c_p}, \quad (11.12)$$

the equation can also be expressed as

$$\frac{DT}{Dt} + \gamma T \left( \frac{D\bar{\epsilon}_t}{Dt} - \beta_T \frac{DT}{Dt} \right) + \nabla \cdot (-\alpha \nabla T) = \frac{Q}{\rho c_p} \quad (11.13)$$

with the thermal diffusivity  $\alpha$ . In [1], the thermal strain rate is neglected, i.e. the elastic strain rate is approximated by the total strain rate.

Assuming quasi static stress equilibrium, an equation of linear momentum balance in the solid phase can be given as

$$\nabla \cdot \boldsymbol{\sigma} + \rho \mathbf{g} = 0 \quad (11.14)$$

with gravity acceleration vector  $\mathbf{g}$ . The constitutive equation for stress and strain is given in an incremental form as

$$d\boldsymbol{\sigma} = \mathbf{D} : (d\boldsymbol{\epsilon} - \alpha_T \mathbf{I}dT) \quad (11.15)$$

where  $\mathbf{D}$  is the tangential stiffness matrix,  $\boldsymbol{\epsilon}$  is the total strain tensor,  $\alpha_T = 1/3\beta_T$  is the linear thermal expansion coefficient, and  $\mathbf{I}$  is the identity tensor.

## 11.2 Problem Definition

This example considers temperature evolution in a cylindrical sample under uniaxial compression (Fig. 11.1). The sample has a radius of 2.5 cm and a length of 10 cm. The sample temperature is initially homogeneously distributed and can locally evolve depending on the loading condition and interaction with surroundings. In this study, the loading condition is divided into two stages (Fig. 11.2). In the first 15 min, the deformation is carried out slowly by linearly increasing the loading pressure. In the second stage, the loading stress is kept constant over another 15 min. Initial and boundary conditions of the problem are illustrated in Fig. 11.1.

In order to demonstrate effects of the stress rate and the system temperature on the heating process, we test with different loading rates ( $dF/dt = F_{\max}/\Delta t$  with  $F_{\max} = 10, 20, 30$  MPa and  $\Delta t = 15$  min., i.e.  $dF/dt = 0.67, 1.33, 2$  MPa/min.) and

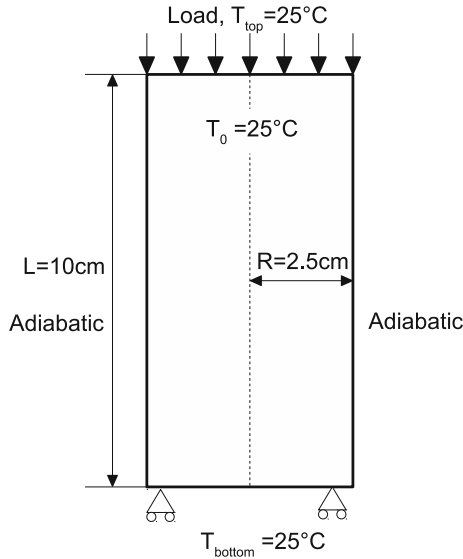


Fig. 11.1 Uniaxial compression of a cylindrical sample under adiabatic condition for a case  $T_0=25^\circ\text{C}$

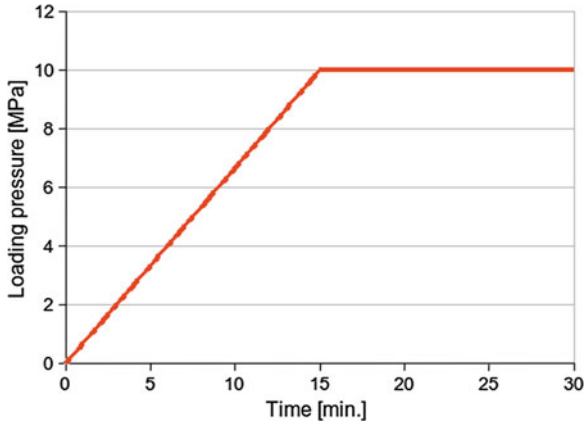


Fig. 11.2 Time varying loading pressure on the top surface for  $F_{\text{max}}=10\text{MPa}$

with different initial and ambient temperatures ( $T_0 = 25, 50, 75^\circ\text{C}$ ). For material dependence on temperature evolutions, we test the following materials.

- Bentheim sandstone
- Crystalline rock
- Iron

**Table 11.1** Material properties

	Bentheim sandstone [3]	Crystalline rock	Iron
Solid phase Density	2650 kg/m <sup>3</sup>	2640 kg/m <sup>3</sup>	7870 kg/m <sup>3</sup>
Specific heat	730 J/(kg K)	990 J/(kg K)	450 J/(kg K)
Thermal conductivity	7 W/(m K)	2.86 W/(m K)	80.4 W/(m K)
Young's modulus	25 GPa	35 GPa	210 GPa
Poisson ratio	0.16	0.25	0.29
Linear thermal expansion coefficient	1e-5 K <sup>-1</sup>	1e-5 K <sup>-1</sup>	1.2e-5 K <sup>-1</sup>
Medium (at 25 °C) Porosity	23 %	1 %	0 %
Thermal diffusivity	3.62e-6 m <sup>2</sup> /s	1.09e-6 m <sup>2</sup> /s	22.7e-6 m <sup>2</sup> /s
Grüneisen parameter	0.247	0.271	1.69
$\beta_T / (\rho c_p)$	2.01e-11 Pa <sup>-1</sup>	1.16e-11 Pa <sup>-1</sup>	1.02e-11 Pa <sup>-1</sup>

**Table 11.2** Air properties

Temperature	25 °C	50 °C	75 °C
Density	1.2 kg/m <sup>3</sup>	1.08 kg/m <sup>3</sup>	1 kg/m <sup>3</sup>
Specific heat	1005 J/(kg K)	1008 J/(kg K)	1010 J/(kg K)
Thermal conductivity	0.027 W/(m K)	0.0278 W/(m K)	0.0297 W/(m K)

For all rock samples, we assume effective bulk properties for dry and drained condition, although the Bentheim sandstone has a porosity of approximately 23%. The effective properties are calculated by taking an arithmetic mean of all phase properties weighted by their volume fractions. Moreover, all material properties are assumed to be constant because of little temperature changes in this problem. The gravity force is also neglected due to the small sample size. Parameters of all the materials and air are listed in Tables 11.1 and 11.2.

### 11.3 Analytical Solution

[4] presented analytical solutions for temperature evolution in the cylindrical sample, based on assumptions that thermal strain is negligible and temperature in the heat production term can be approximated by the constant reference temperature. The solutions are separately provided for the two stages as follows:

- First stage: constant strain rate ( $0 \leq t < \bar{t}$ )

$$T(z, t) = T_0 - \frac{4}{\pi^3} \gamma T_0 \dot{\epsilon}_0 (1 - 2\nu) \frac{L^2}{\alpha} \sum_{1^n}^{\infty} \left[ \frac{1 - e^{-n^2 t / \tau_1}}{n^3} \sin(n\pi \frac{z}{L}) \right] \quad (11.16)$$

- Second stage: constant strain ( $\bar{t} \leq t$ )

$$T(z, t) = T_0 - \frac{4}{\pi^3} \gamma T_0 \dot{\epsilon}_0 (1 - 2\nu) \frac{L^2}{\alpha} \sum_{1^n}^{\infty} \left[ \frac{1 - e^{-n^2 \bar{t} / \tau_1}}{n^3} e^{-n^2 (t - \bar{t}) / \tau_1} \sin(n\pi \frac{z}{L}) \right] \tag{11.17}$$

where  $n$  is odd number,  $\gamma$  is the Grüneisen parameter,  $T_0$  is the reference temperature of the undeformed sample,  $\epsilon_0$  is the given longitudinal strain rate for the first stage,  $\nu$  is Poisson’s ratio,  $L$  is the sample length,  $\alpha$  is thermal diffusivity, and  $\tau$  is the time constant given by  $\tau_1 = L^2 / (\pi^2 \alpha)$ .

### 11.4 Numerical Solution

An axisymmetric FEM model is used to solve the coupled thermal and mechanical problem in OpenGeoSys. Along the symmetric axis, zero displacement in the radial direction is additionally imposed as boundary conditions. The domain is spatially discretized with 100 quadrilateral elements having constant element size of 5 mm. Time step size is homogeneously set to 15 s.

### 11.5 Results

Figures 11.3, 11.4 and 11.5 compare analytical and numerical solutions of temperature increments at the vertically middle of the sample ( $z = L/2$ ) for different

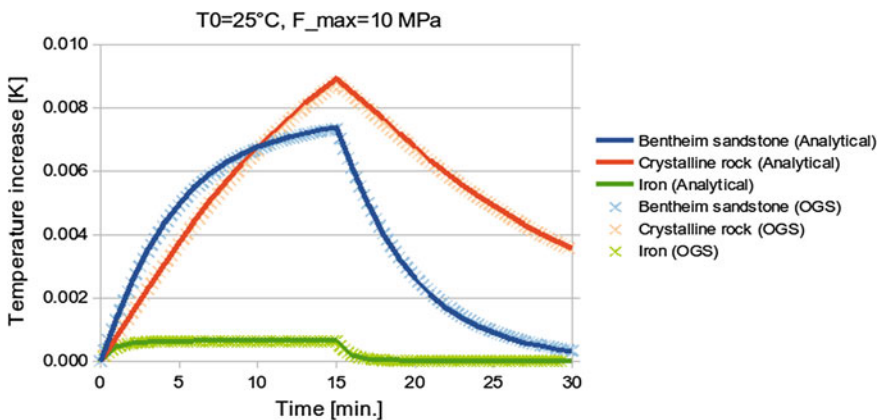


**Fig. 11.3** Temperature increase curves for different materials at  $F_{max} = 10\text{MPa}$ ,  $T_0 = 25^\circ\text{C}$  (observed at the vertically middle of the sample)

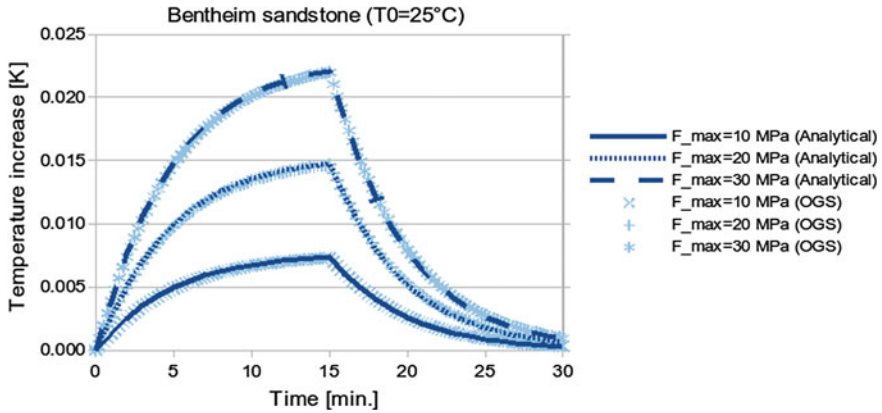


Fig. 11.4 Temperature increase curves for different loading rates with Bentheim sandstone at  $T_0 = 25^\circ\text{C}$  (observed at the vertically middle of the sample)

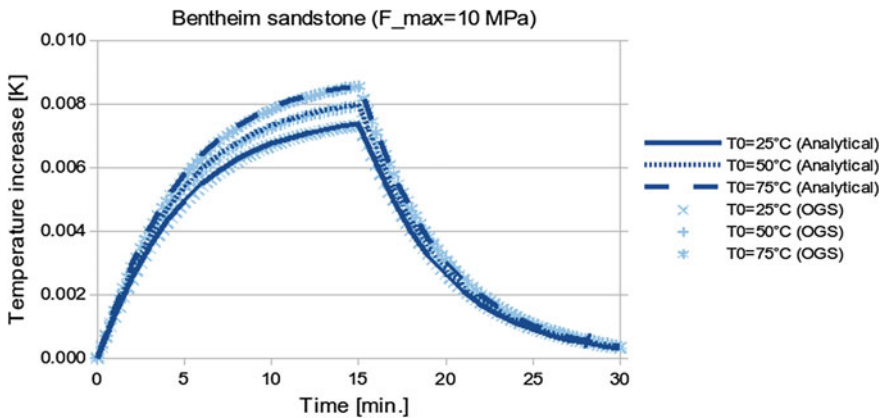


Fig. 11.5 Temperature increase curves for different initial temperatures with Bentheim sandstone at  $F_{\text{max}} = 10\text{ MPa}$  (observed at the vertically middle of the sample)

materials, different loading rates, and different system temperatures. Results are summarized as follows:

- For all the test cases, during the first 15 min, temperatures of all the samples gradually increase as the loading pressure is increased with the constant rate until the pressure reaches its maximum. Once the loading pressure is kept constant after 15 min, the stress-induced heating stops and the sample temperature starts to drop down due to heat conduction into surroundings.
- Material dependence of the heating behavior is shown in Fig. 11.3. Temperature evolves faster in the Bentheim sandstone as  $\beta_T / (\rho c_p)$  of the material is larger than the other materials (Table 11.1).

- Effects of the stress rate (or the strain rate) and the system temperature on the heating are presented in Figs. 11.4 and 11.5 for the Bentheim sandstone. Higher pressurization rate and higher system temperature lead to larger heat production in a linear fashion. Note that the heating is scaled by absolute temperature, not by temperature in Celsius degree.
- For this specific problem, the sample temperature can reach equilibrium while pressurization because of heat conduction into the top and bottom surfaces where the ambient temperature is imposed. Materials with higher thermal diffusivity have lower equilibrium temperature (see Iron case in Fig. 11.3). Maximum temperature increase is ca 0.009 K for the crystalline rock which has the lowest thermal diffusivity (Table 11.1).
- For all the materials, both analytical and numerical solutions show good agreements, because temperature increase in this study is very low ( $<0.1$  K) and the influence of the thermal strain ( $<1e-4$  %) is negligible compared to the elastic strain (e.g.  $>0.04$  % for Bentheim sandstone).

## References

1. M. Beghi, M. Berra, G. Caglioti, and A. Fazzi. A thermoelastic method to measure the thermal expansion coefficient. *Materials and Structures*, 19(1):65–69, 1986.
2. R. W. Lewis and B. A. Schrefler. *The Finite Element Method in the Static and Dynamic Deformation and Consolidation of Porous Media (Second Edition)*. Wiley, 1998.
3. P. Baud, E. Klein, and T.F. Wong. Compaction localization in porous sandstones: spatial evolution of damage and acoustic emission activity. *Journal of Structural Geology*, 26(4):603–624, 2004.
4. M. Beghi and C.E. Bottani. A thermoelastic method to accurately measure the grüneisen parameter and thermal diffusivity. *Applied physics*, 23(1):57–59, 1980.

# Chapter 12

## Reactive Transport

Christof Beyer, Thomas Nagel and Haibing Shao

### 12.1 Kinetic Dissolution of Non-aqueous Phase Liquids

Christof Beyer and Sebastian Bauer

Dissolution of organic contaminants from non-aqueous phase liquid (NAPL) source zones and their spreading in groundwater is an ubiquitous problem especially in urban regions. The simulation of kinetic NAPL dissolution processes in OpenGeoSys is based on a simplified two-phase flow model (water and NAPL) and describes the transfer of mass between water and NAPL phases by a system of ordinary differential equations. The two-phase flow model is simplified by assuming the NAPL phase to be present in residual saturation only, and hence being immobile. A change of the NAPL saturation may occur only through the NAPL dissolution process. In the current implementation, a pressure-saturation ( $P_w - S_n$ ) formulation is used for the two phase flow problem. For the implementation of the two-phase flow and transport equations please refer to [1].

Conceptually, the NAPL phase consists of all components present in the NAPL. A NAPL phase may be distributed in different NAPL geometries (pools, blobs of different shapes and sizes; amount:  $j = 0, \dots, n_j$ ). An individual organic component can be present in a reference volume at the same time in several NAPL pools and NAPL blobs of individual initial volume and surface area. The NAPL dissolution process is modeled as an exchange process between the immobile components in the NAPL and the corresponding mobile aqueous phase components.

---

C. Beyer (✉)

GeoHydroModellierung, Institut für Geowissenschaften, Christian-Albrechts-Universität zu Kiel, Ludewig-Meyn-Str. 10, 24118 Kiel, Germany  
e-mail: cb@gpi.uni-kiel.de

T. Nagel · H. Shao

Department of Environmental Informatics,  
Helmholtz Centre for Environmental Research GmbH-UFZ,  
Permoserstraße 15, 04318 Leipzig, Germany

© Springer International Publishing Switzerland 2015

O. Kolditz et al. (eds.), *Thermo-Hydro-Mechanical-Chemical Processes in Fractured Porous Media: Modelling and Benchmarking*, Terrestrial Environmental Sciences,  
DOI 10.1007/978-3-319-11894-9\_12

255

In general, mass transfer between the NAPL and the aqueous phase for individual components  $i$  can be described by Fick's 1st law

$$\frac{\partial M_i}{\partial t} = ka (C_{w,i}^{sat} - C_{w,i}) \quad (12.1)$$

The rate of mass transfer [ $\text{M T}^{-1}$ ] depends mainly on the concentration difference between the equilibrium concentration  $C_{w,i}^{sat}$  [ $\text{M L}^{-3}$ ] and the actual concentration  $C_{w,i}$  [ $\text{M L}^{-3}$ ] in the water phase as well as on the mass transfer parameter  $k$  [ $\text{L T}^{-1}$ ] and the water-NAPL contact area  $a$  [ $\text{L}^2$ ]. Mass transfer results in a change of concentration of component  $i$  in the aqueous phase and the corresponding component in the NAPL phase geometry  $j$ ,  $C_{n,j,i}$  [ $\text{M L}_{NAPL}^{-3}$ ]. To convert the change of mass into a change of concentration in water, the volumetric fraction of water in the REV must be considered, which is given by the product of water saturation  $S_w$  and porosity  $n$  and remains constant during the time step, with

$$nS_w \frac{\partial C_{w,i}}{\partial t} = \sum_j k_j a_j (C_{w,j,i}^{sat} - C_{w,i}) \quad (12.2)$$

$$V_{n,j} \frac{\partial C_{n,j,i}}{\partial t} = -k_j a_j (C_{w,j,i}^{sat} - C_{w,i}) \quad (12.3)$$

where  $C_{w,i,j}^{sat}$ ,  $k_j$  and  $a_j$  must be computed for each individual blob or pool geometry  $j$ . For NAPL mixtures  $C_{w,i,j}^{sat}$  is calculated according to Raoult's law

$$C_{w,j,i}^{sat} = C_{w,i}^{sat\_pure} \gamma_i \frac{C_{n,j,i}}{\sum_i C_{n,j,i}} \quad (12.4)$$

where  $C_{w,i}^{sat\_pure}$  [ $\text{M L}_{water}^{-3}$ ] is the pure phase aqueous solubility and  $\gamma_i$  [-] the activity coefficient of component  $i$  in the NAPL.

The mass transfer coefficient  $k$  for each blob geometry  $j$  can be estimated by different empirical correlations (see e.g. [2]). Here, a model of [3] is employed

$$k_j = SF \left( \frac{\rho_w v_a d_{50}}{\mu_w} \right)^{RE} \left( \frac{\mu_w}{D_{aq} \rho_w} \right)^{SE} \frac{D_{aq}}{d_{50}} \quad (12.5)$$

where  $d_{50}$  [L] is the mean grain size diameter,  $D_{aq}$  [ $\text{L}^2 \text{T}^{-1}$ ] is the coefficient of diffusion in water,  $SF$  [-] is the Sherwood-factor and  $RE$  [-] and  $SE$  [-] are the Reynolds- and Schmidt-exponents, as the two terms in brackets are the Reynolds- and Schmidt-numbers, respectively.

The volume fraction of NAPL blob geometry  $j$ ,  $V_{n,j}$  [ $\text{L}_{NAPL}^3 \text{L}_{REV}^{-3}$ ], in the reference volume is given by

$$V_{n,j} = \sum_i \frac{M_{n,j,i}}{\rho_i} \quad (12.6)$$

where  $M_{n,j,i}$  [ $\text{M L}_{REV}^{-3}$ ] is the mass of a single component in the reference volume and  $\rho_i$  [ $\text{M L}_{component}^{-3}$ ] its pure phase density. Based on assumptions with regard to the initial geometry of the NAPL distribution (i.e. dimension, number and shape (sphere, cylinder, pancake, ...)) the initial concentration and volume distribution leads to an approximate initial surface area  $a^0$  [ $\text{L}^2 \text{L}_{REV}^{-3}$ ]. For a specific NAPL geometry  $j$ ,  $a_j^0$  can be derived from the total mass of NAPL present and the shape and size of the assumed NAPL geometry (pool, cylindrical or spherical blobs). For spherical blobs, e.g. an approximation given by [4] can be used

$$a_j^0 = \frac{3nS_n}{r_b} \quad (12.7)$$

where  $r_b$  is the mean radius of the spherical blobs, which can be approximated by  $d_{50}/4$ . The updated surface area  $a^{t+1}$  after computation of NAPL dissolution is quantified from the previous surface area  $a^t$  and the ratio of volumes after ( $V^{t+1}$ ) and before ( $V^t$ ) NAPL dissolution

$$a_j^{t+1} = a_j^t \left( \frac{V_{n,j}^{t+1}}{V_{n,j}^t} \right)^\zeta \quad (12.8)$$

where  $\zeta$  [-] depends on the assumed geometry of the NAPL distribution and is  $2/3$  for spherical blobs,  $0.5$  for cylindrical blobs and  $0$  for pools, as their surface area remains almost constant over time.

For a NAPL geometry (i.e. a single pool or blob) consisting of a number of  $i$  components, the total NAPL volume  $V_n$  [ $\text{m}_{NAPL}^3 \text{m}_{REV}^{-3}$ ] in the REV is given by

$$V_n = \sum_i \frac{C_i}{\rho_i^m} \quad (12.9)$$

where  $C_i$  ( $\text{mol m}_{REV}^{-3}$ ) is the NAPL components concentration and  $\rho_i^m$  ( $\text{mol m}_{NAPL}^{-3}$ ) its molar density, and  $S_n = V_n/n$ .

### 12.1.1 Hansen and Kueper Benchmark

The kinetic dissolution model is validated against an analytical solution by Hansen and Kueper [5]. The Hansen and Kueper model was developed to quantify the temporally changing composition of a residual multi-component NAPL body in moving groundwater and the consequent changes of the NAPL constituents concentrations in

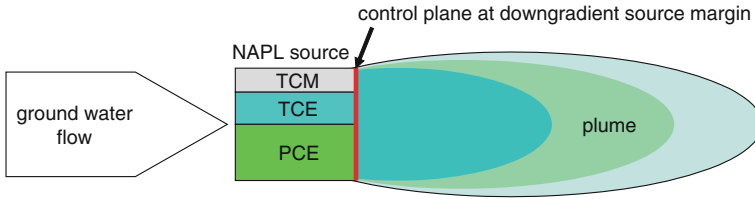


**Fig. 12.1** Conceptualization of the Hansen and Kueper analytical solution ([5]): Example of a three component residual NAPL source zone in a moving groundwater body and source emission

the surrounding groundwater. It is suited for both, pooled configurations and residual NAPL in blob geometries and—as any analytical model—is based on a number of simplifying assumptions:

- The model predicts the NAPL composition as well as aqueous phase concentrations at the downstream end of the NAPL source zone (Fig. 12.1).
- Intra-NAPL diffusion is fast in relation to phase partitioning.
- For pools the local equilibrium assumption is employed, i.e. inter-phase mass transfer is faster than solute transport away from the NAPL.
- Within a zone of residual NAPL, NAPL saturation and mixing are sufficient to allow the assumption of a uniform concentration composition at the downstream end of the source zone (perfectly mixed source), which follows Raoult’s law (global equilibrium assumption).
- The component composition of the NAPL is spatially invariant at a particular instant in time.
- Dissolution kinetics are fast at all times (equilibrium dissolution).
- NAPL saturation, effective porosity and water flux through the source are constant in time.

**12.1.1.1 Definition**

The Hansen and Kueper model for a residual NAPL source zone was represented as a one-dimensional numerical model of 10 m length in  $x$  direction using linear finite elements and a spatial discretization  $\Delta x = 0.333$  m. The perfectly mixed residual NAPL source zone is represented as a zone of blobs at a single node of the finite element mesh directly downgradient of the left hand side model boundary at  $x = 0.333$  m (Fig. 12.2).

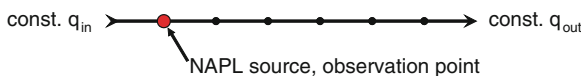


**Fig. 12.2** Representation of the Hansen and Kueper analytical solution ([5]) in a numerical model. The red dot represents the position of the NAPL blob zone in the linear finite element mesh

**Table 12.1** Physicochemical properties and initial concentrations of the immobile NAPL species

Parameter	PCE	TCE	TCM	Total	Unit
Molar weight	0.166	0.131	0.154		kg mol <sup>-1</sup>
Molar density	9770.8	11111.1	12395.3		mol m <sup>3</sup>
Max. aq. solubility	1.15	10.65	72.86		mol/m <sup>3</sup>
Concentration	122.14	111.11	30.99	264.24	mol/m <sup>3</sup> <sub>REV</sub>
Volume per m <sup>3</sup> <sub>REV</sub>	0.013	0.010	0.003	0.025	m <sup>3</sup>
Mass per m <sup>3</sup> <sub>REV</sub>	20.254	14.599	4.767	39.620	kg

The temporally constant flux through the NAPL source is induced by source terms of  $q_{in} = -q_{out} = 1.157 \cdot 10^{-6} \text{ m s}^{-1}$  at the left and right hand side model boundaries, respectively (Fig. 12.2). The NAPL consists of the three chlorinated hydrocarbon species perchloroethene (PCE), trichloroethene (TCE) and tetrachloromethane (TCM). Accordingly, three immobile NAPL species plus three corresponding mobile species are defined in the model. Table 12.1 lists physicochemical parameters and initial amounts or concentrations, respectively, assumed for the three immobile NAPL species in this simulation.

Corresponding mobile species in the aqueous phase share the same physicochemical properties. Initial concentrations at the second node of the mesh (i.e. at the NAPL source position) correspond the equilibrium concentrations according to Raoult's law and the initial moles of the immobile NAPL components and assuming activity coefficients of all three components in the NAPL as 1.0, i.e.  $C_{PCE} = 0.532$ ,  $C_{TCE} = 4.478$  and  $C_{TCM} = 8.545 \text{ mol m}^{-3}$ , respectively. Elsewhere, initial concentrations (as well as upstream boundary conditions) are set to  $C = 1.0 \cdot 10^{-10} \text{ mol m}^{-3}$ . In the NAPL source  $S_n = 0.10$  and  $S_w = 0.90$ , accordingly, while  $S_w = 1.0$  and  $S_n = 0.0$  elsewhere. Water phase relative permeability  $k_{rw}$  [-] is described by the Brooks-Corey model

$$k_{rw} = (S_e)^{\frac{2+3\lambda}{\lambda}} \quad (12.10)$$

with  $\lambda$  [-] the Brooks-Corey parameter and  $S_e$  [-] the effective saturation

$$S_e = \frac{S_w - S_{rw}}{1 - S_{rw}} \quad (12.11)$$

All other relevant model parameters are summarized in Table 12.2.

The initial interfacial area  $a^0$  is set to a very large value of  $5000.0 \text{ m}^2 \text{ m}_{REV}^{-3}$  in order to guarantee fast (i.e. quasi equilibrium) NAPL dissolution kinetics, as assumed by the analytical solution. Also, the geometry exponent  $\zeta$  is set to a value of 0.0 in order to keep the interfacial area constant over time. The simulation is run for 3200 time steps of 10,800 s length.

**Table 12.2** Model parameters used for the Hansen and Kueper benchmark

Parameter	Value	Unit
Model length $x$	10	m
Model length $y$	1.0	m
Model length $z$	1.0	m
Element length $x$	0.333	m
Porosity $n$	0.25	–
Permeability $k$	$1.54249 \cdot 10^{-11}$	$\text{m}^2$
Residual water saturation $S_{r_w}$	0.05	–
Maximum water saturation $S_{s_w}$	1.0	–
Residual NAPL saturation $S_{r_n}$	0.2	–
$\lambda$ (Brooks-Corey parameter)	3.86	–
Density of water $\rho_w$	999.7	$\text{kg m}^{-3}$
Viscosity of water $\mu_w$	$1.307 \cdot 10^{-3}$	Pa s
Mean grain diameter $d_{50}$	0.001	m
Sherwood factor $SF$	1.15	–
Reynolds exponent $RE$	0.654	–
Schmidt exponent $SE$	0.486	–
Geometry exponent $\zeta$	0.0	–
Initial interfacial area $a_0$	5000.0	$\text{m}^2 \text{m}_{REV}^{-3}$
Initial water pressure ( $x, t = 0$ )	98067.0	Pa

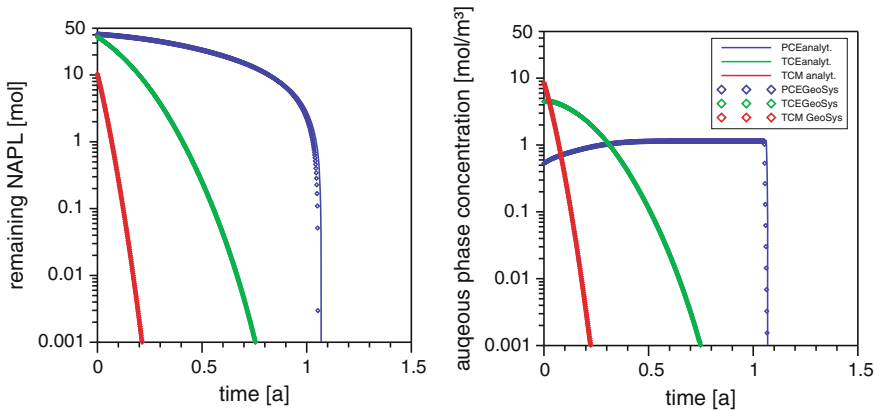


**Fig. 12.3** Total amounts of PCE, TCE and TCM in the NAPL phase (*left diagram*) and corresponding aqueous phase concentrations at the downgradient source zone margin (*right diagram*) as functions of time; *full lines* analytical solution of Hansen and Kueper [5], *symbols* OpenGeoSys simulation results

### 12.1.1.2 Results

Figure 12.3 presents the amounts of the the three immobile species PCE, TCE and TCM in the NAPL phase (left diagram) and the corresponding aqueous phase

concentrations (i.e. the source emission; right diagram) as functions of time. Full lines are for the analytical solution, while symbols represent results of the numerical simulation. The agreement is excellent over a concentration range of several orders of magnitude. TCM, which has the highest pure phase aqueous solubility is depleted fastest from the source. TCM and especially PCE depletion requires significantly longer time periods. Aqueous phase concentrations of PCE drop almost instantaneously, once the remaining amount of PCE in the NAPL falls below 0.28 mol.

## 12.2 Kinetic Mineral Dissolution/Precipitation

Christof Beyer and Sebastian Bauer

In OpenGeoSys the simulation of kinetic dissolution or precipitation of a mineral phase  $M$  [ $\text{ML}_{\text{solid}}^{-3}$ ] in a fully saturated porous medium is based on a Lasaga type rate law ([6, 7])

$$\frac{\partial M}{\partial t} = K^{\text{tot}} A |1 - \Omega^\theta|^\eta \text{sgn}(1 - \Omega^\theta) (1 - n)^{-1} \quad (12.12)$$

where  $K^{\text{tot}}$  [ $\text{ML}_{\text{mineral}}^{-2} \text{T}^{-1}$ ] is an overall rate constant,  $A$  [ $\text{L}_{\text{mineral}}^2 \text{L}_{\text{aquifer}}^{-3}$ ] the mineral's reactive surface area,  $\theta$  and  $\eta$  are empirical exponents, and  $n$  [ $\text{L}_{\text{water}}^3 \text{L}_{\text{aquifer}}^{-3}$ ] is porosity, as division by  $(1 - n)$  is required for unit conversion.  $\text{sgn}$  is the sign function, i.e. either  $-1$  for dissolution or  $+1$  for precipitation of the mineral.  $\Omega$  is the ion activity product divided by the equilibrium constant  $K$  of the mineral-water reaction

$$\Omega = \frac{\prod_{i=1}^n \gamma_i^{\nu_i} C_i^{\nu_i}}{K} \quad (12.13)$$

where  $\gamma_i$  [-] is the activity coefficient of species  $C_i$  ( $\text{mol kgw}^{-1}$ ) and  $\nu_i$  [-] the corresponding stoichiometric coefficient.

Parameter  $A$  [ $\text{L}_{\text{aquifer}}^2 \text{L}_{\text{mineral}}^{-3}$ ] of Eq. (12.12) for a mineral can be calculated from measured mineral specific reactive surface areas by multiplication with aquifer bulk density and the minerals solid volume fraction.  $K^{\text{tot}}$  consists of a so called base mechanism rate constant  $K^b$  and optional concentration dependent contributions from acid, alkaline or other catalysing or inhibiting species mechanisms

$$K^{\text{tot}} = K^b + \sum_{i=1}^n K^i \prod_{j=1}^m \gamma_{ij}^{\beta_{ij}} C_{ij}^{\beta_{ij}} \quad (12.14)$$

where  $K^i$  [ $\text{ML}^{-2} \text{T}^{-1}$ ] is the  $i$ th mechanism's rate constant and  $\beta_{ij}$  is an empirical exponent for the  $j$ th species of the  $i$ th mechanism. Temperature dependence of rate constants  $K^b$  or  $K^i$  in Eq. (12.14) is calculated by the Arrhenius correction, i.e.

$$K^i = K_{25}^i \exp\left(\frac{-E_a^i}{R} \left[\frac{1}{T} - \frac{1}{298.15}\right]\right) \quad (12.15)$$

where  $K_{25}^i$  [ $\text{ML}^{-2}\text{T}^{-1}$ ] is the reaction rate constant of mechanism  $i$  at 298.15 K,  $E_a^i$  [ $\text{JM}^{-1}$ ] the corresponding activation energy,  $R$  [ $\text{JM}^{-1}\text{K}^{-1}$ ] the universal gas constant (i.e.  $8.314\text{Jmol}^{-1}\text{K}^{-1}$ ) and  $T$  [K] the absolute ambient temperature. The production or consumption of aqueous species  $C_i$  due to precipitation or dissolution of mineral  $M$  is coupled to Eq. (12.12) via the stoichiometric coefficients  $\nu_i$ .

$$\frac{\partial C_i}{\partial t} = \nu_i \frac{\partial M}{\partial t} \quad (12.16)$$

### 12.2.1 Simulation of a Kinetic Calcite/Dolomite Dissolution Front

This benchmark is based on a reactive transport problem described in Chap. 15.1 of [1], where a 0.5 m long one-dimensional column that initially contains calcite is continuously flushed by a magnesium chloride solution (Fig. 12.4). The injection of the magnesium chloride solution induces a dissolution of the calcite and a temporary precipitation of dolomite. This benchmark was originally presented by [8].

In contrast to the simulation described in [1], where calcite and dolomite reactions were simulated as equilibrium reactions, here both are simulated as kinetically limited. The coupled OpenGeoSys-ChemApp code ([9, 10]) is used for this purpose and compared against OpenGeoSys-Phreeqc.

#### 12.2.1.1 Numerical Model

The relevant media properties of this benchmark are listed in Table 12.3.

Calcite and dolomite kinetics are governed by two mechanisms, respectively, contributing to the total rate constants, a neutral (or baseterm) and an acid mechanism, which nonlinearly depend on the activity of  $\text{H}^+$ . Calcite kinetics is considerably faster than the dolomite reaction. The surface areas for both minerals are assumed constant over time for the sake of simplicity. Table 12.4 lists the parameters of the kinetic calcite and dolomite reactions, which were taken from [11].

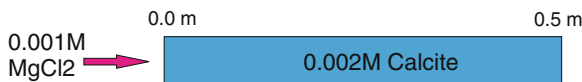


Fig. 12.4 Model domain

### 12.2.1.2 Results

The model is run for a period of 210 time steps of 100 s length, respectively. Simulation results are compared after 21000 s at the end of the simulation (Fig. 12.5), where solid lines are for the kinetic OpenGeoSys-ChemApp simulation, while dashed lines with symbols represent the results of the equivalent OpenGeoSys-Phreeqc model. The kinetics of calcite dissolution, dolomite precipitation and its redissolution result in smoothed dissolution fronts and lower amounts of precipitated dolomite in comparison to the equilibrium reactive transport simulation (cf. [1]). Agreement of results between OpenGeoSys-ChemApp and OpenGeoSys-Phreeqc is very close, with only slight differences in the shape of the Mg concentration profile.

**Table 12.3** Material properties for the calcite dissolution benchmark

Parameter	Value	Unit
Column length	0.5	m
Effective porosity	0.32	–
Bulk density	$1.8 \times 10^3$	kg/m <sup>3</sup>
Longitudinal dispersivity	0.0067	m
Pore velocity	$9.375 \times 10^{-6}$	m/sec
Flow rate	$3 \times 10^{-6}$	m <sup>3</sup> /sec
Temperature	298.15	K

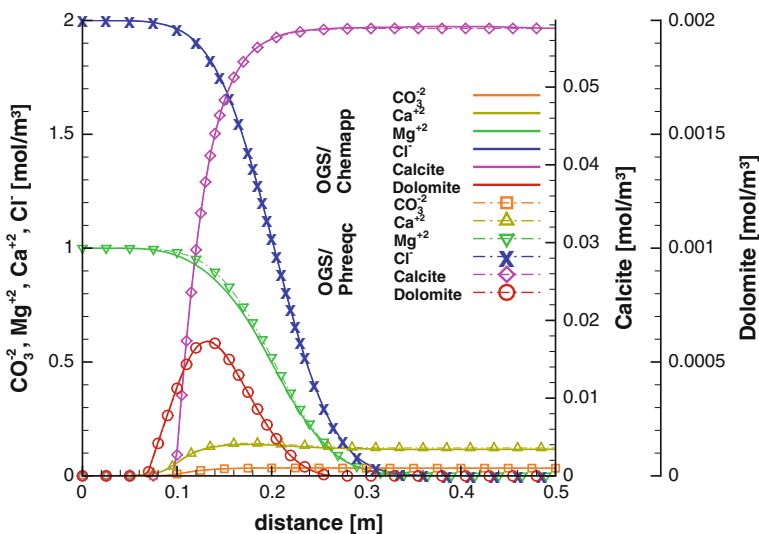


**Fig. 12.5** Benchmark results from OpenGeoSys-ChemApp and OpenGeoSys-Phreeqc

**Table 12.4** Parameters for calcite and dolomite dissolution kinetics

Parameter	Calcite	Dolomite	Unit
$A$	3.20	0.32	$\text{m}^2/\text{m}^2_{\text{aquifer}}$
$\theta$	1.0	1.0	-
$\eta$	1.0	1.0	-
$E_a$ (neutral)	23500	52200	J/mol
$\log(K_{25})$ (neutral)	-5.81	-7.53	$\text{mol}/\text{m}^2/\text{s}$
$E_a$ (acid)	14400	36100	J/mol
$\log(K_{25})$ (acid)	-0.30	-3.19	$\text{mol}/\text{m}^2/\text{s}$
Species (acid)	$H^+$	$H^+$	-
$\beta$	1.0	0.5	-

## 12.3 Local Thermal Nonequilibrium and Gas–Solid Reactions

Thomas Nagel and Haibing Shao

### 12.3.1 Introduction

Certain local thermodynamic and transport conditions inside a porous medium can cause local thermal non-equilibrium (TNEQ) between the solid and fluid phases. Instead of a mixture energy balance, separate energy balance equations for each phase are applied and give rise to individual temperature variables for those phases. Consequently, the heat transfer between the phases can be modelled. In this chapter the implemented T<sup>2</sup>HC model (where the exponent 2 stands for the two heat transport equations necessary to account for TNEQ) is benchmarked. Details of the implementation and further literature can be found in [12].

### 12.3.2 Interphase Heat Transfer

The objective of this benchmark is to verify the heat transfer implementation between solid and fluid. Both are given their individual initial temperatures and are allowed to exchange heat. Consider a porous solid filled with an ideal gas, in this case nitrogen. The system is homogeneous and completely closed off, i.e. neither mass nor heat fluxes are allowed across the system boundaries. The solid skeleton is considered rigid, the porosity constant, chemical reactions are suppressed. Therefore, the density of the gas inside the medium will not change. Heat sources/sinks, mass transfer, conductive or convective heat transport are thus not present. The energy balance for the ideal gas then simply reads

$$k_G \frac{\partial T_G}{\partial t} = h_{SG}(T_S - T_G) + \phi \frac{\partial p}{\partial t} \quad \text{with} \quad k_\alpha = \phi_\alpha \rho_\alpha R c_{p\alpha} \quad \text{with} \quad \alpha = S, G \quad (12.17)$$

Solid and gas temperature are not independent. The total energy balance reads

$$k_G \frac{\partial T_G}{\partial t} + k_S \frac{\partial T_S}{\partial t} = \phi_G \frac{\partial p}{\partial t} \quad (12.18)$$

With the constant gas density  $\rho_{GR} = \rho_{GR0}$  we find using the ideal gas relation

$$\frac{\partial p}{\partial t} = \frac{\rho_{GR0} R}{M} \frac{\partial T_G}{\partial t} = \frac{p_0}{T_{G0}} \frac{\partial T_G}{\partial t} \quad \text{with} \quad \rho_{GR0} = \frac{p_0 M}{RT_{G0}} \quad (12.19)$$

Integration of the overall energy equation yields (with  $T_{\alpha 0} = T_\alpha(t=0)$ )

$$k_G(T_G - T_{G0}) + k_S(T_S - T_{S0}) = \phi_G \frac{p_0}{T_{G0}}(T_G - T_{G0}) \quad (12.20)$$

$$T_S = T_{S0} + \frac{1}{k_S} \left( \underbrace{\phi_G \frac{p_0}{T_{G0}}}_{:=k_p} - k_G \right) (T_G - T_{G0}) \quad (12.21)$$

Thus, the solution for  $T_G$  can be found after some rearrangements to be

$$T_G = \frac{1}{(k_p - k_G - k_S)} [k_S(T_{S0} - T_{G0})e^{-t/\tau} - k_S T_{S0} + (k_p - k_G)T_{G0}] \quad (12.22)$$

$$\text{with} \quad \tau = \frac{k_S(k_p - k_G)}{h_{SG}(k_p - k_G - k_S)} \quad (12.23)$$

The exemplary parameter set is listed in Table 12.5. The values are chosen such that temperature changes due to heat transfer are visible in both phases.

With this parameter set, a time constant  $\tau = 0.124$  s follows. The simulation time was thus set to 1 s with a time step size of 0.002 s. The spatial discretisation is not of significance in this homogeneous problem which was simulated using one dimensional elements. Good agreement between the numerically calculated temperature

**Table 12.5** Parameter values for interphase heat transfer verification

$h_{SG}$ [W/(m <sup>3</sup> K)]	$\phi_G$ [-]	$\rho_{SR}$ [kg/m <sup>3</sup> ]	$\rho_{GR0}$ [kg/m <sup>3</sup> ]	$c_{pG}$ [J/(kg K)]
1000.0	0.5	1.0	0.436	1012
$c_{pS}$ [J/(kg K)]	$T_{G0}$ [°C]	$T_{S0}$ [°C]		
1200	500	200		

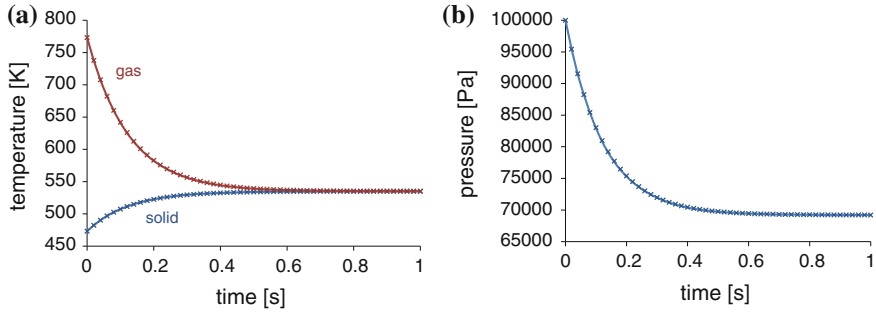


**Fig. 12.6** Verification of interphase heat transfer. *Solid lines* denote the analytical solution, *crosses mark* the numerical solution. **a** Solid and gas temperature profiles. **b** Gas pressure

profiles for both the solid and the gas phase were found (Fig. 12.6a). It can be seen that a common temperature is reached due to interphase heat transfer that is determined by the overall heat capacities of both the solid and gas phases. Additionally, in Fig. 12.6b the gas pressure profile calculated by OGS is compared to the analytical solution obtained by the ideal gas law.

### 12.3.3 Interphase Mass Transfer and Heat of Reaction

In this example, the behaviour of the model when mass transfer occurs between the phases is verified. Consider a closed off system similar to the one described in the previous example. The porous body is filled with a mixture of nitrogen and vapour modelled as ideal gasses. To obtain an analytical solution,  $h_{SG} \rightarrow \infty$  is assumed so that  $T_G = T_S = T$ . Under the described conditions we add the gas and solid energy balance

$$\rho_G c_{pG} \frac{\partial T}{\partial t} - \frac{\partial \phi_{GP}}{\partial t} = 0 \quad (12.24)$$

$$\rho_S c_{pS} \frac{\partial T}{\partial t} = \frac{\partial \rho_S}{\partial t} \Delta h \quad (12.25)$$

to obtain

$$(\rho_G c_{pG} + \rho_S c_{pS}) \frac{\partial T}{\partial t} - \frac{\partial \phi_{GP}}{\partial t} = \frac{\partial \rho_S}{\partial t} \Delta h \quad (12.26)$$

Using the ideal gas law, the closed system assumption, and considering nitrogen as non-reactive we find

$$\frac{\partial \phi_{GP}}{\partial t} = \frac{RT}{M_V} \frac{\partial \rho_V}{\partial t} + R \underbrace{\frac{\partial T}{\partial t} \left( \frac{\rho_V}{M_V} + \frac{\rho_N}{M_N} \right)}_{=R \frac{\partial T}{\partial t} \frac{\rho_G}{M_G}} \quad (12.27)$$

With the mass balance constraint  $\hat{\rho}_S = -\hat{\rho}_V = -\hat{\rho}_G$  the energy balance thus reads

$$(\rho_G c_{vG} + \rho_S c_{pS}) \frac{\partial T}{\partial t} = \frac{\partial \rho_S}{\partial t} \left( \Delta h - \frac{R}{M_V} T \right) \quad (12.28)$$

For simplicity we now numerically set  $c_{pS} = c_{vG} = \bar{c}$  and further note that  $\rho_G + \rho_S = \rho = \text{const}$ . Integration yields

$$T = \frac{M_V}{R} \left[ \Delta h - \left( \Delta h - \frac{R}{M_V} T_0 \right) e^{-(\rho_S - \rho_{S0}) \frac{R}{M_V \bar{c} \rho}} \right] \quad (12.29)$$

To illustrate both the forward and the backward reaction, the reaction rate was modelled with a trigonometric function such that the solid density evolution was sinusoidal (amplitude  $\tilde{\rho}$ , angular frequency  $\omega$ )

$$\hat{\rho}_S(t) = \tilde{\rho} \cos(\omega t) \quad (12.30)$$

From this reaction rate, the following composition relations can be derived analytically:

$$\rho_{SR}(t) = \rho_{SR0} + \frac{\tilde{\rho} \sin(\omega t)}{1 - \phi_G}, \quad \rho_{GR}(t) = \rho_{GR0} - \frac{\tilde{\rho} \sin(\omega t)}{\phi_G} \quad (12.31)$$

$$\rho_{VR}(t) = \rho_{VR0} - \frac{\tilde{\rho} \sin(\omega t)}{\phi_G}, \quad x_{mV}(t) = \frac{\rho_{VR}(t)}{\rho_{GR}(t)} \quad (12.32)$$

With the conversion from mass into mole fractions the molar mass of the gas mixture is found along with the gas pressure (time dependency implicit)

$$x_{nV} = \frac{M_N x_{mV}}{M_N x_{mV} + M_V (1 - x_{mV})} \quad (12.33)$$

$$M_G(x_{nV}) = M_V x_{nV} + M_N (1 - x_{nV}) \quad (12.34)$$

$$p(t) = \frac{\rho_{GR} R T}{M_G} \quad (12.35)$$

The exemplary parameter set is listed in Table 12.6. The values are chosen such that temperature changes due to mass transfer are visible in both phases. The numerical model was run with the full TNEQ implementation albeit with a very high value for  $h_{SG}$ . Additionally, the heat of reaction was varied to illustrate its effect:  $\Delta h = \{0.0, 10^5, 5 \cdot 10^5\}$  J/kg. A time step size of 0.001 s was chosen for a time interval of 1 s. Similar to the previous example, the homogeneity of the considered system does

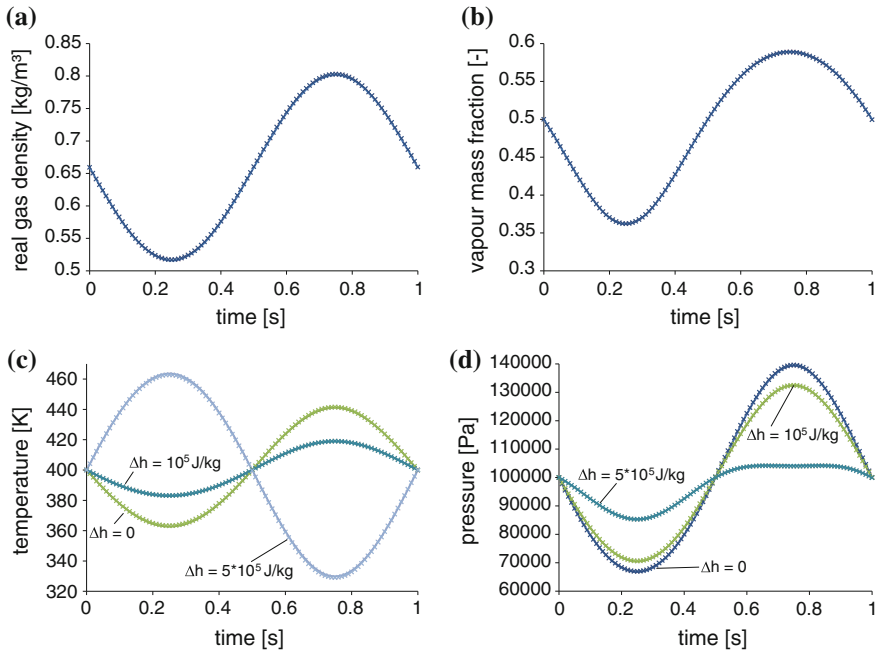


**Fig. 12.7** Verification of interphase mass transfer. *Solid lines* denote the analytical solution, *crosses mark* the numerical solution. **a** Gas density. **b** Vapour mass fraction. **c** Temperature profiles (marked with the respective reaction enthalpies). **d** Gas pressure profiles (marked with the respective reaction enthalpies)

not cause any special requirements for its spatial discretisation. 1D elements were used.

The model correctly reproduced the conditions of thermal equilibrium. The numerically obtained gas real density and vapour mass fraction profiles compare well with the analytical solution (Fig. 12.7a, b). During the initial stage of the reaction the gas loses mass while the solid (not shown) gains that amount of mass. During the back reaction the opposite effect occurs. An equally good match is obtained for the temperature profiles (Fig. 12.7c). If no heat of reaction is released, the gas simply cools down as its density and pressure drop. The solid phase follows this trend due to the very low density chosen here for demonstration purposes. The temperature fluctuation is lower when the exothermic heat of reaction  $\Delta h = 10^5$  J/kg is considered.

**Table 12.6** Parameter values for interphase mass transfer verification

$\phi_G$ [-]	$\rho_{SR0}$ [kg/m <sup>3</sup> ]	$\rho_{GR0}$ [kg/m <sup>3</sup> ]	$\bar{c}$ [J/(kg K)]
0.7	1.0	0.659	620.57
$T_{G0} = T_{S0}$ [K]	$\omega$ [Hz]	$\tilde{\rho}$ [kg/m <sup>3</sup> ]	$x_{mv0}$ [-]
400	$2\pi$	0.1	0.5

**Table 12.7** Relevant material parameters for the interphase friction benchmark

$\phi_G$	$k$	$\mu\nu$	$\lambda_{GR}$	$\lambda_{SR}$
0.8	$5 \cdot 10^{-12} \text{ m}^2$	$1 \cdot 10^{-5} \text{ Ns/m}^2$	10 W/m K	0.4 W/m K

If the heat of reaction is increased even further to  $\Delta h = 5 \cdot 10^5 \text{ J/kg}$ , the temperature profile switches signs and follows the opposite trend as the heat released in the solid phase becomes the dominant effect. In the gas pressure profiles this switch of sign can be observed as well along with an increasingly non-sinusoidal trend in the pressure profile (Fig. 12.7d).

### 12.3.4 Interphase Friction

When a fluid moves through a porous solid, the interphase friction generates heat. In local TNEQ models, this friction term can either be assigned to the fluid phase as the convection term  $\phi_G T_G \alpha_T \text{grad}(\phi_G p) \cdot \mathbf{v}_G$  or to the solid phase as the momentum interaction term  $\hat{\mathbf{p}}_G \cdot \mathbf{w}_G$ . The former is done in OGS as part of the advection matrix calculation, the latter as part of the RHS calculation. For testing purposes it can also be neglected completely.

Both versions should produce identical results for thermal equilibrium, i.e. when the interphase heat transfer coefficient  $h_{SG}$  is chosen sufficiently high so that solid and gas temperatures remain virtually identical at all times.

#### 12.3.4.1 Model

A square domain with 400 bilinear quadratic elements was modelled and subjected to a diagonal flow pattern (once steady state is reached) by applying pressure and temperature boundary conditions as shown in Fig. 12.8. Ideal gas behaviour was assumed for the fluid (nitrogen) and the system was sealed with respect to the heat flux vectors for both phases where no temperature boundary condition is indicated in Fig. 12.8. The analysis was run until temperature and flow fields had evolved to a steady state. Relevant material parameters are listed in Table 12.7.

#### 12.3.4.2 Results

The mesh and the resultant pressure distribution are shown in Fig. 12.9a. The pressure gradient drives a diagonal flow pattern and the temperature distribution was plotted along the dashed line indicated in Fig. 12.9a. The temperature profiles are identical for the cases where the interphase friction term is added implicitly to the fluid energy balance or explicitly on the RHS of the solid energy balance (Fig. 12.9b). If the term is neglected altogether, the gas cools down due to the expansion (pressure drop)

it undergoes and subsequently cools down the solid with it until a steady state is reached (Fig. 12.9b). The latter is an unphysical result.

### 12.3.5 Steady State Heat Conduction with Heat Generation and Convection Boundary Conditions

#### 12.3.5.1 Model

For each phase (fluid and solid), that is for each energy balance equation used in the T<sup>2</sup>HC model, convective boundary conditions were implemented. Convective boundary conditions specify the heat flux across a surface as

$$\mathbf{q} \cdot \mathbf{n} = h(T - T_\infty) \tag{12.36}$$

where  $h$  is the surface heat transfer coefficient depending on the convective conditions as well as material pairs, and  $T_\infty$  is the ambient temperature.

Consider a cylindrical rod with a constant heat source  $r_\alpha$  per unit mass of phase  $\alpha$  generated by nuclear processes, electric currents or some far field. An axisymmetric model will be set up. Due to the axial homogeneity of the problem the 2D mesh (Fig. 12.10a) can further be simplified to a 1D representation (Fig. 12.10b).

Simulations were run until a steady state was achieved and the temperature profiles compared to the analytical solutions derived below. 20 linear elements with a bias towards the open boundary were used in the 1D simulations. For the 2D simulations, 30 biased elements were employed in the radial direction and 2 in the (gradient-free) axial direction. Sufficiently small time steps were allowed to ensure convergence.

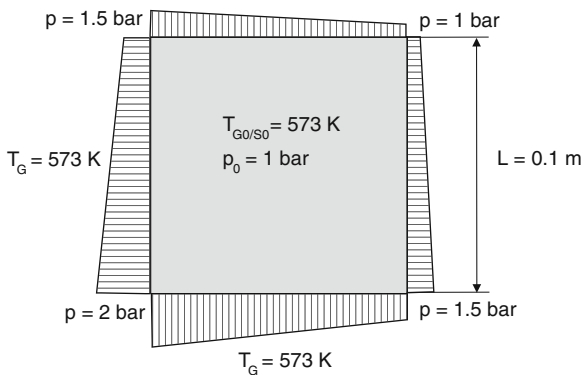
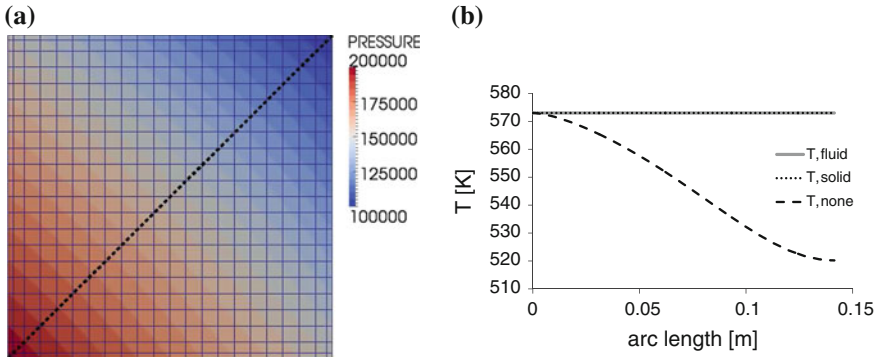
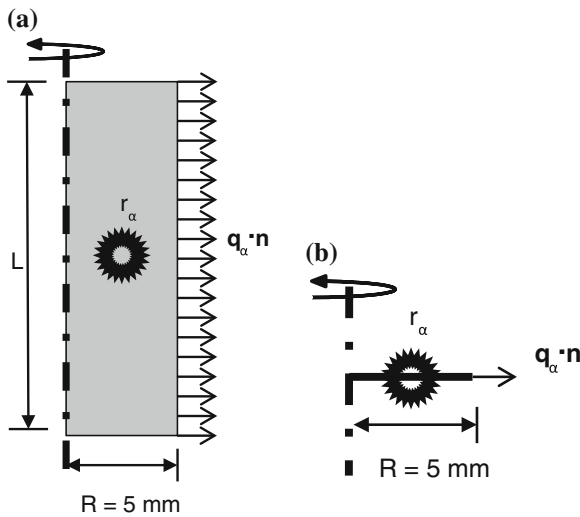


Fig. 12.8 Boundary and initial conditions for interphase friction benchmark



**Fig. 12.9** **a** Mesh and pressure distribution. *Line* indicates the cut along which the temperature distributions in **b** are plotted for the various governing equations. **a** Pressure distribution. **b** Temperature profiles



**Fig. 12.10** Axisymmetric model representations of the cylindrical rod problem. **a** 2D mesh. **b** 1D mesh

### 12.3.5.2 Analytical Solution—Cylindrical Coordinates

Consider porous solid filled with a stationary fluid of constant density. Only the steady state problem involving heat conduction, the heat source and the convection boundary condition will be solved. We further suppress any heat exchange between the fluid and the solid phase (volumetric heat transfer coefficient  $h_{SG} = 0$ ) so that their temperatures evolve independently. With homogeneous and isotropic thermal conductivities and volume fractions the problem then reads

$$-\frac{\rho_{\alpha R} r_{\alpha}}{\lambda_{\alpha R}} = \frac{1}{r} \frac{d}{dr} \left( r \frac{dT_{\alpha}}{dr} \right) \quad (12.37)$$

Integration yields:

$$T_{\alpha}(r) = -\frac{\rho_{\alpha R} r_{\alpha}}{4\lambda_{\alpha R}} r^2 + C_1 \ln r + C_2 \quad (12.38)$$

Regularity at  $r = 0$  requires  $C_1 = 0$  and leaves  $C_2$  to be determined by the boundary condition:

$$\mathbf{q}_{\alpha} \cdot \mathbf{n} \Big|_{r=R} = -\phi_{\alpha} \lambda_{\alpha R} \text{grad } T_{\alpha} \Big|_{r=R} = -\phi_{\alpha} \lambda_{\alpha R} \frac{dT_{\alpha}}{dr} \Big|_{r=R} \quad (12.39)$$

$$\frac{dT_{\alpha}}{dr} \Big|_{r=R} = -\frac{h_{\alpha} \phi_{\alpha} (T \Big|_{r=R} - T_{\infty})}{\phi_{\alpha} \lambda_{\alpha R}} \quad (12.40)$$

With this, the surface temperature is found as

$$T \Big|_{r=R} = T_{\infty} + \frac{\rho_{\alpha R} r_{\alpha}}{2h_{\alpha}} R \quad (12.41)$$

The steady state temperature profile thus follows as

$$T_{\alpha}(r) = T_{\infty} + \frac{\rho_{\alpha R} r_{\alpha} R^2}{4\lambda_{\alpha R}} \left[ 1 + \frac{2\lambda_{\alpha R}}{Rh_{\alpha}} - \left( \frac{r}{R} \right)^2 \right] \quad (12.42)$$

### 12.3.5.3 Local Thermal Equilibrium

In an additional simulation, the behaviour under local thermal equilibrium was verified. Consider therefore the case where  $h_{SG} \rightarrow \infty$ , such that  $T_{\alpha} = T \forall \alpha$  and additionally assume that  $r_G = 0$  (only the solid contains a heat source). The analytical solution then reads

$$T(r) = T_{\infty} + \frac{\rho_{SR} r_S R^2}{4\lambda_{\text{eff}}} \left[ 1 + \frac{2\lambda_{\text{eff}}}{Rh_{\text{eff}}} - \left( \frac{r}{R} \right)^2 \right] \quad (12.43)$$

with

$$\lambda_{\text{eff}} = \phi_S \lambda_{SR} + \phi_G \lambda_{GR} \quad (12.44)$$

$$h_{\text{eff}} = \phi_S h_S + \phi_G h_G \quad (12.45)$$

This problem was only run on a 1D mesh.

### 12.3.5.4 Analytical Solution—Cartesian Coordinates

For reasons of additional verification, the above meshes are used for an analysis in Cartesian coordinates as well (now a plate instead of a rod is modelled). Starting from the same equation as above but in Cartesian coordinates with symmetry conditions at  $x = 0$  and convection boundary conditions at  $x = L$  we find:

$$-\frac{\rho_{\alpha R} r_{\alpha}}{\lambda_{\alpha R}} = \frac{d^2 T_{\alpha}}{dx^2} \tag{12.46}$$

Integration yields:

$$T_{\alpha}(x) = -\frac{\rho_{\alpha R} r_{\alpha}}{2\lambda_{\alpha R}} x^2 + C_1 x + C_2 \tag{12.47}$$

With the symmetry condition  $T_{\alpha,x}|_{x=0} = 0$  we find  $C_1 = 0$ . On the outer surface we employ the convective boundary condition

$$\mathbf{q}_{\alpha} \cdot \mathbf{n}|_{x=L} = -\phi_{\alpha} \lambda_{\alpha R} \text{grad } T_{\alpha}|_{x=L} = -\phi_{\alpha} \lambda_{\alpha R} \left. \frac{dT_{\alpha}}{dx} \right|_{x=L} \tag{12.48}$$

$$\left. \frac{dT_{\alpha}}{dx} \right|_{x=L} = -\frac{h_{\alpha} \phi_{\alpha} (T|_{x=L} - T_{\infty})}{\phi_{\alpha} \lambda_{\alpha R}} \tag{12.49}$$

With this, the surface temperature is found as

$$T|_{x=L} = T_{\infty} + \frac{\rho_{\alpha R} r_{\alpha}}{h_{\alpha}} L \tag{12.50}$$

The steady state temperature profile thus follows as

$$T_{\alpha}(x) = T_{\infty} + \frac{\rho_{\alpha R} r_{\alpha} L^2}{2\lambda_{\alpha R}} \left[ 1 + \frac{2\lambda_{\alpha R}}{Lh_{\alpha}} - \left(\frac{x}{L}\right)^2 \right] \tag{12.51}$$

**Table 12.8** Geometric, material and ambient parameters for the convective heat transfer boundary condition under TNEQ

$\lambda_{SR}$	$\lambda_{GR}$	$h_{aS}$	$h_{aG}$
0.2 W/mK	10 W/mK	10 W/m <sup>2</sup> K	1 W/m <sup>2</sup> K
$\rho_{SR}$	$\rho_{GR}$	$r_S$	$r_G$
1000 kg/m <sup>3</sup>	1 kg/m <sup>3</sup>	10 W/kg	500 W/kg
$T_{\infty}$	R	$\phi_G$	
293 K	0.05 m	0.8	

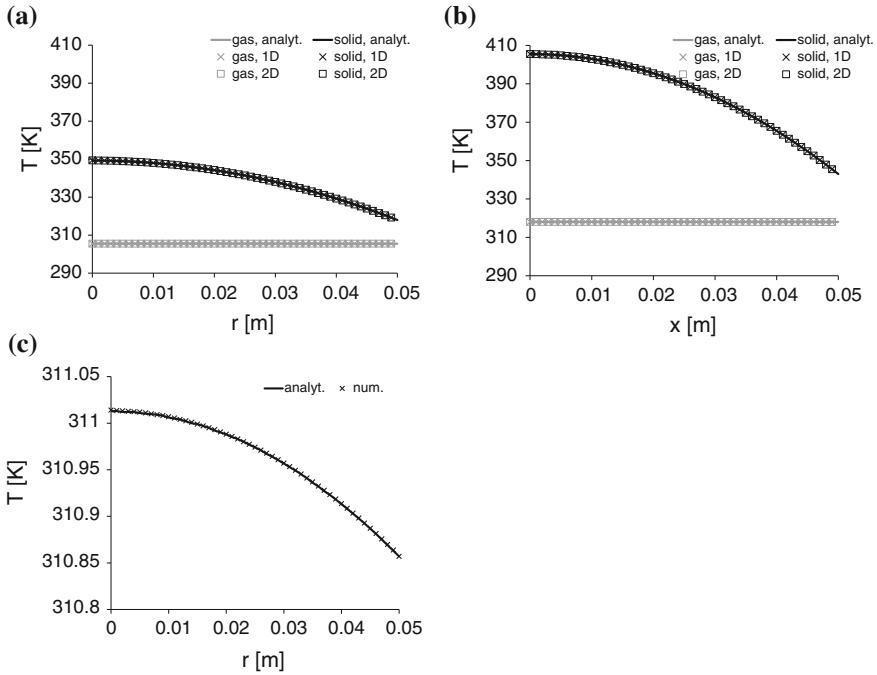


**Fig. 12.11** Axisymmetric model representations of the cylindrical rod problem under local TNEQ and TEQ conditions (a, c); 2D model representation of the plate problem under TNEQ conditions (b). **a** Cylindrical coordinates, TNEQ, **b** Cartesian coordinates, TNEQ, **c** Cylindrical coordinates, TEQ

### 12.3.5.5 Results

The material parameters chosen for demonstration purposes are listed in Table 12.8. The numerical implementation reproduces the analytical solutions well (Fig. 12.11). The parabolic profile is clearly visible for the solid temperatures. In case of local TNEQ, the independent gas temperature profiles are nearly flat due to the higher heat conductivity in relation to internal heat generation and heat transition to the boundary (Figs. 12.11a, b). In case of local TEQ, both phases follow the common temperature profile as expected (Fig. 12.11c).

## References

1. O. Kolditz, U.-J. Görke, H. Shao, and W. Wang. *Thermo-Hydro-Mechanical-Chemical Processes in Porous Media: Benchmarks and Examples*. Lecture notes in computational science and engineering. Springer, 2012.
2. S. E. Powers, L. M. Abriola, J. S. Dunkin, and W.J. Weber Jr. Phenomenological models for transient NAPL-water mass-transfer processes. *Journal of Contaminant Hydrology*, 16:1–33, 1994.

3. S. A. Bradford and L. M. Abriola. Dissolution of residual tetrachloroethylene in fractional wettability porous media: Incorporation of interfacial area estimates. *Water Resources Research*, 37:1183–1195, 2001.
4. P. Grathwohl. *Diffusion in Natural Porous Media*. Topics in Environmental Fluid Mechanics. Kluwer, 1998.
5. S. K. Hansen and B. H. Kueper. An analytical solution to multi-component NAPL dissolution equations. *Advances in Water Resources*, 30:382–388, 2007.
6. A. C. Lasaga, J. M. Soler, J. Ganor, T. E. Burch, and K. L. Nagy. Chemical weathering rate laws and global geochemical cycles. *Geochimica Cosmochimica Acta*, 58:2361–2386, 1994.
7. A. C. Lasaga. Fundamental approaches in describing mineral dissolution and precipitation rates. In *White A.F., Brantley S.L. (eds) Chemical Weathering Rates of Silicates Minerals, Reviews in Mineralogy 31, BookCrafters, Chelsea*, 1995.
8. P. Engesgaard and K. L. Kipp. A geochemical transport model for redox-controlled movement of mineral fronts in groundwater flow systems: A case of nitrate removal by oxidation of pyrite. *Water Resources Research*, 28:2829–2843, 1992.
9. C. Beyer, D. Li, M. de Lucia, M. Kuehn, and S. Bauer. Modelling  $CO_2$ - induced fluid-rock interaction in the altensalzwedel gas reservoir, part II-coupled reactive transport simulations. *Environmental Earth Sciences*, 67:573–588, 2012.
10. D. Li, S. Bauer, K. Benisch, B. Graupner, and C. Beyer. OpenGeoSys-ChemApp: a coupled simulator for reactive transport in multiphase systems: Code development and application at a representative  $CO_2$  storage formation in Northern Germany. *Acta Geotechnica*, page published online, 2013.
11. J. L. Palandri and Y. K. Kharaka. A compilation of rate parameters of water-mineral interaction kinetics for application to geochemical modelling. Technical report, US Geol Survey Water-Resources Investigations Report 04-1068, 2004.
12. T. Nagel, H. Shao, A.K. Singh, N. Watanabe, C. Roskopf, M. Linder, A. Woerner, and O. Kolditz. Non-equilibrium thermochemical heat storage in porous media: Part 1 - conceptual model. *Energy*, 60:254–270, 2013.

# Appendix A

## Introduction to OpenGeoSys (OGS): OGS—Overview

This part is mainly from the OGS overview paper [1] and updated with new information and results since 2012.

### A.1 Background

Coupled process modeling has been considered in various engineering problems and geo-scientific applications since the computation method was introduced for problems of soil consolidation, dam construction and oil/gas field exploration in early 1970. However, substantial progress in experimental and theoretical studies regarding the fully coupled effects of temperature, hydraulics and mechanics, as well as chemistry, in fractured porous media was just made in the last two decades due mainly to demands from the performance and safety assessment of high-level nuclear waste repositories. Numerical methods and computer codes have been developed successfully within the international DECOVALEX project ([www.decovalex.com](http://www.decovalex.com)). Meanwhile a wider range of applications associated with THMC coupled problems such as geothermal reservoir engineering, CO<sub>2</sub> and energy storage, construction of underground repositories etc. can be found in different international conferences, e.g. GeoProc (<http://www.mech.uwa.edu.au/research/geoproc>), ComGeo (<http://www.com-geo.org/>).

For a long-term performance and safety assessment of a nuclear waste repository in a deep geological formation, an important issue is to guarantee the isolation of an underground repository. To answer this question, solute transport processes under the coupled conditions involving mechanical stability, thermal loading from the high-level waste, and chemistry in the groundwater should be predicted numerically. Also, for construction planning of such a complex and the implementation of experimental data gained from in situ tests, a multiple process coupled code is required.

Through the rapid development of computer technology, complicated geoscientific problems can be analyzed in a coupled manner using modern numerical codes.

However, the understanding of the complicated coupled processes based on the experimental data available and implementation of the developed algorithm into the numerical codes are major challenge for scientists, which require interdisciplinary and interactive cooperation.

Quality management is nowadays a standard tool for production and development to ensure the high quality of a produced result. A numerical code dealing with the coupled THMC process is a highly complicated software product since the different processes have different characteristic features, e.g. time and spatial scales, nonlinearities, and interaction degree etc. To maintain a high quality of the developed code, benchmark testing is therefore necessary, especially in the case that scientists from different disciplines and organizations are working on the same code. Therefore, code verification and validation of selected test cases are documented during the code development, and finally a benchmarking book for the code development is produced and quality ensured [2].

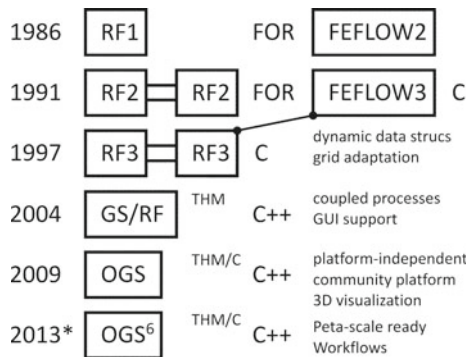
## A.2 Historical Note

Considerable efforts have been made in the past for porous media code development to address above mentioned problems in geosciences and hydrology, e.g. TOUGH [3, 4], STOMP [5], HydroGeoSphere [6], FEFLOW [7, 8], SUTRA [9, 10], DUMUX [11, 12], MIN3P [13], MT3D [14] or in particle hydrodynamics [15]. In the abstract we describe the continuous development of OGS beginning in the eighties (Fig. A.1).

### *RockFlow-F/FEFLOW-C*

In the mid eighties there was a request by the Federal Institute of Geosciences (BGR) to the Institute of Hydromechanics (University of Hannover) concerning the development of a simulation program for fractured rock. The idea of RockFlow (RF) was then born and the development of a computer code based on multi-dimensional FEM

Fig. A.1 OGS history



in order to represent flow processes in complex geological structures. At the same time at the Academy of Sciences (Chemnitz) the FEFLOW code was being developed for density-dependent flow processes in porous media [16, 17]. The pioneering work of RF-1 was done in a series of doctoral dissertations [18–21]. Both codes FEFLOW and RockFlow were implemented with FORTRAN at that time.

The next stage in the early nineties was related to the coupling of the individual RF-1 modules through file interfaces and the improvement of computational efficiency, e.g. by introducing an iterative equation solver. RF-2 was successfully used in several application projects in the fields of waste deposition and geothermal energy [22, 23]. A scientific “market” for RF in Applied Geoscience was opened.

### ***RockFlow-C***

It was soon determined that the coupling of the different RF modules via file interface was inefficient. Moreover, for the use of grid-adaptive methods, dynamic data structures were necessary. Consequently, in the late nineties a complete re-organization of RF was started. The implementation of RF-3 was started in C [24, 25]. Major research topics of the RF group were multi-phase flow [26], grid adaptation [27], reactive transport [28], and deformation processes [29]. Besides the numerical parts, geometric modeling and meshing methods became more and more important for real-world applications [30, 31].

### ***GeoSys/RockFlow-C++***

Due to the increasing functionality, the RF code became more and more sophisticated and difficult to handle. Consequently, the introduction of object-oriented methods was necessary. RF-4 or now GeoSys was (again) completely re-designed and rewritten in C++ [32, 33]. Several doctoral theses have been completed in the fields of geotechnical simulation (DECOVALEX project, [34–36]), contaminant hydrology (Virtual Aquifer project, [37–39]), geothermal reservoir modelling (Urach Spa project, [40]). Alongside computational mechanics, progress had been made in the pre-processing for numerical analysis [41–43]. First GeoSys/RockFlow habilitations had been completed [44–46]. As mentioned in the beginning, it is impossible to cite everything. Other important works during the Tübingen time are e.g. [47–49] concerning particle tracking, coupled hydrosystems, and reactive transport simulation.

### ***OpenGeoSys***

The new challenge for GeoSys is to continue its development as a distributed open-source project, i.e. sharing and widening the knowledge, as people from the OGS group receive offers and move to other places, and as the number



**Fig. A.2** VISLAB application

of GeoSys partners increases. At the Helmholtz Centre for Environmental Research in Leipzig a new research platform TESSIN is available, which combines high-performance-computing (HPCLab) and high-end visualization facilities (VISLab, Fig. A.2, Appendix E). Visualization provides a scientific tool for insight into large and complex data sets [50]. The graphical-user-interface (GUI) has become a valuable tool for visual data management and analysis [51] (Appendix C) A considerable amount of time is spent to prepare OGS for student teaching and training courses, e.g. in the HIGRADE graduate school program. Post-processing becomes more and more important as more and more information becomes available, due to high-resolution measurement techniques and HPC itself. A first medium-size HPC application has been realized in geotechnical modeling [52].

The next PhD generation has grown up within the open-source framework showing the large variety of OGS applicability in hydrology [53], reactive transport processes [54], groundwater optimization [55], geothermal reservoir analysis [56], as well as high-resolution modelling of the water uptake in root systems [57].

Since the publication of the volume one of the THMC Benchmark Book several new PhDs projects have been successfully completed: modelling mixing and reactive transport processes compared with laboratory experiments [58], subsurface flow and salt transport in the Thuringian basin [59], particle tracking for non-linear flow processes [60], gas migration in saturated argillaceous rock [61], thermal equations of state for CO<sub>2</sub> [62], application to radionuclide waste disposal concepts (DECOVALEX 2011) [63], density-dependent flows at different scales [64].



Fig. A.3 OGS Website



Fig. A.4 OGS partner institutions

Meanwhile OGS is profiting a lot from the community support, e.g. concerning the development of pre- and postprocessing tools, e.g. GINA [65] and MeshIT developments [66, 67]. OGS has a new Webpage (Fig. A.3) which should attract more attention to the open source project and at the same time being a community hub as well as providing information about recent activities. The current OGS partners are depicted in Fig. A.4.

## References

1. O. Kolditz, S. Bauer, L. Bilke, N. Boettcher, J.O. Delfs, T. Fischer, U.J. Goerke, T. Kalbacher, G. Kosakowski, C.I. McDermott, C.H. Park, F. Radu, K. Rink, H. Shao, H.B. Shao, F. Sun, Y.Y. Sun, A.K. Singh, J. Taron, M. Walther, W. Wang, N. Watanabe, Y. Wu, M. Xie, W. Xu, and B. Zehner. OpenGeoSys: An open-source initiative for numerical simulation of thermo-hydro-mechanical/chemical (THM/C) processes in porous media. *Environmental Earth Sciences*, 67(2):589–599, 2012.
2. O. Kolditz, U. J. Görke, H. Shao, and W. Wang, editors. *Lecture Notes in Computational Science and Engineering 86: Thermo-Hydro-Mechanical-Chemical Processes in Fractured Porous Media*. Springer Heidelberg, Dordrecht, London, New York, 1 edition, 2012.
3. K. Pruess. The TOUGH codes - A family of simulation tools for multiphase flow and transport processes in permeable media. *Vadose Zone Journal*, 3(3):738–746, 2004.
4. T.F. Xu, E. Sonnenthal, N. Spycher, and K. Pruess. TOUGHREACT - A simulation program for non-isothermal multiphase reactive geochemical transport in variably saturated geologic media: Applications to geothermal injectivity and CO<sub>2</sub> geological sequestration. *Computers & Geosciences*, 32(2):145–165, 2006.
5. M.D. White, M. Oostrom, and M.L. Rockhold. Scalable modeling of carbon tetrachloride migration at the hanford site using the STOMP simulator. *Vadose Zone Journal*, 7(2):654–666, 2008.
6. E.A. Sudicky, J.P. Jones, Y.J. Park, A.E. Brookfield, and D. Colautti. Simulating complex flow and transport dynamics in an integrated surface-subsurface modeling framework. *Geosciences Journal*, 12(2):107–122, 2008.
7. H.J.G. Diersch and O. Kolditz. Variable-density flow and transport in porous media: Approaches and challenges. *Advances in Water Resources*, 25(8–12): 899–944, 2002.
8. H.J.G. Diersch. *FEFLOW: Finite Element Modeling of Flow, Mass and Heat Transport in Porous and Fractured Media*. Springer Publisher, Heidelberg-Berlin, 2014.
9. H.W. Reeves, P.M. Thibodeau, and R.G. Underwood. Incorporation of total stress changes into the ground water model SUTRA. *Ground Water*, 38(1):89–98, 2000.
10. A.R. Piggott, A.G. Bobba, and J.N. Xiang. Inverse analysis implementation of the SUTRA groundwater model. *Ground Water*, 32(5):829–836, 1994.
11. S. Freiboth, H. Class, R. Helmig, and et al. A model for multiphase flow and transport in porous media including a phenomenological approach to account for deformation—a model concept and its validation within a code intercomparison study. *Computational Geosciences*, 13(3):281–300, 2009.
12. B. Flemisch, M. Darcis, K. Erbertseder, B. Faigle, B. Lauser, K. Mosthaf, S. Muthing, P. Nuske, A. Tatomir, M. Wolff, and R. Helmig. DuMux: DUNE for

- multi-phase, component, scale, physics, . . . flow and transport in porous media. *Advances in Water Resources*, 34(9):1102–1112, 2011.
13. K.U. Mayer and K.T.B. MacQuarrie. Solution of the MoMaS reactive transport benchmark with MIN3P-model formulation and simulation results. *Computational Geosciences*, 14(3):405–419, 2010.
  14. H. Prommer, D.A. Barry, and C. Zheng. MODFLOW/MT3DMS-based reactive multicomponent transport modeling. *Ground Water*, 41(2):247–257, 2003.
  15. A.M. Tartakovsky, P. Meakin, and T.D. Scheibe. Simulations of reactive transport and precipitation with smoothed particle hydrodynamics. *Journal Computational Physics*, 222(2):654–672, 2007.
  16. H.J. Diersch. Finite-element modeling of recirculating density-driven saltwater intrusion processes in groundwater. *Advances in Water Resources*, 11(1):25–43, 1988.
  17. O. Kolditz. *Zur Modellierung und Simulation geothermischer Transportprozesse in untertägigen Zirkulationssystemen*. Dissertation, Akademie der Wissenschaften der DDR, Berlin, 1990.
  18. K.P. Kroehn. *Simulation von Transportvorgängen im klüftigen Gestein mit der Methode der Finiten Elemente*. PhD thesis, Institute of Fluid Mechanics, Hannover University, 1991.
  19. J. Wollrath. *Ein Strömungs- und Transportmodell fuer klüftiges Gestein und Untersuchungen zu homogenen Ersatzsystemen*. PhD thesis, Institute of Fluid Mechanics, Hannover University, 1990.
  20. R. Helmig. *Theorie und Numerik der Mehrphasenströmungen in geklüfteten porösen Medien*. PhD thesis, Institute of Fluid Mechanics, Hannover University, 1993.
  21. H. Shao. *Simulation von Strömungs- und Transportvorgängen im geklüfteten porösen Medien mit gekoppelten Finite-Element- und Rand-Element-Methoden*. PhD thesis, Institute of Fluid Mechanics, Hannover University, 1994.
  22. T. Lege. *Modellierung des Klüftgesteins als geologische Barriere fuer Deponien*. PhD thesis, Institute of Fluid Mechanics, Hannover University, 1995.
  23. O. Kolditz. *Stoff- und Waermetransport im Klüftgestein*. Habilitation, Institute of Fluid Mechanics, Hannover University, 1996.
  24. M. Schulze-Ruhfus. *Adaptive Verfeinerung und Vergroerberung gekoppelter 1D/2D/3D Elemente*. Diploma thesis, Institute of Fluid Mechanics, Hannover University, 1996.
  25. C. Barlag. *Adaptive Methoden zur Modellierung von Stofftransport im Klüftgestein*. PhD thesis, Institute of Fluid Mechanics, Hannover University, 1997.
  26. C. Thorenz. *Model adaptive simulation of multiphase and density driven flow in fractured and porous media*. PhD thesis, Institute of Fluid Mechanics, Hannover University, 2001.
  27. R. Kaiser. *Gitteradaption für die Finite-Elemente-Modellierung gekoppelter Prozesse in klüftig-porösen Medien*. PhD thesis, Institute of Fluid Mechanics, Hannover University, 2001.

28. A. Habbar. *Direkte und inverse Modellierung reaktiver Transportprozesse in klüftig-porösen Medien*. PhD thesis, Institute of Fluid Mechanics, Hannover University, 2001.
29. M. Kohlmeier. *Coupling of thermal, hydraulic and mechanical processes for geotechnical simulations of partially saturated porous media*. PhD thesis, Institute of Fluid Mechanics, Hannover University, 2006.
30. T. Rother. *Geometric modelling geo-systems*. PhD thesis, Institute of Fluid Mechanics, Hannover University, 2001.
31. S. Moenicks. *Grid generation for simulation of flow and transport processes in fractured porous media*. PhD thesis, Institute of Fluid Mechanics, Hannover University, 2004.
32. O. Kolditz and S. Bauer. A process-oriented approach to computing multi-field problems in porous media. *Journal of Hydroinformatics*, 6:225–244, 2004.
33. W. Wang and O. Kolditz. Object-oriented finite element analysis of thermo-hydro-mechanical (thm) problems in porous media. *International Journal for Numerical Methods in Engineering*, 69(1):162–201, 2007.
34. I. Engelhardt. *Experimental and numerical investigations with respect to the material properties of geotechnical barriers*. PhD thesis, Tuebingen University, 2003.
35. J. de Jonge. *Contributions to computational geotechnics: Non-isothermal flow in low-permeable porous media*. PhD thesis, GeoHydrology and HydroInformatics, Center for Applied Geosciences, Tuebingen University, 2004.
36. R. Walsh. *Numerical modeling of THM coupled processes in fractured porous media*. PhD thesis, GeoHydrology and HydroInformatics, Center for Applied Geosciences, Tuebingen University, 2007.
37. M. Beinhorn. *Contributions to computational hydrology: Non-linear flow processes in subsurface and surface hydrosystems*. PhD thesis, GeoHydrology and HydroInformatics, Center for Applied Geosciences, Tuebingen University, 2005.
38. C. Beyer. *Applied numerical modeling of saturated / unsaturated flow and reactive contaminant transport: evaluation of site investigation strategies and assessment of environmental impact*. PhD thesis, GeoHydrology and HydroInformatics, Center for Applied Geosciences, Tuebingen University, 2007.
39. B. Miles. *Practical approaches to modeling natural attenuation processes at LNAPL contaminated sites*. PhD thesis, GeoHydrology and HydroInformatics, Center for Applied Geosciences, Tuebingen University, 2007.
40. H. Tenzer. *Comparison of the exploration and evaluation techniques of Hot Dry Rock Enhanced Geothermal sites at Soultz-sous-Forêts and Urach Spa in the framework of the geomechanical facies concept*. PhD thesis, GeoHydrology and HydroInformatics, Center for Applied Geosciences, Tuebingen University, 2006.
41. T. Kalbacher. *Geometric modelling and 3-D visualization of hydrogeological systems: Software desing and application*. PhD thesis, GeoHydrology and HydroInformatics, Center for Applied Geosciences, Tuebingen University, 2006.

42. J. Gronewold. *Entwicklung eines Internet-Informationssystems zur Modellierung natürlicher Ruckhalte- und Abbauprozesse im Grundwasser*. PhD thesis, GeoHydrology and HydroInformatics, Center for Applied Geosciences, Tuebingen University, 2006.
43. C. Chen. *Integrating GIS methods for the analysis of geosystems*. PhD thesis, GeoHydrology and HydroInformatics, Center for Applied Geosciences, Tuebingen University, 2006.
44. S. Bauer. *Process based numerical modelling as a tool for aquifer characterization and groundwater quality evaluation*. Habilitation, GeoHydrology and HydroInformatics, Center for Applied Geosciences, Tuebingen University, 2006.
45. C.I. McDermott. *Reservoir Engineering and System Analysis: Hydraulic, Thermal and Geomechanical Coupled Processes in Geosystems*. Habilitation, GeoHydrology and HydroInformatics, Center for Applied Geosciences, Tuebingen University, 2006.
46. G. Kosakowski. *Transport in fractured media: Concepts, Models, and Applications*. Habilitation, GeoHydrology and HydroInformatics, Center for Applied Geosciences, Tuebingen University, 2007.
47. C.-H. Park, C. Beyer, S. Bauer, and O. Kolditz. A study of preferential flow in heterogeneous media using random walk particle tracking. *Geosciences Journal*, 12(3):285–297, 2008.
48. O. Kolditz, J.-O. Delfs, C. Buerger, M. Beinhorn, and C.-H. Park. Numerical analysis of coupled hydrosystems based on an object-oriented compartment approach. *Journal of Hydroinformatics*, 10(3):227–244, 2008.
49. M. Xie, S. Bauer, O. Kolditz, T. Nowak, and H. Shao. Numerical simulation of reactive processes in an experiment with partially saturated bentonite. *Journal of Contaminant Hydrology*, 83(1–2):122–147, 2006.
50. B. Zehner, N. Watanabe, and O. Kolditz. Visualization of gridded scalar data with uncertainty in geosciences. *Computers and Geosciences*, 36(10):1268–1275, 2010.
51. K. Rink, T. Kalbacher, and O. Kolditz. Visual data exploration for hydrological analysis. *Environmental Earth Sciences*, 65(5):1395–1403, 2012.
52. W. Wang, G. Kosakowski, and O. Kolditz. A parallel finite element scheme for thermo-hydro-mechanical (thm) coupled problems in porous media. *Computers and Geosciences*, 35(8):1631–1641, 2009.
53. J.-O. Delfs. *An Euler-Lagrangian concept for transport processes in coupled hydrosystems*. PhD thesis, GeoHydrology and HydroInformatics, Center for Applied Geosciences, Tuebingen University in cooperation with Helmholtz Centre for Environmental Research UFZ and Technische Universität Dresden, 2010.
54. H. Shao. *Modelling reactive transport processes in porous media*. PhD thesis, Technische Universität Dresden, Chair of Applied Environmental System Analysis, Helmholtz Centre for Environmental Research UFZ, Department of Environmental Informatics, 2010.

55. F. Sun. *Computational hydrosystem analysis: Applications to the Meijiang and Nankou catchments in China*. PhD thesis, Technische Universität Dresden, Chair of Applied Environmental System Analysis, Helmholtz Centre for Environmental Research UFZ, Department of Environmental Informatics, 2011.
56. N. Watanabe. *Finite element method for coupled thermo-hydro-mechanical processes in discretely fractured and non-fractured porous media*. PhD thesis, Technische Universität Dresden, Chair of Applied Environmental System Analysis, Helmholtz Centre for Environmental Research UFZ, Department of Environmental Informatics, 2012.
57. T. Kalbacher, J.-O. Delfs, H. Shao, W. Wang, M. Walther, L. Samaniego, C. Schneider, R. Kumar, A. Musolff, F. Centler, F. Sun, A. Hildebrandt, R. Liedl, D. Borchardt, P. Krebs, and O. Kolditz. The IWAS-ToolBox: Software coupling for an integrated water resources management. *Environmental Earth Sciences*, 65(5):1367–1380, 2012.
58. E. Ballarini. *Transverse mixing in conservative and reactive transport: numerical simulation of homogeneous and heterogeneous laboratory experiments*. PhD thesis, Christian-Albrechts Universität zu Kiel, 2012.
59. A. Zech. *Impact of Aquifer Heterogeneity on Subsurface Flow and Salt Transport at Different Scales*. PhD thesis, Friedrich-Schiller Universität Jena, Helmholtz Centre for Environmental Research UFZ, Department of Computational Hydrosystems, 2012.
60. Y.Y. Sun. *Water quality simulation with particle tracking method*. PhD thesis, Technische Universität Dresden, Chair of Applied Environmental System Analysis, Helmholtz Centre for Environmental Research UFZ, Department of Environmental Informatics, 2013.
61. W. Xu. *Investigation of gas migration in saturated argillaceous rock*. PhD thesis, Technische Universität Dresden, Chair of Applied Environmental System Analysis, Helmholtz Centre for Environmental Research UFZ, Department of Environmental Informatics, 2013.
62. N. Boettcher. *Evaluation of thermal equations of state for CO<sub>2</sub> in numerical simulations*. PhD thesis, Technische Universität Dresden, Institut für Grundwasserwirtschaft, 2013.
63. M. English. *Coupled process modelling with applications to radionuclide storage and disposal*. PhD thesis, University of Edinburgh, 2013.
64. M. Walther. *Variable-Density Flow Processes in Porous Media On Small, Medium and Regional Scales*. PhD thesis, Technische Universität Dresden, Institut für Grundwasserwirtschaft, 2014.
65. T. Nowak, H. Kunz, D. Dixon, W. Wang, U.-J. Goerke, and O. Kolditz. Coupled 3-d thermo-hydro-mechanical analysis of geotechnological in situ tests. *International Journal of Rock Mechanics and Mining Sciences*, 48(1):1–15, 2011.
66. G. Bloecher and G. Zimmermann. Settle3D - A numerical generator for artificial porous media. *Computers & Geosciences*, 34(12):1827–1842, 2008.
67. M. Cacace, B.O. Kaiser, and B. Lewerenz. Geothermal energy in sedimentary basins: What we can learn from regional numerical models. *Chemie der Erde - Geochemistry*, 70(3):33–46, 2010.

# Appendix B

## OGS—Software Engineering

Lars Bilke

The OpenGeoSys software development community is distributed all over the world and people with different backgrounds are contributing code to a complex software system. The following points have to be addressed for successful software development:

- Platform independent code
- A single build system
- A version control system
- A collaborative project web site
- Continuous builds and testing
- Providing binaries and documentation for end users

OpenGeoSys should run on a PC as well as on a computing cluster regardless of the operating system. Therefore the code should not include any platform specific feature or library. Instead open source and platform independent libraries like Qt<sup>1</sup> for the graphical user interface or VTK<sup>2</sup> for visualization algorithms are used so that developers can simply use the platform or tools they want.

Despite the use of platform independent code and libraries, in the end there must be platform specific build settings such as Unix makefiles or project files for integrated development environments like Visual Studio or Eclipse. These are generated by the CMake<sup>3</sup> build system which is configured using platform independent configuration files. Also, CMake enables so-called *out of source builds* which means that all the generated files are separated from the source code. This makes it easier to manage the source code in a version control system.

---

<sup>1</sup> Qt: <http://qt-project.org>.

<sup>2</sup> The Visualization Toolkit: <http://www.vtk.org>.

<sup>3</sup> CMake: <http://www.cmake.org>.

A source code management and version control system is a definite requirement for distributed software development. For this purpose subversion<sup>4</sup> is used, which enables developers to work on separate versions (*branches*) of the software and to merge those versions at some point to the official one.

The version control system is integrated into an information and collaboration website based on a wiki<sup>5</sup> system. The wiki is used for collecting information such as tutorials, application examples and case studies. Discussions take place in the OpenGeoSys mailing list.<sup>6</sup>

To improve code stability and to verify code correctness a continuous build and testing system, based on the Jenkins Continuous Integration Server,<sup>7</sup> has been established. This server is connected to the version control system and does the following on every code change:

- Compiles (*builds*) the code on every supported platform (Linux, Windows, MacOS)
- Runs a comprehensive test suite of over 170 benchmarks
- Verifies the test results
- Runs software development related metrics on the code (like compiler warnings, code complexity, static analysis tools)
- Generates source code documentation
- Provides binaries for end users and uploads them to [www.opengeosys.org](http://www.opengeosys.org)
- Informs developers on errors

These points enhance the software development process considerably. Firstly, platform independence is maintained. Additionally, errors in the source code, and at which time they were introduced, can be tracked down easily. Lastly, developers gain access to code analysis tools and up-to-date source code documentation without the need to install it on their own machines.

Figure B.1 shows an overview of the software engineering workflow and concludes this section.

---

<sup>4</sup> Subversion: <http://subversion.tigris.org/>.

<sup>5</sup> TracWiki: <http://trac.edgewall.org/wiki/TracWiki>.

<sup>6</sup> OGS-Mailinglist: <http://groups.google.com/group/ogs6>.

<sup>7</sup> Jenkins: <http://jenkins-ci.org/>.

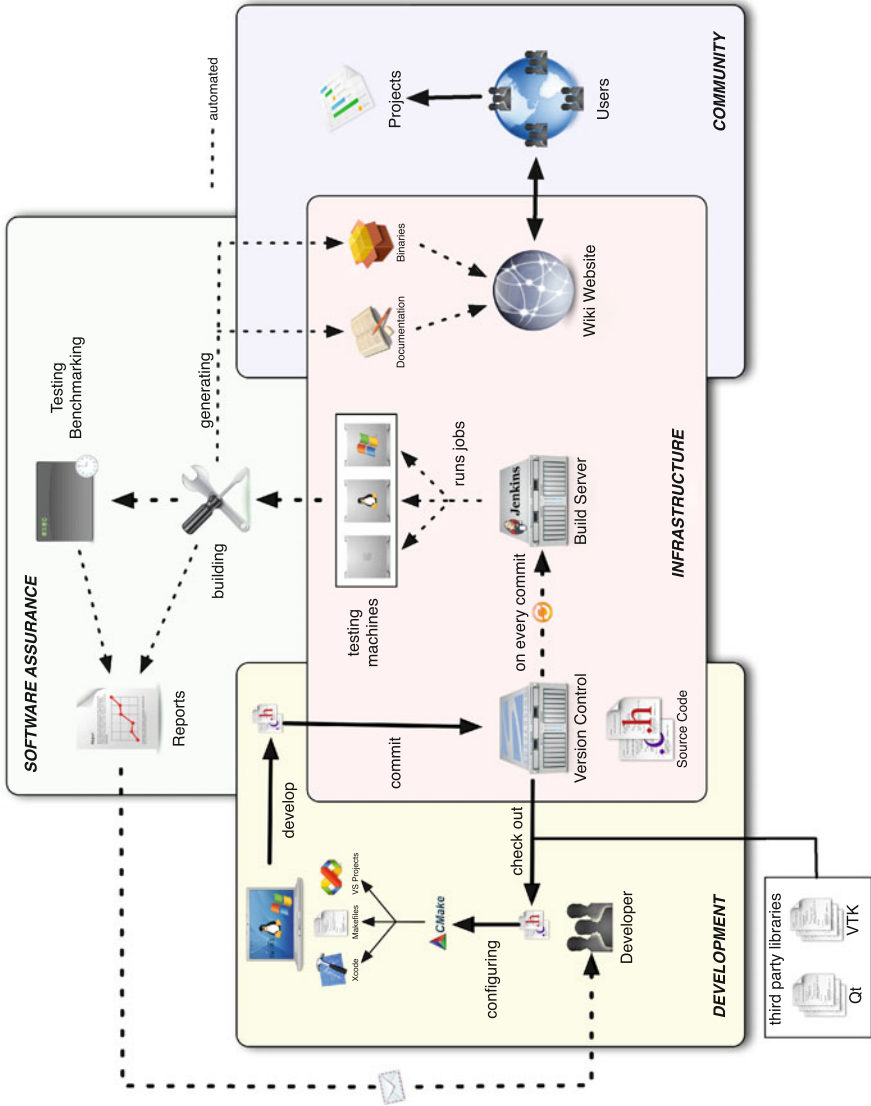


Fig. B.1 Overview of the OpenGeoSys software engineering workflow

# Appendix C

## Data Preprocessing and Model Setup with OGS

Karsten Rink

The *OpenGeoSys* software framework contains multiple algorithms for the simulation of (coupled) thermal, hydrological, mechanical and chemical processes using a large amount of FEM-related functionality and various numerical solvers. However, it does not provide functionality to actually set up a model. As a command line tool, it also does not support data visualization or modification; and even simulation results cannot be directly verified without the help of other software.

To address these issues, the *OpenGeoSys Data Explorer* has been developed as a graphical user interface for *OpenGeoSys* (Fig. C.1). This framework allows to visualize and assess input data as well as simulation results in a 3D space. Additional non-spatial information, such as time series data or borehole stratigraphies attached to 3D data sets, may be viewed in separate 2D windows. As with the *OpenGeoSys* simulation software itself, the *Data Explorer* is platform independent and employs the same basic data structures and file formats as the command line tool. In addition, it does also provide a large number of interfaces for the import of files created by established geoscientific software products such as the geographic information system *ArcGIS*, the groundwater modeling software *GMS* and, to a certain degree, complex software solutions used in the mining or petroleum industry such as *Petrel* or *Gocad*. For an overview of supported file formats see Table C.1. Furthermore, all data sets can be exported to established graphics formats, allowing to create visualization projects for presenting complex environmental data and simulations in an easy-to-understand manner (see Appendix E for details).

The *Data Explorer* supports users when preparing simulations by allowing them to see how various data sets complement or interact with each other. When heterogeneous data sets from different sources are integrated into a model, inconsistencies between those data sets are a frequently encountered problem. Typical examples in the scope of hydrological data include the course of rivers not quite matching the underlying terrain model, subsurface layers penetrating each other or boreholes

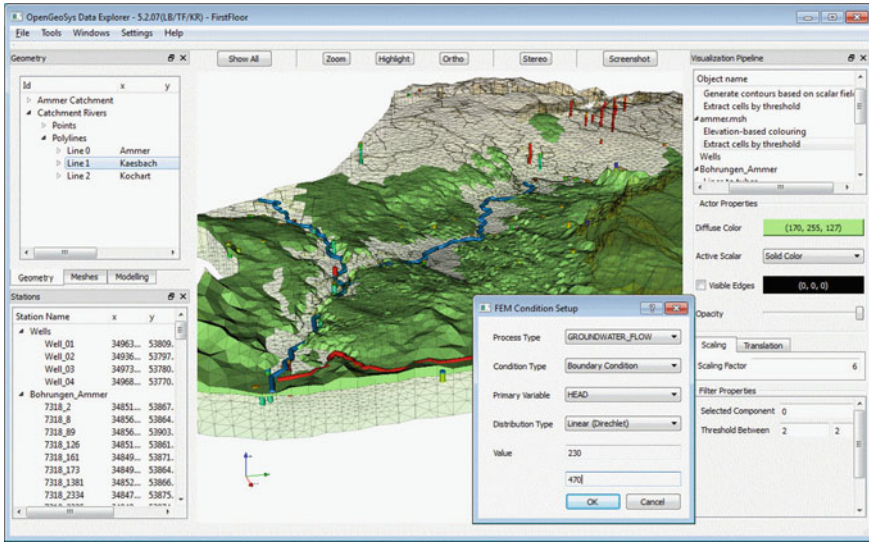


**Fig. C.1** The graphical user interface of the *Data Explorer* showing a number of data sets from a groundwater recharge study [1]

**Table C.1** Overview of existing interfaces

Data type	Formats/Programmes
Raster data	GeoTIFF, Esri ASCII Raster, NetCDF, JPEG, etc.
Features	Esri Shapes, Petrel borehole data, GMS borehole data
Meshes	FEFLOW, GMS, GMSH, TetGen, VTK, etc.
Time series data	CSV, WaterML
Graphic formats	VTK, OpenSG, Unity, VRML

not starting at ground level but instead above or below the surface. The reasons for such inconsistencies are manifold and can be attributed to different data acquisition methods (such as remote sensing data scanned from orbit via satellites, borehole logs created manually using core samples, etc.), data conversion problems, artifacts in the data (e.g. due to cloud cover or water reflection in satellite data or extreme weather events at observation sites) or human errors when transferring data. However, if models for the simulation of processes such as groundwater recharge are based on faulty or conflicting information they might produce erroneous or deceptive results.

The option to visualize the data in an interactive 3D scene allows to at least roughly assess the quality of the data and detect inconsistencies, artifacts or missing information by visual inspection. The *Data Explorer* provides a number of visualization options to support users in this assessment process by allowing the adjustment of a number of parameters for each data set. Generic parameters such as super elevation factors, transparency, or the color lookup table used for depicting data sets can be easily defined. More advanced algorithms include the selection of specific materials or

stratigraphic layers while concealing the rest of the data set, highlighting certain features for better visibility, and the calculation of isosurfaces from volumetric data [2]. In addition, the framework shows the underlying data of visualized objects (such as point coordinates, mesh element information, etc.) in tabular form in a separate menu for verifying information based on exact numbers. The *Data Explorer* offers several options for modifying data sets to a certain degree. For example, geometric surfaces can be triangulated, polylines can be connected in a user-defined sequence and data might be converted or mapped to other data sets using a number of different algorithms. In addition, the material groups of existing models can be changed, mesh elements can be removed based on a number of criteria and subsets of existing domains can be extracted based on triangulated surfaces [3].

Finite element meshes can be created from geometry data and, optionally, digital elevation models. Parameters such as the density of mesh elements and the degree of adaptive refinement towards selected features can be defined by the user. Point and line data used during the triangulation process will be integrated into the mesh structure as mesh nodes or edges, respectively (Fig. C.3a). Initial and boundary conditions can then be created and assigned either to these geometric objects or directly to mesh nodes (Fig. C.2). For existing meshes it is also possible to check the quality of all mesh elements with respect to well-establish criteria. Implemented metrics include the ratio of the longest to shortest element edge or the equiangular skew (i.e. deviation from the optimal inner angle of an element). Results of such an analysis are mapped onto the mesh (Fig. C.3a, b, c) and can be further refined using a number of visualization techniques, incorporating other data sets when required.

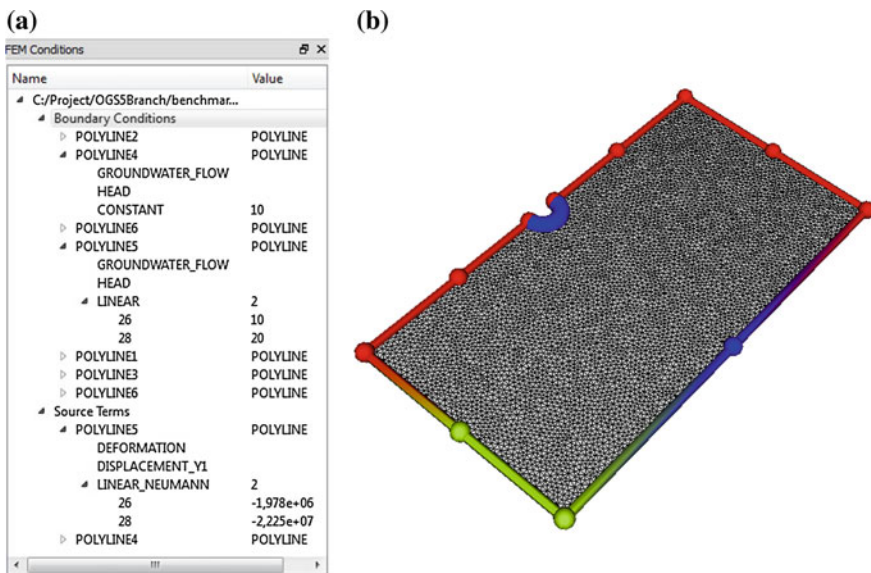


**Fig. C.2** Example for visualization of FEM related data. Depicted are a number of boundary conditions for a FEM Mesh along with detailed information about their properties

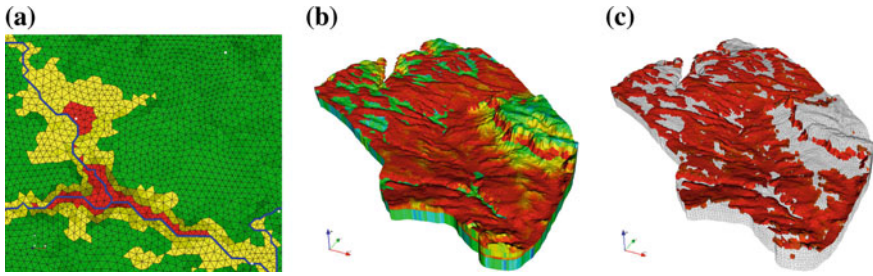


**Fig. C.3** Mesh quality validation: **a** Embedding geometric information representing rivers (*blue*) and wells (*white*) into the mesh structure. **b** Element quality based on edge ratio. *Red/orange* signifies large differences in edge length, *green/blue* signifies roughly equilateral elements. **c** Further analysis reveals that elements with a large edge ratio are the result of a thin surface layer

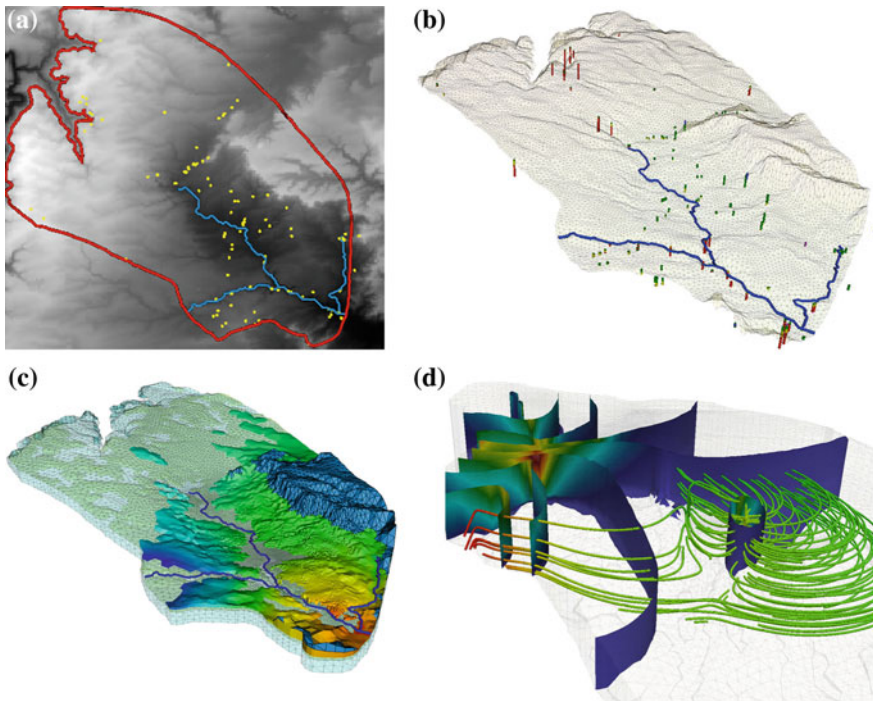


**Fig. C.4** Visualization of data sets at various stages of the modeling process. **a** Input data from geographic information systems (GIS). **b** 3D surface model based on GIS data. **c** Subsurface model with layers interpolated based on borehole data. Different information is displayed for each geological layer. **d** Representation of simulation results using established visualization techniques such as isosurface and streamtracers

Once simulation results are available, they can be visualized concurrently with input and model data in the *Data Explorer*. Such an integrated visualization is helpful for verifying the plausibility of simulation results. Correlations to input data sets might become visible and a comparison between observed and simulated parameters is easily accomplished. An overview over the data visualization at various stages of the modeling process is given in Fig. C.4.

For more information on the topics discussed in this appendix, the interested reader is referred to articles on model creation [3] and visualization [2] using the *OpenGeoSys Data Explorer*. A comprehensive specification of the functionality of the framework can also be found in the *OpenGeoSys Data Explorer User Manual* [4] available from <http://www.opengeosys.org> together with the simulation software and user interface.

**Acknowledgements** We would like to thank Benny Selle for provided the data from the *Ammer* groundwater study [1] that have been the basis for all figures in this appendix. This study is part of the WESS project (Water & Earth System Science), which is supported by a grant from the Ministry of Science, Research and Arts of Baden-Württemberg (AZ Zu 33-721.3-2) and the Helmholtz Center for Environmental Research, Leipzig (UFZ).

## References

1. B. Selle, K. Rink, and O. Kolditz. Recharge and discharge controls on groundwater travel times and flow paths to production wells for the ammer catchment in southwestern germany. *Environmental Earth Sciences*, 69(2):443–452, 2013.
2. K. Rink, L. Bilke, and O. Kolditz. Visualisation Strategies for Environmental Modelling Data. *Env Earth Sci*, 2014.
3. K. Rink, T. Fischer, B. Selle, and O. Kolditz. A Data Exploration Framework for Validation and Setup of Hydrological Models. *Env Earth Sci*, 69(2):469–477, 2013.
4. K. Rink. The OpenGeoSys Data Explorer Manual. Technical report, Department of Environmental Informatics, Helmholtz Centre for Environmental Research - UFZ, Leipzig, Germany, 2013.

# Appendix D

## GINA-OGS

**Herbert Kunz**

During the development of the numerical code OpenGeoSys, a program GINA as a pre- and post-processing tool, was developed by the German Federal Institute for Geosciences and Natural Resources (BGR). As an OpenGeoSys user, the development of GINA has continuously matched the requests of applicants. In the field of deep geological disposal of radioactive waste, coupled THMC process modelling is vital for planning and evaluation of experiments in the underground laboratory, for process understanding, and for long-term safety assessment with the complicated geological and geotechnical geometry (Fig. D.1). With the help of GINA, time-consuming handling of pre- and post-processing for a FE-simulation is easy.

The main features of this interactive graphical user interface tool GINA are:

### Pre-processing

- Geometrical data for FE meshing The geometrical objects (points, polylines, surfaces and volumes) can be defined using coordinates input and/or with a mouse, which are the basic objects in the code OpenGeoSys for mesh generating, definition of initial and boundary conditions, and results viewing
- Preparing of finite element parameters Necessary parameters and conditions (initial conditions, boundary conditions, and material properties) can be interactively defined using keyboard and mouse input

### Mesh Generation

A mesh generator for structured meshes in 2D (quad) and 3D (prism and hexahedral) elements is implemented in GINA. A special feature for the generation of finite element mesh for a fracture network with surrounding rock mass was developed in

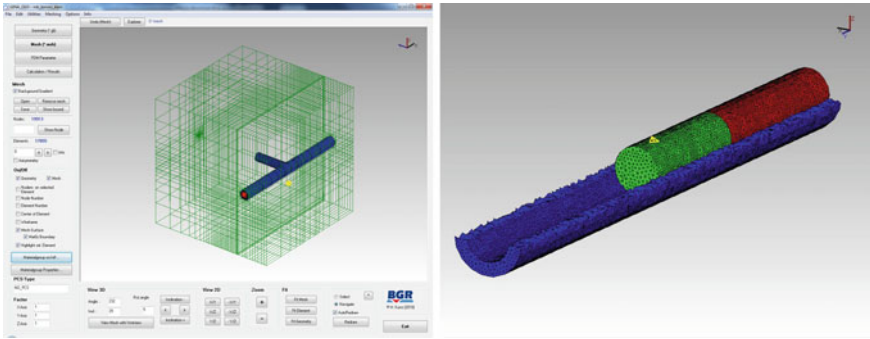


**Fig. D.1** GINA functions and generated mesh of a rock-EDZ-tunnel system

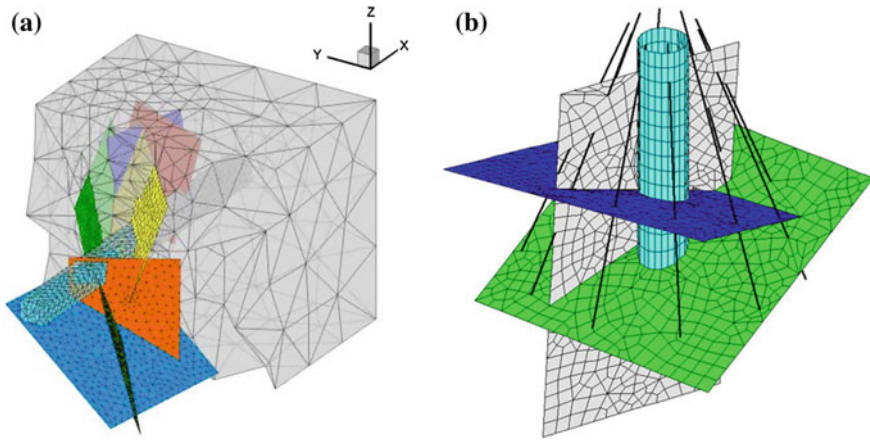


**Fig. D.2** Finite element mesh for a coupled fracture network and rock mass model (a) and fracture-borehole system (b)

the course of the BGR investigation program for fracture flow at Grimsel Test Site (Switzerland) (Fig. D.2).

For the unstructured meshes in 2D and 3D, an interface to the open source software, e.g. GMSH ([www.geuz.org/gmsh](http://www.geuz.org/gmsh)) for unstructured triangle and quad-elements and TetGen (<http://tetgen.berlios.de>) for tetrahedral elements, is implemented in GINA. With the help of the interface, a high quality mesh of 2D and 3D complex structures can be generated using GMSH and Tetgen based on the geometrical objects in the code OpenGeoSys.

## **Post-processing**

Using the post-processing functions, simulation results from the OpenGeoSys can be visualized and evaluated during model calculation in the following cases:

- Contour, colour, and isoline plots in the 2D domain
- X/Y - diagram versus time or along a polyline
- Convert to mechanical principle stress from stress field and viewing in vector form

## **Data Interface**

To interact with other programs GINA has the following import and export formats:

- Import File Formats: GMSH, TetGen, Tecplot, DXF, ASCII.
- Export File Formats: GMSH, TetGen, JPG, VRML, Excel

## **Contact Information**

For more information, please contact: [herbert.kunz@bgr.de](mailto:herbert.kunz@bgr.de)

# Appendix E

## Scientific Visualization and Virtual Reality

Carolyn Helbig and Lars Bilke

The first question that appears, when it comes to the matter of spending time for generating a visualization to represent research results, is: Why all the effort? Is it really worth it? This article wants to give basic insights into scientific visualization. With the help of an example workflow, the possibilities of supporting the analysis of research results are shown. Furthermore, we describe how to use a virtual reality (VR) environment for presenting visualizations and specify the benefits of its use.

The term *Scientific Visualization* was introduced in 1987 by the National Science Foundation (NSF) in the *Visualization in Scientific Computing* report and defined it as the use of computer graphics for the analysis and presentation of computed or measured scientific data [1]. The first image classified as scientific visualization is from John Snow, who drew a map of London and tagged the houses of the people who suffered from Cholera, in 1854. With the help of this map, he could detect a correlation between water supply and the disease incidents. This is meant to be the first time when someone used graphics for the analysis of a certain question.

Later on, in 1994 H. Senay and E. Ignatius defined scientific visualization as a tool that “[...] supports scientists and relations, to prove or disprove hypotheses, and discover new phenomena using graphical techniques. The primary objective in data visualization is to gain insight into an information space by mapping data onto graphical primitives” [2]. Because a huge variety of scientific fields play a role in this process, scientific visualization combines knowledge from various disciplines and therefore is an interdisciplinary area.

The goals of scientific visualization can be generally classified in three categories. The first one is the exploration, where nothing is known about the data at the beginning. It is used for getting a first insight into the data and for detecting interesting areas. The second is the analysis based on one or more hypothesis, which are going to be proved and at the end verified or falsified. When the exploration and analysis phase is completed, the visualization can be used for presentation in order to communicate the results to colleagues, stakeholders, or project leaders.

One domain of scientific visualization deals with the visualization of environmental data. Growing environmental problems in a complex, globalized world are explored in research projects. Because of an expansion of observation activities, the

amount of data grows very quickly. Analyzing it can be challenging and leads to an increasing impact of scientific visualization. In the following, a workflow for visualization of weather and climate data is presented as a showcase. Atmospheric science is an important area in consideration of the fact that climate change will influence our environment and living conditions in the future. For that matter, climate simulations are needed to predict possible changes which generate large data sets. The visual combination of simulation data with observation data, data based on different models, or even with models of various fields of science, offered by scientific visualization brings important benefits for the analysis of research results. It helps to identify correlations and to study key processes.

To manage the process from heterogeneous simulation and observation raw data to an interactive visualization, which can be displayed on a desktop computer or in an interactive virtual reality environment, a workflow that contains a plurality of preprocessing steps is needed (see Fig. E.1). It includes a set of software applications and scripts. The outcomes of it are easy-to-understand visualizations of complex data sets that are the basis for the evaluation and verification of models as well as for scientific communication and interdisciplinary discussions of the research results.

The workflow includes three steps: data integration, visualization methods and data composition, and presentation and evaluation. In the first step the data is provided by a number of sources; they can include research facilities, regional authorities and in some projects companies. In addition, the data used for the visualization is very heterogeneous. It consists of raster data (e.g. observed data), multi-dimensional arrays (e.g. simulation data) and vector data (e.g. borders, observation sites). All data includes coordinates for geo referencing as well as the corresponding coordinate system and projection. In our example, the simulation data is provided by the Institute of Physics and Meteorology of the University of Hohenheim as part of the WESS project [4]. Other data used for the case study include administrative divisions, river networks, water bodies, political boundaries, and raster data such as the digital elevation model. For the visualization of atmospheric models, there are variables from three different compartments: atmosphere, surface and soil. To analyze atmospheric processes it is necessary to examine the interaction and influences between these compartments. For including all the data into the visualization

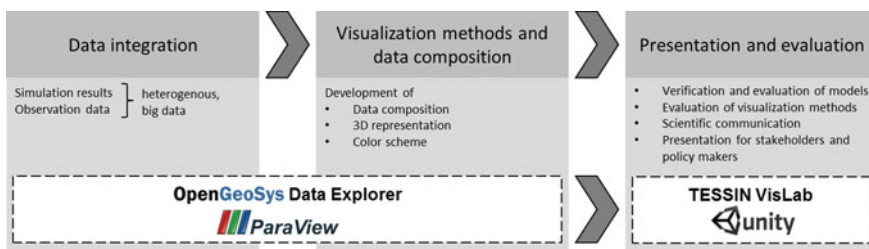


**Fig. E.1** The example workflow includes three steps that lead from data integration to the presentation of the visualization. The recommended software is all freely available [3]

system, some pre-processing like format conversions and coordinate transformations is necessary. Therefore we used ParaView and the OpenGeoSys Data Explorer.

The second step of the workflow is the development of appropriate visualization methods for the variables of the data. Choosing the appropriate representation for each variable and developing a color scheme for the set of variables helps to distinguish them. Attributes such as color (hue, brightness, and saturation), opacity, and shape can be used. Combinations of these can also be appropriate. If the resolution of the data is too high to make every value visible, it can be useful to select only a subset. This can be done by defining a range for values, choosing values randomly, or by down-sampling the data. In some cases, even concatenations of these selections are suitable. Figures E.2 and E.3 show two examples of the visualization results: The first one is used to give an overview of the case study area and in the second one simulation and observation data is visually combined.

The third step of the workflow includes the presentation and evaluation. It is used for scientific communication and presentation for stakeholders and policy makers as well as to verify and evaluate research results. Our working environment is

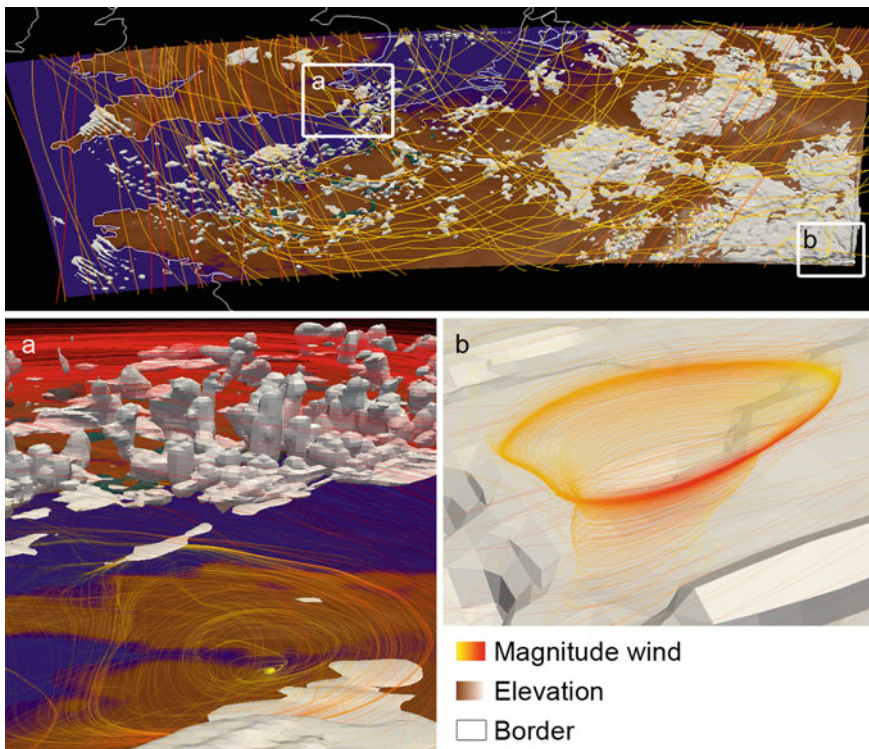


**Fig. E.2** The visualization provides an overview that helps to identify interesting structures like turbulences in (a) and (b). They can be examined in detail in a following step, for example by extracting a subset of the region [3]

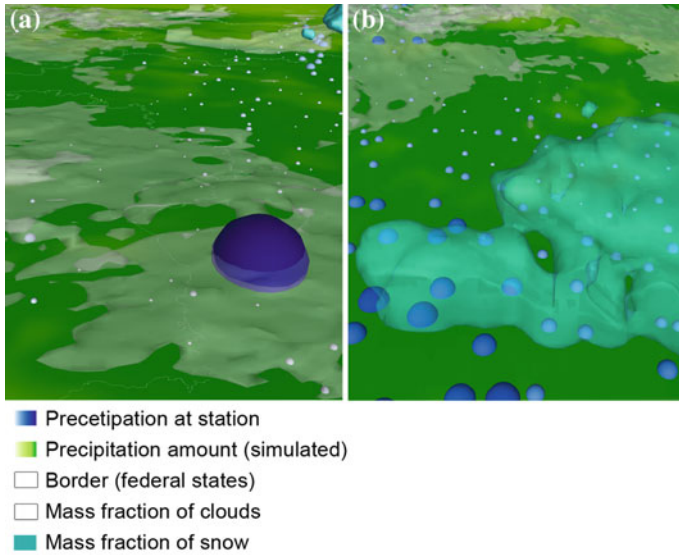


**Fig. E.3** The visual combination of simulation and observation data is used to detect inconsistencies or even errors like in (a) where one station value is significantly higher than the values at all neighbor stations. Figure (b) shows the overlapping of the simulated precipitation (isosurfaces) and the precipitation that was measured at weather stations (spheres) [3]

the TESSIN VISLab of the Helmholtz Centre for Environmental Research—UFZ. The hardware setup of the VISLab uses a back projection-based stereoscopic visualization environment with an approximately  $6 \times 3$  meter large main screen and corresponding projections on the floor and two side wings. In order to achieve a high resolution of nearly  $6400 \times 1800$  pixels, 13 projectors are used to run this system. Images are generated alternating for the left and the right eye and users wear special glasses which separate these images, resulting in a real three-dimensional view. For the stereo separation we can switch between two technologies—active stereo using shutter glasses and passive stereo using Infitec technology. We use an optical tracking system, compensating for movement of the observer. Images are computed such that correct perspective is maintained. A pointer device allows for interaction with the virtual environment. Our VR system helps us to better understand complex data sets as well as to present a challenging scientific question in a comprehensible way. The advantages of such VR environments for analyzing scientific data have been extensively studied [5, 6].

**Acknowledgements** We gratefully acknowledge the simulation data support of Hans Stefan-Bauer and Volker Wulfmeyer from the University of Hohenheim, Institute of Physics and Meteorology, Stuttgart and Dr. Andreas Marx (Helmholtz Center for Environmental Research) as well as CERA (Climate and Environmental Retrieving and Archiving) for providing the observation data. The first author would like to

express her gratitude to the European Social Fund (ESF) for the funding of the scholarship as part of the program “Europa fördert Sachsen”. We thank HIGRADE, the graduate school of UFZ [7], and CompeTE+ the school for doctoral students at the HTWK. The presented example of the visualization of atmospheric data is part of the WESS project, WESS is supported by a grant from the Ministry of Science, Research and Arts of Baden-Württemberg (AZ Zu 33-721.3-2) and the Helmholtz Center for Environmental Research, Leipzig.

## References

1. B.H. McCormick, T.A. DeFanti, and M.D. Brown. Visualization in scientific computing. *Computer Graphics*, 21:3–14, 1987.
2. H. Senay and E. Ignatius. A Knowledge-Based System for Visualization Design. *IEEE Computer Graphics & Applications*, 14:36–47, 1994.
3. C. Helbig, K. Rink, H.S. Bauer, V. Wulfmeyer, M. Frank, and O. Kolditz. Concept and workflow for 3D visualization of atmospheric data in a virtual reality environment for analytical approaches. *Environmental Earth Sciences*, 2014.
4. P. Grathwohl, H. Rügner, T. Wöhling, et al. Catchments as reactors—A comprehensive approach for water fluxes and solute turnover. *Environmental Earth Sciences*, 69(2):317–333, 2013.
5. B. Laha and D.A. Bowman. Identifying the Benefits of Immersion in Virtual Reality for Volume Data Visualization. In *Immersive Visualization Revisited Workshop of the IEEE VR conference*, pages 1–2, 2012.
6. E. Verbree, G. van Maren, R. Germs, F. Jansen, and M.-J. Kraak. Interaction in virtual world views-linking 3D GIS with VR. *International Journal of Geographical Information Science*, 13(4):385–396, June 1999.
7. B. Selle, K. Rink, and O. Kolditz. Recharge and discharge controls on groundwater travel times and flow paths to production wells for the ammer catchment in southwestern germany. *Environmental Earth Sciences*, 69(2):443–452, 2013.

# Appendix F

## OGS High-Performance-Computing

Wenqing Wang and Thomas Fischer

As described in the previous chapters, the thermo-hydro-mechanical/chemical (THMC) processes or their coupling in porous media within a specified domain can be described by partial differential equations (PDEs) for numerical modeling. Normally in real applications, these PDEs have to be solved numerically due to the complexity of the material or the geometrical nonlinearity and the irregularity in the studied geometrical domain.

As a first step of numerical modeling, a PDE has to be linearized by using the Newton or the Picard method if it is nonlinear. The linearized PDE can then be solved numerically, and the finite element method (FEM) is used for this purpose in OGS. As an essential procedure for the FEM, the studied geometrical domain has to be discretized into elements for the local and global assembly of vectors and matrices. The most resource-consuming tasks in the FEM consist of:

1. Computing entries of local matrices and adding them into a global system of linear equations—the local and global assembly, respectively.
2. Solving the global system of linear equations.

If the FEM is applied to solve an actual, large-scale problem, such as geothermal energy storage, CO<sub>2</sub> storage, nuclear waste storage and so on, for accurate results, the amount of computational resources including hardware and time can easily hit the physical limits of a computer. Therefore, the computational efficiency is a crucial issue to be taken into consideration when one deals with such real problems.

Nowadays, parallel computing is regarded as a promising and powerful approach to enhance the computational efficiency due to the dramatic progress in computer technology accompanied with price-dropping in recent decades.

In principle, there are two programming approaches for parallel computing: the shared memory approach and the distributed memory approach. In OGS, both approaches are used. The shared memory approach is implemented by using OpenMP (<http://openmp.org>) to parallelize the loops in one the iterative linear solvers in OGS. The distributed memory approach is employed for the parallelization of the most two resource-consuming tasks addressed above. For this purpose, the domain decomposition method [1] is used to partition computational tasks of the FEM, and

the parallelization is realized by using the Message Passing Interface standard (MPI, [2]). The details about our implementation and its verification are described in our two research papers [3, 4].

## F.1 Domain Decomposition Approach

The first step of the parallelization of the FEM is to decompose the mesh into sub-domains. For parallel computing, each compute core is assigned with the computation of one sub-domain. Hence, the global system of linear equations (matrix and right-hand side) is distributed among several compute cores. In our framework, this distributed system of linear equations is solved by a parallelized Krylov subspace method [5].

The decomposition has two aims: distribute the work as equally as possible to the compute cores and minimize the amount of communication between the compute cores because in most cases, communication results in waiting time.

There are two approaches for decomposing the mesh:

- Partitioning mesh by elements.
- Partitioning mesh by nodes.

### *Partitioning Mesh by Elements*

Partitioning mesh by elements decomposes the mesh such that every element belongs exactly to one sub-domain that is handled by one compute core. The local assembly—integration over the element—has the advantage that it does not require data communication from other sub-domains, i.e. for this task there is no communication needed among the compute cores.

On the other hand, there are element nodes shared by different sub-domains. In the FEM, each node is associated to a row and a column in the matrix and the right-hand side vector of the global system of linear equations. Since this system of linear equations is distributed to different compute cores, the element nodes shared by different sub-domains need inter-compute-node communication to update the associated values in the linear solver.

This approach is realized in OGS using MPI. The scalability is verified with a 3D THM problem on different platforms [3].

### *Partitioning Mesh by Nodes*

Partitioning mesh by nodes decomposes the mesh such that every element node belongs to exactly one sub-domain. As a consequence, there exist some elements

whose nodes belong to different sub-domains. These nodes are often referred to as ghost nodes. For the local assembly of elements consisting of at least one ghost node, i.e. the numerical integration over those elements, the information needed for the integration has to be computed and stored multiple times.

On the other hand, since mesh nodes are affiliated to exactly one sub-domain, the partitioning mesh by nodes approach does not need communication to update the entries within the global system of linear equations. This implies that one can parallelize the linear solver without any compute node communication for the vectors that are used in the solver. Under such consideration, the communication load during the linear solver can be reduced dramatically.

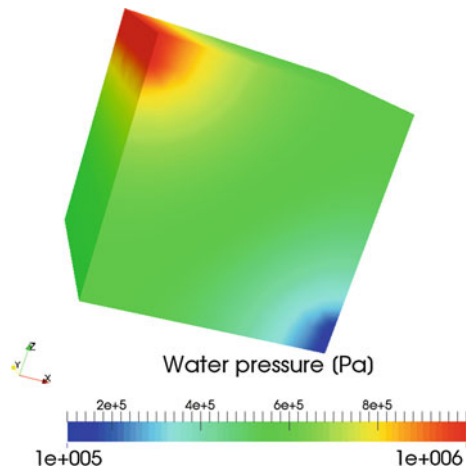
In OGS, this approach is implemented using the matrix and vector routines of PETSc [6], and the implementation has been investigated by several examples including a real application [4].

## F.2 Scalability Test with 10k Computer Cores

For the scalability test, a simple steady state problem is solved by the second parallelization approach using PETSc. The test domain consists of a cube with the dimensions  $10 \times 10 \times 10 \text{ m}^3$ , which is discretized into 15,624,750 hexahedra with 15,437,999 nodes. The domain contains a homogeneous porous medium which has a permeability of  $10^{-14} \text{ m}^2$ . The fluid viscosity is  $10^{-3} \text{ Pa s}$ . There are different pressures at two areas in the vicinity of two opposite edges as shown in Fig. F.1. The boundary values are  $10^6$  and  $10^5 \text{ Pa}$ , respectively.

One time step is solved for this steady state pressure distribution problem.

**Fig. F.1** Pore pressure distribution in a cubic domain of homogeneous porous medium



## Sequential I/O

In this case, the partitioned sub-domain meshes are written in a single ASCII file. During the execution of the program, the compute core with rank 0 reads the partitioned mesh data from the file. Then this compute core transmits chunks of the data to the corresponding compute core.

To demonstrate the scalability of the code, several parallel jobs have been conducted on JUQUEEN<sup>8</sup> with 512, 2,048, 4,096, and 10,000 cores, respectively. To solve the system of linear equations, we use the conjugate gradient method in combination with the parallel block Jacobi preconditioner *bjacobi* of PETSc [5].

The number of iterations for the convergence with a tolerance of  $10^{-7}$  is around 700 in all these jobs.

The time consumption in different computational tasks of the FEM in all finished jobs is listed in Table F.1, where the task of equation assembly includes the assembly of matrices and vectors, and applying the boundary conditions to the system of linear equations. One can see in Table F.1 that reading the mesh uses most of the computational time. The reading process is realized by setting one core to read ACSII sub-domain mesh data and passing the data to the corresponding data by using MPI\_BCast. Obviously, the reading process is not ideally parallelized, and its enhancement would be to employ MPI native reading function and use a binary mesh file. If many time steps are to be analyzed in a problem, the time necessary to read the mesh in a simulation will be a small portion of the total run time. Anyway, the reading of the mesh data only takes place once in a run of the program. Figure F.2 shows the speedup of the equation assembly and the linear solver of the present test.

## Parallel I/O

To improve the performance of I/O, the partition tool was changed in order to enable it to write all sub-domain meshes into a single binary file. Then, the reading of the mesh was re-implemented so as to allow multiple processors to read data from a common

**Table F.1** Time in seconds used in major computational tasks

Cores	Total	Mesh reading	Assembly	Linear solver	Others
512	1,370.81	1,171.70	79.75	87.85	39.60
2,048	1,379.22	1,312.49	21.45	21.94	23.83
4,096	1,546.23	1,438.89	13.71	11.55	79.92
10,000	1,802.76	1,624.53	8.49	5.19	161.25

<sup>8</sup> JUQUEEN is large supercomputer at the Institute for Advanced Simulation (IAS), Jülich Supercomputing Centre (JSC). In November 2013, JUQUEEN was listed at position 8 of the Top 500 supercomputers.

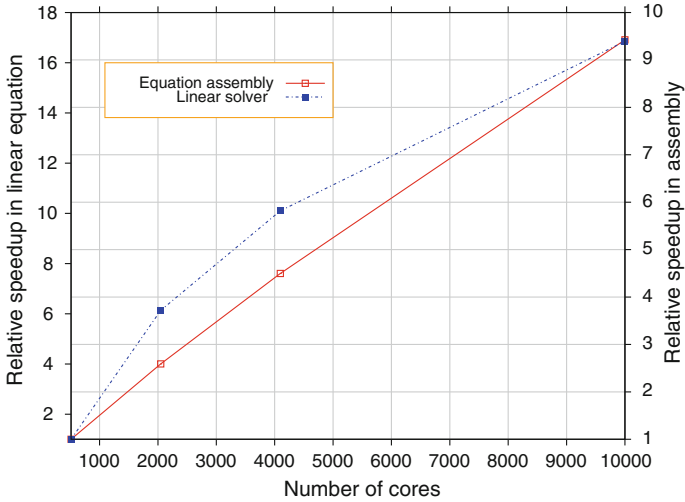


**Fig. F.2** Relative speedup in the assembly and the linear solver (starts with 512 cores)

**Table F.2** Time in seconds used in major computational tasks with the improved mesh reading

Cores	Total	Mesh reading	Assembly	Linear solver	Others
512	215.27	16.72	79.25	87.81	31.49
10,000	191.43	83.77	8.34	5.14	94.19

file simultaneously. Two tests with 512 and 10,000 partitions are carried out, and the results show that the time consumed in reading mesh has dropped significantly as shown in Table F.2.

### Remarks

A steady state problem is solved with the PETSc powered parallel OGS software for the test. If the problem is considered a transient one, and it is solved in  $n$  time steps, we can estimate the speedup of the parallel computing of the entire problem based on the present test results by the following formula

$$\text{speedup} = \frac{16.720083 + 31.4937 + 79.248473n + 87.81238n}{83.765145 + 94.188 + 8.34255n + 5.136329n}. \quad (\text{F.1})$$

Formula (F.1) is derived based on the data given in Table F.2 and the fact that the mesh data is only read once in the program. Figure F.3 shows the curve of formula (F.1). One can see from Fig. F.3 that the speedup approaches its limit of around 12 when the number of the time steps is larger than 300. In other words, we can get a speedup of 12 if the problem is transient and it has solved more than 300 time

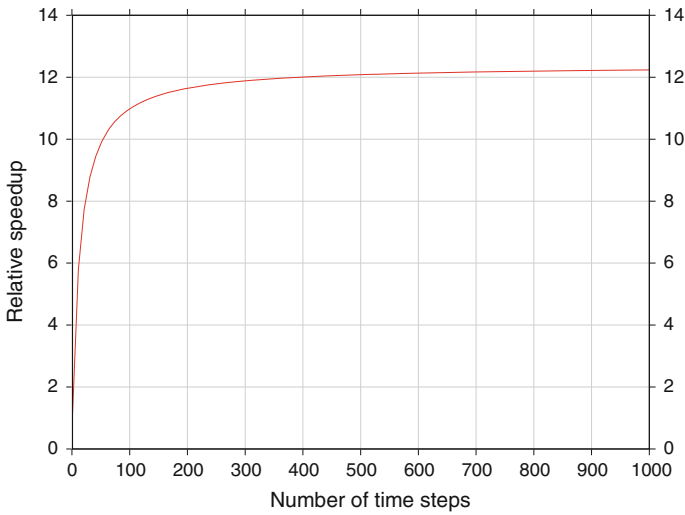


**Fig. F.3** Speedup estimations regarding to the number of time steps

steps. Ideally for the maximum number of partitions employed in the present test, the speed limit is  $10,000/512 \approx 19$  if every piece of the computational tasks is ideally parallelized and if there is no communication overhead at all.

The availability of high-performance-computing (HPC) infrastructures for research and even more importantly the availability of open-source software for HPC applications such as simulations of CO<sub>2</sub> migration at real reservoir scale

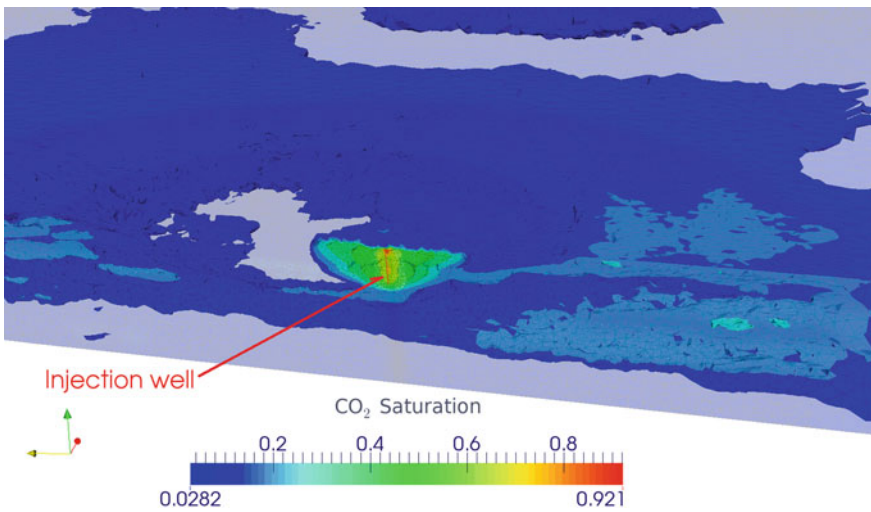


**Fig. F.4** Simulated CO<sub>2</sub> migration in a real reservoir

(Fig. F.4, [4, 7]) will provide scientific tools for resolving the paradigm of solving “complex physics at complex geometries” problems in the near future.

## References

1. Barry Smith, Petter Bjorstad, and William Gropp. *Domain decomposition: parallel multilevel methods for elliptic partial differential equations*. Cambridge University Press, 2004.
2. Lyndon Clarke, Ian Glendinning, and Rolf Hempel. The MPI message passing interface standard. In *Programming environments for massively parallel distributed systems*, pages 213–218. Springer, 1994.
3. W. Wang, G. Kosakowski, and O. Kolditz. A parallel finite element scheme for thermo-hydro-mechanical (thm) coupled problems in porous media. *Computers & Geosciences*, 35(8):1631–1641, 2009.
4. W. Wang, B. Zehner, Böttcher N., Görke U. J., and O. Kolditz. Parallel finite element solver for modeling two-phase flow processes in porous media: Opengeosys with petsc. *Computers & Geosciences*, under revision, 2014.
5. Yousef Saad. *Iterative methods for sparse linear systems*. Siam, 2003.
6. S. Balay, J. Brown, K. Buschelman, V. Eijkhout, W.D. Gropp, D. Kaushik, M.G. Knepley, L. Curfman McInnes, B.F. Smith, and H. Zhang. PETSc users manual. Technical Report ANL-95/11 - Revision 3.4, Argonne National Laboratory, 2013.
7. T. Kempka and M. Kuehn. Numerical simulations of CO<sub>2</sub> arrival times and reservoir pressure coincide with observations from the ketzin pilot site, germany. *Environmental Earth Sciences*, 70(8):3675–3685, 2013.